PRINCIPLES AND APPLICATIONS OF WAVEFRONT CODING

by

Gonzalo D. Muyo Nieto

Submitted for the Degree of

Doctor of Philosophy

at Heriot-Watt University

on Completion of Research in the

School of Engineering and Physical Sciences

June 2007

Abstract

The aim of the work reported in this thesis was to investigate the physical principles and potential applications of wavefront coding. This technique enables extended depth of field and greatly reduced sensitivity to defocus-related and higher-order aberrations whilst maintaining diffraction-limited resolution in incoherent imaging systems. Wavefront coding involves the introduction of an asymmetric refractive mask close to the aperture stop so as to encode the image with a specific point spread function that, when combined with decoding of the recorded image, can enable accurate image acquisition even in the presence of aberrations.

In practical imaging systems, this enhancement is subject to a range of constraints and limitations which have been neglected in previous works. We show that although wavefront coding has sometimes been presented as a panacea, it is more realistic to consider it as an additional parameter in the optimisation process. This research explores the trade offs involved in the application of wavefront coding to low-cost imaging systems for use in the thermal infrared and visible imaging systems, showing how very useful performance enhancements can be achieved in practical systems. Some of the original contributions of this work include the design of new phase masks, a new understanding of the fundamental physical principles in terms of the decomposition of the optical transfer function, appraisal of the restoration issues (detector sampling, noise amplification and artefacts in the digitally processed image) and the design and manufacture of a wavefront-coded infrared singlet.

To Ana and Elena.

Acknowledgements

I would like to thank Dr. Andy Harvey, my supervisor, for his many suggestions and constant support in the development of this research. I most especially appreciate his assistance and understanding as my personal circumstances became more complicated. Not many supervisors would have been as supportive and flexible as he has.

Samir Mezouari shared with me his knowledge of imaging systems with phase masks and provided many useful references and friendly encouragement. I would also like to thank my colleagues David Fletcher-Holmes, Alistair Gorman, Bertrand Lucotte, Mads Demenikov and Beatriz Grafulla of the Imaging Concept Group for their company and good humour: you have made a big difference; especially my office mates Eid Alabboud and the late Sonny Ramachandran, for the great time we had together.

I wish to thank the *epicurians* Abyd and Andresinho for their friendship, forged in that unique house in 15 Mentone Terrace. Also Simona, Manuel Maarek, Laurent and many others that I had the pleasure to meet.

Of course, I am grateful to my parents Alfredo and Elena, sister and brothers Elena, Alfredo and Fede. Thanks to Nines, Maricarmen and Elena I. An especial remembrance to Jovita.

I am indebted *for life* to my wife Ana (finally, you will have the weekends back to normal). Thanks a lot for your support during these difficult years of PhD. I was lucky to have had you for that. Thanks too for having been willing to leave the job you loved in Spain and move to Scotland so that I could take up this appointment at Heriot Watt University. Our stay in Edinburgh will always bring good memories. Most of all thank you for our intelligent, beautiful and happy *croquetilla* Elena who

lightens up our life everyday.

This work was carried out with funding from QinetiQ (Malvern, UK). I am grateful to this organisation and in particular to Dave Huckridge for making this project possible.

Edinburgh — Gonzalo Muyo

June, 2007

ACADEMIC REGISTRY
Research Thesis Submission

Name:	GONZALO D. MUYO NIETO		
School/PGI:	ENGINEERING AND PHYSICAL SCIENCES		
Version: *(i.e. First, Resubmission, Final)*	FINAL	Degree Sought:	PHD

Declaration

In accordance with the appropriate regulations I hereby submit my thesis and I declare that:

1) the thesis embodies the results of my own work and has been composed by myself
2) where appropriate, I have made acknowledgement of the work of others and have made reference to work carried out in collaboration with other persons
3) the thesis is the correct version of the thesis for submission*.
4) my thesis for the award referred to, deposited in the Heriot-Watt University Library, should be made available for loan or photocopying, subject to such conditions as the Librarian may require
5) I understand that as a student of the University I am required to abide by the Regulations of the University and to conform to its discipline.

* *Please note that it is the responsibility of the candidate to ensure that the correct version of the thesis is submitted.*

Signature of Candidate:	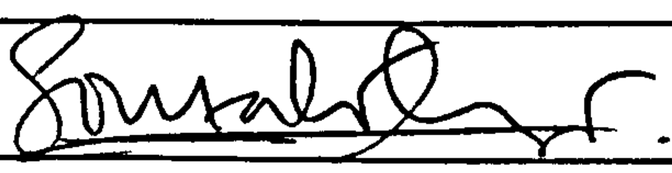	Date:	26th July 2007

Submission

Submitted By *(name in capitals)*:	GONZALO MUYO
Signature of Individual Submitting:	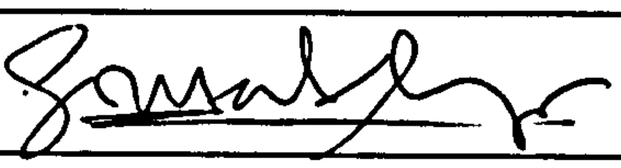
Date Submitted:	26th July 2007

For Completion in Academic Registry

Received in the Academic Registry by *(name in capitals)*:	J. WALLACE.		
Method of Submission *(Handed in to Academic Registry; posted through internal/external mail)*:	HANDED INTO ACADEMIC REGISTRY.		
Signature:		Date:	26-7-07.

Declaration

In the course of this thesis I have acknowledged the contributions to my research made by collaborators. The rest of the work presented here is mine alone.

Important contributions were made in the following areas

- Chapter 3: It was Samir Mezouari's suggestion to extend his previous work in order to produce a new phase mask for the alleviation of coma and astigmatism. He collaborated with me on the derivation of the quartic phase mask. The second part of the chapter originated from a significant mathematical error found in a journal paper. As a result, we collaborated with the author S.S. Sherif on the derivation of an antisymmetric phase mask for a circular aperture that mitigates the effect of defocus.

- Chapter 6: Amritpal Singh (Saab Bofors Dynamics, Sweden) carried out the digital image processing on the images acquired with the uncooled thermal singlet. He contributed both his expertise and algorithms. The germanium singlet was designed and manufactured by Qioptiq (UK).

Contents

Publications

Several peer-reviewed journal and conference papers in the field of imaging have resulted from my research:

Papers in journals:

- G. Muyo and A. R. Harvey, "Decomposition of the optical transfer function: wavefront coding systems", Opt. Letters, Vol. 30, 2005.

- S. Mezouari, G. Muyo and A. R. Harvey, "Circularly symmetric phase filters for control of primary third-order aberrations: coma and astigmatism", J. Opt. Soc. Am. A, Vol. 23, 2006.

- S. S. Sherif and G. Muyo and A. R. Harvey, "Comment on 'extended depth of field in hybrid imaging systems: circular aperture' ", J. Mod. Optics, Vol. 52, 2005.

Two journal papers pending:

- G. Muyo and A.R. Harvey, "Aliasing effect in a wavefront coding system with a cubic phase mask," this paper summarises chapter 5 and it will be submitted to J. Mod. Optics.

- G. Muyo, A. Singh, M. Andersson, D. Huckridge and A. R. Harvey, "Optimised thermal imaging with a singlet and pupil plane encoding: experimental realization," this paper summarises part of chapter 6 and it will be submitted to Opt. Express.

Chapter in book:

- A. R. Harvey, G. Muyo and S. Mezouari, "Wavefront-coded, hybrid imaging for the alleviation of optical aberrations," Encyclopedia of Materials: Science and Technology (in press).

Article in magazine:

- A. R. Harvey and G. Muyo, "Wavefront coding slims down imaging systems," Optics and Laser Europe magazine, Dec. 2006.

Conference papers and oral presentations:

- G. Muyo, A. Singh, M. Andersson, D. Huckridge and A. R. Harvey, "Optimized thermal imaging with a singlet and pupil plane encoding: experimental realization," Proc. SPIE Vol. 6395, 2006.

- G. Muyo and A. R. Harvey, "Principles and performance comparison of phase masks for the alleviation of optical aberration," Photon06, Manchester, 2006.

- G. Muyo, A. R. Harvey and A. Singh, "High performance thermal imaging with a singlet and pupil plane encoding," Proc. SPIE Vol. 5987, 2005.

- G Muyo and A. R. Harvey, "Wavefront coding and its applications," Young researchers conference in Physics, Institute of Physics, London, 2005.

- G Muyo and A. R. Harvey, "Decomposition of the OTF: Wavefront Coding as a Cornu Spiral," Topical meeting on Advanced Optical Imaging of the European Optical Society, Imperial College, London, 2005.

- G. Muyo and A. R. Harvey, "Wavefront Coding for athermalization of infrared imaging systems," Proc. SPIE Vol. 5612, 2004.

- G. Muyo and A. R. Harvey, "The role of wavefront coding in thermal imaging," Photon04, Glasgow, 2004.

- S. Mezouari, G. Muyo and A. R. Harvey, "Amplitude and phase filters for mitigation of defocus and third-order aberrations," Proc. SPIE Vol. 5249, 2004.

Chapter 1

Introduction

The rapid developments in electronic technology in the past two decades have had a considerable impact on imaging systems [1]. Undoubtedly, the most important contributions come from advanced post-detection digital signal processing and substitution of film by focal plane array sensors*. The on-going expansion of imaging technology taking place in the consumer and military markets is mainly associated to advances in the field of electronics as opposed to the comparatively slower progress achieve in optics. Modern optics has become remarkably dependent on electronics. Nevertheless, in the last few years, a new generation of imaging systems has demonstrated that future advancements in imaging may not be based purely on electronics but on a mutually beneficial symbiosis of optics and electronics. It is therefore necessary to change the conventional and well-established notion of an imaging system as an unconnected sequence of multiple optical components, followed by a detector and followed by post-detection signal processing. This traditional design methodology was already being reviewed back in 1984 when a group investigating the limits of image resolution noticed the potential of increasing the performance of imaging systems by jointly designing the optics, the focal plane array sensor and the post-detection image processing [3]. The performance of this type of system is controlled through joint design and optimization of all the components, and in particular, the post-detection processing which now becomes an integral part and is not added subsequently to enhance the quality of the image as occurs in traditional systems. An imager designed using this approach has been commonly called an *integrated computational imaging system* (ICIS). In an ICIS the task of forming an image does not

*For the first time in 2002, more digital cameras were sold than film cameras [2].

depend solely on the optical components and detector but to a greater extent the digital signal processing. One example of an early type of ICIS was, in an unexpected way, the Hubble Space Telescope: image recovery techniques hit the headlines when they were used to restore early images that suffered from excessive spherical aberration [4]. Since the nature and magnitude of the aberrations were known, it was possible to alleviate them using digital image processing. The telescope operated functionally for three years despite the significant optical defects, until it was finally repaired in orbit.

It was not long before researchers realised the potential advantages that could be gained from premeditatedly introducing aberrations in a computational imaging system. While this may at first appear counterintuitive, it can be beneficial (in some way, it is like defocusing an optical system to correct for spherical aberration). An important example of this specially-designed system is Dowski and Cathey's extended-depth-of-field imaging system [5]. Other notable examples of ICIS systems are Matic and Goodman's spatial filtering architecture [6] and Descour and Dereniak's computer tomography imager [7]. In all these systems the image formed at the detector appears highly distorted and digital processing is necessary to recover the final image.

The imaging technique described by Dowski *et al.* has been called *Wavefront Coding* and provides performance that cannot be matched by traditionally-designed systems: it enables aberration tolerance (specially defocus) to be greatly extended without sacrificing light gathering efficiency or angular resolution. This is important in many applications where fast optics are employed, for instance in microscopy for in-focus imaging of biological samples that are thicker than the microscope's depth of field. Similarly, it could also be used to increase the depth of field of millimeter-wave scanners. The technique also gives the ability to maximize image quality whilst minimizing cost, complexity and weight in the system.

The fundamental concept of wavefront coding involves considering the lens and its associated detector as an imperfect communication channel: a coding mask adds a special phase modulation to the wavefront prior to transmission through the lens and electronic decoding is used to decode the recorded optical image, which is the convolution of an ideal image and the point spread function (PSF) due to the wavefront coding mask. The implementation of this concept is illustrated in Fig. 1.1.

A crucial aspect of wavefront coding is that the PSF should exhibit two im-

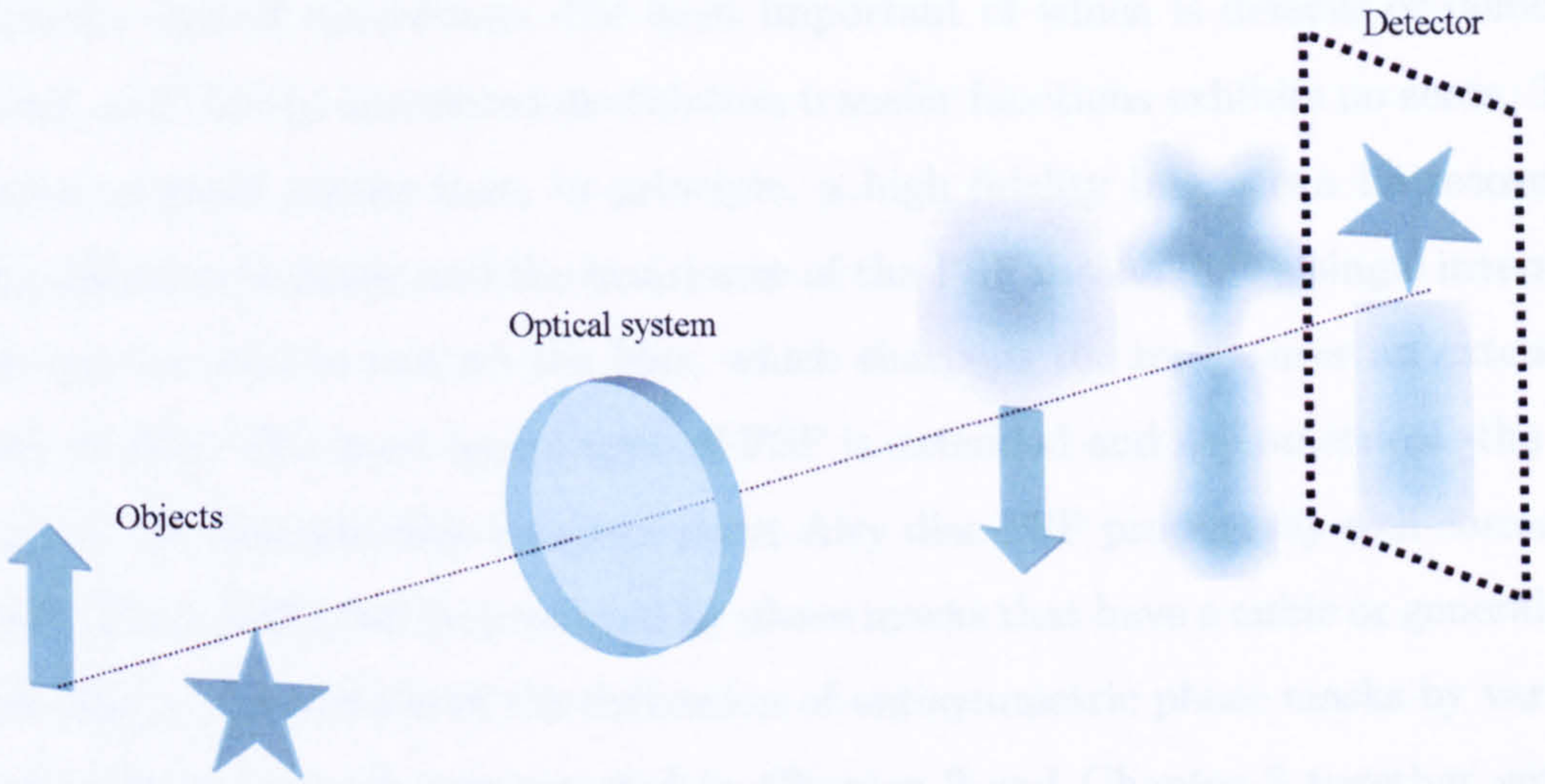

(a) Traditional imaging system.

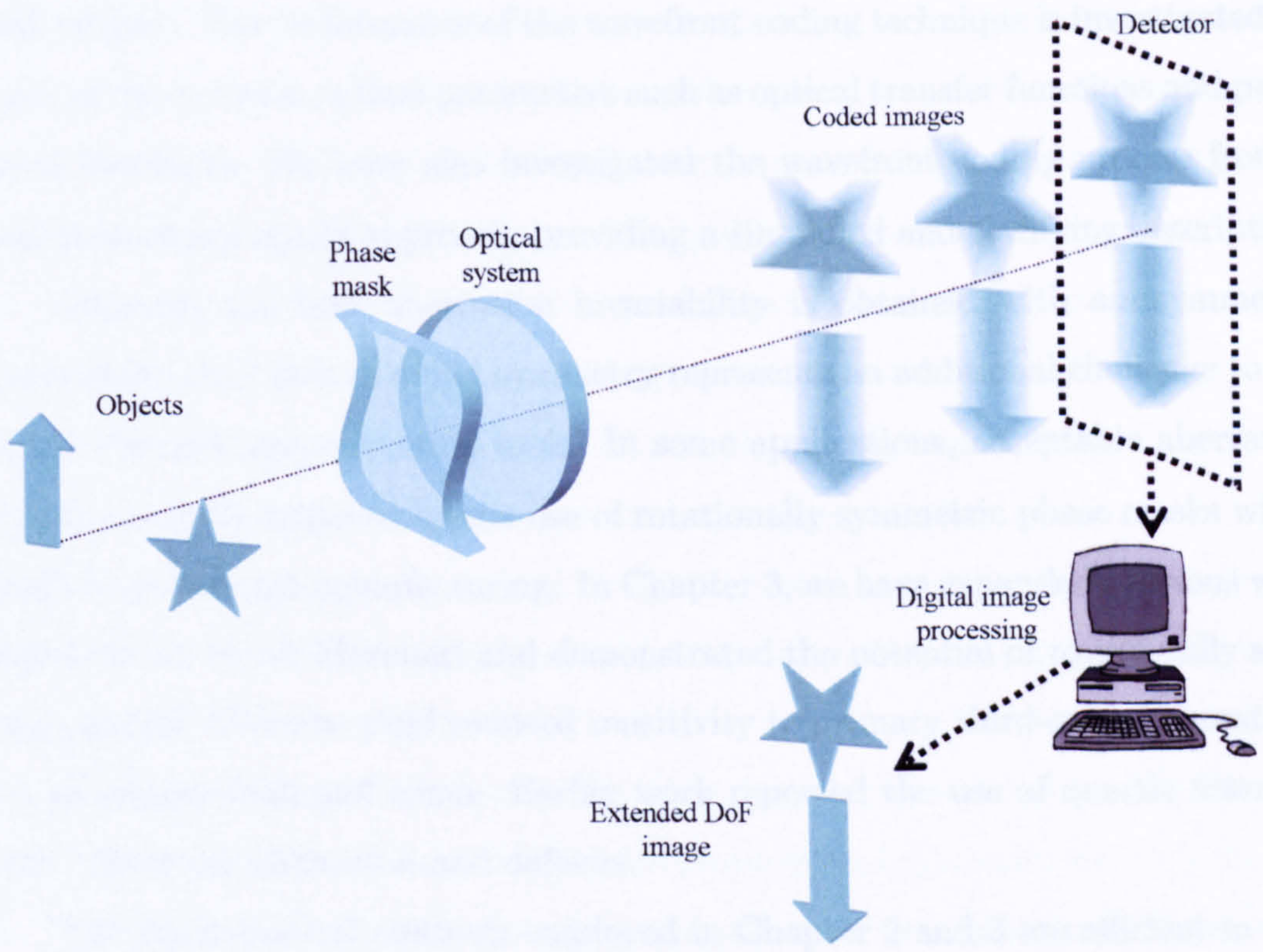

(b) Wavefront coded imaging system.

Figure 1.1: *(a) Traditional imaging system: only one object is in-focus (small depth of field), (b) wavefront coded imaging system: both objects are similarly blurred over the same range of image planes, post-detection digital signal processing is applied at the detector to remove the defocus-invariant blur and produce a sharp image of the objects.*

portant qualities: (a) it is approximately invariant to variations in the magnitude of specific optical aberrations -the most important of which is defocus or defocus-related; and (b) the associated modulation transfer functions exhibits no zeros. The absence of zeros means that, in principle, a high fidelity image can be recovered using digital processing and the invariance of the PSF means that a single inversion filter can be used to remove the blur, which sharpens the image over an extended depth of field. The most useful type of PSF is extended and asymmetrical -the opposite of the characteristic compact point Airy disc PSF produce by well-corrected optics. These PSFs can be produced by phase masks that have a cubic or generalised cubic shape. The details of the derivation of antisymmetric phase masks by various mathematical methods are reported in Chapter 2 and Chapter 3 together with a literature review of the different techniques and methods conceived to increase the depth of field. The performance of the wavefront coding technique is investigated by means of the common optical parameters such as optical transfer functions and point spread functions. We have also investigated the wavefront coding process from a novel geometrical optics approach, providing a simplified and clarifying description.

Although the best aberration invariability is obtained with antisymmetric phase masks, their lack of radial symmetry represents an additional challenge to the current low-cost manufacturing tools. In some applications, acceptable aberration mitigation can be achieved by the use of rotationally symmetric phase masks which benefit from low-cost manufacturing. In Chapter 3, we have expanded previous work carried out by Samir Mezouari and demonstrated the potential of rotationally symmetric quartic filters to yield reduced sensitivity to primary third-order aberrations such as astigmatism and coma. Earlier work reported the use of quartic filters to correct spherical aberration and defocus.

The mathematical methods employed in Chapter 2 and 3 are efficient in synthesizing the shape of wavefront coding phase masks against specific criteria and aberrations, but the performance parameters are not amenable to simple calculation and interpretation and nor do they readily yield a physical insight into the underlying process. In Chapter 4, we report a novel insight into the fundamental physical principles of image formation. Although the approach is pertinent to all aspects of incoherent imaging, its application to wavefront coding is of particular interest; it enables a rather abstract technique involving two-dimensional integrals of oscillatory functions to be simplified in terms of the equation for a straight line

from which we obtain the performance parameters.

The work covered in this thesis is motivated by a need for a comprehensive and reliable evaluation of wavefront coding as well as by the search of novel imaging solutions in military and commercial applications. Wavefront coding has attracted many commercial interests since its conception a decade ago. Recently, this technology has been targeting mass-market consumer and commercial applications such as mobile phones or security and surveillance systems [8]. It is this highly-lucrative market that has certainly helped to overemphasize across the literature the benefits of this technology whilst overlooking the problems and disadvantages that inevitably compromise the performance of wavefront coded imaging systems. There are of course important tradeoffs in the wavefront coding technique. The most prominent of these are artifacts and noise amplification in the restored image. The coding process clearly reduces the contrast of the detected image, image restoration recovers a high-contrast image, but also amplifies the noise accompanying detection. Although a high-quality image can be recorded over a wider range of optical aberrations than by conventional imaging, the signal-to-noise ratio can be considerably poorer than the best image recorded by traditional means. An extensive characterization of the restoration process including the impact of noise amplification in the decoded image is presented in Chapter 5. Also for the first time, we have performed an in-depth study of the effect of detector sampling and aliasing on wavefront coding performance. It is surprising that very little or no research has been done before despite of the functional dependency of wavefront coding on pixelated solid-state detector.

A prominent feature of wavefront coding is that it enables some of the burden for image formation to be shifted from a requirement for high-performance, high-cost imaging lenses to high-performance, low-cost post-detection digital processing. One example where this is becoming increasingly important is in the low-cost thermal imaging used by the military and emergency services. The biggest breakthrough in thermal imaging for low-cost applications came with the advent of uncooled thermal sensors. These devices operate at room temperature, a characteristic that leads to reduced system complexity, size and cost. However, the optics used in thermal imagers are inherently expensive to manufacture. The fast optics required for high sensitivity employ not only multi-element aspheric lenses for aberration control but also infrared transmissive material such as germanium and gallium arsenide, which are expensive

and tend to introduce large amounts of thermal-related defocus and chromatic aberration. Infrared optics therefore offer significant cost challenges to designers. This is the motivation for exploring, in Chapter 6, the use of wavefront coding to extend the operational temperature range (from −20°C to +70°C) of a infrared rifle scope in which no traditional athermalization techniques are implemented. Nevertheless, the technique has the greatest impact when it comes to minimizing field-related aberrations. In collaboration with our project partners, QinetiQ (UK), Qioptiq (UK) and Saab Bofors Dynamics (Sweden), we have employed wavefront coding to demonstrate the world's first high-performance single-element thermal-imaging lens. We show that the imaging system employing this single-element coded lens exhibits image sharpness across the field of view equal to one employing a traditional two-element lens, but with the reduced cost and weight associated with the simpler lens. The penalty for extended performance is a small increase in noise in the detected image, although the overall image quality is clearly superior. Crucially, the image quality is sufficient for many military and emergency-service applications. On-going improvements in detector sensitivity will reduce system noise in uncooled detectors and it will provide scope for the use of wavefront coding in low-cost thermal imagers whilst maintaining current performance levels.

Chapter 2

Theory of Wavefront Coding

Summary. In this chapter we give a review of the concept of depth of field and the theory of wavefront coding. The phase mask responsible for increasing the tolerance to defocus is derived by means of the ambiguity function and stationary phase approximation following a new method. Additionally, a geometrical optics description of the wavefront coding imaging process is presented together with analytical equations of the ray tracing and caustic near the image focal plane. The derivation of the caustic curve provides valuable performance parameters and principles to design new phase masks.

2.1 Depth of Field

The design of optical imaging systems is intricately involved with the control of imaging aberrations. The most prominent of these is defocus, i.e. a displacement between the location of the object and image planes. Defocus also occurs due to chromatic aberration and thermal drift or due to imperfect manufacture and alignment of fixed focus lenses. We consider an optical system to be in-focus when the image features are most sharply defined, and the system is transmitting the broadest bandwidth of spatial frequencies from the corresponding object focal plane. Since, in general, the scene being imaged is three dimensional rather than two dimensional, it becomes unavoidable to consider contributions from out of focus objects which will exhibit a characteristic image blur depending on their displacement from the in-focus plane.

The depth of field is defined as the amount by which the range of the object may be changed whilst retaining acceptable image sharpness [9]. The concept of depth of field rests on the assumption that for a given optical system, there exits

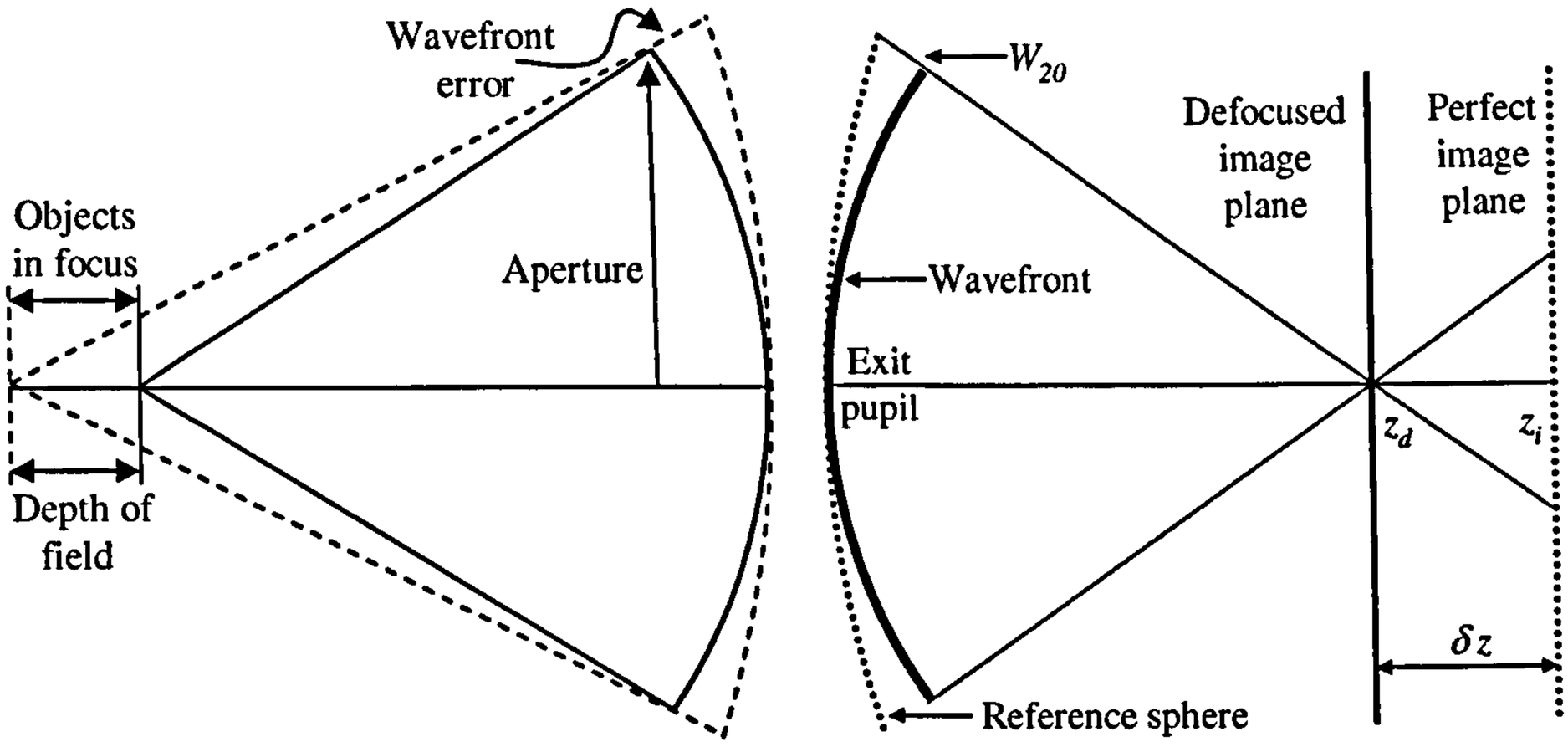

Figure 2.1: *(a) Relationship between wavefront error due to defocus W_{20} and depth of field. (b) The measure of defect of focus in the image space.*

a blur, due to defocus, of small enough size such that it will not adversely affect the performance of the optical system. The relationship between depth of field and defocus aberration is illustrated in Fig. 2.1(a), where a range of objects displaced from the plane of best focus results in a wavefront error. The wavefront error produced by defocus is generally described in terms of the defocus coefficient W_{20} [10]. In the image space, W_{20} measures the defect of focus at the edge of the exit pupil by the optical path length of the intercept between the emergent wavefront and the reference sphere centred at an axial point in the detector plane and an axial point in the plane of best focus, as shown in Fig. 2.1 (b).

The optical path difference W between both wavefronts at any point (x, y) within the exit pupil can be readily calculated from simple geometrical ray tracing in Fig. 2.1(b). It can be demonstrated that the optical path difference is given by

$$W(x,y) = \frac{1}{2}\left(\frac{1}{z_d} - \frac{1}{z_i}\right)(x^2 + y^2). \tag{2.1}$$

where z_d and z_i are the distances from the exit pupil to the defocused plane and image plane respectively. At the edge of a circular exit pupil of radius R, $W(x, y)$ defines the magnitude of the defocus coefficient W_{20}, thus

$$W_{20} = \frac{R^2}{2}\left(\frac{1}{z_d} - \frac{1}{z_i}\right). \tag{2.2}$$

Finally, when the focal length f of the optical system is known, W_{20} can be expressed in a more convenient fashion in terms of the relative displacement δz

between the ideal and detector planes

$$W_{20} = \frac{\delta z}{2}\left(\frac{R}{f}\right)^2. \tag{2.3}$$

The defocus coefficient W_{20} is an appropriate indication of the severity of the focusing error. It can be negative or positive, depending on whether the emerging wavefront lies at the right-hand side or left-hand side of the reference sphere respectively. Some authors [11] tend to describe the focusing error in terms of the defocus parameter ψ, which is defined as

$$\psi = kW_{20}, \tag{2.4}$$

where $k = 2\pi/\lambda$ is the wave number and λ is the wavelength of the illumination. There are several criteria based on the on-axis irradiance of the point spread function for evaluating the defocus tolerance, or more generally the aberration tolerance in optical systems: Strehl ratio [12], Maréchal rule [13] and Rayleigh quarter-wave criterion [14]. However, it is a general practice to consider the Hopkins criterion [5, 11, 15] for determining the depth of field or the maximum amount of defocus that can be tolerated. The Hopkins criterion states that the performance of an optical system is acceptable provided that the defocus parameter ψ is approximately less than 1 ($W_{20} \approx 0.215\lambda$) for a circular aperture. In the image plane this means that a little bit of power would be coupled from the Airy disk, hence brightening the first bright ring and dropping the axial intensity by 80 % of its peak value. In practical terms, however, the point spread function still looks Airy-like to the observer. Throughout this work, we have adopted this criterion as a measure of the defocus invariance potential present in an hybrid optical-digital imaging system.

2.2 Extended-depth-of-field optical systems

Increasing the depth of field of an imaging system has long been an area of extensive research. Traditionally, increased depth of field is achieved in an incoherent optical system by stopping down the aperture of the system, since depth of field is inversely proportional to the size of the aperture, large aperture results in smaller depth of field. Reducing the width of the optical aperture is not however an ideal method to extend the depth of field as two significant problems arise: a loss of angular resolution and a reduction in light power at the image plane, causing a decrease in

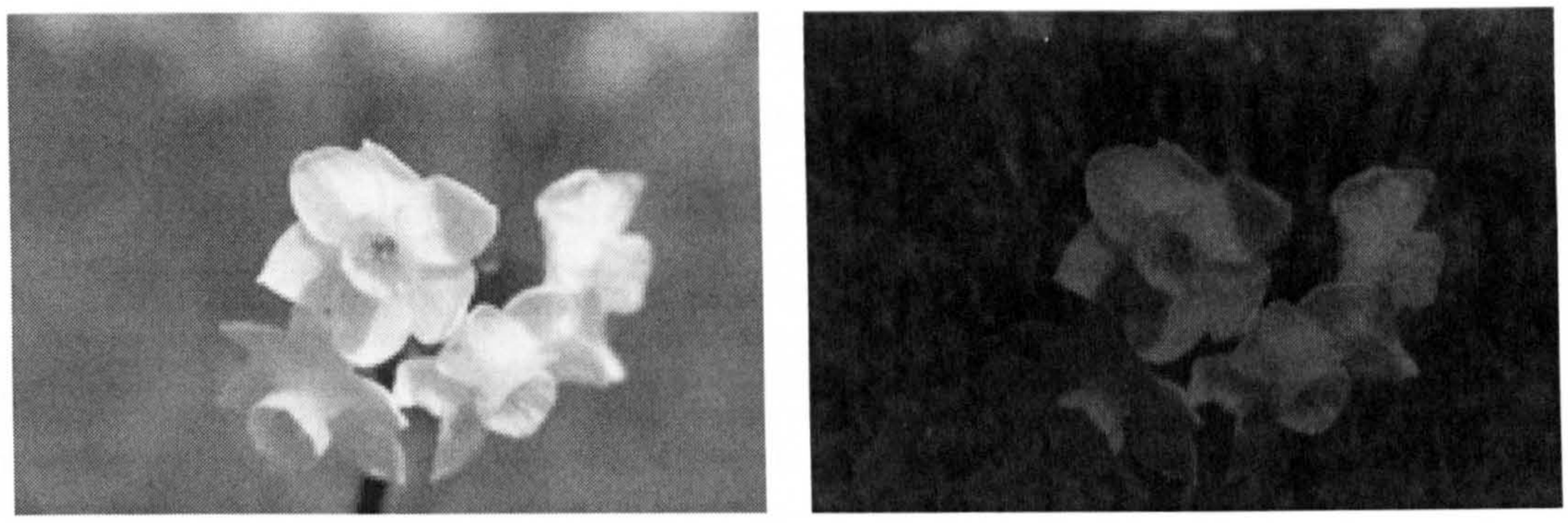

(a) (b)

Figure 2.2: *Depth of field in a traditional optical system fpr two values of the f-number: (a) F/5.6 and (b) reduced aperture F/32 with increased depth of field and reduced light throughput.*

the signal to noise ratio. In addition, the depth of field gained is relatively modest. This is clearly illustrated in Fig. 2.2. The image (a) on the left is from a F/5.6 optical system. It has a very modest depth of field and only a very small part of the image is in focus. The image (b) on the right, illustrates the increased depth of field achieved by stopping down the aperture, from F/5.6 to F/32. The F/32 image has a much larger depth of field and more parts in the image are in focus. The cost of this extended depth of field has been to decrease the aperture radius by a factor of four. This reduced aperture captures less than 1/32 of the optical power throughput acquired by the F/5.6 system and also decreases the angular resolution of the image by a factor of four.

Many attempts have been made to produce an optical system insensitive to defocus and with increased depth of field as evidenced by the volume of literature dedicated to the subject. One of the early methods of increasing the depth of field without apodizers was described by Häusler in 1972 [16]. It required that the focus be continuously varied during the exposure time of the imaging system. As a result, the modulation transfer function (MTF) of the system was an incoherent superposition of the MTFs at different focus positions during the exposure of the camera. Post-detection signal processing was then used to obtain sharp details of the image. Until very recently, the control of defocus and, in general, the reduction of third-order aberrations (such as spherical aberration), were carried out by means of absorptive masks placed in the aperture stop. Annular ring pupil functions have been widely studied because of their known ability to increase the tolerance of defocus

relative to a clear aperture [17, 18, 19]. To avoid some limitations associated with annular apertures, such as low optical throughput, several authors have reported using shade masks that cover the whole pupil aperture [20] or using several annuli [21]. Mino *et al.* [22], demonstrated that by decreasing the amplitude transmittance gradually from the center of the pupil towards its edges the quality of a defocused imaged was slightly improved. Within this field of study, special recognition must be given to the research carried out by Ojeda-Castañeda in reducing the sensitivity to defocus through the application of apodizers to block portions of the aperture [23, 24, 25, 26, 27, 28]. These apodizers clearly absorb optical power which results in a loss of signal-to-noise ratio. In some way, Ojeda-Castañeda's work in Ref.[23], in which an iterative digital restoration algorithm was used to improve substantially the defocused optical transfer function of a previously apodized optical system, can be regarded as a precursor of the current optical-digital hybrid methods. Other techniques obtain relatively limited depth of field by exploiting the concept of a multifocal system, for example, with a quasi-bifocus birefringent lens positioned between two polarizers [29, 30].

In 1995 Dowski *et al.* [5] presented wavefront coding for increasing the depth of field of incoherent imaging systems which did not suffer from the disadvantages of previous techniques mentioned above. Since Wavefront Coding was presented, there has been a recent growth of interest in the use of hybrid optical-digital techniques which incorporate a phase only mask at the aperture stop of an optical system [31, 32, 33, 34, 35, 36, 37, 38, 39, 40, 41, 42]. In techniques were radially symmetric phase masks are employed, the postdetection digital processing is optional. In Zalevsky's work, for instance, an all-optical approach whereby a phase mask consisting of several multiplexed Fresnel lenses positioned in the pupil of an imaging system increases the depth of field significantly without applying any postdetection image processing [36, 43]. Nevertheless the increased depth of field is couple with a reduction in image contrast and resolution. Recently, a binary phase only element with low spatial frequency was placed in the entrance pupil of an imaging system (a mobile phone camera) providing increased depth of focus [44]. The acquired image did not require a digital restoration stage, although one may use digital restoration to achieve better contrast.

2.3 Theory of Wavefront Coding

In this section a mathematical expression of the phase mask function that extends the depth of field of an optical system is derived by means of the stationary phase approximation together with the ambiguity function. Although the starting point of our derivation corresponds to the one originally adopted by Dowski, we have taken an alternative course by assuming a more general phase mask function described as a Taylor series. After lengthy mathematical manipulation similar results are obtained.

2.3.1 Ambiguity function

Since Papoulis [45] applied the Woodward function [46] or ambiguity function to Fourier optics for describing diffraction and image-formation problems, the ambiguity function has proven to be a useful tool for characterizing the performance of the optical transfer function (OTF) of an incoherent optical system in the presence of defocus and various aberrations [15, 47, 48, 49, 50, 31]. The ambiguity function has its origins in radar ranging applications and has been widely examined [51, 52]. Although, the interpretation and usage of the ambiguity function in radar signal processing are entirely different from the optical transfer function, the similarity in the form of both equations has provided with new tools in analyzing imaging systems. Furthermore, it has been shown that the ambiguity function of the pupil function of an optical system is a polar display of the OTF with defocus as variable. This geometrical interpretation yields the OTF for any given amount of focus error [53, 48, 54]. To illustrate the importance of this result, the ambiguity function of a standard rectangular aperture is calculated. According to Ref. [45], the ambiguity function of an unaberrated pupil function $p(x)$ is defined as

$$A(\nu,t)=\frac{\int_{-\infty}^{\infty}p\left(x+\nu/2\right)p\left(x-\nu/2\right)\exp(\mathrm{i}2\pi tx)\mathrm{d}x}{\int_{-\infty}^{\infty}\left|p\left(x\right)\right|^{2}\mathrm{d}x}, \tag{2.5}$$

For simplicity, we consider here only one-dimensional pupils to allow a geometrical representation of the results. The definition of the ambiguity function can be easily extended for two-dimensional pupils, however the ambiguity function would be described in a four-dimensional space and there would be no way to display it.

The one-dimensional OTF of an incoherent optical system is defined as the

autocorrelation of the generalised pupil function $P(x)$ [55]

$$H(\nu) = \frac{\int_{-\infty}^{\infty} P\left(x+\nu/2\right) P^{*}\left(x-\nu/2\right) \mathrm{d}x}{\int_{-\infty}^{\infty} \left|P\left(x\right)\right|^{2} \mathrm{d}x}, \tag{2.6}$$

where x is the normalised pupil coordinate, ν is the normalised spatial frequency. The generalised pupil function is given by

$$P(x) = p(x) \exp[\mathrm{i}kW(x)], \tag{2.7}$$

where the coefficient k represents the wave number, $k = 2\pi/\lambda$ and $W(x)$ is the one-dimensional aberration function. Since the OTF in Eq. (2.6) is expressed in terms of a normalised spatial coordinate, the pupil function $p(x)$ is given thus,

$$p(x) = \begin{cases} 1 & \text{if } |x| \leq 1 \\ 0 & \text{otherwise} \end{cases} \tag{2.8}$$

The generalised pupil function $P(x)$ of a optical system with only defocus aberration is expressed in terms of the defocus coefficient W_{20}

$$P(x) = p(x) \exp\left(\mathrm{i}\frac{2\pi}{\lambda} W_{20} x^{2}\right). \tag{2.9}$$

Thus, substituting Eq. (2.9) into Eq. (2.6), the one-dimensional OTF for a defocused optical system is given by

$$H(\nu; W_{20}) = \frac{1}{2} \int_{-\infty}^{\infty} p(x+\nu/2) p(x-\nu/2) \exp\left[\mathrm{i}\frac{2\pi}{\lambda}(2W_{20}\nu)x\right] \mathrm{d}x. \tag{2.10}$$

A comparison of the expressions of both the ambiguity function in Eq. (2.5) and the defocus OTF in Eq. (2.10), enables one to establish an important relationship for the analysis of defocused imaging systems,

$$H(\nu; W_{20}) = A\left(\nu, t = 2W_{20}\nu/\lambda\right). \tag{2.11}$$

It follows that a projection of the point $(\nu, 2\nu W_{20}/\lambda)$ of the ambiguity function onto the ν-axis yields the OTF for spatial frequency ν and defocus W_{20}. Therefore, the ambiguity function in Eq. (2.5) contains the OTFs for all values of defocus.

The usefulness of the relationship shown in Eq. (2.11) can be readily demonstrated in the case of a rectangularly separable traditional incoherent optical system. The one-dimensional generalised pupil function for such a system is simply $P(x) = p(x) = \mathrm{rect}(x)$, where $\mathrm{rect}(x) = 1$ if $|x| \leq 1$ and $\mathrm{rect}(x) = 0$ otherwise. To

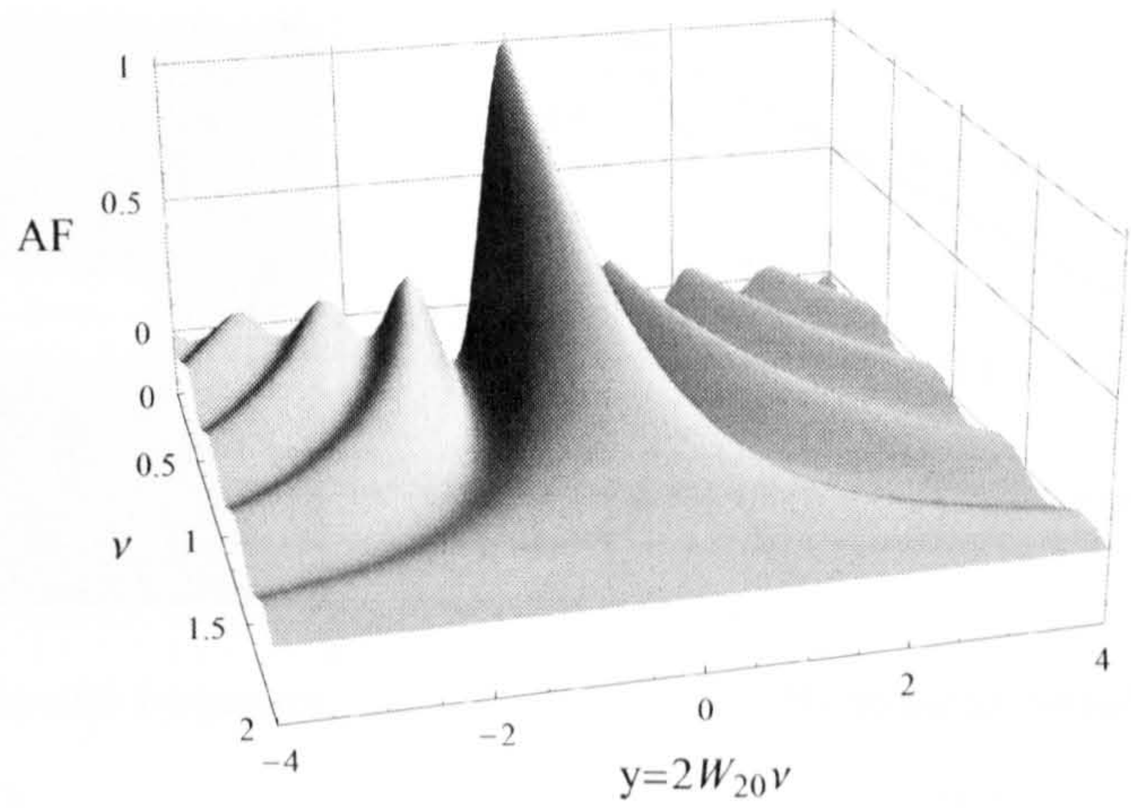

Figure 2.3: *Ambiguity function for a clear uniform rectangular aperture.Defocus coefficient W_{20} in units of wavelength (λ).*

calculate the ambiguity function associated with this aperture, we substitute $P(x)$ in Eq. (2.5) and obtain

$$A(\nu, t) = \left(1 - \frac{|\nu|}{2}\right) \text{sinc}\left[2\pi t \left(1 - \frac{|\nu|}{2}\right)\right] \tag{2.12}$$

where $\text{sinc}\phi = \sin \pi\phi / \pi\phi$. The representation of the two-dimensional ambiguity function of this rectangular pupil is shown in Fig. 2.3, and it allows us to visualize simultaneously all OTFs as a function of defocus. The projection onto the ν-axis of a slice through the origin of the ambiguity function with a slope of $2W_{20}/\lambda$ represents the OTF of the optical system for a defocus value of W_{20}, as shown in the density plot of the ambiguity function of Fig. 2.4(a). For instance, when the radial line is horizontal and coincides with the ν-axis, the OTF corresponds to the in-focus position ($W_{20} = 0$) where most of the energy of the ambiguity function is concentrated. Also shown are the radial lines with slopes of 1 and 2, whose projections onto the ν-axis correspond to defocused OTF with $W_{20} = 0.5\lambda$ and $W_{20} = 1\lambda$ respectively as shown in Fig. 2.4(b). By examination of the Fig. 2.4(a) and (b) we can verify the relationship between the ambiguity function and the OTF shown is Eq. (2.11).

We have shown that the defocus tolerance of an optical system can be evaluated by simple inspection of the ambiguity function. Obviously, optical systems described by various pupil functions will exhibit different ambiguity functions and thus different OTFs. In the next section, the ambiguity function will be used as a design tool to control the pupil function and increase the tolerance to defocus.

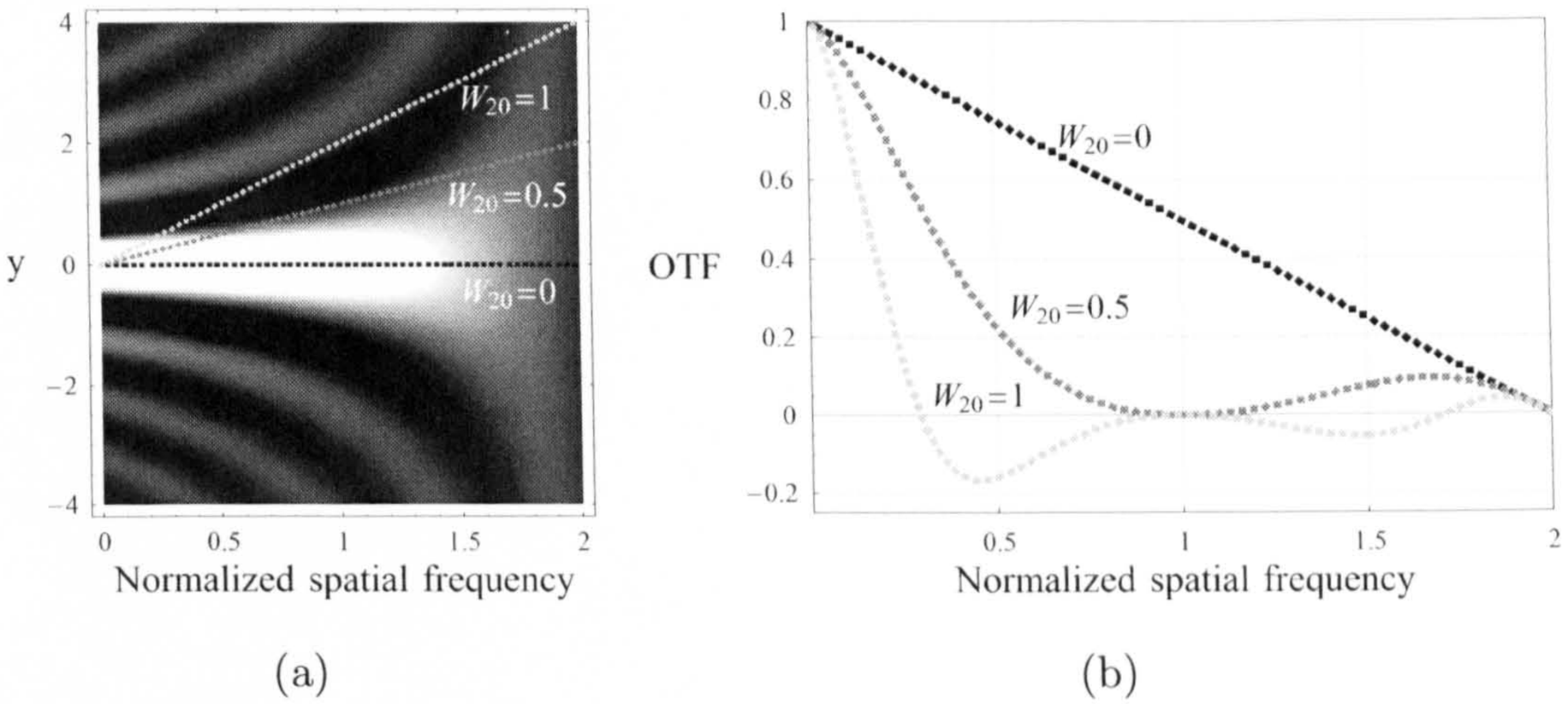

(a) (b)

Figure 2.4: *(a)Density plot of the ambiguity function for a uniform rectangular aperture (the grey-scale has been scaled for enhanced visibility). The radial lines with slopes 0, 1 and 2 in (a) correspond to optical transfer functions in (b) with defocus* $W_{20} = 0, 0.5$ *and* 1, *in units of wavelength* (λ).

This is achieved without substantially reducing the light throughput and resolution. Unfortunately, the use of the ambiguity function to display the performance of incoherent optical systems is restricted to a one-dimensional problem. Only pupil functions that can be described by a rectangularly separable expression, as will be shown in the next section, or circularly symmetric functions as in Refs. [39, 48] can be analyzed with this method.

2.3.2 Design of an extended-depth-of-field optical system

It has been shown that the ambiguity function is an analytical instrument that allows us to examine and design OTFs for all values of defocus simultaneously. Consequently, optical systems with improved depth of field by means of amplitude (central obscurations or gaussian apodizers) or phase filters can be practically detected by simple examination of their corresponding ambiguity functions. In this section, we derive a phase-only filter that produces an ambiguity function invariant to defocus. The choice for a phase filter is dictated by the aim of obtaining maximum light gathering and resolution.

Consider the expression of a one-dimensional generalised pupil function in

normalised coordinates written as

$$P(x) = \begin{cases} \exp[\mathrm{i}\theta(x)] & \text{for } |x| \leq 1 \\ 0 & \text{otherwise} \end{cases} \tag{2.13}$$

where $\theta(x)$ represents an undefined phase delay introduced by the phase mask placed at the pupil plane of an incoherent optical system. The ambiguity function for this general phase mask is obtained by replacing Eq. (2.13) into Eq. (2.5) and adjusting the integration limits to the size of the pupil,

$$A(\nu, t) = \frac{1}{2} \int_{-(1-|\nu|/2)}^{(1-|\nu|/2)} \exp[\mathrm{i}\theta(x+\nu/2)] \exp[-\mathrm{i}\theta(x-\nu/2)] \exp(\mathrm{i}2\pi t x)\mathrm{d}x, \tag{2.14}$$

with $|\nu| \leq 2$. A judicious choice of the non-linear function produces an AF with high tolerance to defocus. To obtain a general solution of this expression, we write the phase function in term of its Taylor series

$$\begin{aligned} \theta(x+\nu/2) \;=\; & \theta(x) + \theta'(x)\left(\frac{\nu}{2}\right) + \frac{1}{2!}\theta''(x)\left(\frac{\nu}{2}\right)^2 + \frac{1}{3!}\theta^{(3)}(x)\left(\frac{\nu}{2}\right)^3 + \cdots \\ & + \frac{1}{n!}\theta^n(x)\left(\frac{\nu}{2}\right)^{(n)} + \cdots \end{aligned} \tag{2.15}$$

and for $\theta(x-\nu/2)$,

$$\begin{aligned} \theta(x-\nu/2) \;=\; & \theta(x) - \theta'(x)\left(\frac{\nu}{2}\right) + \frac{1}{2!}\theta''(x)\left(\frac{\nu}{2}\right)^2 - \frac{1}{3!}\theta^{(3)}(x)\left(\frac{\nu}{2}\right)^3 + \cdots \\ & + \frac{(-1)^n}{n!}\theta^n(x)\left(\frac{\nu}{2}\right)^{(n)} + \cdots \end{aligned} \tag{2.16}$$

By subtracting Eq. (2.16) from Eq. (2.15) and replacing the result into Eq. (2.14), the ambiguity function becomes

$$A(\nu, t) = \int_{-(1-|\nu|/2)}^{(1-|\nu|/2)} \exp[\mathrm{i}p(x)] \exp(\mathrm{i}2\pi t x)\mathrm{d}x, \quad \text{for } |\nu| \leq 2, \tag{2.17}$$

where the function $p(x)$ is defined by

$$p(x) = 2\left[\theta'(x)\left(\frac{\nu}{2}\right) + \frac{1}{3!}\theta^{(3)}(x)\left(\frac{\nu}{2}\right)^3 + \cdots + \frac{1}{(2n+1)!}\theta^{(2n+1)}(x)\left(\frac{\nu}{2}\right)^{2n+1} + \cdots\right] \tag{2.18}$$

The direct evaluation of the integral in Eq.(2.17) is a difficult problem. However, when the phase term $p(x)$ in the integrand varies fast enough, the stationary phase method provides an effective approximation to the ambiguity function. This heuristic approach was first given by Lord Kelvin in 1887 [56], and a rigorous demonstration was later provided by Watson back in 1918 [57]. Since then, researchers have applied this method to solve the ambiguity function. Since this method has been

applied several times across the work presented in this thesis a brief explanation of the stationary phase method has been included in Appendix A. Thus, making use of this tool and Eq. (A-4), the analytical expression of the approximated ambiguity function is given by

$$A(\nu,t) \approx \frac{1}{2}\sqrt{\frac{2\pi}{|p''(x_s)|}}\exp[\mathrm{i}\phi(t)], \tag{2.19}$$

with

$$\phi(t) = 2\pi t x_s + p(x_s), \tag{2.20}$$

x_s is the stationary point and $p''(x)$ denotes the second derivative of the function $p(x)$ with respect to x. The stationary point x_s correspond to the location where the function takes its extreme value and it is given by

$$\left.\frac{\partial\phi(x)}{\partial x}\right|_{x_s} = 0. \tag{2.21}$$

Substituting Eq. (2.20) into Eq. (2.21),

$$\left.\frac{\partial p(x)}{\partial x}\right|_{x_s} + 2\pi t = 0, \tag{2.22}$$

which is written in a short form

$$\frac{\partial p(x_s)}{\partial x} + 2\pi t = 0. \tag{2.23}$$

By differentiating with respect to t, we obtain

$$\frac{\partial^2 p(x_s)}{\partial x^2}\frac{\partial x_s}{\partial t} + 2\pi = 0, \tag{2.24}$$

and deduce the following relationship

$$\frac{\partial x_s}{\partial t} = -\frac{2\pi}{\frac{\partial^2 p(x_s)}{\partial x^2}} = -\frac{2\pi}{p''(x_s)}. \tag{2.25}$$

Substituting this result in Eq. (2.19), the ambiguity function becomes

$$A(\nu,t) \approx \frac{1}{2}\sqrt{\left|\frac{\partial x_s}{\partial t}\right|}\exp[\mathrm{i}\phi(t)]. \tag{2.26}$$

Note from Eq. (2.19), that the magnitude of the ambiguity function is independent of its second parameter t if and only if the second derivative of $p(x)$ with respect to x evaluated at the stationary point x_s is independent of t, or equally from Eq. (2.26), if a linear relation between the stationary point x_s and t holds. The linearity condition can be expressed by

$$p'(x_s) = a_1 x_s + a_0, \tag{2.27}$$

with $a_1 = a_1(\nu) \neq 0$ and $a_0 = a_0(\nu) \neq 0$. Thus, by combining Eq. (2.18) and Eq. (2.27) we obtain the following differential equation for which the phase function $\theta(x)$ represents the solution,

$$p'(x) = 2\left[\theta''(x)\left(\frac{\nu}{2}\right) + \frac{1}{3!}\theta^{(4)}(x)\left(\frac{\nu}{2}\right)^3 + \cdots + \frac{1}{(2n+1)!}\theta^{(2n+2)}(x)\left(\frac{\nu}{2}\right)^{2n+1} + \cdots\right] = a_1 x + a_0. \quad (2.28)$$

The only possible physical solutions are those in which $\theta(x)$ depends only on x. Thus, it is easy to solve the above partial differential equation. By taking the second derivative with respect to x, it yields the following expression

$$\theta^{(4)}(x)\left(\frac{\nu}{2}\right) + \frac{1}{3!}\theta^{(6)}(x)\left(\frac{\nu}{2}\right)^3 + \cdots + \frac{1}{(2n+1)!}\theta^{(2n+4)}(x)\left(\frac{\nu}{2}\right)^{2n+1} + \cdots = 0. \quad (2.29)$$

The left-hand side of this relation Eq. (2.29)is in fact a polynomial with ν as variable. Then it becomes evident that all the coefficients $\theta^{(n)}(x)$ of the polynomial must be zero

$$\theta^{(4)}(x) = \theta^{(6)}(x) = \cdots = \theta^{(2n)}(x) = \cdots = 0. \quad (2.30)$$

Therefore, only the first term $\theta''(x)$ remains in Eq. (2.28) and the determination of $\theta(x)$ is reduced to a simple differential equation of second order

$$\theta''(x) = a_1 x + a_0. \quad (2.31)$$

The integration of Eq. (2.31) poses no difficulty and the general solution of the phase function $\theta(x)$ is simply given by a third-order polynomial

$$\theta(x) = a_3 x^3 + a_2 x^2 + a_1 x + a_0, \quad (2.32)$$

with $a_3 \neq 0$ and real. The constants a_1 and a_0 have been included in the definitions of a_3 and a_2. Eq. (2.32) can be simplified further by dropping the terms x^2 and x without affecting the final result. For instance, the term $a_2 x^2$ is a defocus term that changes the image plane location and can be neglected since the magnitude of the ambiguity function is independent of this parameter, as will be shown below. Likewise, the constants a_1 and a_0 represent respectively the wedge and thickness coefficients of the phase mask and they can be set to zero as they have no physical interest. Therefore, the mask profile that allows increasing depth of field of an optical system is equal to a polynomial of third order degree

$$\theta(x) = a_3 x^3, \quad (2.33)$$

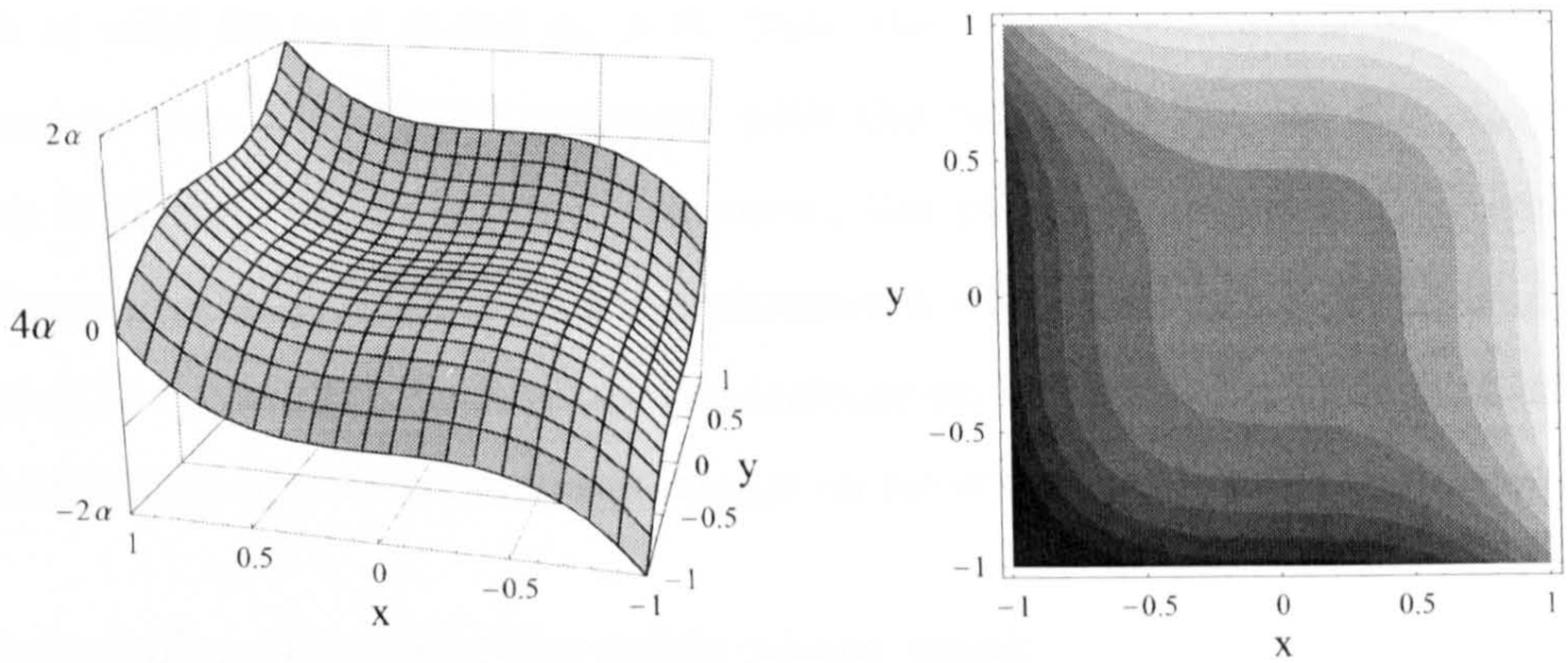

Figure 2.5: *Three-dimensional plot (right)and contour plot (left) of the cubic phase mask with parameter* α.

where the constant a_3 controls the magnitude of the phase retardation function and can be expressed in terms of the design wavelength λ as

$$a_3 = \frac{2\pi\alpha}{\lambda} \tag{2.34}$$

where α accounts for the amount of optical path difference introduced by the phase mask in spatial units. Hence, the needed phase mask will have a cubic shape. Unfortunately, the lack of radial symmetry of the cubic phase mask makes the manufacturing process costly and difficult with a requirement for high precision machining. However, in some mass-production applications, the manufacture of the cubic phase mask could be achieved by a low-cost moulding. The one-dimensional phase function $\theta(x)$ obtained by means of the ambiguity function and the stationary phase methods is readily extended into two dimensions provided the systems is rectangularly separable, the cubic phase mask becomes $\theta(x, y) = a_3(x^3 + y^3)$. A three dimensional surface plot of the antisymmetric phase retardation function of a cubic mask with parameter α and normalised coordinates is shown in Fig. 2.5.

The cubic phase mask yields a stationary point x_s that can be calculated by considering $p(x) = \theta(x + \nu/2) - \theta(x - \nu/2)$ and solving Eq. (2.21),

$$x_s = -\frac{\pi t}{3a_3\nu}. \tag{2.35}$$

Using Eq. (2.26) the magnitude and phase of the ambiguity function within the stationary phase approximation becomes

$$A(\nu, t) \approx \sqrt{\frac{\pi}{12|a_3\nu|}} \exp\left(\mathrm{i}\frac{a_3\nu^3}{4}\right) \exp\left(-\mathrm{i}\frac{\pi^2 t^2}{3a_3\nu}\right) \tag{2.36}$$

which is valid for $\nu \neq 0$ and $a_3 \neq 0$. Note that the magnitude is independent of the second parameter t in agreement with the target set out for the phase mask at the beginning of the section. However, the phase of the estimated ambiguity function remains dependent on the parameter t, which will affect the phase transfer function as t is varied. This phase dependence on t will have a significant effect on the restoration of wavefront coded images as we will show in the following chapters.

Defocus tolerance with the cubic phase mask

In the previous section, a cubic phase mask has shown to produce an approximate ambiguity function $A(\nu, t)$ whose magnitude is unaffected by the parameter t. According to Eq. (2.11), the parameter t is associated with the defocus coefficient W_{20} by the relationship $t = 2W_{20}\nu/\lambda$. By replacing this relationship into Eq. (2.36), we obtain the ambiguity function as a function of the defocus coefficient W_{20}, which is present only in of the phase term. However, this is not the case when the ambiguity function is calculated by means of its exact definition applied to the cubic phase mask, which is given by

$$A(\nu, 2W_{20}\nu/\lambda) = \frac{1}{2}\int_{-(1-|\nu|/2)}^{(1-|\nu|/2)} \exp\left[\mathrm{i}\frac{a_3\nu}{4}(12x^2+\nu^2)\right]\exp(\mathrm{i}4\pi W_{20}\nu x/\lambda)\mathrm{d}x. \quad (2.37)$$

This integral can be analytically solved after some manipulations and by considering $a_3 = 2\pi\alpha/\lambda$, we obtain

$$\begin{aligned} A(\nu, 2W_{20}\nu/\lambda) = \\ \frac{1}{4}\sqrt{\frac{\lambda}{6\alpha\nu}}\exp\left[\mathrm{i}\left(\frac{\pi\alpha\nu^3}{2\lambda}-\frac{\pi}{4}\right)\right]\exp\left(-\mathrm{i}\frac{2\pi\nu W_{20}^2}{3\alpha\lambda}\right)\times \\ \left(\mathrm{erfi}\left\{\frac{1+\mathrm{i}}{4\lambda}[4\pi W_{20}-6\pi\alpha(-2+\nu)]\sqrt{\frac{\nu\lambda}{3\pi\alpha}}\right\}-\right. \\ \left.\mathrm{erfi}\left\{\frac{1+\mathrm{i}}{4\lambda}[4\pi W_{20}+6\pi\alpha(-2+\nu)]\sqrt{\frac{\nu\lambda}{3\pi\alpha}}\right\}\right), \end{aligned} \quad (2.38)$$

where the imaginary error function $\mathrm{erfi}(z)$ is defined as

$$\mathrm{erfi}(z) = -\frac{2\mathrm{i}}{\sqrt{\pi}}\int_0^{\mathrm{i}z}\exp(-s^2)\mathrm{d}s. \quad (2.39)$$

The defocus coefficient W_{20} appears now in both the phase and error functions. In a situation without approximations, the magnitude of the ambiguity function is clearly altered by defocus. Exact ambiguity functions have been calculated for various cubic phase masks with increasing optical-path-difference parameter α and are shown in

Fig. 2.6. The first column shows three-dimensional plots of the magnitude of the ambiguity function and the second column the corresponding grey-scale pictures. For a small value of phase delay $\alpha = 1\lambda$, the ambiguity function exhibits a high narrow edge, similar to that of a clear aperture as shown in Fig. 2.3, with oscillations at its feet. The magnitude of the ambiguity function decreases rapidly as one moves away from the defocus axis t for a given spatial frequency ν. Weak cubic phase masks with low α exhibit little invariance against defocus. In contrast, as we increase the strength of the cubic phase mask to higher values of α, the edge in the central axis of the ambiguity function becomes greatly extended and the oscillations are greatly reduced. Radial lines through the origin of the ambiguity function with $\alpha = 10\lambda$ have nearly the same values for any angular position within a wide range of angles, see Fig. 2.6(d). Therefore, the cubic phase mask with sufficiently large phase delay α, should produce an incoherent optical system with improved tolerance to defocus aberration.

The defocus-dependent terms in the ambiguity function can be effectively minimized so as to be negligible in terms only of the amplitude component, however their effect on the phase component cannot be underestimated. From Eq. (2.38) and for very large values of α, the ambiguity function becomes insensitive to defocus W_{20} when

$$\alpha > \frac{2\pi\nu W_{20}^2}{3\lambda} \tag{2.40}$$

considering the limited range of the normalised spatial frequency $\nu \leq 2$, then

$$\alpha > 4W_{20}^2/\lambda \tag{2.41}$$

This condition ensures the invariance of the ambiguity function and hence the optical transfer function to defocus. In Ref. [5], it was shown that the cubic phase mask parameter α must satisfy $\alpha > 3\lambda$ for the stationary phase approximation to be valid, however, we have demonstrated in Ref.[58] that this inequality needs not to always fulfilled. When α is sufficiently large with respect to defocus, the OTF of the system is practically not modified by defocus aberration and can be considered to equal the in-focus OTF with a cubic phase mask, which is possible to express in terms of analytical functions

$$H(\nu,\alpha) = -\frac{1}{2}\sqrt{\frac{\lambda}{6\alpha\nu}}\exp\left[\mathrm{i}\left(\frac{\pi\alpha\nu^3}{2\lambda} - \frac{\pi}{4}\right)\right]\mathrm{erfi}\left[(1+\mathrm{i})(-2+\nu)\sqrt{\frac{3\pi\alpha\nu}{4\lambda}}\right]. \tag{2.42}$$

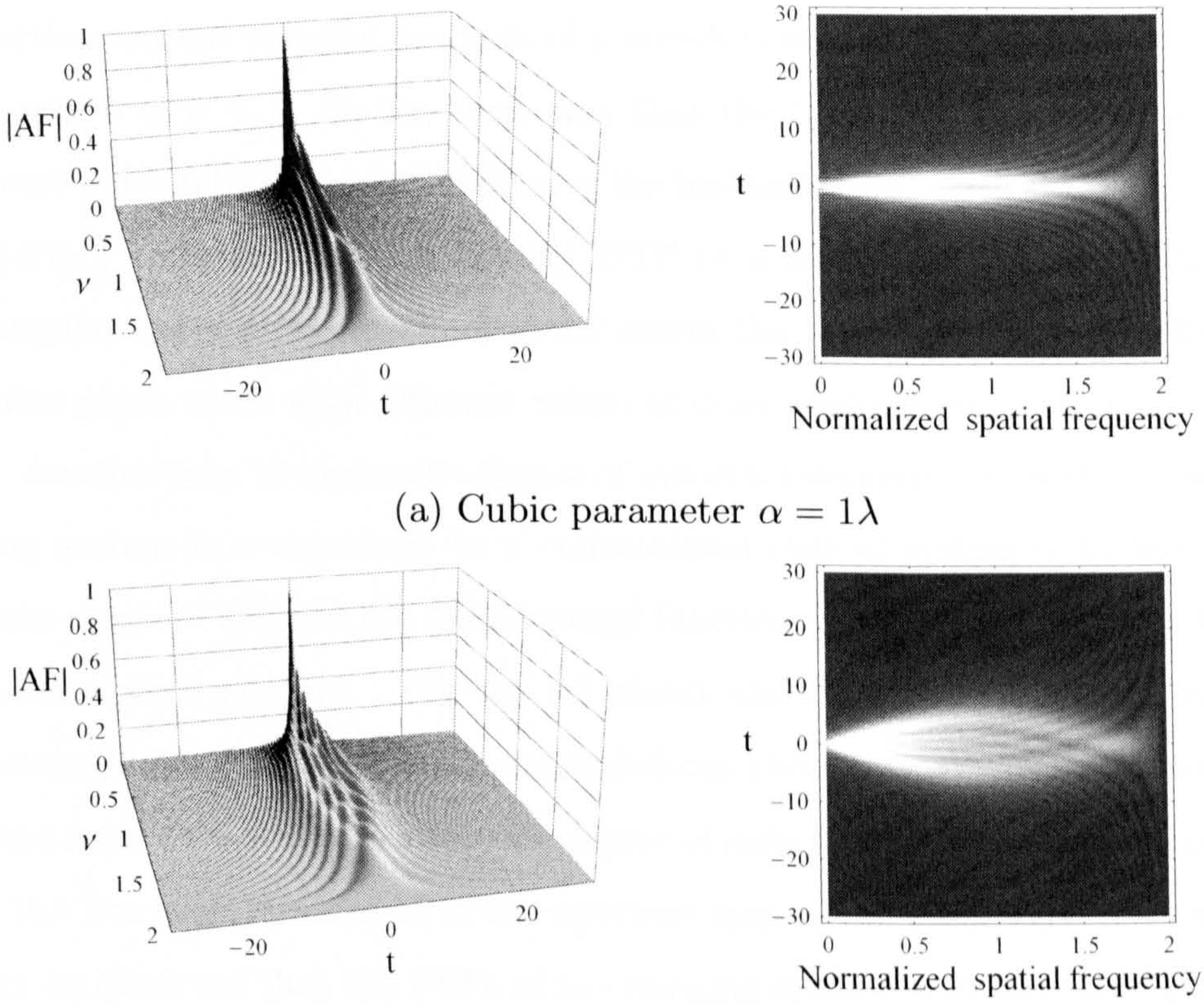

(a) Cubic parameter $\alpha = 1\lambda$

(b) Cubic parameter $\alpha = 2.5\lambda$

(c) Cubic parameter $\alpha = 5\lambda$

(d) Cubic parameter $\alpha = 10\lambda$

Figure 2.6: *Ambiguity functions for various values of the cubic parameter* α.

When the phase mask is removed or $\alpha \rightarrow 0$, the OTF describes the well-known diffraction-limited transfer function of a one-dimensional perfect lens: $H(\nu) = 1 - \nu/2$, with $0 \leq \nu \leq 2$. In the same way that the OTF of a two-dimensional clear aperture is given by the multiplication of the horizontal and vertical OTFs, $H(\nu, \eta) = H(\nu)H(\eta)$, so is the two-dimensional OTF of a wavefront coding system with a rectangular cubic phase mask. Fig. 2.7 shows the magnitude of the OTFs related to cubic phase mask with different values of α and defocus aberration.

Another way to assess the degree of defocus tolerance achieved by a wavefront coding system in comparison to a conventional optical system is to use a spatial domain measure such as the point spread function (PSF). Fig. 2.8 shows the PSFs for both optical systems. The top set shows the PSFs for a standard incoherent diffraction-limited imaging system with defocus aberration $W_{20} = 0, 2\lambda$ and 4λ. The bottom set are the PSFs for the same degree of defocus after a cubic phase mask with $\alpha = 10\lambda$ has been introduced in the aperture stop of the traditional optical system. It can be observed that the PSFs of the imaging system with the cubic phase mask are almost unaffected by defocus, they are *encoded* and completely different from the impulse response of a traditional system. The encoded PSFs are asymmetric and as we have shown above, this results in a phase transfer function which is a nonlinear function of frequency and introduces a lateral shifting of the sinusoidal pattern. Rotationally symmetric PSFs do not produce such shifting (however, as the size of the PSF increases with defocus, there are abrupt lateral shifts in the pattern of a half-wave due to a phase transfer function changing from 0 to π). The intensity distribution of the cubic PSF introduces a specific blur to the coded image which appears shifted and blurred as shown in Fig. 2.9, hence post-detection image processing is required to remove the blur.

Many metrics have been proposed to quantify the defocus invariance against the strength α of a cubic phase mask. These metrics measure the degree of similarity between the in-focus and out-of-focus PSFs or MTFs. For instance, one proposed metric is the angle in Hilbert space between any two PSFs, which is a measure of their similarity [32]. The smaller the angle the more similar the two functions are and vice-versa. Other researchers have applied the PSF's full-width-at-half-maximum (FWHM) criterion [5]. The width of the PSF from the cubic phase mask optical system after postdetection signal processing remains essentially unchanged within a wide range of defocus values. Throughout this work, the performance of

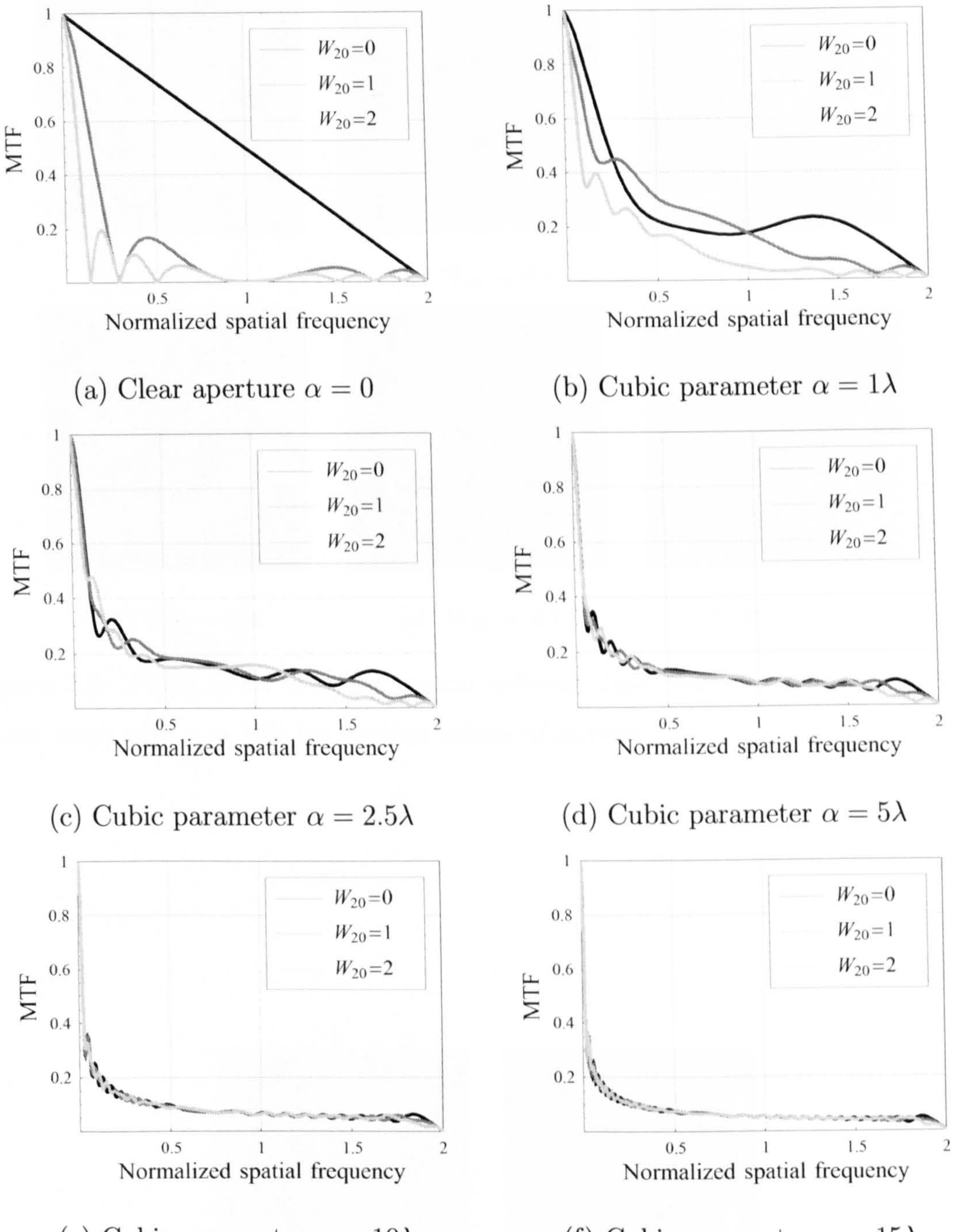

(a) Clear aperture $\alpha = 0$

(b) Cubic parameter $\alpha = 1\lambda$

(c) Cubic parameter $\alpha = 2.5\lambda$

(d) Cubic parameter $\alpha = 5\lambda$

(e) Cubic parameter $\alpha = 10\lambda$

(f) Cubic parameter $\alpha = 15\lambda$

Figure 2.7: *Magnitude of the optical transfer function for various cubic parameters α and focus errors W_{20} (in units of wavelengths). Note the absence of nulls in the wavefront coding MTFs for increasing defocus.*

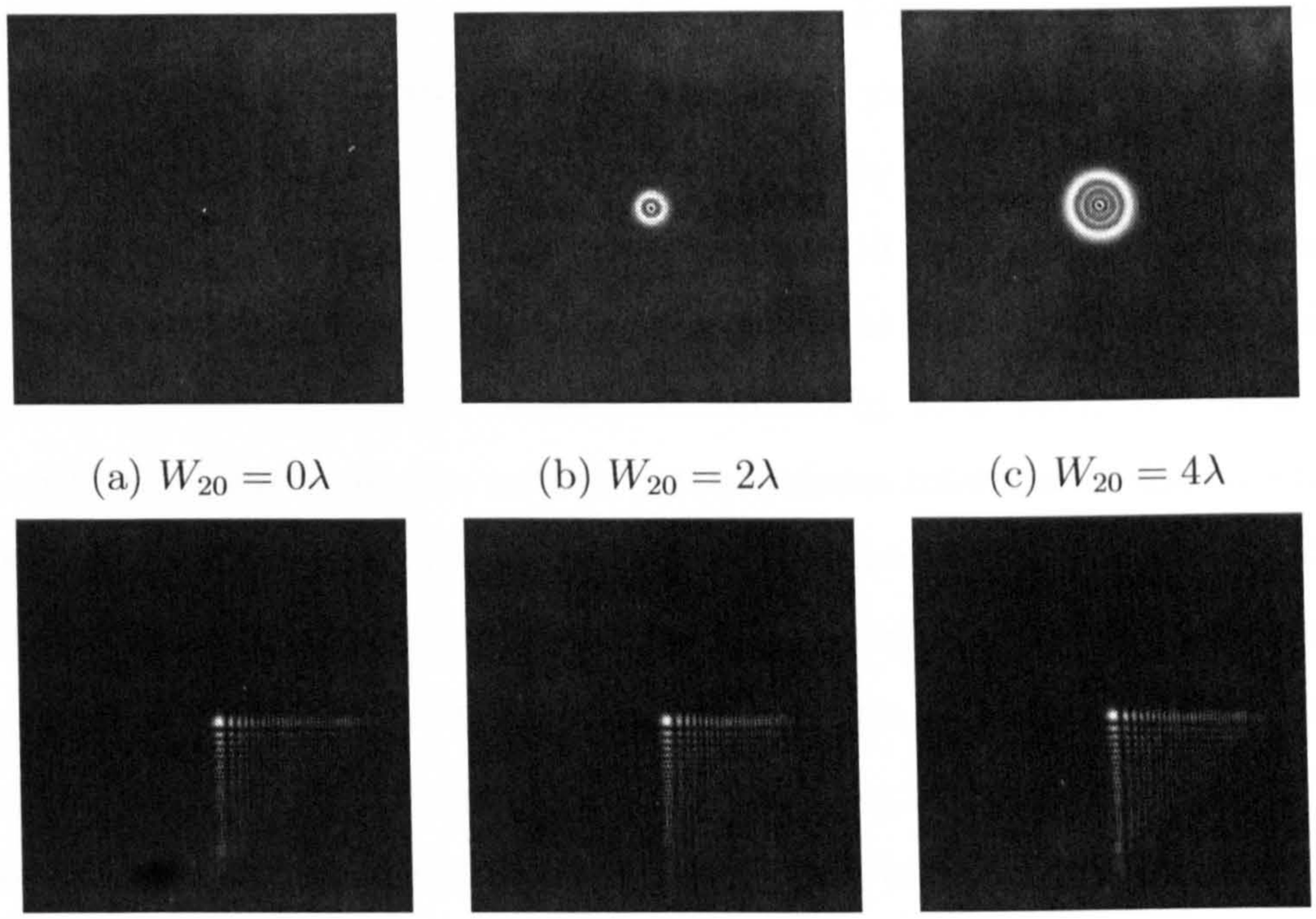

(a) $W_{20} = 0\lambda$ (b) $W_{20} = 2\lambda$ (c) $W_{20} = 4\lambda$

(c) $W_{20} = 0\lambda$ (d) $W_{20} = 2\lambda$ (f) $W_{20} = 4\lambda$

Figure 2.8: *PSFs of an imaging system without (top) and with (bottom) a cubic phase mask with* $\alpha = 10\lambda$ *for various values of defocus.*

Figure 2.9: *Image of Lena acquired with a diffraction-limited imaging system (left) and with a cubic phase mask in the aperture stop of the imaging system (right)*

the cubic phase mask against defocus aberration is evaluated by two simple metric functions of image quality: the Strehl ratio and an MTF variation criterion. These two criteria have been chosen because of their simplicity and generalised usage in quantifying the impact of aberrations. The Strehl ratio is a useful performance criterion defined as the on-axis irradiance produced by the actual wavefront coding system, divided by the on-axis irradiance that would be formed by a diffraction-limited system without the phase mask. A plot of the Strehl ratio as a function of defocus for various cubic phase masks is shown in Fig. 2.10 (left). The cubic phase mask with increasing strengths exhibit better defocus tolerance as the Strehl ratio decreases and becomes practically constant. Note the highly reduced Strehl ratio for high values of α due to the extension and low energy density of the cubic PSF.

A slightly similar criterion, but without considering any parameter of diffraction-limited system, uses the relative variation of the in-focus and out-of-focus MTFs as a metric of defocus invariance. We can express this variation as the volume under the out-of-focus MTF surface divided by the volume under the in-focus MTF surface of the rectangularly separable wavefront coding system, namely

$$s(W_{20},\alpha)=\frac{\iint |H(\mu,W_{20},\alpha)||H(\nu,W_{20},\alpha)|\mathrm{d}\mu\mathrm{d}\nu}{\iint |H(\mu,0,\alpha)||H(\nu,0,\alpha)|\mathrm{d}\mu\mathrm{d}\nu}, \tag{2.43}$$

where $H(\mu,W_{20},\alpha)$ is the one-dimension OTF and μ and ν are the magnitudes of orthogonal spatial frequencies in the Fourier plane. Defocus effects can be translated directly in terms of the reduction in the volume under the MTF surface as displayed in Fig. 2.10 (right). We could somehow extrapolate the Strehl ratio criterion into this MTF metric and consider the parameter $s(W_{20},\alpha)$ in excess of 0.8 as an indication of the degree of defocus invariance. In our opinion, there is a generalised tendency in the literature to specify the extension of depth of field or defocus invariance based upon the criteria referenced and presented above. None of them includes a reliable metric that quantifies the degree of image fidelity and restorability, which would require a combined consideration of the phase and magnitude effects. Let us recall that it is of great importance to also consider the phase of the OTF since it is highly defocus-dependent and gives rise to strong artifacts in the restored image, a preliminary example of this effect is illustrated in Fig.2.11. Quantifying the magnitude of phase effects in image fidelity becomes a specially difficult problem.

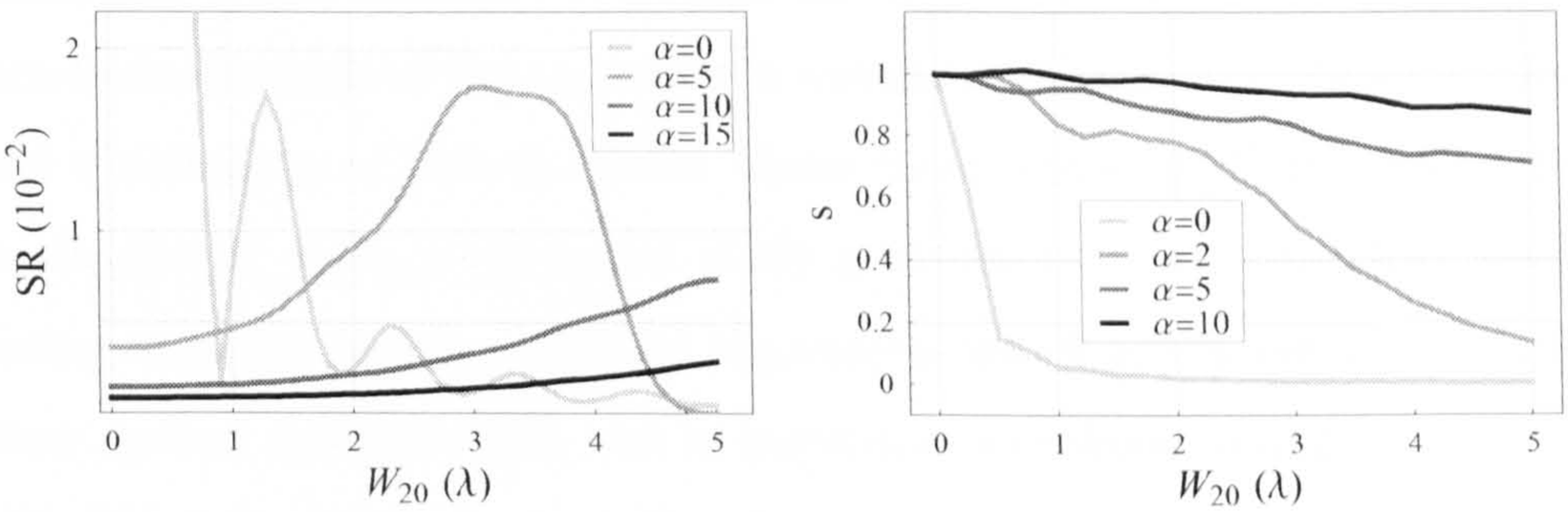

Figure 2.10: *Strehl ratio (left) and MTF variation criterion (right) for various cubic phase mask and defocus values. Cubic parameter α in units of wavelengths.*

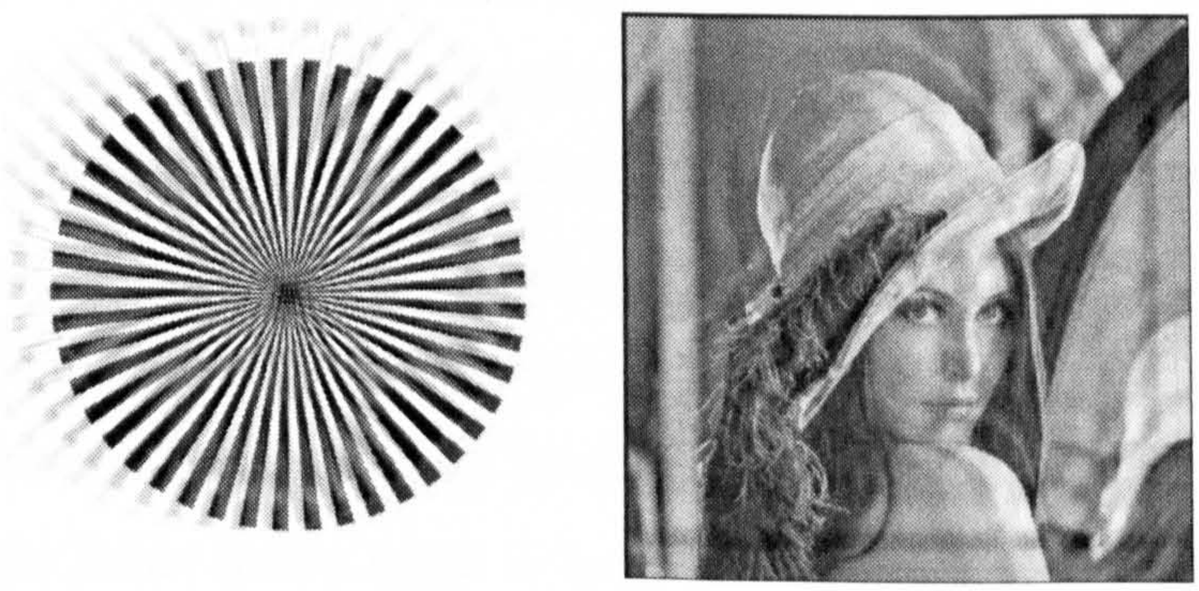

Figure 2.11: *Examples of the effect of phase disparity between the convolution and deconvolution OTFs with wavefront coding.*

Geometrical optics description: Ray trace and caustics

The intricate mathematical derivation of the phase mask by means of the ambiguity function and the stationary phase approximation does not easily provide a physical understanding of the relevance of a cubic function to extend the depth of field. A raytrace-based analysis of the transmitted wavefront allows us to obtain a clarifying physical explanation of how the cubic phase mask operates. Furthermore, from a practical point of view, a ray-based study provides both a tremendous saving in computing time and simple analytical expressions which give a valuable insight into the many optical processes [59], and in particular wavefront coding.

Traditionally, light rays emerging from a point source in the object space are focused by an ideal lens into a point at the image plane. The raytracing of a traditional system is shown in Fig. 2.12(a), where incident parallel rays are focused to a point at the image plane of a conventional ideal lens. A close-up into the region near the focal plane is shown in Fig. 2.12(b). These diagrams have been obtained from the raytracing tool of a commercial optical design software called *Zemax*. The ray diagrams illustrate how the point spread function of a conventional system is very sensitive to defocus. When a cubic phase mask is introduced on the front surface of the ideal lens the rays no longer focus onto a single point but form an extended bundle in the region about the image plane as shown in Fig. 2.12(c). The envelope of the rays forms a caustic described by a nearly parabolic equation. The caustic refers to the curve (or surface) to which the light rays are tangent, defining a boundary of an envelope of rays as a curve of concentrated light [60]. In the part where the caustic is basically flat, there is a slow axial variation in the distribution of the rays. A magnified picture of the caustic in the focal area is shown in Fig. 2.12(d). Thus, as the image plane crosses the caustic curve, the number of rays that contribute to the wave field changes. Contrary to having a single focal point, the point spread function with the cubic phase mask is large and appears to be unchanged over a longer distance along the axis.

From observation of the ray-trace diagram and for a one-dimensional system, we can deduce that the antisymmetric shape of cubic phase element refracts light so that the rays cross the optical axis at different locations: no ray, apart from the on-axis ray, is directed towards the conventional focal point. Furthermore, there are no two rays with the same direction. Note that every ray transmitted by the phase

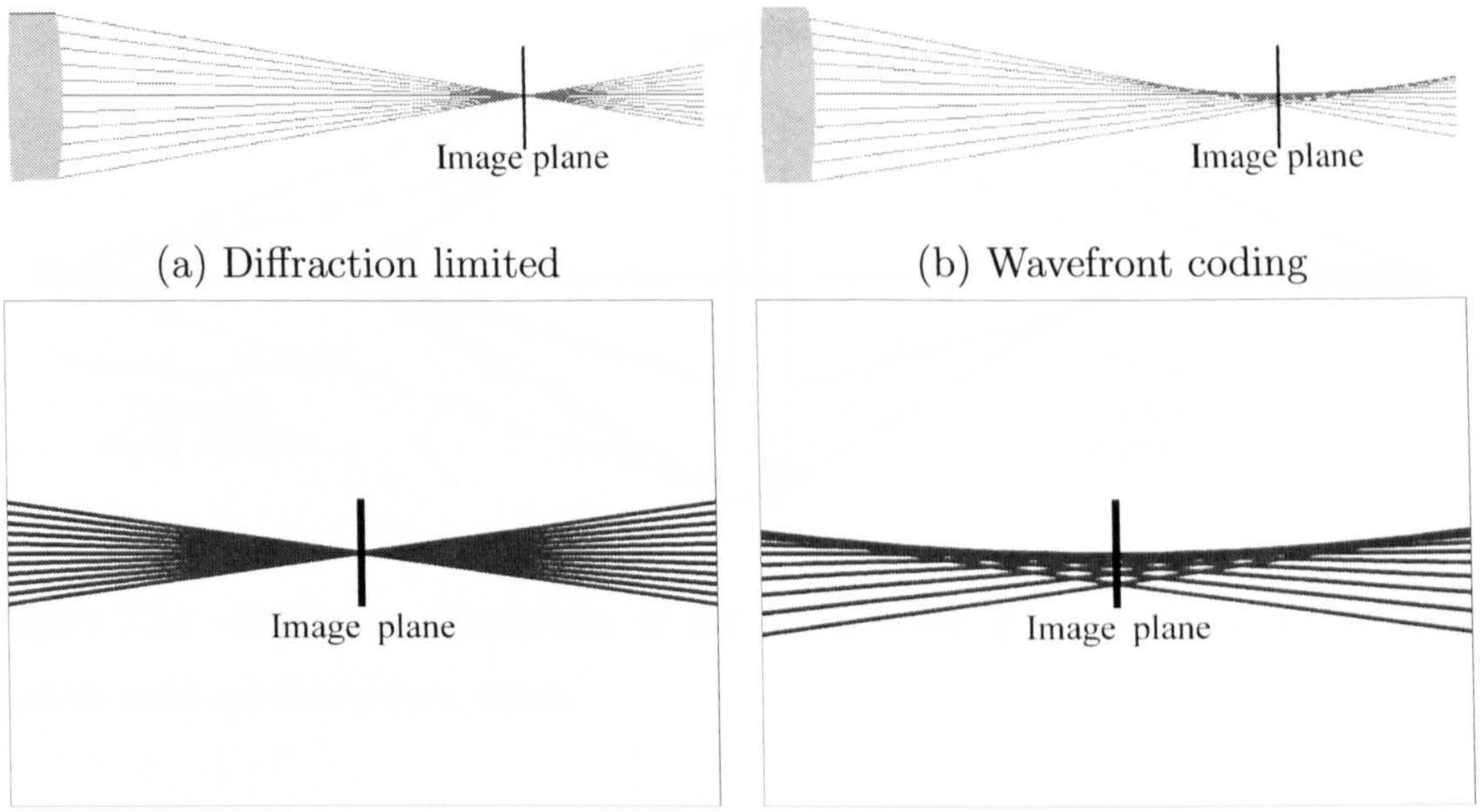

(a) Diffraction limited

(b) Wavefront coding

(c) Close-up in the focal region

(d) Close-up in the focal region

Figure 2.12: *Light focusing in a F/5 lens of focal length f=60mm (a) Image point for a diffraction limited optical system. (b) Caustic for a wavefront coding optical system.*

mask intersects the others at some point.

The functioning principles of the antisymmetric cubic phase mask are identical to those of the circularly symmetric logarithmic phase mask [40] despite having been derived with two entirely different methods. The rotationally symmetric phase mask was derived by Chi *et al.* in 2001 from a purely ray trace analysis together with Fermat's principle. The logarithmic phase mask is continuously multifocal: the focal length varies with the radius so that there is always an annular portion of the lens that provides a the in-focus image of an object point located within designed depth of field. The rest of the annular rings contribute to blurring, which can be reduced by digital image processing. Likewise, although for an antisymmetric phase mask there is no single-focal annular ring, there is always a portion of the cubic phase mask that brings to sharp focus any object point within the aimed depth of field, as illustrated in Fig. 2.13. Despite having the same functioning principles (from the point of view of raytracing) the cubic and logarithmic masks present two significant differences:

1. The antisymmetric shape of the cubic phase mask results in a complex OTF whose phase varies with defocus. The complex nature of the OTF prevents the

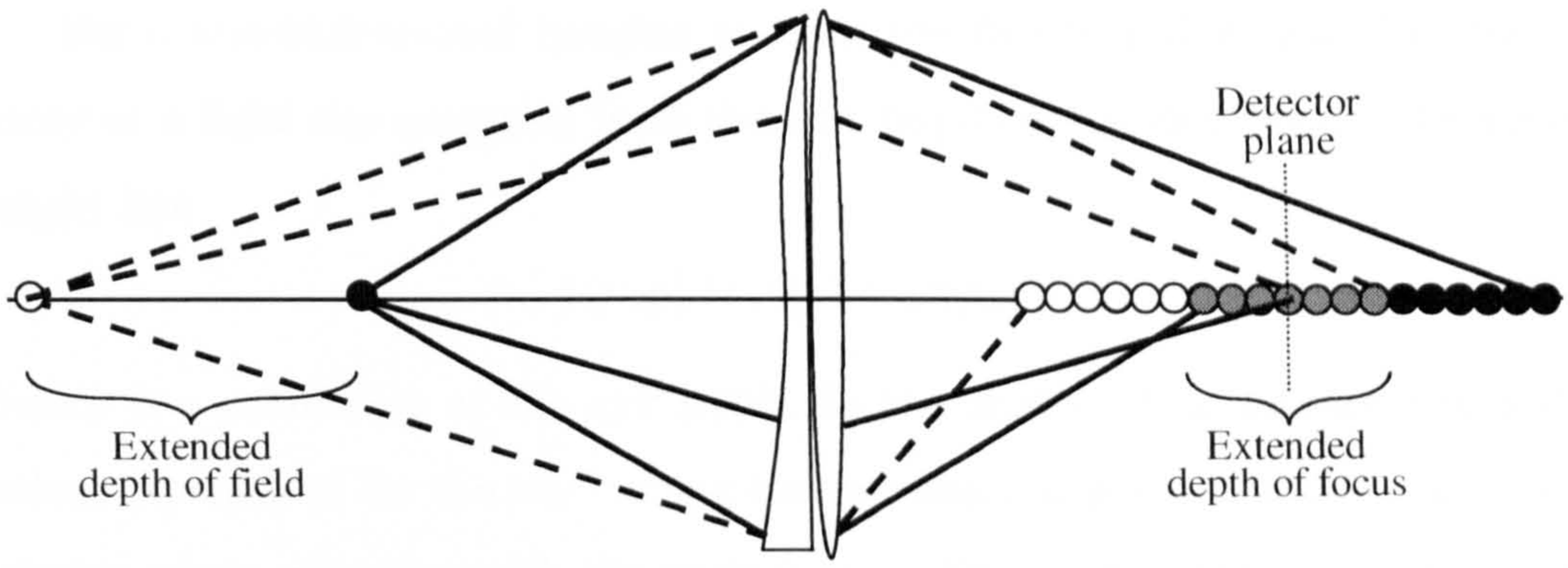

Figure 2.13: *Ray trace description of the functioning of a wavefront coding optical system with a cubic phase mask.*

presence of nulls in the OTF as defocus is increased. On the other hand, the rotationally symmetric profile of the logarithmic phase mask results always in a real OTF for all values of defocus, which may be regarded as advantageous, but it contains nulls and phase inversions at some defocus values. This key aspect, which has important consequences in the restoration of the coded images, will be studied in more detail in the following chapters.

2. The antisymmetric shape of the cubic phase mask introduces no focusing power into the optical system and therefore the OTF is symmetrical about the image focal plane, thus: $H(\nu, W_{20}, \alpha) = H(\nu, -W_{20}, \alpha)$. In contrast, the logarithmic phase mask has focusing power and the point spread functions are no longer symmetrical about the image plane.

By investigating the ray tracing equations it is possible to obtain important parameters that provide quick and valuable information about the performance of an optical system with a cubic phase mask. Using this approach we can not only derive new phase masks to extend the depth of field but also know, for instance, the extent of the geometrical PSF (spot diagram) over the detector area and also the shape and length of the caustic. The size of the spot diagram shows how tightly the rays of light passing through are focused on the image plane. The size of the spot plays a fundamental factor in the computational load of the restoration algorithms and its analytical equation provides a fast way of predicting the kernel size. On the other hand, the length and shape of the caustic curve is directly related to the amount of depth of field obtained with the cubic phase mask.

For a one-dimensional imaging system, the function that describes the trajectory of a light ray emerging from the exit pupil can be described in terms of a straight line

$$f(x,p) = A(p) + B(p)x \tag{2.44}$$

where p is a coordinate at the exit pupil. In the analysis that follows, the mathematical expressions for the ray tracing become less complicated if the y-axis of the cartesian plane coincides with the optical axis. Thus, when $f(x,p)$ is evaluated at $x = 0$ for a ray pupil coordinate p, we obtain the distance $A(p)$ from the pupil plane at which the ray p crosses the optical axis. The slope $B(p)$ controls the direction of the ray. These parameters can be readily calculated from the geometry of the emerging wavefront at the exit pupil. The direction of the ray is calculated from the normal to the wavefront, which for a one-dimensional wavefront $\theta(x)$ is defined as

$$\mathbf{n} = \frac{\partial\theta(x)}{\partial x}\mathbf{x} + \mathbf{y}. \tag{2.45}$$

where $\mathbf{x}$ and $\mathbf{y}$ are the unit vectors for the cartesian axes. We now consider an ideal imaging system in which a cubic phase mask has been placed in the aperture stop. The aperture half-width is R and the distance from the lens to the image plane is d_i. The wavefront equation is a combination of the spherical and cubic wavefronts produced by the ideal lens and phase mask respectively, which yield

$$\theta(x) = d_i - \sqrt{d_i^2 - x^2} + \alpha(x/R)^3 \tag{2.46}$$

where α is the optical path difference introduced by the cubic phase mask at the edge of the aperture. Using Eq. (2.45) and Eq. (2.46) we can calculate the offset $A(p)$ and slope $B(p)$ of the ray function defined in Eq. (2.44), thus

$$A(p) = \frac{\alpha p^3}{R^3} + \frac{3\alpha\left(p^2 - d_i^2\right)p}{R^3 + 3p\alpha\sqrt{d_i^2 - p^2}} + d_i, \tag{2.47}$$

and

$$B(p) = -\frac{1}{p\left(\frac{3p\alpha}{R^3} + \frac{1}{\sqrt{d_i^2 - p^2}}\right)}. \tag{2.48}$$

These two expressions determine the position and direction of any ray in the image space. A wavefront coding system deflects all the rays into different directions but intersecting each other at some point according to displacement $A(p)$. Two rays emerging from the exit pupil at p_1 and p_2 will cross each other when $f(x_{12}, p_1) =$

$f(x_{12}, p_2)$, this condition is met when

$$x_{12} = \frac{M(p_1, p_2)}{N(p_1, p_2)}, \tag{2.49}$$

where the functions M and N are presented in Appendix B. These functions are lengthy and can be omitted in the main derivation. Using Eq. (2.49), we can calculate the value of x at which two infinitesimally adjacent rays p and $p + \delta p$ intersect. This is carried out by taking the limit when $\delta p \longrightarrow 0$, thus

$$x_c(p) = \lim_{\delta p \to 0} \frac{M(p, p + \delta p)}{N(p, p + \delta p)}, \tag{2.50}$$

evaluating further, it yields

$$x_c(p) = -\frac{3p^2\alpha\sqrt{d_i^2 - p^2}\left(-9\alpha^2p^6 + 9\alpha^2d_i^2p^4 + 9R^3\alpha\sqrt{d_i^2 - p^2}p^3 + 4R^6p^2 - R^6d_i^2\right)}{R^6\left[d_i^2R^3 + 6p\alpha\left(d_i^2 - p^2\right)^{3/2}\right]}. \tag{2.51}$$

The caustic curve is formed by the envelope of the refracted rays, and the latter, by the intersection of each ray with its infinitesimally close neighbor. By combining Eq. (2.44) and Eq. (2.51) we obtain a parametric equation $C(p)$ that describes the caustic curve of a wavefront coding optical system

$$\begin{aligned} C_x(p) &= f(x_c(p), p) \\ C_y(p) &= x_c(p) \end{aligned} \tag{2.52}$$

with $-R \leq p \leq R$. Note that parametric curves can be rotated by 90 degrees with respect to the coordinate system by simply exchanging the expressions of the x and y axes. Making use of this property, the coordinate system has been rotated in Eq. (2.52) so that the x-axis and y-axis correspond now to the optical and ray height axes respectively. If the cubic phase mask is removed, the caustic curve is contracted into an image point located at d_i, as is expected from an ideal optical system:

$$\begin{aligned} C_x(p) &= d_i \\ C_y(p) &= 0 \end{aligned} \tag{2.53}$$

which is valid for any ray p. The caustic curve calculated with Eq. (2.52) for an ideal $F/5$ imaging system of focal length 60mm and with a cubic phase mask $\alpha = 10\lambda$ ($\lambda = 0.5\mu$m) is shown in Fig. 2.14(a). The raytracing was calculated using *Zemax*; note the perfect agreement between Eq. (2.52) and the optical design program.

The antisymmetric shape of the cubic phase mask produces a caustic curve that is not exactly symmetrical about the image plane: a pair of rays passing through the

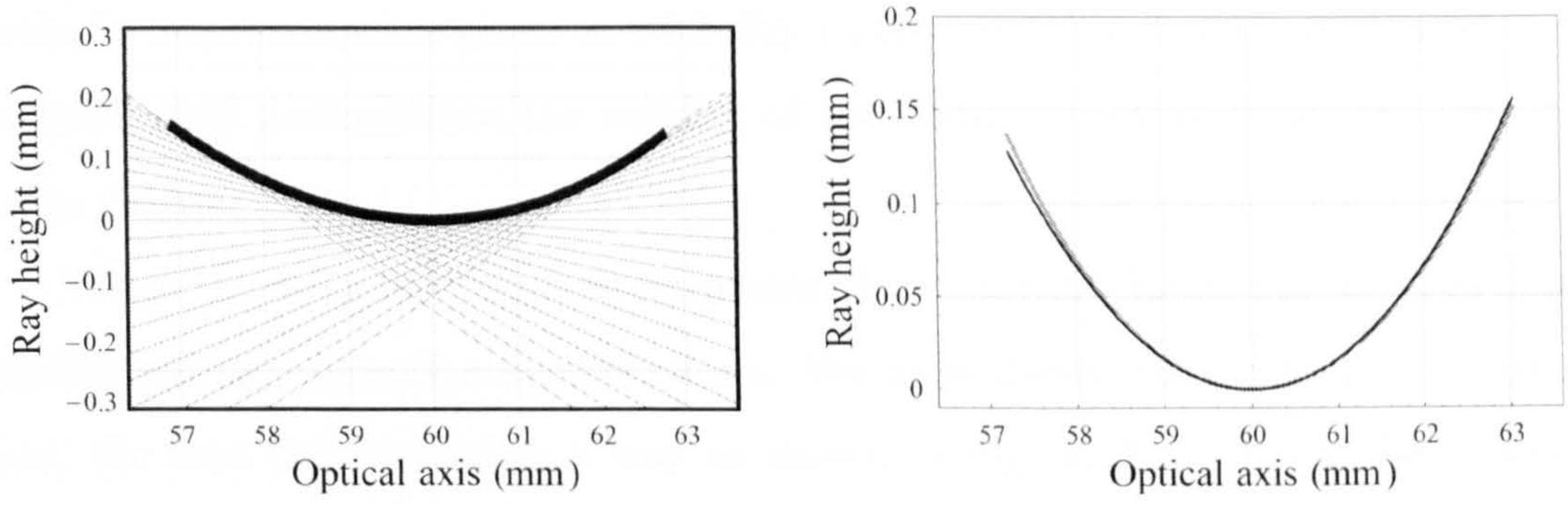

Figure 2.14: *(a) Exaggerated representation of the caustic curve of a wavefront coding system with* $\alpha = 10\lambda$. *(b) Comparison between the exact caustic curve (black) and an approximation with a parabolic function in Eq. (2.55) (grey). The caustic represents the motion of the centroid ray of the point spread function with defocus aberration.*

cubic phase mask at opposite pupil coordinates $-p$ and p will undertake different optical paths and refract at different angles, as we have shown in Fig. 2.13. For this reason, the exact mathematical expression of the caustic curve becomes a long and complicated equation, see Eq. (B-5) in Appendix B. However, since the curvature of the wavefront introduced by the cubic phase mask is in general very small in comparison with the ideal spherical wavefront, the caustic equation simplifies substantially when it is approximated by a simple parabola near the image plane where the caustic curve if essentially flat. The parametric caustic in Eq. (2.52) is replaced by a more elementary parabolic curve defined as

$$C_{approx}(\delta x) = \sigma \delta x^2 \tag{2.54}$$

where δx is a displacement along the optical axis relative to the image plane location and σ is dependent on the cubic parameter α, the aperture radius R and the image distance d_i of the optical system. A detailed derivation of the parameter σ can be found in Appendix B. By replacing σ with its actual expression from Eq. (B-9) we obtain a simple form of the caustic produced by a cubic phase mask

$$C(\delta x) = \frac{R^3}{12 d_i^3 \alpha} \delta x^2, \tag{2.55}$$

which is valid for $\alpha << R^2/6d_i$. As the value of α increases the flat region of the parabola widens and an extended depth of focus is obtained. Fig. 2.14(b) shows a comparison between the caustic curve calculated by means of ray tracing and the

parabolic approximation given in with Eq. (2.55). Both curves are evaluated independently and demonstrate the validity of the deduction of an estimated equation for the caustic.

When the amount of defocus surpasses the acceptable limit, the restored image contains strong artifacts and alterations. We have shown that with a cubic phase plate, the rays are focused in a way as shown in Fig. 2.14(a). It can be observed in the ray trace as the detector plane is moved along the optical axis that a lateral displacement of the PSF takes place. Thus, as the objects being imaged fall outside the region where the caustic is essentially flat, the first detectable effect is a translation of the objects in the scene based upon their distance to the object focal plane. It can also be noticed that the position of the upper border of the PSF varies, which results in substantial modifications in the appearance of the restored the image.

In addition to the shape of the caustic curve, its length projected onto the optical axis plays an important role in achieving an extended the depth of field. The axis extent of the caustic relates to the tolerable displacement allowed along the optical axis before defocus effects actually start to affect the coded image. By obtaining an analytical expression through ray tracing equations enables us to demarcate this axial region of and its correspondence with the cubic parameter α. The length L of the caustic projected onto the optical axis is obtained when the rays at the edges of the aperture $p = \pm R$ intercept their nearby neighbors, so for $\alpha > 0$

$$L = f(x_c(-R), -R) - f(x_c(R), R), \tag{2.56}$$

where f and x_c are given in Eq. (2.52) and Eq. (2.51) respectively. The exact expression for L is given by Eq. (B-12), however a very good approximation can be obtained by considering L directly proportional to α, which in terms of the f-number yields

$$L(\alpha) \approx \left(48\mathrm{F}/\#^2 - 38 + \frac{6}{\mathrm{F}/\#^2}\right)\alpha. \tag{2.57}$$

The length of the caustic projected onto the optical axis of an $F/5$ system of focal length 60mm as a function of the cubic parameter α is shown in Fig. 2.15(b). The plots of the exact and approximated equations can be seen to be virtually identical. The choice of rays passing at the edge of the aperture $p = \pm R$ to calculate the length of the caustic has been driven by the aim of obtaining its full length; however, a more appropriate selection (i.e. $p = \pm R/2$) will further enclose the flat invariant region and provide more realistic estimation of depth of focus. Similar expressions

to Eq. (2.57) and Eq. (B-12) are easily obtained for any pair of rays exiting from the aperture.

Without abandoning the ray tracing approach which offers simple analytical equations, we can continue to extract key performance parameters such as the size of the geometrical PSF or spot diagram. Note the spot diagram is a collection of points, with each point representing a single ray. There is no mutual interference between the rays. It is a useful and reasonable indicator of performance when the spot is much larger than the Airy disk and therefore a consideration of diffraction is not required [61]. The size of the PSF has an important effect on the post-detection restoration and influences the flexibility and precision of the deconvolution filter. It can be very useful to have a quick means of estimating the extent and shape of the PSF. As a rule of thumb, the geometrical PSF may be used in place of the diffraction PSF without significant loss in the restoration quality when the signal-to-noise ratio is less than 30 dB [62]. We can easily calculate the size S of the spot diagram as a function of α at the image plane from Eq. (2.49) by selecting the rays $p = \pm R$, yielding

$$S(\alpha) = \frac{-4\alpha R^4 - 9\alpha^3 R^2 + 3\alpha\left(R^2 + 3\alpha^2\right) d_i^2}{R^3\sqrt{\left(d_i - R\right)\left(R + d_i\right)}}. \tag{2.58}$$

Since α is very small in comparison to R and d_i, a linear relationship between $S(\alpha)$ and α holds, thus Eq. (2.58) can be approximated in terms of f-number by the simpler expression,

$$S(\alpha) \approx \frac{4\left(3F/\#^2 - 1\right)\alpha}{\sqrt{4F/\#^2 - 1}}. \tag{2.59}$$

Fig. 2.15(b) shows the size of the geometric PSF as a function of the cubic parameter α. Note the near-perfect correspondence between the approximation in Eq. (2.59) and the size of the PSFs calculated with *Zemax*.

We have provided a new insight and analytical expressions that describe the effect of the cubic phase mask on the caustic for a one-dimensional aperture. It can be extended to a rectangularly separable aperture in two dimensions but offers no further information. The only aspect to point out is that the bundle of rays passing through the cubic phase mask at an angle of 135 degrees (from the x-axis), see Fig. 2.5(b), will encounter no phase distortion since along this direction $y = -x$ the phase $\theta(x, y)$ is constant. Note that the bundle of rays will be focused into an image point which will lack ability to tolerate defocus.

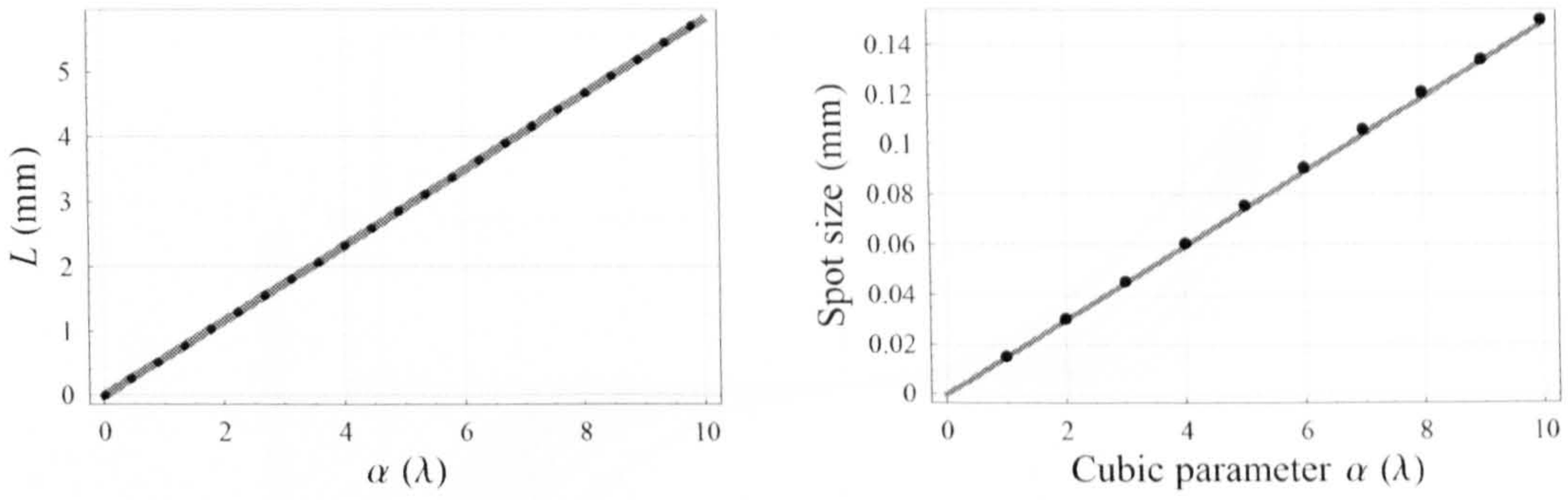

(a) (b)

Figure 2.15: *(a) Length of the caustic onto the optical axis as a function of* α *using exact (solid) and approximated (dotted) equations. (b) Size of the geometric PSF at the image plane as a function of* α *using Eq. (2.59) (solid) and Zemax (dotted).* $F/5$ *optical system,* f*=60mm and* $\lambda = 0.5\mu m$*.*

Phase masks with $\theta(x) = \alpha x^n$

Let us recall that the derivation of the cubic phase mask included two essential approximations: the stationary phase method and a Taylor expansion of the phase shape. Although these approximations allowed us to obtain a satisfactory phase mask shape with a pure cubic profile, investigations have been conducted to search numerically for phase profiles of various polynomial powers that have MTFs that remain practically invariant with defocus. One polynomial family of rectangularly separable mask profiles [63] is given in normalised coordinates by

$$\theta(x) = \alpha \, \text{sign}(x)|x|^n, \tag{2.60}$$

where $\alpha > 0$, $\text{sign}(x) = +1$ for $x > 0$ and $\text{sign}(x) = -1$ for $x < 0$. The parameter α controls the tolerance to defocus by means of the peak-to-valley height of optical path and the exponential parameter n controls the mask profile. Fig. 2.16 illustrates the phase shape for $2 \leq n \leq 9$ in normalised coordinates and with the same optical path difference at the edges of the aperture. Increasing the power n flattens the central region of the profile and increases its curvature around the edges. Sauceda *et al.* [64] explored the use of phase mask profiles with fractional power n that produce MTFs that remain practically invariant to focus errors. From numerical evaluations they concluded that the variations of the defocused MTFs, with respect to the in-focus MTF, are minimized if $n = 3.85$. Other intervals were identified in which the MTF remains practically invariant to defocus error [33]. For example,

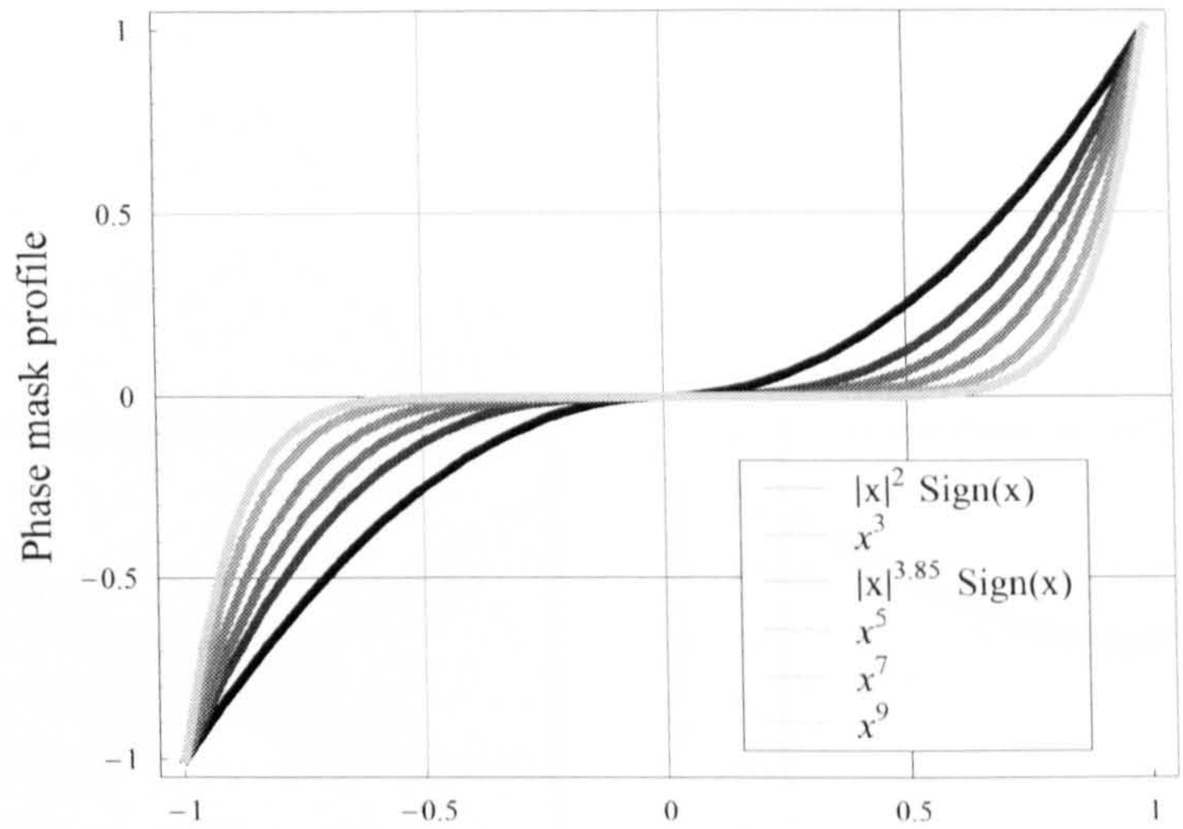

Figure 2.16: *Rectangularly separable phase mask profiles. The shape of this family of phase mask is given by* $\alpha\,\mathrm{sign}(x)x^n$ *with* $2 \leq n \leq 9$ *and* $\alpha = 1$.

similar results using the same metric (yet not as good as those given by the previous expression) are obtained if one sets the fractional power to $n = 4.20$. Certain caution must be taken with the validity of these results as no clear method to evaluate the change in the MTF was properly disclose throughout their investigation. Another study carried out by Mezouari [65] concluded that the optimum fraction power was $n = 2.85$. This result was obtained after calculating numerically the average change in the MTF as a function of defocus with respect to the in-focus MTF.

All these studies that aim to find the optimum phase profile depend greatly on the chosen criterion that evaluates the variation of certain parameter (MTF, PSF, etc) with respect to defocus. Obviously, the vast diversity of criteria gives rise to a disparity of results as we have just shown. However, a simple analysis of the caustics produced by the different phase profiles provides a clear understanding and an indication of adequate phase profiles. Furthermore, it saves many hours of computer modeling. Fig. 2.17 shows ray tracing and caustics for phase masks with $2 \leq n \leq 9$ and with the same optical path difference at the edge of the aperture. It can be observed that wavefronts departing from a nearly cubic shape produce caustics that change abruptly with axial displacement and whose depression region narrows towards the image plane, just as it occurs in a diffraction-limited system. These caustics have lost capability to tolerate defocus . In addition, as the power n increase the energy density of the PSF concentrates closer to the optical axis whilst

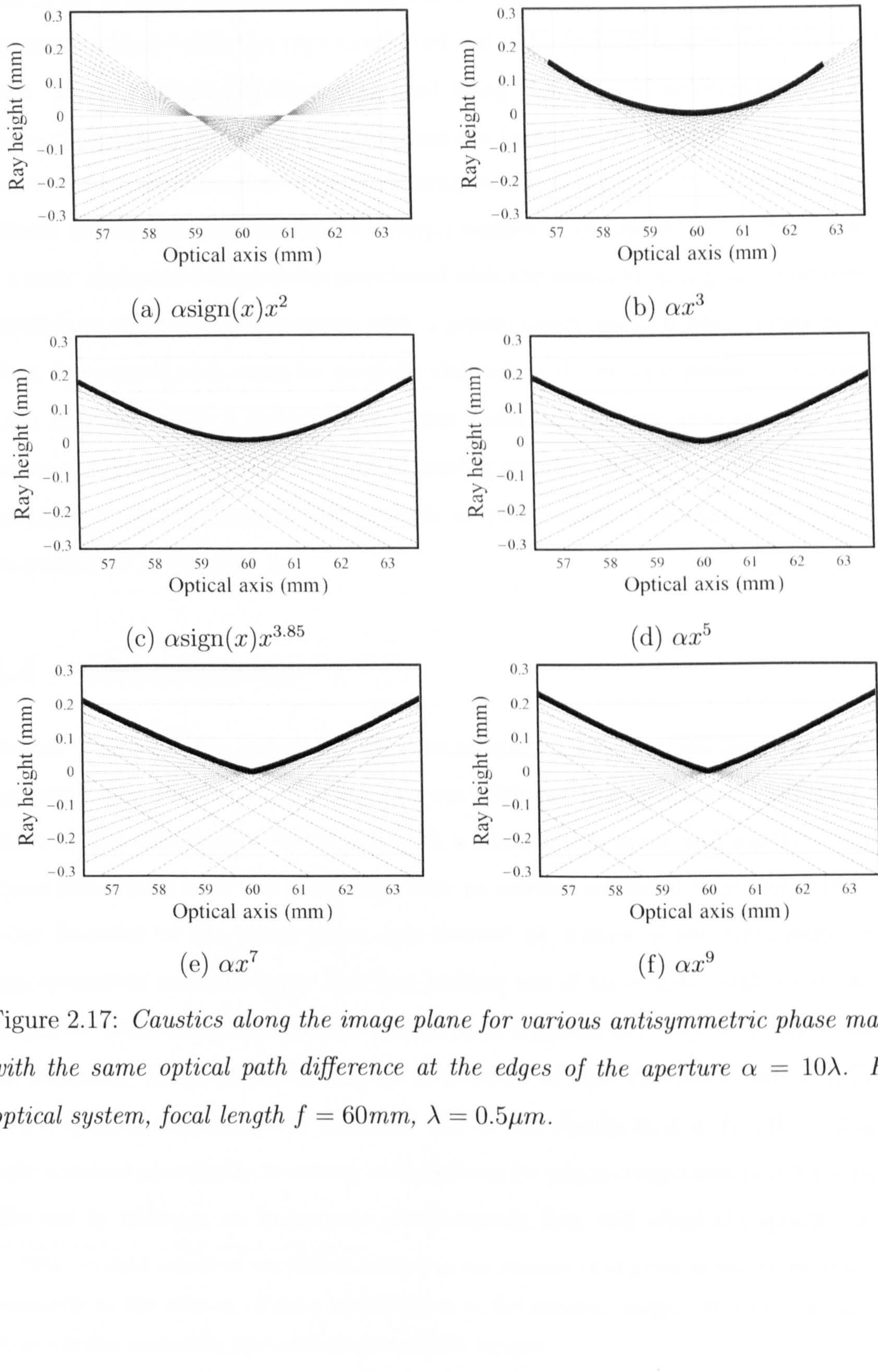

Figure 2.17: *Caustics along the image plane for various antisymmetric phase masks with the same optical path difference at the edges of the aperture* $\alpha = 10\lambda$. *F/5 optical system, focal length* $f = 60mm$, $\lambda = 0.5\mu m$.

broadening the physical extend of the PSF (ideally, the optimum phase mask should give maximum extended depth of field with the smallest PSF size*). Therefore, the highly condensed energy in the axial region quickly becomes diffused by increasing defocus producing an effect contrary to that of an extended-depth-of-focus system. This is an evident consequence of having a phase mask with a progressively flat central area that leaves the rays unaffected and subsequently focused into an image point. Some authors [66] have suggested using this type of antisymmetric phase masks with a flat central region to increase the height of the resulting MTF and reduce the noise amplification in the final image whilst retaining some ability to reduce defocus aberration. Nevertheless, the improvement in the height of the MTF comes at a cost: the spatial frequencies associated with the unmodified region become more sensitive to defocus in comparison with a continuously varying phase mask profile. Thus, the central area must be carefully defined as the general region of a stopped down aperture where a system would have a suitable defocus invariance for a particular application, despite the fact of having reduced spatial resolution and light throughput. Further results and analysis on phase masks with flat central regions are presented in Chapter 4.

2.4 Conclusions

We have introduced a technique called wavefront coding that increases the defocus insensitivity in incoherent imaging systems. This method consists in modifying the phase of the transmitted wavefront with a cubic phase mask and applying digital signal processing onto the detected image to achieve extended depth of field. The cubic function of the phase mask was derived by means of the stationary phase approximation and ambiguity function making use of an original mathematical approach in which the phase mask is described in a generalised way by a Taylor series. Additionally, an exact mathematical expression of the wavefront coding OTF in terms of error functions was obtained and it was shown that although its magnitude remains practically invariant with defocus its phase component is indeed highly affected by defocus, an important consideration that will affect the quality of the

*The physical extent of the PSF is related to the amount of blurring in the coded image and eventually to the amount of noise amplification in the restored image. Broader PSFs increase deconvolution processing time and produce noisier images.

decoded images.

An original geometrical optics description of the wavefront coding technique has also been presented. We have presented a new understanding of how the coding phase mask works based on simple tracing of rays and their mutual intersections to from a caustic. Furthermore, important performance parameters of wavefront coding systems have been extracted from the caustic equation, these include projection of the caustic onto the optical axis (related to the amount of extended depth of focus), profile of the caustic curve and size of the spot diagram. We have also demonstrated within the geometrical optics representation that the most appropriate phase masks for increased defocus invariance are given by functions with cubic power or near.

The elementary equations of geometrical optics offer a new scope for the design -by analytical or numerical means- of antisymmetric phase mask profiles that shall be certainly explored in future work. The antisymmetric attribute will be necessary to ensure that no nulls occur in the MTF.

Chapter 3

Phase masks for control of primary third-order aberrations: coma, astigmatism and defocus

Summary. In the first part of the chapter, we investigate the use of pupil plane phase retardation functions that reduce the variation of the intensity of the focal point of incoherent imaging systems that suffer from primary third-order aberrations such as coma and astigmatism. A quartic phase retardation function is derived by means of the Strehl ratio that gives an improved modulation transfer function (MTF) which remains practically invariant for moderate amounts of coma and astigmatism. In the second part, an antisymmetric phase mask for a circular aperture that alleviates the effect of defocus is derived in terms of Zernike polynomials.

1 Rotationally symmetric quartic phase mask

1.1 Introduction

Until very recently, the control and reduction of third-order aberrations, such as spherical aberration, were carried out by means of amplitude filters. Various types of amplitude filters have been reported in the literature starting from the use of annular apertures where the effective pupil is considerably reduced (the pinhole camera is the extreme example), to those that employ the whole aperture using shaded filters. Of special interest are the annular apodizers derived by Ojeda-Castañeda [24, 26]. Amplitude filters alleviate aberrations at the expense of the light transmitted by the optical system. With the widespread introduction of digital signal processing

techniques, phase masks offer the advantage of improved optical resolution and light gathering as is the case with wavefront coded imaging systems [5]. The enhancement in the performance achieved by this wavefront coding technique is accompanied by a significant reduction in the signal-to-noise ratio and presence of artifacts in the restored image, as we report in Chapter 4. Furthermore, the non-rotationally symmetric shape of the phase mask shape means it is problematic and costly to manufacture using traditional methods such as diamond machining. Several novel approaches providing increased control of defocus with rotationally symmetric phase masks have been demonstrated experimentally [40, 44]. Although their defocus-control performances has proved to be inferior to the cubic antisymmetric phase masks, they are adequate in some potential applications in the field of ophthalmology [67].

In this chapter, we extend the previous work carried out at Heriot-Watt University in which radially symmetric phase masks with logarithmic and quartic profiles that reduce the sensitivity of incoherent imaging systems to variations in defocus and spherical aberrations were derived [68, 38, 34]. Practically, the quartic filter has been successfully employed to increase of depth of focus of an optical system for tracking stars [69]. Using a similar process, based on the evaluation of the Strehl ratio [12], in the next two sections we show that quartic filters also yield reduced sensitivity to coma and astigmatism. The choice of axially symmetric quartic filter is driven by the ease of manufacturing this optical element. The evaluation of the Strehl ratio is the parameter mostly used to estimate the energy distribution along the optical axis and to assess the quality of the point spread function (PSF) near to the focal plane. Although various parameters can be used, such as the optical transfer function or the Wigner distribution function [70], the Strehl ratio is commonly used for its simplicity. This is particularly evident when it is possible to derive an analytical expression as often occurs in rotationally symmetric system. In the second part of the chapter, an antisymmetric phase mask is obtained using the equation of the total intensity distribution across the focal plane and not just its axial measure.

The normalised central intensity of the point spread function at the image plane of an optical system is given by [55]

$$I = C\left|\int_0^{2\pi}\int_0^1 P(r)\exp\left[ikW(r,\theta)\right] r\mathrm{d}r\mathrm{d}\theta\right|^2, \tag{3-1}$$

where the exit pupil plane is represented in polar coordinates (r, θ), k is the wave number $2\pi/\lambda$, C is a normalization constant, $W(r, \theta)$ is the wave aberration function and $P(r)$ denotes the pupil function with $P(r) = 1$ for $0 \leq r \leq 1$, and $P(r) = 0$ elsewhere. The radial coordinate r is normalised to the radius of the pupil. A rotationally symmetric mask described by a phase function $\Phi(r)$, that is intended to reduce third order aberrations is placed in the pupil plane, thus Eq. (3-1) becomes

$$I = C \left| \int_0^{2\pi} \int_0^1 P(r) \exp \left\{ ik \left[W(r, \theta) + \Phi(r) \right] \right\} r dr d\theta \right|^2 . \tag{3-2}$$

For an imaging system that suffers from primary third-order aberrations restricted to coma W_{31} and astigmatism W_{22}, the function $W(r, \theta)$ is written in terms of Zernike polynomials as

$$W(r, \theta) = W_{31} r^3 \cos\theta + W_{22} r^2 \cos^2\theta. \tag{3-3}$$

This last expression can be written in a convenient form by employing a change of variable in the radial coordinate r,

$$r^2 = \xi + \frac{1}{2}. \tag{3-4}$$

In the new coordinates system (ξ, θ), the aberration function is rewritten as

$$\tilde{W}(\xi, \theta) = W_{31} \left(\xi + \frac{1}{2} \right)^{3/2} \cos\theta + W_{22} \left(\xi + \frac{1}{2} \right) \cos^2\theta, \tag{3-5}$$

and the analytical expression of the axial intensity in Eq. (3-1) becomes,

$$I = C \left| \int_0^{2\pi} \int_{-1/2}^{1/2} \exp \left\{ ik \left[\tilde{W}(\xi, \theta) + \tilde{\Phi}(\xi) \right] \right\} d\xi d\theta \right|^2 , \tag{3-6}$$

where the superscript ˜ denotes functions expressed in the new radial coordinate ξ.

The present work is restricted to the study of imaging systems in which only one residual third-order aberration, such as coma or astigmatism, is present. Third order spherical aberration and defocus were an object of study in Ref. [38, 68], in which by means of the same methodology, logarithmic and quartic functions were derived and exhibited high tolerance to spherical aberration and defocus.

1.2 Coma

Coma is introduced by misalignment or tilt of optical elements or as an inherent aberration associated with off-axis imaging. It can be problematic in Newtonian telescopes using non-hyperbolic mirrors [71], even for small fields of view.

From Eq. (3-6), the central intensity at the image plane of an optical system suffering from coma is given in the transformed coordinate system by

$$I(W_{31}) = \left| \int_0^{2\pi} \int_{-1/2}^{1/2} \exp\left\{ \mathrm{i}k \left[W_{31}(\xi + 1/2)^{3/2} + \tilde{\Phi}(\xi) \right] \right\} \mathrm{d}\xi \mathrm{d}\theta \right|^2, \qquad (3\text{-}7)$$

where the normalizing constant has been dropped. By integrating Eq. (3-7) over θ, we obtain

$$I(W_{31}) = \left| \int_{-1/2}^{1/2} J_0\left(kW_{31}(\xi + 1/2)^{3/2}\right) \exp\left[\mathrm{i}k\tilde{\Phi}(\xi)\right] \mathrm{d}\xi \mathrm{d}\theta \right|^2, \qquad (3\text{-}8)$$

where J_0 denotes a zero-order Bessel function of the first kind.

The aim of this work is to find an expression for the phase function $\tilde{\Phi}(\xi)$, which yields an irradiance distribution with reduced sensitivity to coma. To evaluate the integral in Eq. (3-8) the stationary phase method is employed [72], which assumes that the major contribution to the integral occurs at the point ξ_s, called the stationary point, where the phase function of the integrand is varying slowly. The stationary phase method has been extensively used in this thesis and a brief overview of this mathematical tool can be found in Appendix A. The intensity in Eq. (3-8) can be approximated by

$$I(W_{31}) \approx A \frac{\left[J_0\left(kW_{31}(\xi + 1/2)^{3/2}\right)\right]^2}{\tilde{\Phi}''(\xi_s)}, \qquad (3\text{-}9)$$

where A is a real-valued multiplicative constant and the superscript $''$ represents the second derivative of the phase function. The stationary point ξ_s, is given by

$$\tilde{\Phi}'(\xi)\Big|_{\xi_s} = 0. \qquad (3\text{-}10)$$

Expression (3-9) is valid only if the phase function $\tilde{\Phi}(\xi)$ satisfies the following condition [73],

$$\frac{3}{2}kW_{31}\sqrt{\xi + 1/2} \left| \frac{J_1\left(kW_{31}(\xi + 1/2)^{3/2}\right)}{J_0\left(kW_{31}(\xi + 1/2)^{3/2}\right)} \right| < \sqrt{\frac{k\tilde{\Phi}''(\xi_s)}{4\pi}}, \qquad (3\text{-}11)$$

for

$$\left| \xi_s \pm \frac{1}{2} \right| > \sqrt{\frac{4\pi}{k\tilde{\Phi}''(\xi_s)}}, \qquad (3\text{-}12)$$

where J_1 denotes a first-order Bessel function of the first kind.

When the stationary point is outside the boundary of integration $-1/2 < \xi_s < 1/2$, both the amplitude of the intensity at the focal point and the optical resolution

are dramatically reduced. Note that when the stationary point is near the border of the integration domain $\xi_s \approx -1/2$, Eq. (3-9) is no longer valid as the boundary effects become important and should be taken into account. According to the expression of axial intensity in Eq. (3-9), the effect of coma W_{31} is explicitly manifest only in the argument of the Bessel function as a factor of $(\xi_s + 1/2)^{3/2}$. It is therefore possible to reduce the impact of coma by choosing a particular phase function $\tilde{\Phi}(\xi_s)$, that yields a stationary point which has a value that is close to the boundary point $\xi_s \approx -1/2$ whilst satisfying the condition given by Eq. (3-11). Practically, in the presence of moderate amounts of coma and when the stationary point is located about the integration boundary $\xi_s \approx -1/2$ the argument of the Bessel function in Eq. (3-9) becomes sufficiently small so that it can be approximated by

$$I(W_{31}) \approx A\frac{\left[J_0\left(kW_{31}(\xi + 1/2)^{3/2}\right)\right]^2}{\tilde{\Phi}''(\xi_s)} \approx A\frac{1}{\tilde{\Phi}''(\xi_s)}. \tag{3-13}$$

This expression for the intensity is comparable to Eq. (5) of Ref. [38], where the phase retardation function $\tilde{\Phi}(\xi)$ that yields enhanced axial intensity invariance is given by a quartic function (i.e. $\tilde{\Phi}(\xi) = \textit{constant}$). Furthermore, this solution is given by the same phase function reported by Zalvidea *et al.* [70] in which quartic phase filters are employed to reduce defocus aberration. The quartic function is expressed in the modified radial coordinate ξ as

$$\tilde{\Phi}(\xi) = \alpha\xi^2 + \alpha_0\xi, \tag{3-14}$$

where the constants α and α_0 are real-valued. In the radial coordinate r, the phase function is written as

$$\Phi(\xi) = \alpha(r^2 - 1/2)^2 + \alpha_0(r^2 - 1/2). \tag{3-15}$$

Note that the parameter α_0 only controls the amount of focal shift along the optical axis. The stationary point ξ_s is then deduced by substituting Eq. (3-14) into Eq. (3-10), to yield

$$\xi_s = -\frac{\alpha_0}{2\alpha}, \tag{3-16}$$

which in turn can be substituted into Eq. (3-13) to give

$$I(W_{31}) \approx \frac{A}{2\alpha}\left[J_0\left(kW_{31}\left(-\frac{\alpha_0}{2\alpha} + \frac{1}{2}\right)^{3/2}\right)\right]^2. \tag{3-17}$$

The ratio of the quartic filter parameters α/α_0 determines the variation of the axial intensity $I(W_{31})$ for increasing values of coma W_{31}. Large values of α and α_0

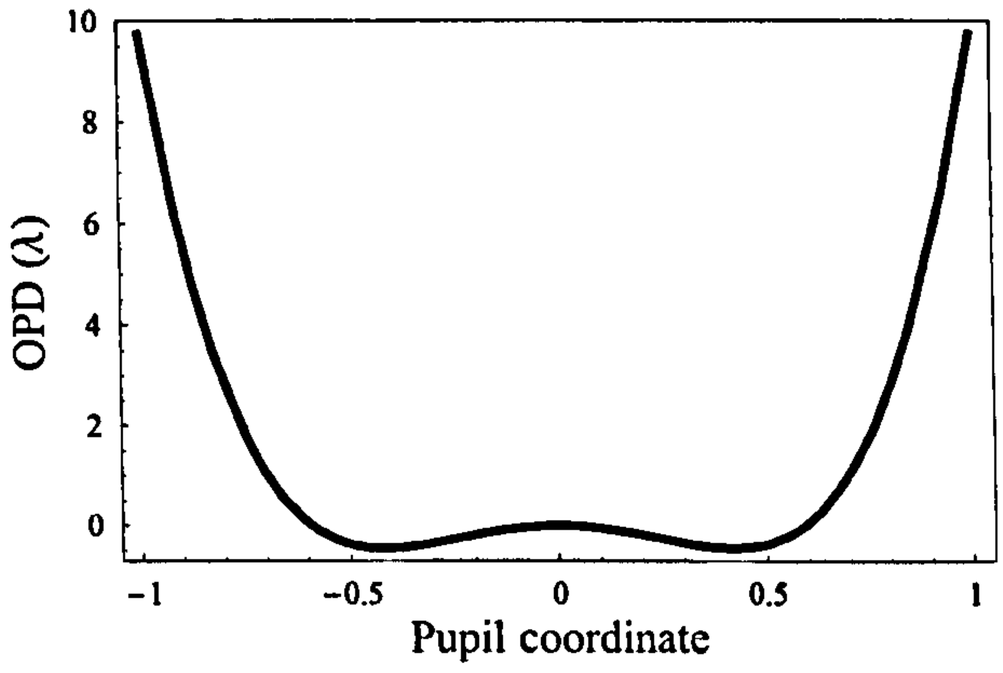

Figure 3.1: *Cross section, in normalised units, of the optical path difference introduced by a rotationally symmetric quartic phase mask with* $\alpha = 15\lambda$ *and* $\alpha_0 = 9.75\lambda$.

produce broad point spread functions with low axial intensity, which results in a reduction of the magnitude of the MTF and its cut-off frequency. Therefore practical optical systems based on this technique require a tradeoff between tolerance to aberrations and reduction in resolution. The values of the quartic filter parameters are obtained using algorithms based on user-defined merit functions with constraints in the magnitude of the axial intensity and/or the magnitude of the modulation transfer function (MTF). In the present work, the numerical value of α and α_0 are obtained by setting the MTF constraints to an effective cutoff frequency of 0.5 (normalised units) while attaining maximum average value in its magnitude. After optimization, a quartic filter was designed with $\alpha = 15\lambda$ and $\alpha_0 = 9.75\lambda$, for a illumination wavelength of λ. A cross section of the optical path difference introduced by the rotationally symmetric quartic mask is shown in Fig. (3.1). These values result in a stationary point $\xi_s = 0.325$, which satisfies the boundary conditions of Eq. (3-11), and allow a reduction in the effect of coma on the Strehl ratio as shown in Fig. (3.2). Further assessment of the performance achieved by the quartic mask is carried out by numerical simulation of the MTF subject to various amounts of coma, W_{31}. To appreciate the performance of the quartic mask, the MTFs of an optical system with and without a quartic mask are shown in Fig. (3.3). It can be observed that both the quartic mask MTFs remain practically constant for $0\lambda \leq W_{31} \leq 3\lambda$ waves and offer improved tolerance to coma aberration at a cost of reduced resolution. The consequence of using the quartic filter is to raise the relative spatial frequency response of the imaging system at medium frequencies and to prevent

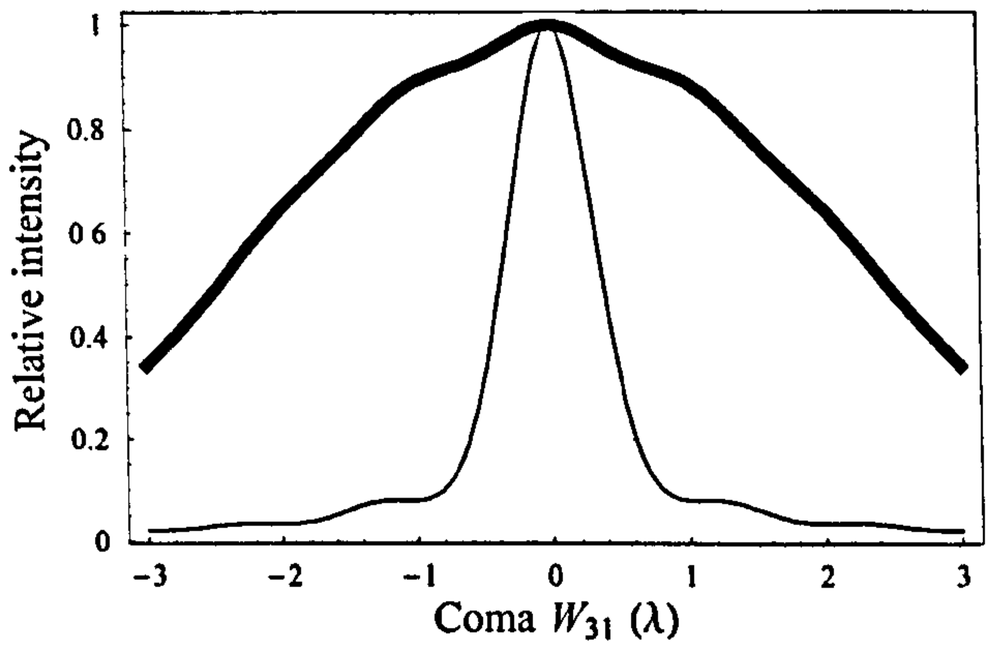

Figure 3.2: *Variation of the central intensity as a function of coma* W_{31} *with a quartic filter with* $\alpha = 15\lambda$ *and* $\alpha_0 = 9.75\lambda$ *(thick curve) and without a quartic filter (thin curve). The normalization coefficient for the quartic filter intensity is 0.045.*

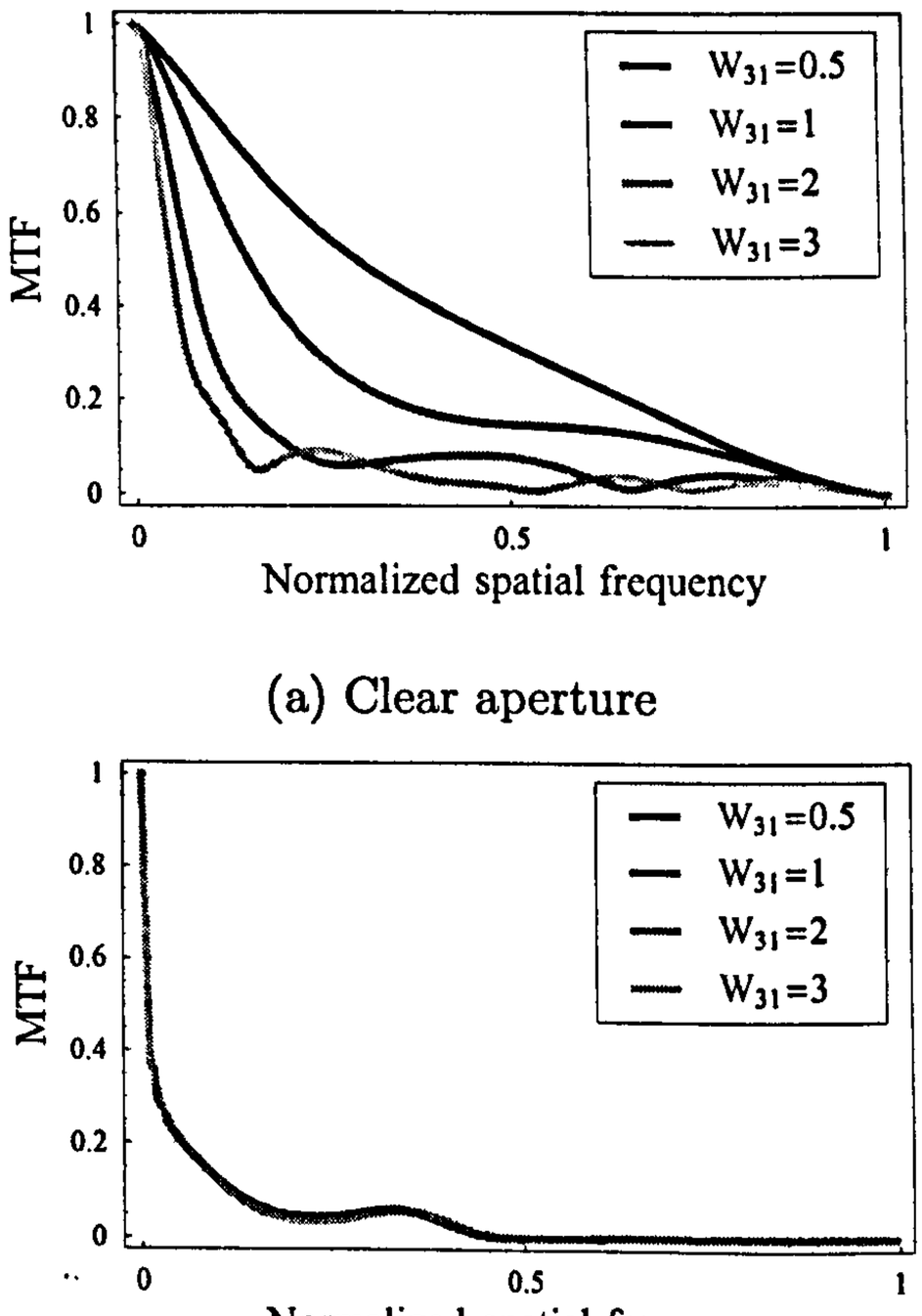

(a) Clear aperture

(b) Quartic filter

Figure 3.3: *Computed MTFs for an imaging system suffering from coma* W_{31} *(top) and with a quartic filter with* $\alpha = 15\lambda$ *and* $\alpha_0 = 9.75\lambda$ *(bottom). Coma aberration* W_{31} *in units of wavelength.*

the MTF from undergoing any zero value within the designed bandpass. Thus, no loss of information occurs within the bandpass and a single inverse deconvolution kernel can be applied to restore the image for aimed values of coma. It is also worth noting that the reduction in the effective cutoff frequency will reduce the effects of aliasing in many pixelated imaging systems. To complement the analysis, PSFs were calculated for an optical system with and without the quartic filter, see Fig. (3.4). Finally, we complete the study with a qualitative assessment of the performance of the quartic mask by simulating the images detected at various values of coma aberration. We employ the USAF target to evaluate the effect of this aberration. In the left column of Fig. (3.5), the simulated images from a optical system suffering from coma are shown, the coma coefficient $W_{31} = 0.5, 1, 2, 3$ in units of wavelength λ. It is manifest that coma produces both a considerable loss of contrast at all frequencies and blurring to the image. As coma increases, the blurring begins to acquire the characteristic comet-like shape of the PSF, where light distribution is not radially symmetric. When the quartic mask is inserted in the imaging system, the detected images appear to be significantly less affected by coma: all images display the same blurring properties whilst retaining certain degree of sharpness. For instance, when $W_{31} = 3$, the detected image contains more information and sharpness than the image of a clear aperture. However, the gain in tolerance is joined with a substantial loss of contrast and high spatial frequencies. Note that the Strehl ratio is less than 0.05. Digital image processing can be used to recover a diffraction limited image with reduced resolution. It becomes clear from the observation that quartic filter provides an enhancement in alleviating coma.

1.3 Astigmatism

In a simple optical system astigmatism increases with the square of the field angle. It is a common aberration found in human eyes, due to anamorphism of the cornea, and is normally accompanied by defocus. Special ophthalmic lenses or refractive surgery are used to compensate for its effects. We propose an alternative method, based on a phase filter, which produces point spread functions which are practically unaffected by astigmatism.

The variation of the intensity at the focal point of an imaging system suffering

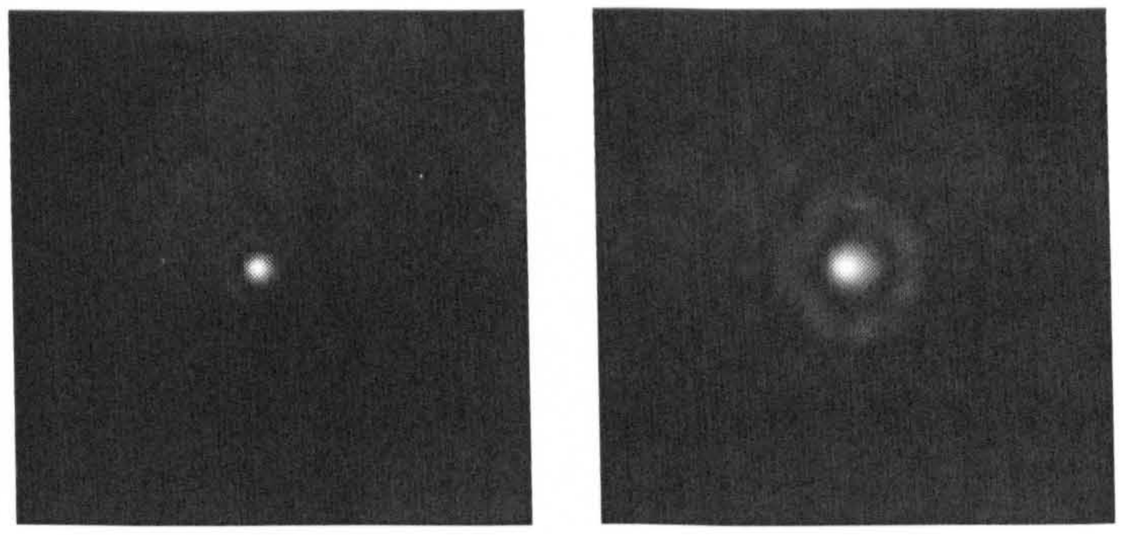

(a) $W_{31} = 0.5\lambda$

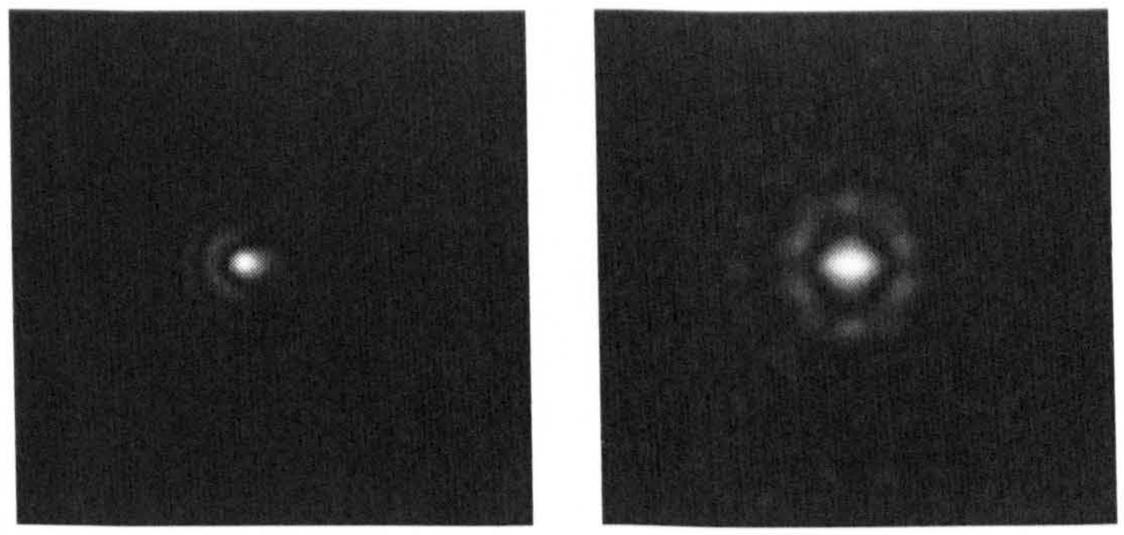

(b) $W_{31} = 1\lambda$

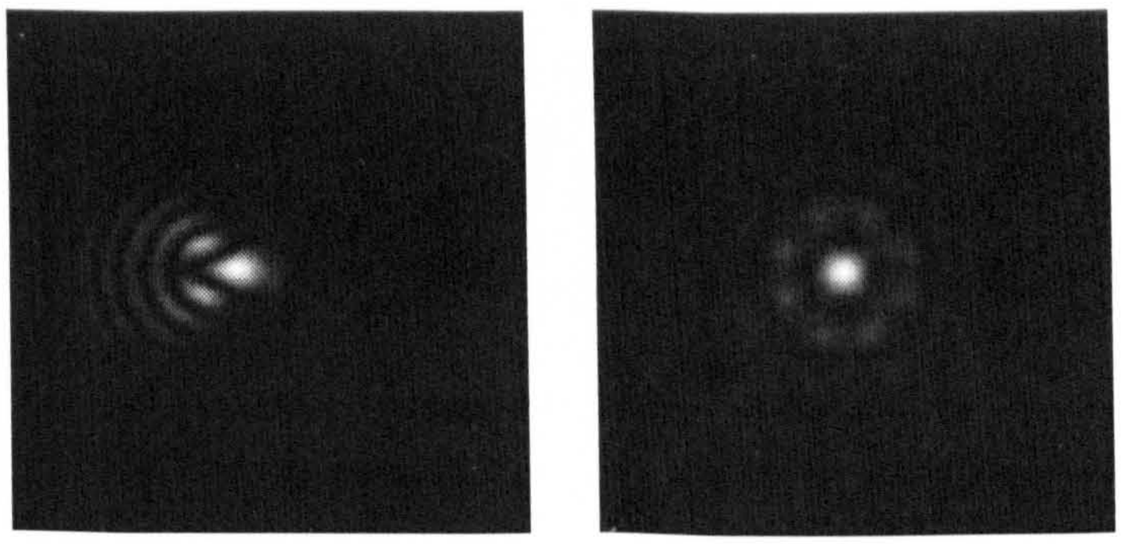

(c) $W_{31} = 2\lambda$

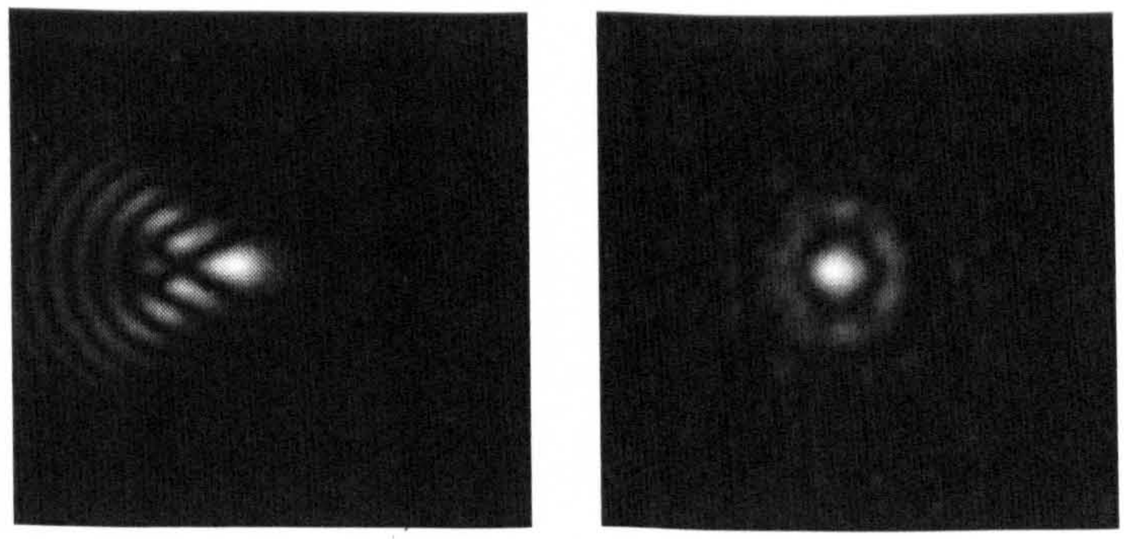

(d) $W_{31} = 3\lambda$

Figure 3.4: *Computed PSFs for a clear aperture suffering from coma* W_{31} *(left) and with a quartic filter* ($\alpha = 15\lambda$ *and* $\alpha_0 = 9.75\lambda$)*(right).*

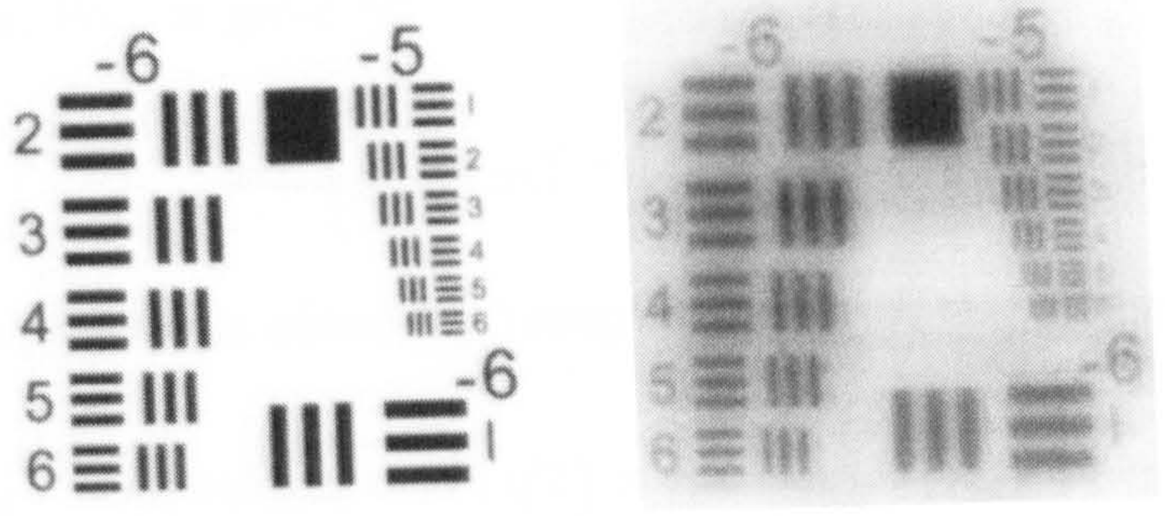

(a) $W_{31} = 0.5\lambda$

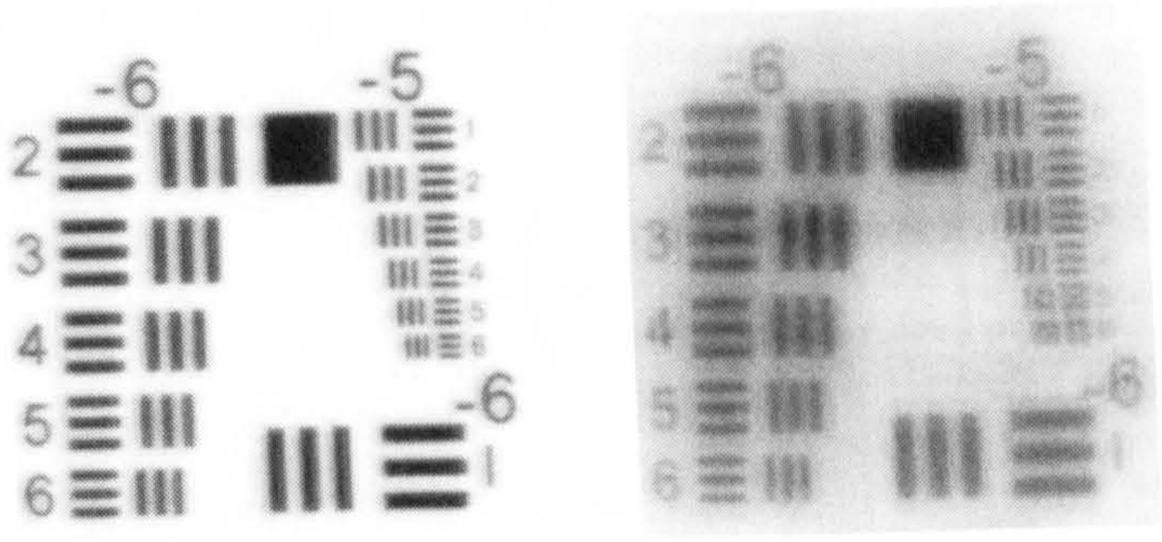

(b) $W_{31} = 1\lambda$

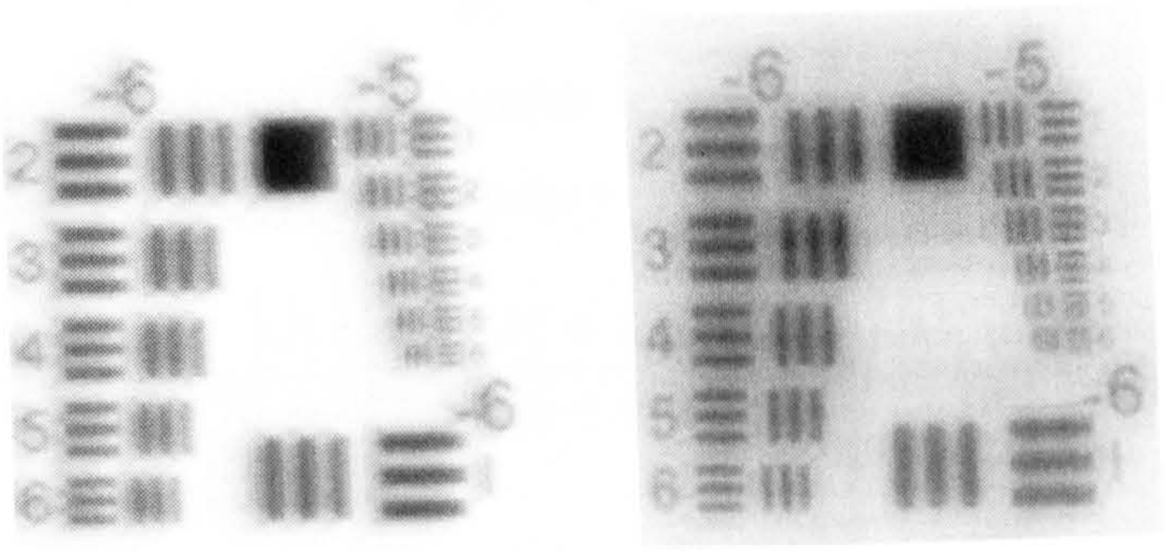

(c) $W_{31} = 2\lambda$

(d) $W_{31} = 3\lambda$

Figure 3.5: *Simulated images of the USAF target of an optical system suffering from coma (left) and with a quartic phase mask inserted in the aperture stop* ($\alpha = 15\lambda$ *and* $\alpha_0 = 9.75\lambda$) *(right).*

only astigmatism, W_{22}, is given by

$$I(W_{22}) = \left| \int_0^{2\pi} \int_{-1/2}^{1/2} \exp\left\{ ik \left[W_{22}(\xi + 1/2)\cos^2\theta + \tilde{\Phi}(\xi) \right] \right\} d\xi d\theta \right|^2 . \qquad (3\text{-}18)$$

An analytical expression is obtain by integrating over θ, the intensity becomes

$$I(W_{22}) = \left| \int_{-1/2}^{1/2} J_0\Big(kW_{22}(\xi + 1/2)/2 \Big) \times \exp\left\{ ik \left[W_{22}\xi/2 + \tilde{\Phi}(\xi) \right] \right\} d\xi d\theta \right|^2 , \qquad (3\text{-}19)$$

which can be approximated by means of the stationary phase method used in the previous section for coma, as

$$I(W_{22}) \approx B \frac{\left[J_0\left(\frac{1}{2} kW_{22} \left(\xi_s + \frac{1}{2} \right) \right) \right]^2}{|\tilde{\Phi}''(\xi_s)|}, \qquad (3\text{-}20)$$

where B is a real-valued constant and ξ_s is the stationary point defined by

$$\tilde{\Phi}'(\xi)\Big|_{\xi_s} + \frac{1}{2} W_{22} = 0. \qquad (3\text{-}21)$$

The approximation to the axial intensity in Eq. (3-20) is only valid if the phase function $\tilde{\Phi}$ satisfies the following boundary condition

$$\frac{1}{2} kW_{22} \left| \frac{J_1\left(\frac{1}{2} kW_{22}(\xi + 1/2) \right)}{J_0\left(\frac{1}{2} kW_{22}(\xi + 1/2) \right)} \right| < \sqrt{\frac{k\tilde{\Phi}''(\xi_s)}{4\pi}}, \qquad (3\text{-}22)$$

for

$$\left| \xi_s \pm \frac{1}{2} \right| > \sqrt{\frac{4\pi}{k\tilde{\Phi}''(\xi_s)}}, \qquad (3\text{-}23)$$

According to Eq. (3-20), the expression for the intensity contains astigmatism parameter W_{22} only in the argument of the Bessel function which has a coefficient of $(\xi_s + 1/2)$. Note that Eq. (3-21) is distinct from Eq. (3-10) only by the additional term $W_{22}/2$. Therefore, as in the previous analysis for coma, the same phase retardation $\tilde{\Phi}(\xi)$ that describes the quartic phase filter could also be used to attenuate the effect of astigmatism at the focal point when the stationary point satisfies the boundary condition given by Eq. (3-21). The expression of the intensity in the approximation Eq. (3-20) is rewritten as

$$I(W_{22}) \approx \frac{B}{2\alpha} \left[J_0\left(\frac{1}{2} kW_{22} \left(-\frac{W_{22}}{4\alpha} - \frac{\alpha_0}{2\alpha} + \frac{1}{2} \right) \right) \right]^2 . \qquad (3\text{-}24)$$

For sufficiently large values of α and modest astigmatism, the term $W_{22}/4\alpha$ can be neglected and the expression of the intensity as a function of W_{22} becomes analogous

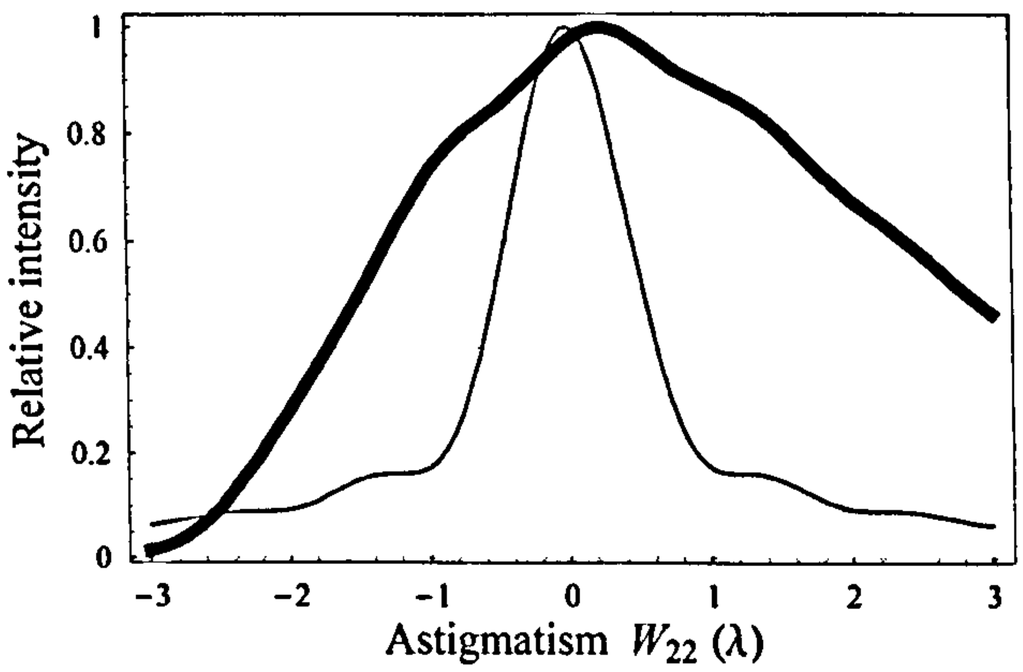

Figure 3.6: *Variation of the central intensity as a function of astigmatism W_{22} with a quartic filter with $\alpha = 15\lambda$ and $\alpha_0 = 9.75\lambda$ (thick curve) and without a quartic filter (thin curve). The normalization coefficient for the quartic filter intensity is 0.046.*

to that for coma W_{31} (see approximation given in Eq. (3-17). It should be noted however, that high values of α that compensate for large amounts of astigmatism also result in a suppressed MTF and lower contrast in the image so that careful assessment in the selection of the parameters of the quartic mask is necessary to trade contrast against aberration invariance.

The relative central intensity produced by the quartic mask with the same parameters as previously, $\alpha = 15\lambda$ and $\alpha_0 = 9.75\lambda$, is shown in Fig. (3.6) for various amounts of astigmatism. The dependence of the position of the stationary point on astigmatism is clearly manifested by the asymmetry of the relative intensity at either side of $W_{22} = 0$. For decreasing negative W_{22} the stationary point is moved towards the boundary at $\xi = -1/2$, requiring a higher value than $\alpha = 15\lambda$ in order to compensate for both the boundary effects and large negative W_{22}. On the other hand, positive W_{22} tend to move the stationary point away from the boundary, diminish its effects on the intensity variation only affected now by astigmatism. The performance of the quartic filter in the presence of astigmatism is analyzed in the spatial frequency domain by calculation of the MTFs for $0\lambda \leq W_{22} \leq 3\lambda$, see Fig. (3.7). In a similar fashion to the effect of coma on the MTF, the MTFs remain fairly invariant and the cutoff frequency has been reduced by a factor of 2, giving rise to broader point spread functions, as shown in Fig. (3.8).

A qualitative assessment of the performance of the quartic mask in the presence of astigmatism is carried out by computing images of the USAF target formed at the

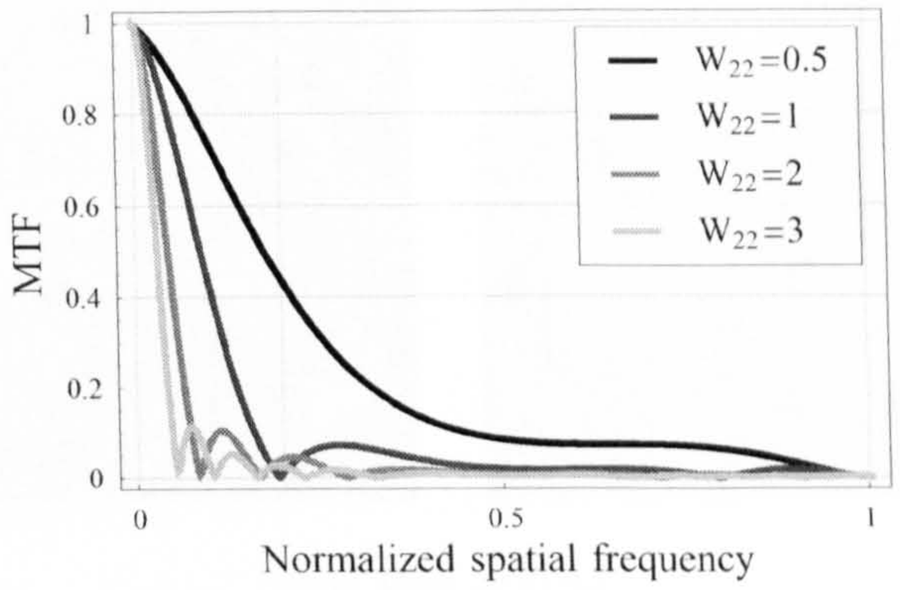

(a) Clear aperture

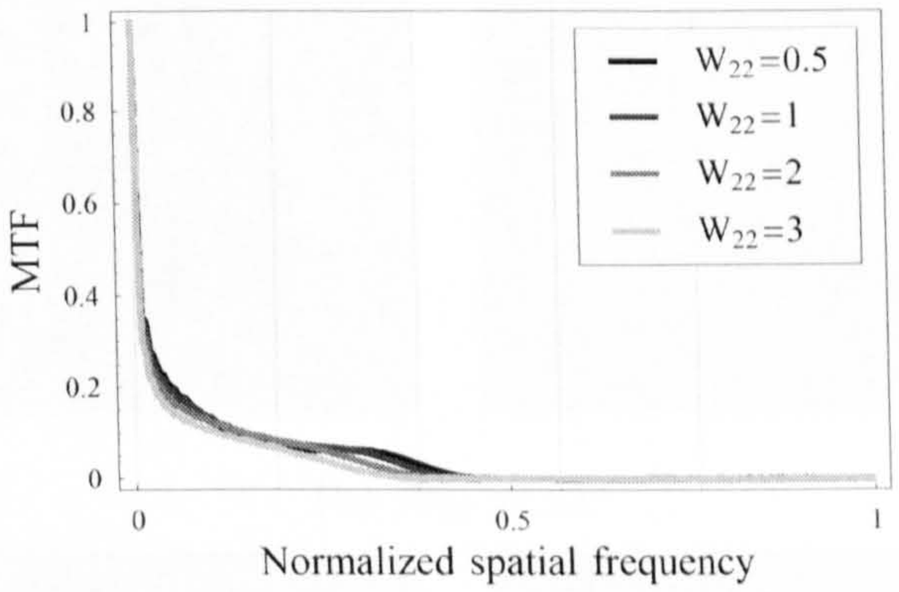

(b) Quartic filter

Figure 3.7: *Computed MTFs for an imaging system suffering from astigmatism* W_{22} *(top) and with a quartic filter with* $\alpha = 15\lambda$ *and* $\alpha_0 = 9.75\lambda$ *(bottom). Coma aberration* W_{22} *in units of wavelength.*

detector. In the left column of Fig. (3.9), the images from a optical system suffering from astigmatism are shown with the astigmatism coefficients $W_{22} = 0.5, 1, 2, 3$ in units of wavelength λ. It is clearly displayed that astigmatism produces a strong directional blurring accompanied with loss of contrast. As astigmatism increases, the blurring becomes more acute in the horizontal direction and it can be appreciated that phase reversal take place, see image at $W_{22} = 2\lambda$. When the quartic mask is introduced in the aperture stop, the detected images are substantially less affected by the astigmatic blur. It can be observed that the images for various values of W_{22} exhibit similar sharpness and quality. In the same fashion as for a coma-aberrated optical system, with astigmatism the gain in tolerance is joined with an important loss of contrast. However, note that the phase reversals have disappeared and the image features are distinctively defined. The contrast can raise by employing inverse digital filtering. It is therefore clear from the examination of the images that quartic

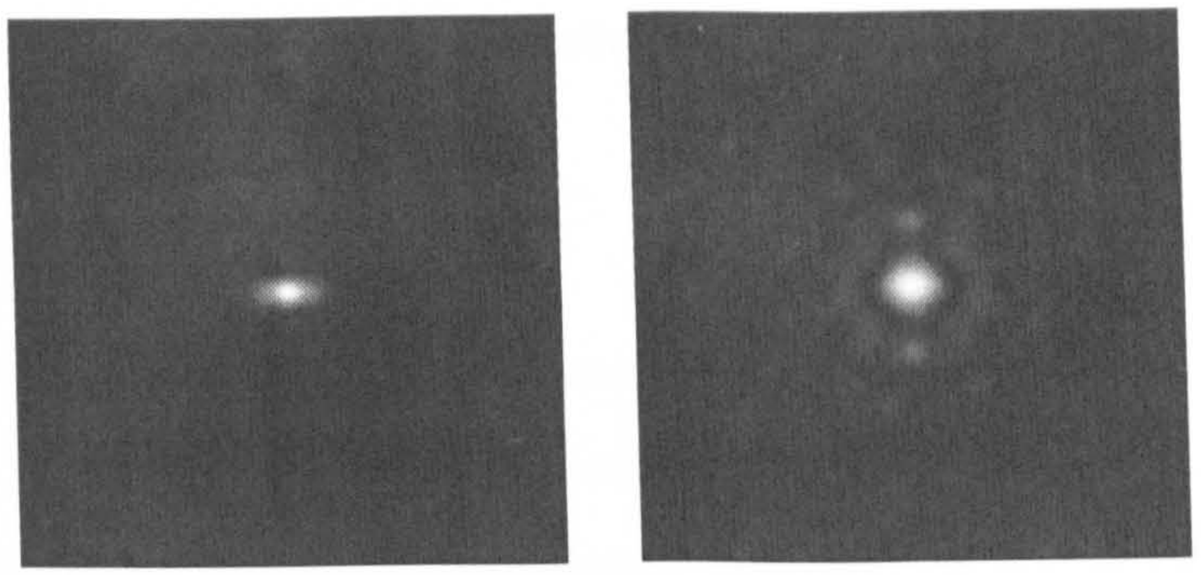

(a) $W_{22} = 0.5\lambda$

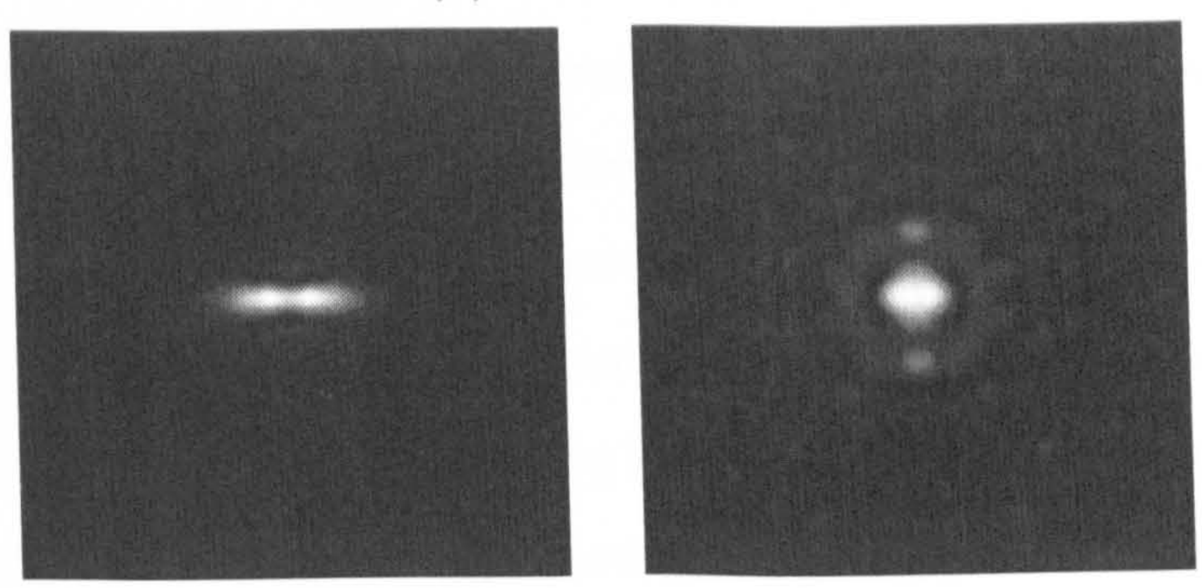

(b) $W_{22} = 1\lambda$

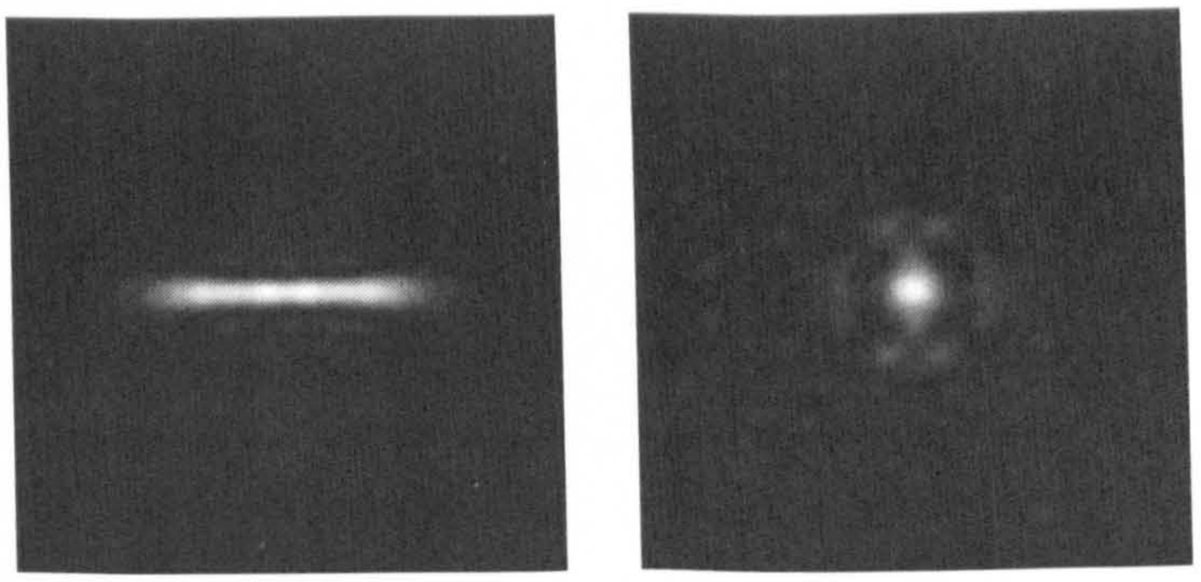

(c) $W_{22} = 2\lambda$

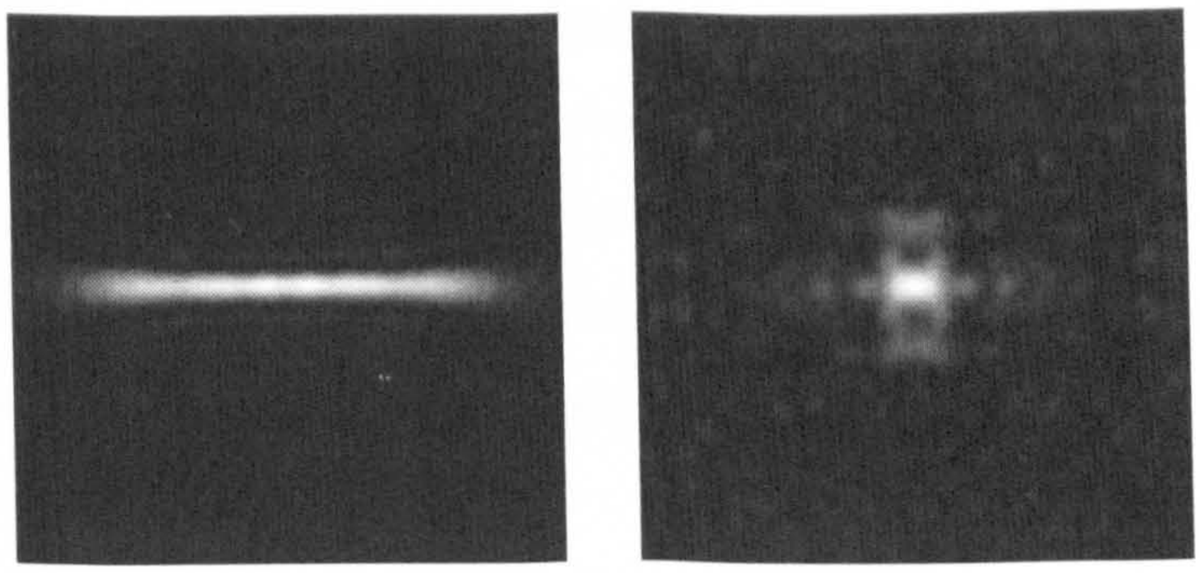

(d) $W_{22} = 3\lambda$

Figure 3.8: *Computed PSFs for a clear aperture suffering from astigmatism* W_{22} *(left) and with a quartic filter* ($\alpha = 15\lambda$ *and* $\alpha_0 = 9.75\lambda$)*(right).*

filter provides an enhancement in alleviating astigmatism.

1.4 Discussion

The stationary phase method has been used to obtain a phase filter which, in principle, provides reduced sensitivity to coma and to astigmatism; in both cases the numerically calculated MTF remains almost constant as the parameter for either astigmatism or coma is varied. Note that the quality of the final images presented could be improved by digital signal processing techniques. However, the purpose of our research is to present what is achievable only by means of optical manipulations. This work presented here complements work previously published (Ref. [5, 10]) where QFs have been shown to enhance the tolerance to defocus and spherical aberration. It is notable that the effective cut-off frequency is also reduced indicating that for applications employing pixelated detectors these filters may be usefully employed as anti-aliasing filters.

2 Antisymmetric phase mask for circular aperture

2.1 Introduction

A recent paper by Sherif *et al.* [32] reported the derivation of an aspherical phase plate, which when placed at the exit pupil of a conventional imaging system and combined with digital processing of the recorded images, exhibits an increased depth of field. We identified an error in the derivation of this phase plate, which makes the reported extension of depth-of-field invalid. In this section, we obtain an optimum phase plate and develop the relevant results.

2.2 Phase mask derivation

In the previous chapter we have shown how the use of the one-dimensional ambiguity function can help to design rectangularly separable pupil functions in order to provide an optical system with the desire performance over a range of defocus. The definition of the ambiguity function cannot easily be extended for analyzing circular pupils, as it is the case of the majority of optical systems, since the AF

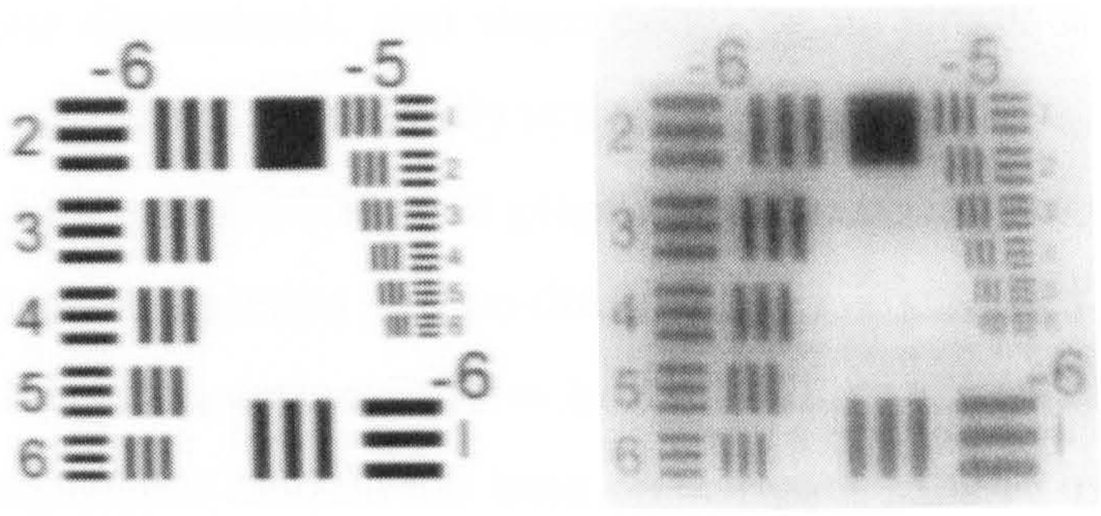

(a) $W_{22} = 0.5\lambda$

(b) $W_{22} = 1\lambda$

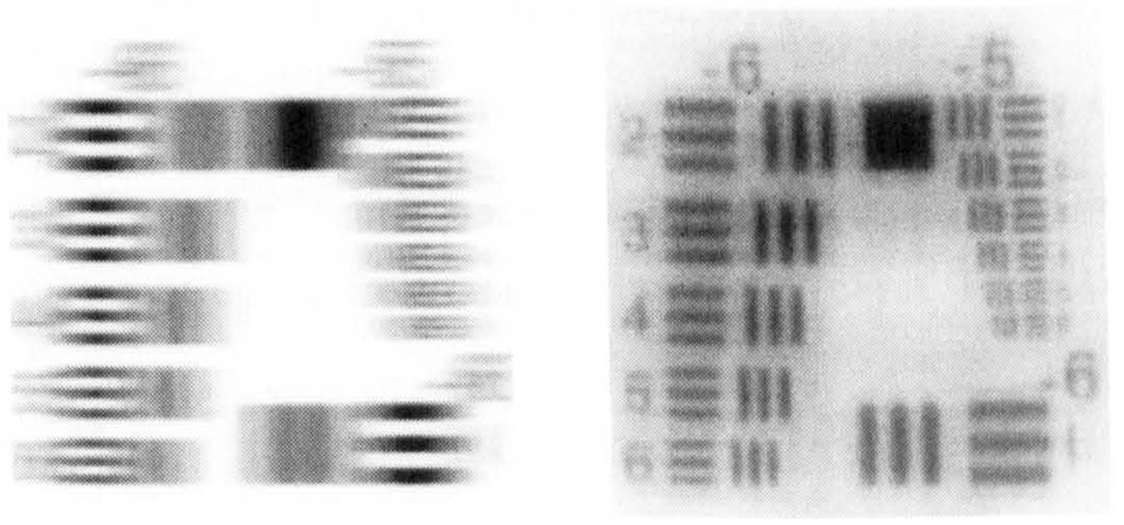

(c) $W_{22} = 2\lambda$

(d) $W_{22} = 3\lambda$

Figure 3.9: *Simulated images of the USAF target of an optical system suffering from astigmatism (left) and with a quartic phase mask ($\alpha = 15\lambda$ and $\alpha_0 = 9.75\lambda$) inserted in the aperture stop (right).*

would become four dimensional, and there would be no simple way to display it. Nevertheless, in the case of rotationally symmetric pupil functions, a modified ambiguity function has been derived that graphically illustrates the effects of defocus on the optical transfer function in two-dimensional systems [48]. Antisymmetric phase mask for circular apertures cannot be deduced with ambiguity function and one valid but complicated method has been be proposed instead by Sherif [74]. The method employs directly the equation of an aberrated point spread function and allows obtaining phase mask functions with non-specific circular apertures.

The axial intensity of the point spread function of a defocused diffraction-limited system with a circular aperture is given by [55]

$$I = C\left|\int_0^{2\pi}\int_0^1 P(r)\exp\left[\mathrm{i}kW_{20}r^2\right] r\mathrm{d}r\mathrm{d}\theta\right|^2, \tag{3-25}$$

where the exit pupil plane is represented in polar coordinates (r,θ), k is the wave number $2\pi/\lambda$, λ is the wavelength,C is a normalization constant, W_{20} is the defocus coefficient and $P(r)$ denotes the pupil function with $P(r) = 1$ for $0 \leq r \leq 1$, and $P(r) = 0$ elsewhere. The radial coordinate r is normalised to the radius of the pupil. An antisymmetric phase mask described by a phase function $\Phi(r,\theta)$, that is intended to alleviate defocus is inserted in the pupil plane, Eq. (3-25) becomes

$$I = C\left|\int_0^{2\pi}\int_0^1 P(r)\exp\left\{\mathrm{i}k\left[W_{20}r^2 + \Phi(r,\theta)\right]\right\} r\mathrm{d}r\mathrm{d}\theta\right|^2. \tag{3-26}$$

The desirable phase mask codes the wavefront in such a way that the PSF is invariant with defocus. The antisymmetric property of the mask ensures that it has no focusing power and therefore the PSF axial symmetry condition is met: $I(-W_{20}) = I(W_{20})$.

Sherif demonstrates that the term $\Phi(r,\theta)$ in the previous equation must satisfy the following expression, which can be considered as the condition for extended depth of field in optical systems with circular apertures and antisymmetric phase masks,

$$\begin{aligned} &3r\Phi_{rr}\Phi_{\theta\theta} - 3r\Phi_{\theta\theta}\Phi_{r\theta}^2 - 3\Phi_r\Phi_{\theta\theta}^2 + \\ &\quad r\Phi_r\Phi_{\theta\theta r}\Phi_{\theta\theta} - r\Phi_r\Phi_{\theta\theta\theta}\Phi_{\theta r} - r^2\Phi_{rr}\Phi_{\theta\theta r}\Phi_{\theta\theta} \\ &\quad r^2\Phi_{rr}\Phi_{\theta\theta\theta}\Phi_{\theta r} - r^2\Phi_{rrr}\Phi_{\theta\theta}^2 + 3r^2\Phi_{\theta r}\Phi_{\theta rr}\Phi_{\theta\theta} - 2r^2\Phi_{r\theta\theta}\Phi_{r\theta}^2\Big|_{r=r_s,\theta=\theta_s} = 0, \end{aligned} \tag{3-27}$$

where Φ_i,Φ_{ij},Φ_{ijk} correspond to the first, second and third derivatives with respect to r and/or θ variables and evaluated at the stationary points r_s and θ_s. This

equation was derived after applying the axial symmetry condition and stationary phase method to the defocused point spread function (PSF) of an optical system with a circular aperture. For further detail on the method of stationary phase refer to Appendix A. Our calculation replicates this expression.

It was assumed that the condition for extended depth-of-field has a separable solution $\Phi(r,\theta)$ that could be written as

$$\Phi(r,\theta) = R(r)\Theta(\theta) = -\alpha r^m \theta^n, \tag{3-28}$$

where α is a constant. It was stated that when this term $\Phi(r,\theta)$ is substituted into equation Eq. (3-27), the resultant index equation which m and n must satisfy is

$$m^2n^2 - 2m^2n - 3mn^2 + 6mn - 4m - 8n - 8 = 0, \tag{3-29}$$

whereas, we find instead that the following expression must be satisfied:

$$2n^2 + mn - 4n - m + 2 = 0. \tag{3-30}$$

This has a profound effect on the values of m that are a solution in Eq. (3-28). Since the extended depth-of-field PSF has to meet the axial symmetry condition which implies that the phase mask function has to be antisymmetric, i.e. $\Phi(r,\theta) = -\Phi(r,\theta+\pi)$, thus n must be an odd positive integer; the smallest odd positive integer value for n that yields a non-trivial $\Phi(r,\theta)$, is n=3. Inserting this in our new expression in Eq. (3-30), we obtain m =-4. A negative value for m is problematic, as it would always result in a phase singularity at $r = 0$. This phase singularity would make any solution obtained by this approach physically unrealistic. Thus another approach to solve equation Eq. (3-27) is necessary.

2.3 Optimum circular phase plate to extend the depth of field

To obtain $\Phi(r,\theta)$ that satisfies the condition for extended depth of field, we expand it as a weighted sum of Zernike polynomials:

$$\Phi(r,\theta) = \alpha \sum_{m=0}^{\infty}\sum_{n=0}^{\infty} a_{mn} U_{mn}(r,\theta) \tag{3-31}$$

where α is a constant which determines the thickness of the phase plate. To ensure that $\Phi(r,\theta)$ satisfies the axial symmetry condition, we restrict the above summations

a_{10}	a_{11}	a_{30}	a_{31}	a_{32}	a_{33}
-0.67	-0.15	0.07	0.13	-0.42	0.10
a_{50}	a_{51}	a_{52}	a_{53}	a_{54}	a_{55}
0.03	-0.04	-0.05	0.08	-0.05	0.04

Table 3.1: *Expansion Zernike coefficients for optimum mask.*

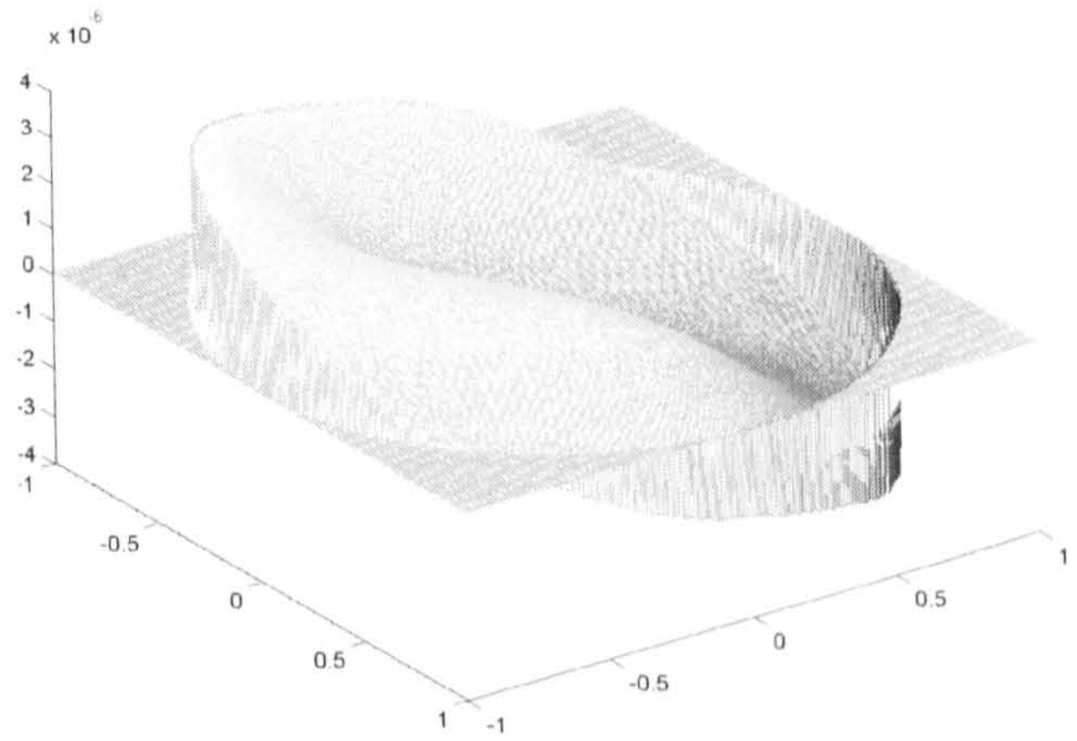

Figure 3.10: *Profile of the extended depth-of-field phase plate*

to odd orders of $n - 2m$. We also limit these summations to fifth degree Zernike polynomials U_{mn} as is usually done in aberration analysis. The definition of Zernike polynomials are given by Malacara in Ref.[75]. We substitute Eq. (3-31) into Eq. (3-27) and use the *Adaptive Simulated Annealing* optimization method [76, 77] to obtain the expansion Zernike coefficients a_{mn} that minimize the magnitude of the resultant equation. It is beyond the scope of this work to give a detailed description of the optimization. The expansion coefficients of the optimum extended-depth-of-field phase plate, shown in Fig. (3.10), are given in Table (3.1). The peak-to-valley optical path difference introduced by the phase mask is control by the parameter α, affects the tradeoff between depth-of-field extension and irreversible blurring due to possible nulls in the modulation transfer function of the imaging system.

2.4 Phase mask performance with defocus

A quantitative way to show the extension of depth of field in a given system is to plot the angles in Hilbert space between its in-focus and out-of-focus point spread functions for different parameter values. The angle in Hilbert space between any

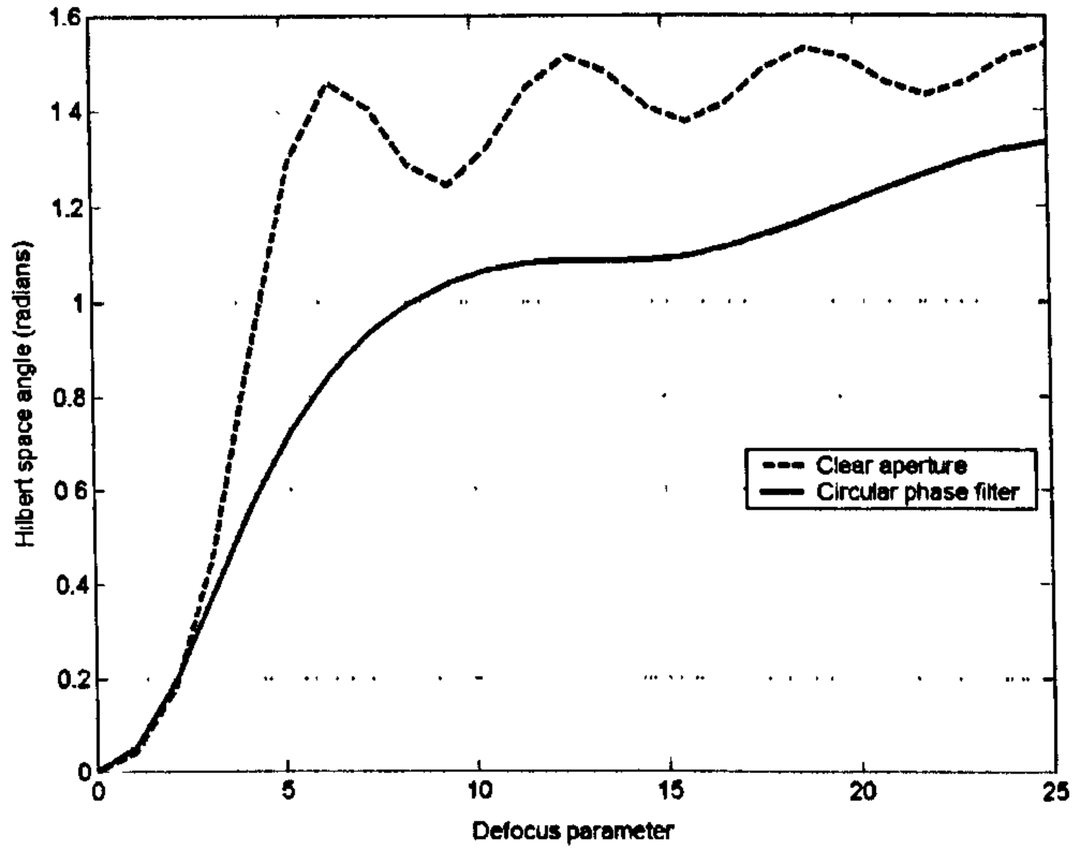

Figure 3.11: *Hilbert space angles using a clear aperture and using the extended depth-of-field phase plate*

two functions is a measure of the similarity between these two functions [32]. The smaller the angle between the two functions, the more similar are the two functions, and vice versa. Thus, it is a metric to quantify the defocused image blurring, the angle in Hilbert space between a defocused PSF and the in-focus PSF. In Fig. (3.11) we show these angles for the same imaging system used in Ref. [32]. From Fig. (3.11) we note that all the angles shown, which correspond to different defocus parameter values, become smaller when our phase plate is introduced at the pupil of an imaging with a clear circular aperture. Thus the PSF of an imaging system with the circular antisymmetric phase plate at its exit pupil varies less with defocus compared to the PSF of a similar standard system.

To demonstrate the extension of the depth of field, we compare two sets of computer-simulated images of a spoke target for different defocus parameter values. The first set (left column of Fig. (3.12)) is obtained using a standard incoherent imaging system similar to the one used in Ref. [74] and the second set (right column of Fig. (3.12)) is obtained using the same system, but with the new phase mask at its exit pupil. From Fig. (3.12) we note that the variation in the image quality with defocus is much less with the standard system indicating a much increased depth of field. The quantitative improvement in depth of field in a specific imaging system is determined by the value of α used in equation Eq. (3-31). The value of α used in our present calculations is $\alpha = 3.8 \times 10^{-6} m$. By comparing Fig. and Fig. (3.12)

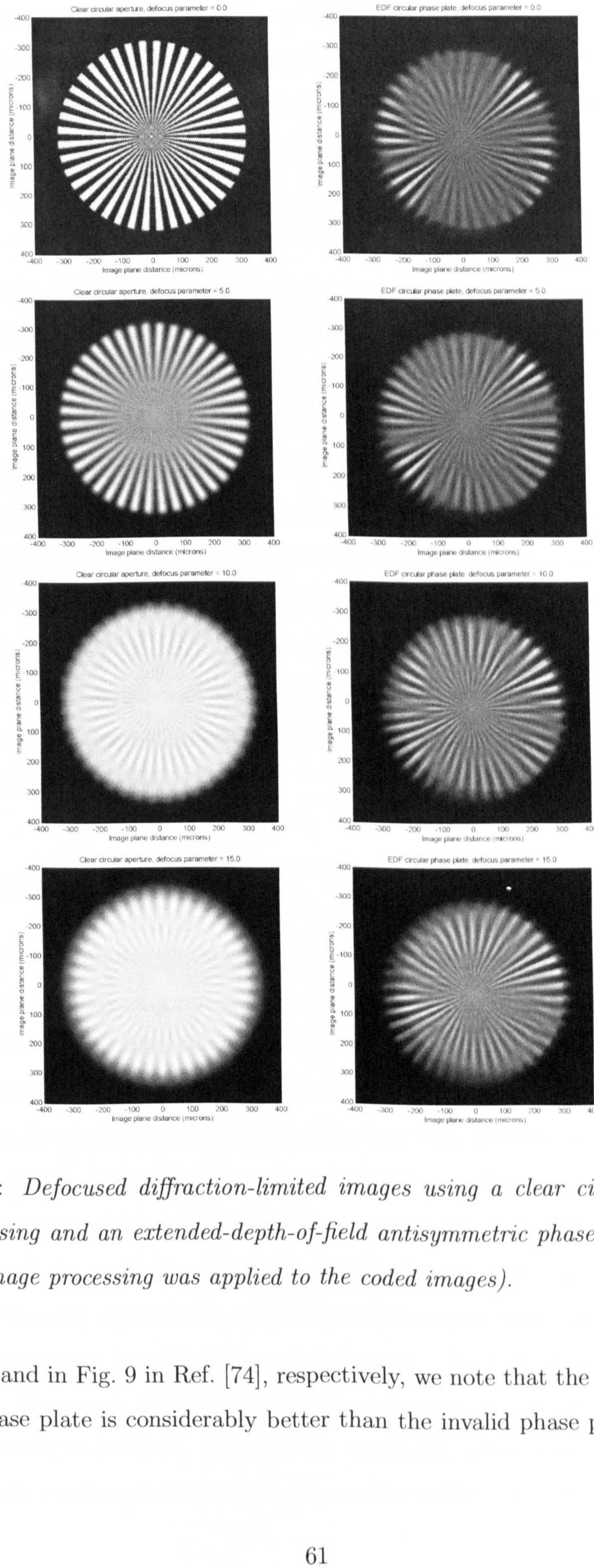

Figure 3.12: *Defocused diffraction-limited images using a clear circular aperture (left) and using and an extended-depth-of-field antisymmetric phase mask (no post detection image processing was applied to the coded images).*

with Fig. 5 and in Fig. 9 in Ref. [74], respectively, we note that the performance of our new phase plate is considerably better than the invalid phase plate derived in Ref. [74].

Based on an optical system with a circular aperture, Kubala *et al.* [78] have suggested a particular circular aspheric phase mask called the *cosine form mask* that increases the tolerance to aberrations, especially defocus-related such as field curvature, astigmatism and defocus. Mathematically, the cosine form is describe by

$$\Phi(r,\theta) = \sum_{i=1}^{N} \alpha_i r_i^{\beta} \cos(w_i\theta + \varphi_i), \tag{3-32}$$

where the weight on each term is given by α_i and the radian frequencies and phase offsets of each term are given by w_i and φ_i respectively. The odd-cosine phase mask has never been analytically derived in the existing literature: certainly, there exits no analytical method in the frequency or space domain that allows obtaining such equation. The key aspect of the performance of this phase mask is its antisymmetry given by the cosine term, which ensures an increased defocus alleviation as we show in the following chapter. A particular advantage of the cosine-shaped mask over the cubic-shaped mask is the manufacturing process in comparison to the traditional cubic phase mask. The surface of the cosine-shaped mask at any given radius is composed of a fixed number of sinusoidal terms. The number and parameters of the sinusoidal terms can be matched to the fabrication method being used to ensure high quality manufacturing.

3 Conclusions

We have derived a quartic phase mask by applying the method of stationary phase to the central intensity of a generic circularly symmetric phase function. The performance of the quartic filter showed a reduction in sensitivity to coma and astigmatism without the requirement of post-detection processing, even for extreme values of aberration. In previous work, defocus mitigation with the quartic phase mask was also reported. The extended performance is coupled with a practical reduction in the cutoff frequency of the optical system and suppression of the MTF, which results in a decrease in the resolution and contrast of the image. However, this may not be problematic in some applications, such as barcode readers or machine vision, where contrast is important but not an essential element. The lack of zeros in the MTF means that, in general, the quality of detected images can be improved by digital signal processing techniques. The radially symmetric phase filters do not reduce the sensitivity to aberrations as efficiently as the cubic phase filter, but offer the

advantage of low-cost manufacture. A particular interesting observation is the fact that the quartic filter derived here is nearly identical to the symmetric logarithmic filter obtained by Chi [40] when the latter is designed to provide defocus tolerance from a point near the optical system to infinity. Both filters have been derived using different methods: the quartic filter by considering the wave nature of light and diffractive integrals and the logarithmic filter by ray-tracing and Fermat's principle.

In the second part of the chapter, we have reported a new derivation of a extended-depth-of-field antisymmetric phase mask by means of a spatial-domain method. By inserting the circular phase mask at the aperture stop of a diffraction-limited incoherent optical system, it is possible to extend the depth of field. A quantitative evaluation in terms of the Hilbert angle of the variation of the PSF with defocus was presented together with a qualitative demonstration with computer-simulated images for different defocus parameter values. In our opinion, the mathematical complexity, numerical optimization and numerous approximations involved in obtaining the circular antisymmetric phase mask, indicate that this spatial-domain method is a cumbersome tool to use. Similar results, for instance, can be obtained with rectangularly-separable antisymmetric phase masks placed in circular apertures and derived by simpler methods (ambiguity function, geometrical optics, etc.) as we show in the next Chapter.

Chapter 4

Decomposition of the optical transfer function: wavefront coded imaging system

Summary. We describe the mapping of the optical transfer function (OTF) of an incoherent imaging system into a geometrical representation. We show that for defocused traditional and wavefront-coded systems the OTF can be represented as a generalised Cornu spiral when a cubic phase mask is employed. This novel representation provides a physical insight into the way in which wavefront coding can increase the depth of field of an imaging system and permits analytical quantification of salient OTF parameters, such as the depth of focus, the location of nulls, and amplitude and phase modulation of the wavefront-coding OTF.

1 Introduction

The optical transfer function* (OTF) is a critical parameter of aberrated optical systems. Except in restricted cases, such as when the well-known Fourier transform relationships are valid [80], the numerical methods of wave-optics analysis can obscure the underlying physical processes of OTF formation. We show here how a geometrical analysis of a phasor representation of a decomposed OTF enables an improved description and quantification of OTF parameters to be made. Although this approach is pertinent to all aspects of incoherent image formation, its application to wavefront coding is of particular interest. We have shown that, when it is combined with digital postprocessing, a mask placed in the pupil plane of a

*An interesting historical background for the OTF can be found in [79].

conventional imager produces greatly reduced sensitivity to defocus-related optical aberrations [5, 81, 38]. The resultant OTFs are approximately invariant over a restricted range of defocus, but there has been no reported analytical treatment of the range of defocus invariance, of the magnitude of departures from invariance, or of a physical, wave-optics explanation of the underlying physical processes. In this chapter we demonstrate that the OTF of a defocused wavefront coding system can be considered in terms of a *generalised Cornu spiral* (GCS) and that the performance parameters of a wavefront coding system can be readily derived from the geometry of such a spiral. We start by describing how the OTF can be decomposed to enable its composition to be plotted as a curve in the complex plane. We then apply this technique to an imaging system, incorporating first defocus and then both defocus and a cubic phase function.

2 The OTF of a wavefront coding optical system

2.1 Young's slits and the OTF

For clarity and without loss of generality, the analysis is restricted to the case of a one-dimensional optical system. The optical transfer function of an incoherent imaging system is given by the normalised autocorrelation of the pupil function $P(x)$ [55]:

$$H(f) = \int_{-\infty}^{+\infty} P\left(x + \frac{\lambda z_i f}{2}\right) P^*\left(x - \frac{\lambda z_i f}{2}\right) \mathrm{d}x \Big/ \int_{-\infty}^{+\infty} |P(x)|^2 \mathrm{d}x, \qquad (4\text{-}1)$$

where x is the transverse linear coordinate,f is the spatial frequency, λ is the wavelength and z_i is the distance from the aperture stop to the image plane (radius of the Gaussian sphere). The OTF for an exit pupil of width R can be expressed

$$H(f) = \int_{-\infty}^{+\infty} P\left(x + R\frac{f}{f_{max}}\right) P^*\left(x - R\frac{f}{f_{max}}\right) \mathrm{d}x \Big/ \int_{-\infty}^{+\infty} |P(x)|^2 \mathrm{d}x, \qquad (4\text{-}2)$$

where f_{max} is the cut-off spatial frequency and Rf/f_{max} corresponds to a pupil-plane coordinate representing spatial frequencies f. Physically, Eq. (4-2) can be interpreted in terms of the integral of Young's fringes of spatial frequencies f due to the integral of all possible aperture pairs of separation $2Rf/f_{max}$ within the pupil [55]. The numerator represents the region of overlap of two displaced pupil functions, one centred at Rf/f_{max} and the other at $-Rf/f_{max}$. In the absence of

aberrations, the area of overlap for a particular spacing is proportional to the OTF for the corresponding frequency f. The denominator is a normalizing factor. When the separation is so large that the two pupils have no region in common, the value of the frequency transfer function is clearly zero; thus, spatial frequencies larger than a certain cut-off frequency are not transmitted by the system. In this particular case, for a one-dimensional aperture of width R, the pupils will not overlap when the spacing is larger than $2R$.

When a fringe pattern of a particular frequency f is generated in the image plane, an interference effect takes place. This pattern can only be produced by the interference of light emerging from two separate regions (or Young's pinholes) placed at the exit pupil of the system, with a separation $2Rf/f_{max}$ between pinholes. Yet, for this particular spacing, many pairs of pinholes can be included in the pupil of the system. Each of them producing the same interference pattern of frequency f. The number of ways a particular pair of Young's pinholes can be fit into the exit pupil is determined by the weighting factor applied by the system to that frequency component f. In terms of the OTF, this relative weight for the frequency f is proportional to the area of overlap of two pupils separated by the corresponding spacing. Therefore, as the separation between pairs of Young's pinholes increases, generating higher spatial frequencies, there will be fewer ways in which these pinholes can be embraced by the pupil and as result the OTF will decrease, reaching the value zero at the cut-off frequency. At this particular frequency the separation between the pair of pinholes will be larger than the pupil, and consequently that frequency will not be transmitted by the system, as the pinholes cannot be fit in the pupil.

2.2 Effect of defocus aberration on the OTF

As mentioned in the previous section, each infinitesimal element in the area of overlap represents the contribution to the OTF of a single pair of Young's pinholes. It will be seen that decomposing the integral of the OTF in Eq. (4-2) into the complex amplitudes of the component interferograms helps us to understand the composition of the $H(f)$. To this end we define the integral

$$L(r',\nu) = \int_0^{r'} h(r,\nu)\mathrm{d}r \Big/ \int_{-1}^{1} h(r,0)\mathrm{d}r, \tag{4-3}$$

with $h(r,\nu) = P(r+\nu)P^*(r-\nu)$ and $h(r,0) = |P(r)|^2$, where $r = x/R$ is the normalised pupil coordinate and $\nu = f/f_{max}$ is the normalised spatial frequency. Note that the normalised OTF given in Eq. (4-2) is given by

$$H(\nu) = L(1-\nu,\nu) - L(-1+\nu,\nu). \tag{4-4}$$

This enables the contributions to $L(\nu)$ to be depicted in a manner redolent to how the Cornu spiral describes diffraction of coherent light at an edge; the caveat is that the phasors $h(r,\nu)$ represent the intensity and spatial phase of interference fringes rather than complex amplitude of the optical field. We represent incremental contributions $h(r,\nu)dr$ by phasors and perform the integral in Eq. (4-3) as r' is varied between zero and the negative limit $-1+\nu$ and between zero and the positive limit $1-\nu$. This enables the contribution to $L(\nu)$ to be identified as a function of the pupil-plane displacement r'. We consider first a simple pupil for which $P(r) = 1$ for $|r| \leq 1$ and $P(r) = 0$ for $|r| > 1$; the pupil function is real and so l is real for all r and for all ν; $H(\nu)$ is then purely real for all ν and the OTF $H(\nu) = 1-\nu$ has the characteristic triangular form due to the linear variation of the autocorrelation function with ν.

As an illustration of the usefulness of this approach, and before considering its application to wavefront coding, we consider first the decomposition of the OTF of an optical system that suffers only from defocus, which we represent by a quadratic phase factor. The pupil function that describes the defocused wavefront is given by

$$P(r, w_{20}) = p(r)\exp(\mathrm{i}kw_{20}r^2), \tag{4-5}$$

with $p(r) = 1$ for $|r| \leq 1$ and $p(r) = 0$ elsewhere, w_{20} is the defocus coefficient in units of wavelengths and $k = 2\pi$. The expression for the interferogram phasor representing a pair of Young's slits is given by

$$h(r,\nu;w_{20}) = \exp(\mathrm{i}8\pi w_{20}\nu r), \tag{4-6}$$

so that the phasor contributions to $H(\nu)$ have a phase that varies linearly with offset r; that is, $L(r',\nu)$ describes the arc of a circle traced from the origin in the complex plane. The sense of this arc is clockwise for increasingly positive r' and anticlockwise for increasingly negative r'. The defocused OTF, $H(\nu;w_{20}) = L(1-\nu,\nu;w_{20}) - L(-1+\nu,\nu;w_{20})$, is the vector displacement between the ends of these two arcs. The Hermitian nature of $h(r,\nu;w_{20})$ means that the integral represented by $L(r',\nu;w_{20})$ is always real. The variation of $H(\nu;w_{20})$, $L(1-\nu,\nu;w_{20})$

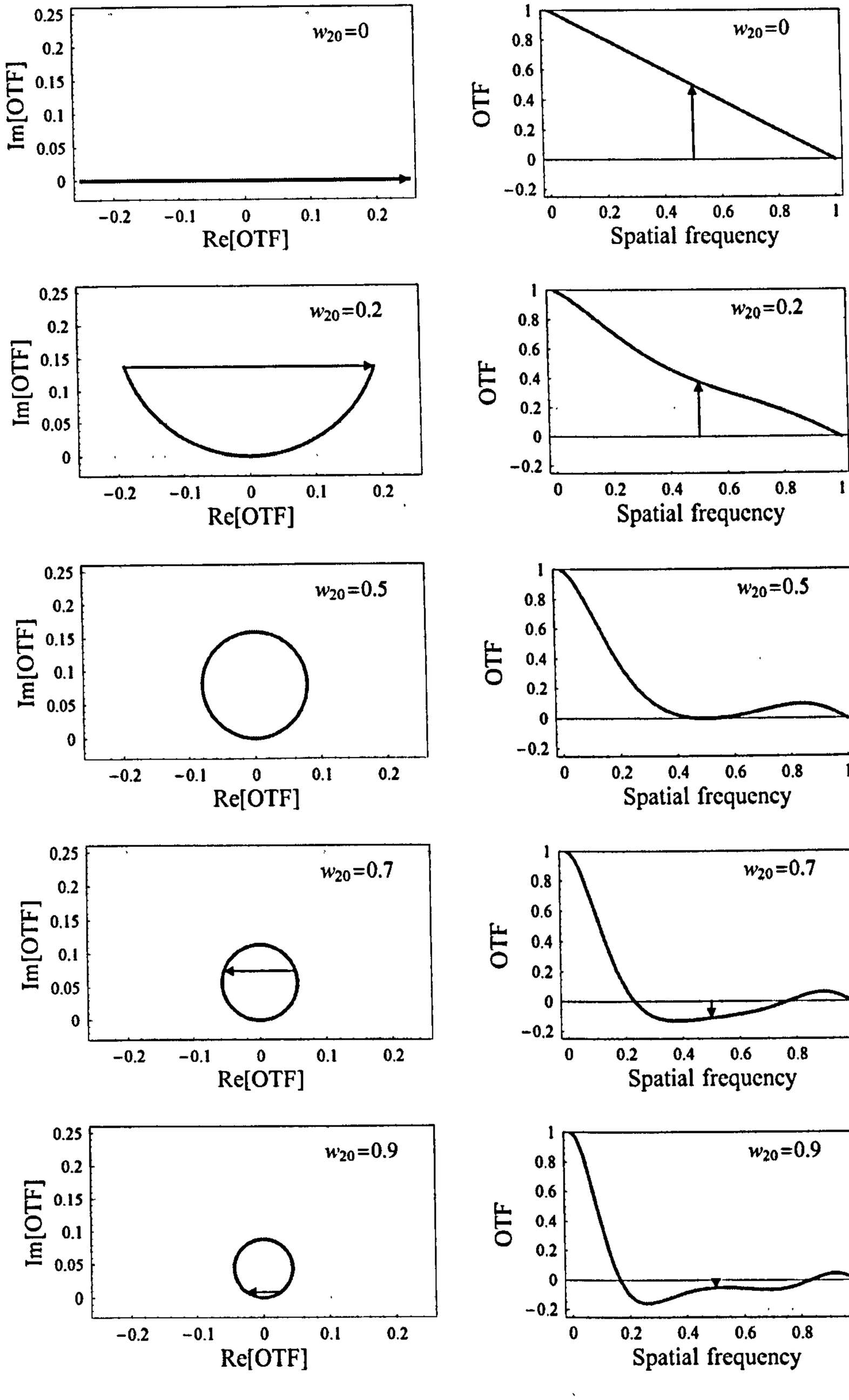

Figure 4.1: *Traditional defocused OTFs depicted as arc circles (left) for* $\nu = 0.5$ *and no wavefront coding. Note the presence of nulls and phase reversal in the OTF (right). Defocus* w_{20} *in units of wavelength.*

and $L(-1+\nu, \nu; w_{20})$ is illustrated in Fig. 4.1 for a spatial frequency $\nu = 0.5$ and for a range of values of w_{20}.

For a specific value of ν, nulls occurs in the defocused OTF when the gradient of the phasor at both limits $r' = 1 - \nu$ and $r' = -1 + \nu$ is zero; that is, the phasors must satisfy the following condition

$$h(1-\nu, \nu; w_{20}) = h(-1+\nu, \nu; w_{20}) = \exp(\mathrm{i}n\pi), \tag{4-7}$$

where n is a non-zero positive integer. This enables us to write

$$w_{20} = n\frac{\pm 1}{8\nu(1-\nu)}, \tag{4-8}$$

for the values of positive and negative defocus, in wavelengths, that introduce zeros at spatial frequency ν. It is clear from this interpretation that any degree of optical aberration will cause the phasors to curve, reducing the magnitude of the OTF. Furthermore, it can be appreciated from Fig. 4.1 that when the pupil function is even, the magnitude of $H(\nu; w_{20})$ decreases rapidly with added defocus and, for $w20 \geq 0.5$, nulls and phase reversals are introduced.

In this case, this unique decomposition of the OTF into its constituent phasors enables a simple and elegant explanation of the location of the zeros to be made, a result that can also be found in optics textbooks, such as Ref. [55].

2.3 Effect of a cubic phase mask on the OTF

As mentioned previously, a rectangular, linearly separable cubic pupil function and various other circular, odd pupil functions produce OTFs that vary slowly with defocus and with an absence of nulls, even for large defocus. We now show how this decomposition of the OTF provides a simple explanation and parameterization of the wavefront coding process. We consider a one-dimensional, defocused optical system in which a cubic phase mask with peak-to-valley displacement 2α, in units of wavelengths, is located in the pupil. The generalised pupil function for this system is

$$P(r, w_{20}, \alpha) = p(r)\exp[\mathrm{i}2\pi(w_{20}r^2 + \alpha r^3)], \tag{4-9}$$

with $p(r) = 1$ for $|r| \leq 1$ and $p(r) = 0$ otherwise. The interferogram phasors are thus given by

$$h(r, \nu; w_{20}, \alpha) = \exp[\mathrm{i}4\pi\nu(3\alpha r^2 + 2w_{20}r + \alpha\nu^2)]. \tag{4-10}$$

The complex decomposition of the OTF is obtained by inserting Eq. (4-10) into Eq. (4-3) and plotting the variation of $L(r', \nu; w_{20}, \alpha)$ as r' varies between $-1 + \nu$

and $1-\nu$:

$$L(r',\nu;w_{20},\alpha)=\frac{1}{2}\int_0^{r'}\exp[\mathrm{i}4\pi\nu(3\alpha r^2+2w_{20}r+\alpha\nu^2)]\mathrm{d}r, \tag{4-11}$$

where $1/2$ is the normalizing factor in Eq. (4-3). This resulting integral describes arc-length parameterized curves known as generalised Cornu spirals (GCS) or clothoids [82]. Although an analytical expression for the phasor $L(r',\nu;w_{20},\alpha)$ and the OTF $H(\nu;w_{20},\alpha)$ can be obtained in terms of error functions as we have shown in Chapter 2, a physical understanding and analysis of the wavefront coding process is more readily obtained from consideration of the simpler expression of Eq. (4-10). The three terms in the exponential contribute to a compound curve in the complex plane with three distinct components; the constant term, $\alpha\nu^2$, yields a linear section; the quadratic term, $3\alpha r^2$, induces a diminishing clockwise spiral for both positive and negative pupil displacements and, when w_{20} is sufficiently large, the term linear in r, $2w_{20}r$, introduces arcs of a circle similar to normal defocus as described above. Consequently, when w_{20} is sufficiently small the compound curve consists of two clockwise spirals separated by a linear section and for large w_{20} the curve more closely resembles a circle, although the additional linear and quadratic terms tend to give it a spiral form so that nulls are not introduced into the OTF. The contribution $L(r',\nu;w_{20},\alpha)$ is plotted in Fig. 4.2 for $\alpha=2$ and as defocus w_{20} is varied from 0 to 4 for a normalised spatial frequency of $\nu=0.5$. Also shown are the corresponding modulation transfer functions (MTFs) for this system. The resultant OTF at frequency ν, $H(\nu;w_{20},\alpha)$, is indicated by the resultant phasor between the inner ends of the two spirals. It can be seen that increasing positive defocus causes the spiral structure to rotate about the origin so that one spiral becomes more tightly wound whilst the opposite spiral unwinds in a manner such that, in terms of the MTF $|H(\nu;w_{20},\alpha)|$, the effect of one approximately counteracts the other. For negative defocus the rotation is also clockwise but produces tightening and loosening of the coils about the foci opposite those of positive defocus. In consequence, the MTF remains approximately constant until one spiral is completely wound around its origin and the other spiral is completely unwound; as the magnitude of w_{20} increases beyond the point at which one spiral is completely unwound, the MTF decreases rapidly. Physically, the coiling for positive and negative r' represents the resultant of the combined effects of the cubic phase mask and the defocus; a tightening in the spirals occurs when the cubic phase mask introduces phase-front curvature that is

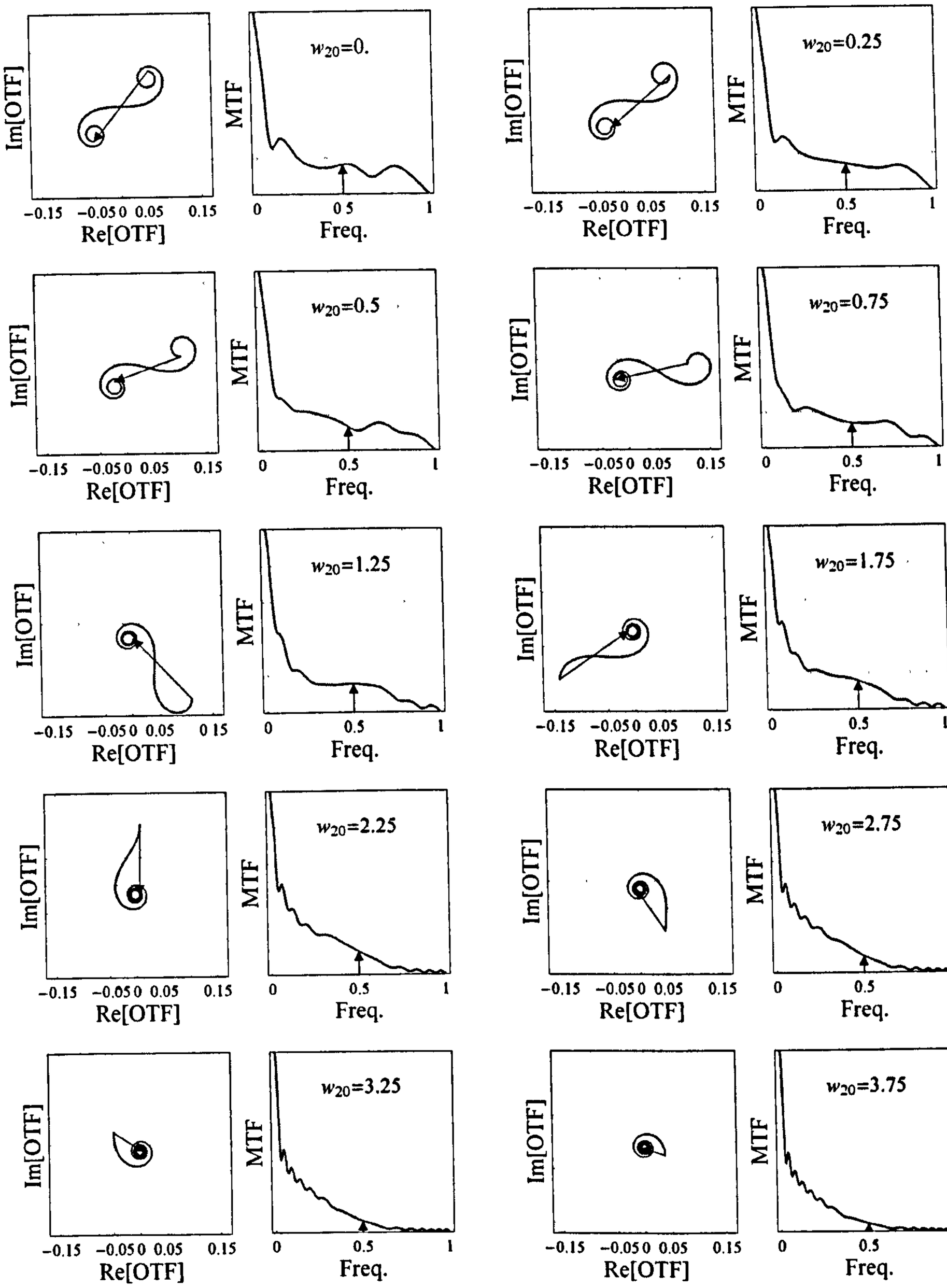

Figure 4.2: *Wavefront coding OTFs and MTFs depicted as generalised Cornu spirals for* $\alpha = 5$ *and* $\nu = 0.5$ *as defocus* w_{20} *increases.*

in the same sense as the quadratic defocus and loosening of the spirals occurs when the cubic phase mask tends to cancel the quadratic defocus. It can be appreciated from this picture how reduced sensitivity to defocus is facilitated by an odd pupil function.

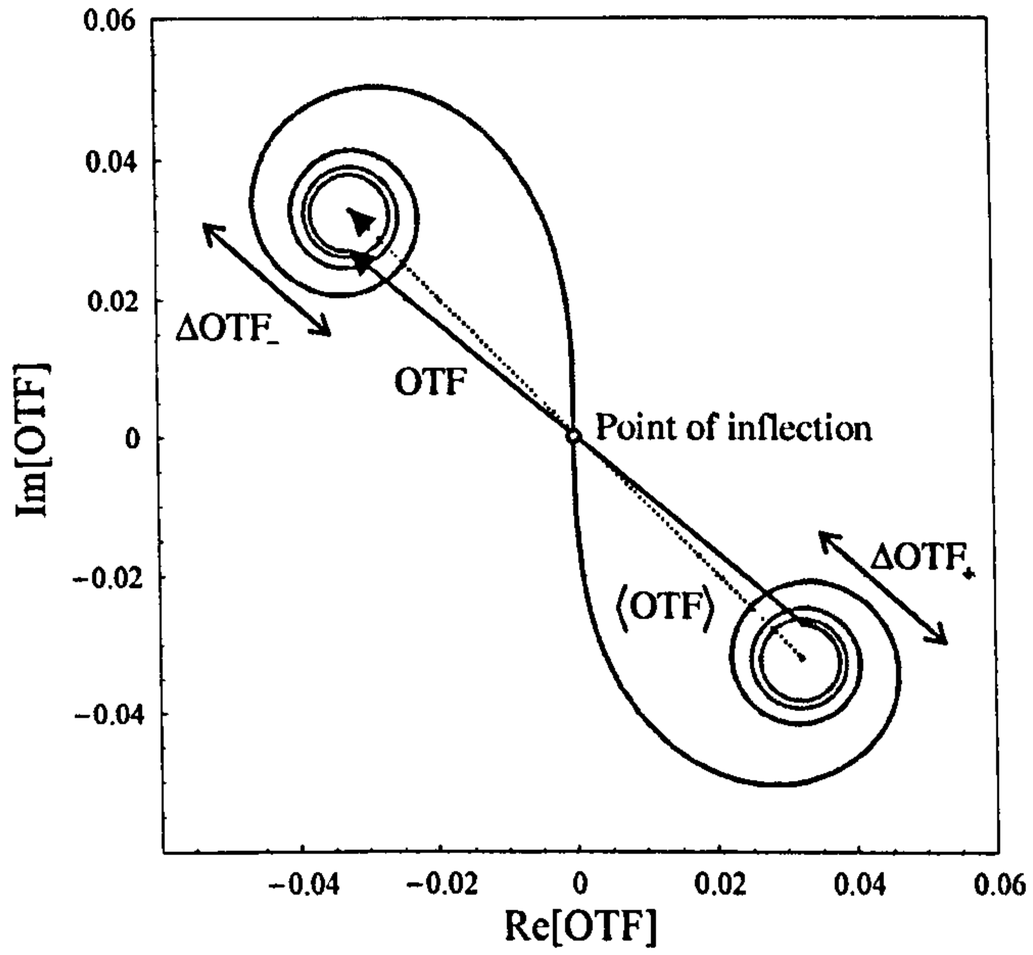

Figure 4.3: *Relationship between the geometry of a generalised Cornu spiral and the performance parameters of a wavefront coding system for normalised spatial frequency* $\nu = 0.5$ *and* $\alpha = 5$ *(in units of wavelength).*

Having shown how decomposition of the OTF enables wavefront coding to be described as a CGS, we now show how we can use the geometry of the Cornu spiral shown in Fig. 4.3 to estimate important parameters such as

1. An approximation to the value for the MTF $|H(\nu; w_{20}, \alpha)|$.

2. The maximum value of w_{20} for which the MTF can be considered to be approximately constant.

3. The magnitude of amplitude modulation of the MTF within this 'invariance' region.

4. The magnitude of the phase modulation introduced.

Previous descriptions of wavefront coding do not provide any estimates of the second of these parameters and predict that the latter two are equal to zero.

The spatial-frequency integral in Eq. (4-11) converges rapidly to the foci of the spiral with increasing pupil-plane displacement r', and so an approximation of the mean value of the OTF can be calculated by taking the limit $r' \to \pm\infty$ in

$L(r', \nu; w_{20}, \alpha)$, thus,

$$\langle H(\nu; w_{20}, \alpha) \rangle = \lim_{r' \to +\infty} L(r', \nu; w_{20}, \alpha) - \lim_{r' \to -\infty} L(r', \nu; w_{20}, \alpha), \tag{4-12}$$

operating further,

$$\langle H(\nu; w_{20}, \alpha) \rangle = \frac{(1+\mathrm{i})}{4\sqrt{6\alpha\nu}} \exp\left[-\mathrm{i}4\pi\nu\left(-\alpha\nu^2 + \frac{w_{20}^2}{3\alpha}\right)\right]. \tag{4-13}$$

The GCS rotates clockwise as w_{20} is increased in both positive and negative directions. In the ray picture, as we have shown in Chapter 2, this phase variation of the OTF represents the parabolic shape of the caustic along which the center of the point-spread function moves with varying defocus. The mean MTF is calculated by taking the modulus of the previous expression

$$|\langle H(\nu; w_{20}, \alpha) \rangle| = \frac{1}{\sqrt{48\alpha\nu}} \tag{4-14}$$

which is independent of the defocus coefficient and gives a straightforward estimation of the height reduction of the MTF as a function of the cubic parameter α. This expression is valid for moderate and large values of α and spatial frequencies $0 < \nu < 1$. Fig. (4.4) shows the actual wavefront coding MTFs and the approximated MTFs using Eq. (4-14) for various values of α. It can be observed from the spiral diagrams in Fig. 4.4 that as the cubic parameter α increases, the approximated MTFs become closer to the exact MTFs due to the more substantial coiling and convergence of the spirals towards the foci. In addition, the highly suppressed MTFs remain unchanged by greater values of defocus as more of this is required to unwrap one end of the spiral. Unintentionally, we have found by means of the spiral argument the direct geometrical representation of the stationary phase method applied in Chapter 2 to derive the cubic phase mask: greater values of α generate rapidly-convergent spirals with increased defocus invariance which result in superior validity of the stationary phase approximation.

When one end of the spiral is completely unwrapped, increasing defocus causes the MTF to drop rapidly. We define the maximum value for defocus invariance as that value of w_{20} for which the spiral is sufficiently unwrapped that the end coincides with the point of inflection midway between the two foci of the spiral, that is, the point at which the MTF is reduced to 50% of the mean value. A measure of the defocus invariance or unwrapping of the spiral can be obtained from the curvature κ of the spiral. The curvature κ at displacement r' on a GCS plotted in the complex

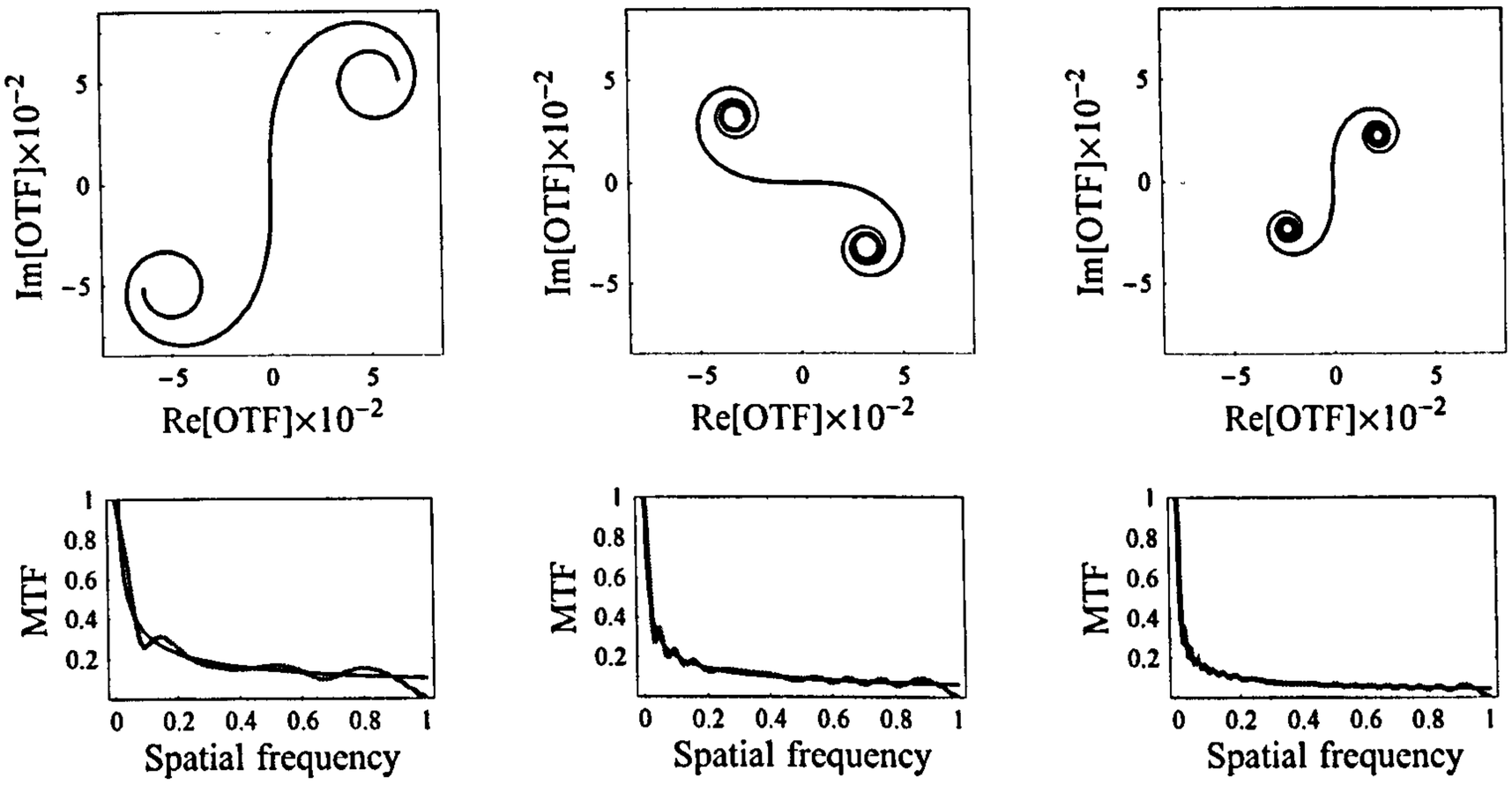

(a) $\alpha = 2$ (b) $\alpha = 5$ (c) $\alpha = 10$

Figure 4.4: *(Top) spiral coiling for* $\nu = 0.5$ *and with cubic parameter* $\alpha = 2, 5$ *and* 10 *(in units of wavelength); bottom, the corresponding exact (gray) and approximated (black) MTFs of the wavefront coding system.*

plane, can be calculated using the conventional definition from differential geometry of curve [83]:

$$\kappa(r') = \frac{\dot{x}\ddot{y} - \dot{y}\ddot{x}}{(\dot{x}^2 + \dot{y}^2)^{3/2}}, \tag{4-15}$$

where $x = \mathrm{Re}[L(r', \nu; w_{20}, \alpha)]$, $y = \mathrm{Im}[L(r', \nu; w_{20}, \alpha)]$ and each dot denotes a differentiation with respect to r'. We obtain the curvature at any point on the spiral by replacing Eq. (4-11) into Eq. (4-15) which yields

$$\kappa(r') = 16\pi\nu(w_{20} + 3\alpha r'). \tag{4-16}$$

That is, the curvature varies linearly along the spiral and for a particular displacement r' along the curve, varies linearly with w_{20}. Thus, neglecting the rotation of the entire spiral, the effect of defocus is to slide length of the curve along itself, wrapping around one locus as it unwraps from another as shown in Fig. 4.2. It can thus be appreciated that a measure of the maximum value of w_{20} for which the MTF is approximately constant can be considered to be the value for which either end of the spiral ($r' = 1 - \nu$ or $r' = -1 + \nu$) passes through the point of inflection, or zero curvature, that is, for $\kappa = 0$, thus

$$\kappa(\pm(1 - \nu)) = 16\pi\nu[w_{20} \pm 3\alpha(1 - \nu)] = 0, \tag{4-17}$$

solving this expression, we obtain

$$|w_{20}|_{max} = 3\alpha(1-\nu). \tag{4-18}$$

The point of inflection is equidistance between the foci of the spirals and so corresponds to a halving reduction in the value of MTF with respect to the mean value given by Eq. (4-14). The result given in Eq. (4-18) also highlights the maximum tolerable defocus is dependent on the spatial frequency and that for the higher spatial frequencies the tolerance remains small. It is therefore evident that knowledge of w_{20} and α allows us to predict the point at which the exact MTF depart from its approximation, providing a measure of the operational spatial frequency bandwidth for a given defocus.

The representation in Fig. 4.3 of the OTF vector between the ends of the spiral oscillating in amplitude and phase about the mean OTF vector joining the foci of the spiral, clearly indicates the amplitude and phase modulation of the OTF that accompanies defocus. The magnitudes of the amplitude and phase modulations can be estimated from the geometry of this representation. Projection of the displacement vectors from each foci (i.e. for $r' \rightarrow \pm\infty$) to the respective extremes of the spiral at $r' = \pm(1-\nu)$ onto the mean OTF vector yields the amplitude modulation $M_{\parallel}$ whilst projection in the orthogonal direction $M_{\perp}$ yields the phase modulation $\Delta\theta$. A complete derivation of the following results can be found in Appendix D. It can thus be shown that the amplitude modulation is given by

$$\begin{aligned} M_{\parallel}(\nu; w_{20}, \alpha) \;=\; & \frac{1}{16\pi\nu}\left(\frac{\cos\{(4\pi\nu/3\alpha)[w_{20}-3\alpha(1-\nu)]^2+(\pi/4)\}}{w_{20}-3\alpha(1-\nu)}\right. \\ & \left.-\frac{\cos\{(4\pi\nu/3\alpha)[w_{20}+3\alpha(1-\nu)]^2+(\pi/4)\}}{w_{20}+3\alpha(1-\nu)}\right), \end{aligned} \tag{4-19}$$

where each of the two components within the boldface parentheses corresponds to modulation at either end of the spiral. For increasing defocus and practical values of α, one of the spirals is much more tightly wound than the other and so a good approximation can be obtained by neglecting one of the terms in brackets to yield:

$$M_{\parallel}(\nu; w_{20}, \alpha) \approx \frac{\cos\{(4\pi\nu/3\alpha)[w_{20}-3\alpha(1-\nu)]^2+(\pi/4)\}}{16\pi\nu[w_{20}-3\alpha(1-\nu)]}, \tag{4-20}$$

which is valid for $w_{20} > 0$. By neglecting the cosine oscillation, the amplitude modulation of the OTF is then constrained within the following domain

$$|M_{\parallel}(\nu; w_{20}, \alpha)| \leq \left|\frac{1}{16\pi\nu[w_{20}-3\alpha(1-\nu)]}\right|, \tag{4-21}$$

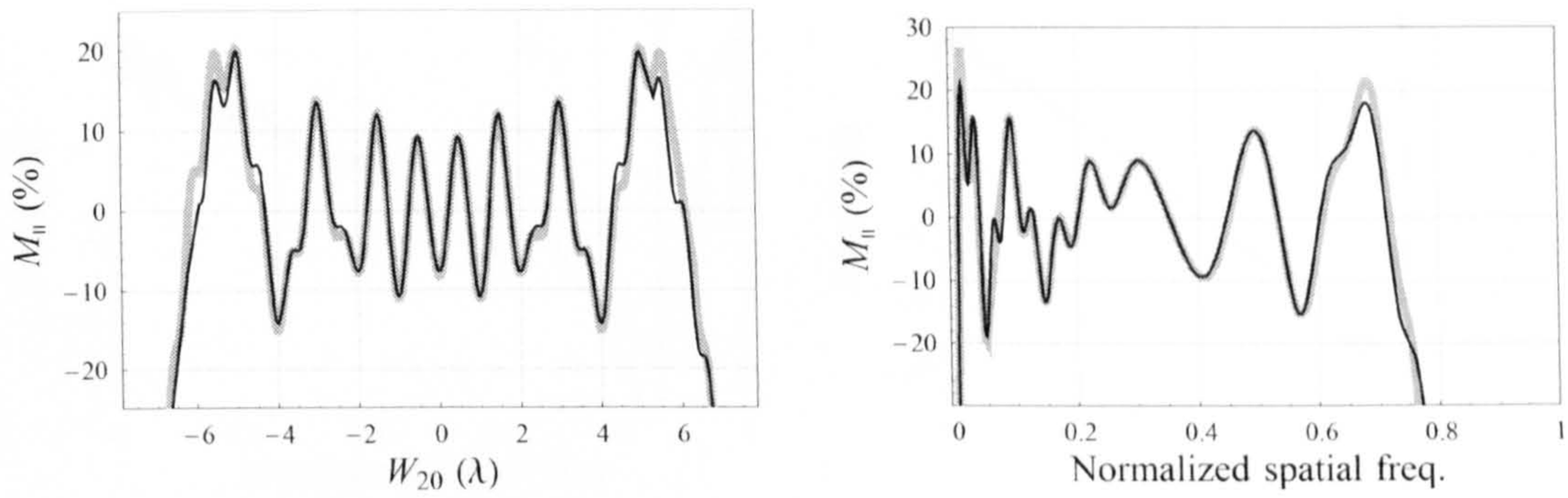

(a) (b)

Figure 4.5: *Amplitude modulation (a) for $\alpha = 5$ and $\nu = 0.5$ as a function of defocus and (b) for $w_{20} = 3$ as a function of spatial frequency. Black curve represents Eq. (4-19); and the gray curve, the actual amplitude modulation.*

for $0 < w_{20} < 3\alpha(1-\nu)$. For $\alpha = 5$ and $\nu = 0.5$, Fig. 4.5(a) depicts as a function of defocus the amplitude modulation given in Eq. (4-19) with respect the mean MTF value. The small amplitude fluctuations on top of the main variation are caused by the tightening of the end of the spiral increasingly wrapped by defocus. That is why the small fluctuations can be neglected in Eq. (4-19) to derive a simpler expression given by Eq. (4-20). In this figure, the analytical result of the amplitude modulation is compared with the modulation obtained by an independent numerically-based method which confirms the validity of Eq. (4-19) for $|w_{20}| < 3\alpha(1-\nu)$. From these expression, useful performance parameters can be readily obtain, for example the amplitude modulation for $\alpha = 5$ and $\nu = 0.5$ is of $\sim \pm 10\%$ at $w_{20} = 3$ (half way of the defocus range) and $\sim \pm 20\%$ at $w_{20} = 5$ (near the validity limit). Similarly, Fig. 4.5(b) shows the amplitude modulation as a function of spatial frequency for $\alpha = 5$ and $w_{20} = 3$. For this particular case, it can be clearly seen than when $\nu \geq 1 - |w_{20}|/3\alpha = 0.8$ our expressions are no longer valid since the spirals within that frequency range are completely unwound and the MTF drops a factor of 50% or more.

Based on the same geometrical arguments we now calculate the phase modulation with respect to the mean OTF that occurs in the unraveling end of the spiral for increasing positive defocus (again, we neglect the small phase angle in the wrapping focus). The modulation orthogonal to the mean OTF, $M_{\perp}$, is readily obtained by replacing the cosine by a sine function in Eq. (4-20) and for $w_{20} > 0$ we obtain the

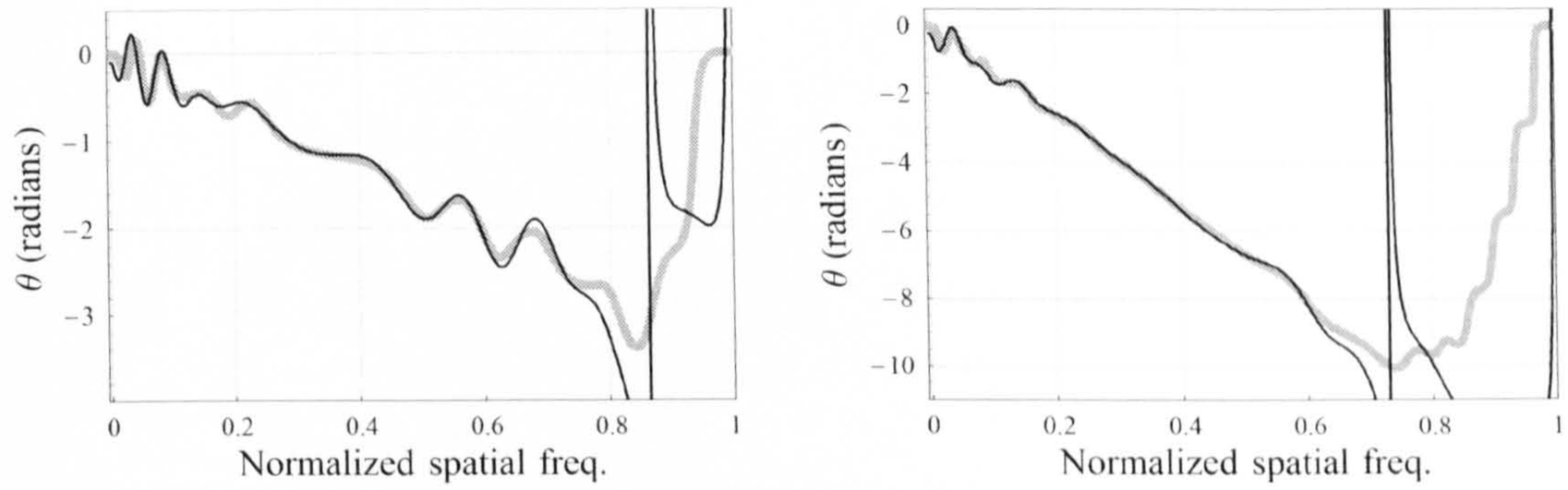

Figure 4.6: *Unwrapped exact (gray)and approximated (black) phase modulation as a function of normalised spatial frequency for* $w_{20} = 2$*, left; and* $w_{20} = 4$*, right.*

amplitude of the phase modulation:

$$\Delta\theta \approx \frac{\sqrt{3\alpha\nu}}{2\pi\nu[w_{20} - 3\alpha(1-\nu)]} \times \sin\{(4\pi\nu/3\alpha)[w_{20} - 3\alpha(1-\nu)]^2 + (\pi/4)\}. \quad (4\text{-}22)$$

The overall phase modulation is finally obtained by adding the overall rotation of the foci and the fluctuations produced by the unraveling of the extreme of the spiral

$$\theta \approx -4\pi\nu\left(-\alpha\nu^2 + \frac{w_{20}}{3\alpha}\right) + \Delta\theta. \quad (4\text{-}23)$$

The phase modulation θ as a function of spatial frequency is shown in Fig. 4.6 for $\alpha = 5$ and two defocus values: $w_{20} = 2$ and $w_{20} = 4$. There is a substantial agreement between the exact phase modulation and its approximation derived on purely geometrical grounds. In the same way as for the amplitude modulation, the estimate of the phase modulation is valid within the frequency range $\nu \geq 1 - |w_{20}|/3\alpha$ where the corresponding spirals are not completely unwound. Within this region a linear relationship between phase modulation and spatial frequency holds. The slope of the linear curve accounts for the amount of defocus introduced (with w_{20} the slope is null and the curve coincides with the horizonal axis). Therefore, defocus aberration produces a linear translation of the low spatial frequencies. For high spatial frequencies, defocus not only reduces the MTF considerably but produces fast phase variations. As we will see in Chapter 5, the phase modulation has a greater impact than the amplitude modulation on the restoration of the coded images. Phase mismatches between the deconvolution and convolution kernels give rise to artifacts and replication in the processed image.

In summary, by decomposing the OTF, we have presented a unique method which provides a clear understanding of the physical process of wavefront coding

and allows extraction performance parameters by means of analytical expressions and simple geometrical considerations. For the first time, this description of the wavefront coded OTF explains and quantifies the artifacts and edge replication that are found in the restored image. In the next section, we extend the decomposition of the optical transfer function to 2D pupils with rectangular and circular apertures.

3 Rectangularly separable phase mask in 2D

The decomposition of the optical transfer function into the complex amplitudes of the component interferograms for 1D wavefront coding system allows us to obtain analytical solutions of the performance parameters and to understand the physical principles which extend the depth of field. Moreover, the novel perspective presented here facilitates new ways into the design of phase masks to alleviate optical aberrations. Although the OTF decomposition method has been implemented analytically for a 1D imaging system, it can be extended in the same way into a 2D system. Unfortunately, for 2D optical systems with non-separable pupil functions the OTF decomposition is restricted mainly to numerical evaluation, nevertheless in cases where the pupil function is rectangularly separable it is still possible to obtain valuable insight and basic performance expressions.

The phase masks that provide an extended depth of field and which have been derived assuming rectangularly separable condition have all been found to be antisymmetric. As we have demonstrated in the previous section, antisymmetric profiles favour greater tolerance to defocus. Examples of these type of phase masks which will be assessed using the OTF decomposition method include

- Cubic phase mask with a rectangular or circular aperture.

- Other rectangularly separable phase masks: high order polynomial $n > 3$ [63, 33, 64] and logarithmic phase mask [32].

Cubic phase mask with a rectangular aperture

The decomposition of the OTF, when applied to a 2D rectangular aperture with a cubic phase mask, provides analytical solutions for the performance parameters along the horizontal and vertical axes of the OTF, i.e. when a pair of spatial frequencies in the Fourier plane satisfies $(\xi = 0, \eta)$ or $(\xi, \eta = 0)$. In this particular

case, the geometrical representation of the phasor interferograms at each spatial frequency also depicts a generalised Cornu spiral which, in turn, is described by the same expressions derived for the case of a 1D aperture. The derivation and results for the OTF's horizontal and vertical axes of a rectangular aperture are not included herein as no new information is provided. However, outside these favourable axes it is still possible to extract mathematical expressions that disclose key information about the performance of an optical system with a cubic phase mask. Of special interest is the performance along the spatial frequencies axes where $\xi = \eta$ and $\xi = -\eta$ (at 45 and 135 degrees respectively).

In order to perform an analytical OTF decomposition along these spatial frequency axes it is necessary to apply a rotation operation to the cartesian coordinate system so that one of the spatial frequency variables, i.e. η, is removed from the autocorrelation integral and only one arc-length parameter is left to describe the curve. This requirement arises from the fact that the incremental contributions of the OTF integral in the cartesian plane occur simultaneously along the x and y directions which result in two arc-length parameters that no longer describe a curve but a surface, which in most cases is difficult to represent pictorially.

The pupil function for defocus and a cubic phase mask in the new cartesian coordinate system rotated clockwise by an angle θ about the origin can be expressed as

$$\begin{aligned} P(x,y;\theta) &= p(x,y;\theta)\exp\Big(\mathrm{i}2\pi\Big\{w_{20}(x^2+y^2)+ \\ &\qquad \alpha\left[(y\cos\theta - x\sin\theta)^3 + (x\cos\theta + y\sin\theta)^3\right]\Big\}\Big) \end{aligned} \tag{4-24}$$

with $p(x,y;\theta) = 1$ for values of x and y which fall inside a unit half-width square pupil centred in the origin and rotated an angle θ, and $p(x,y;\theta) = 0$ elsewhere. The pupil function is described in normalised coordinates and w_{20} and α are in units of wavelength. The phasor interferogram in 2D is also represented by the region of overlap of two displaced pupil functions and rotated by an angle θ, thus $h(x,y,\xi,\eta;\theta) = P(x+\xi,y+\eta;\theta)P^*(x-\xi,y-\eta;\theta)$. Let us recall that the rotation operation allows us to set $\eta = 0$ for any value of θ. Following the same procedure as for the one-dimensional example, the expression of the phasor interferogram is inserted into Eq. (4-3) for the 2D case, that is

$$L(x',\xi;\theta) = \frac{1}{4}\int_0^{x'}\int_{C_a}^{C_b} h(x,y,\xi,0;\theta)\mathrm{d}x\mathrm{d}y \tag{4-25}$$

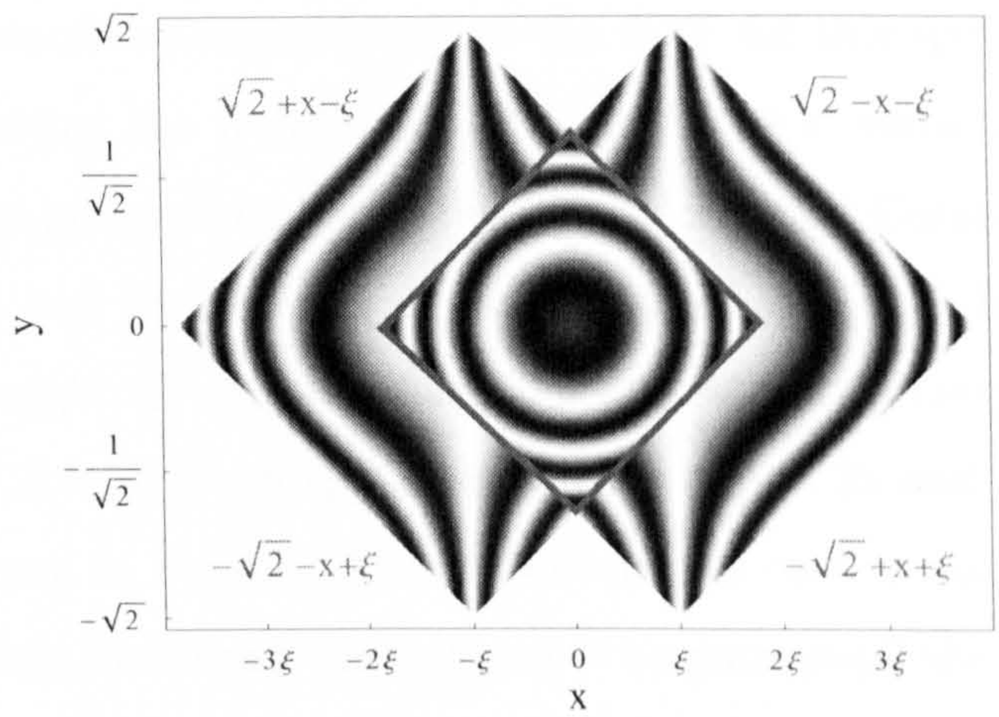

Figure 4.7: *Density plot of the real part of the autocorrelation function at spatial frequency ξ laying at 45 degrees of a square aperture with a cubic phase mask ($\alpha = 2$). The overlapping region is delimitated by four straight curves with equations shown next to them.*

where 1/4 is a 2D normalizing factor and corresponds to the area of the square pupil. The domain of integration C for the y variable is represented by four straight lines that demarcate the area of overlap of two displaced pupils as is shown in Fig. 4.7. For a angle of rotation $\theta = \pi/4$ or $\theta = 3\pi/4$ (45 and 135 degrees respectively) the equations of the bounding curves are readily extracted from the geometry of the overlapping pupils, see Fig. 4.7, which yields

$$C = \begin{cases} C_a = -\sqrt{2} + x + \xi \quad \text{and} \quad C_b = \sqrt{2} - x - \xi, & \text{if } x' > 0 \\ C_a = -\sqrt{2} - x + \xi \quad \text{and} \quad C_b = \sqrt{2} + x - \xi, & \text{if } x' < 0. \end{cases}$$

After rotation of $\theta = \pi/4$, the phasor interferogram results in

$$h(x, y, \xi, 0; \pi/4) = \exp[\mathrm{i}4\pi\xi x(2w_{20} + \sqrt{2}\alpha y)]. \tag{4-26}$$

Replacing Eq. (4-26) in Eq. (4-25), and evaluating further taking into account the limits of integration, we obtain

$$L(x', \xi; \pi/4) = \frac{\mathrm{i}}{48\sqrt{2}\pi\alpha\xi} \int_0^{x'} \frac{1}{x} \Big(\exp\{\mathrm{i}4\pi x\xi[2w_{20} - 3\alpha(-2 + \sqrt{2}x + \sqrt{2}\xi)]\} \tag{4-27}$$
$$- \exp\{\mathrm{i}4\pi x\xi[2w_{20} + 3\alpha(-2 + \sqrt{2}x + \sqrt{2}\xi)]\} \Big) \mathrm{d}x$$

for $x' > 0$, and

$$L(x', \xi; \pi/4) = \frac{\mathrm{i}}{48\sqrt{2}\pi\alpha\xi} \int_0^{x'} \frac{1}{x} \Big(\exp\{\mathrm{i}4\pi x\xi[2w_{20} - 3\alpha(2 + \sqrt{2}x - \sqrt{2}\xi)]\} \tag{4-28}$$
$$- \exp\{\mathrm{i}4\pi x\xi[2w_{20} + 3\alpha(2 + \sqrt{2}x - \sqrt{2}\xi)]\} \Big) \mathrm{d}x$$

for $x' < 0$. The complex decomposition of the OTF for this spatial frequency axis is obtained by plotting the variation of $L(x', \xi; \pi/4)$ as x' varies between $-\sqrt{2}+\xi$ and $\sqrt{2}-\xi$. These integrals no longer describe generalised Cornu spirals, as occurs for the horizontal and vertical axis of the *unrotated* 2D OTF, but arc-like curves traced from the origin of the complex plane and with symmetry around it. The contribution $L(x', \xi; \pi/4)$ for a spatial frequency $\xi = 0.25$ and $\alpha = 2$ as defocus is increased is shown in Fig.4.8. Also shown are the corresponding MTFs for this frequency axes. Note that along the diagonal of a square pupil the normalised spatial frequency cutoff is $\sqrt{2}$. Two important results that have an important effect in the performance of a wavefront coding system can be drawn from the figure:

1. MTFs produced by a cubic phase mask are extremely suppressed along the diagonals of a square pupil and become further reduced for increasing values of defocus.

2. The OTF is the vector displacement between the extremes of the two arc curves, $H(\xi; \pi/4) = L(\sqrt{2}-\xi, \xi; \pi/4) - L(-\sqrt{2}+\xi, \xi; \pi/4)$, therefore the symmetry of the arc results in real-valued OTFs for any value of α and w_{20}. Thus, no phase variation is introduced by defocus.

For the particular example shown in Fig.4.8, the MTF is approximately 10 times lower than the MTF for the same spatial frequency on the horizontal axis. The abrupt drop in the MTF outside the horizontal and vertical spatial frequency axes will give rise to significant noise amplification when postdetection signal processing is applied. In addition, the noise amplification across an image will not be uniformly distributed but it will depend on the magnitude of the spatial frequency and its orientation. As mentioned above, the phase of the spatial frequencies laying on the $\theta = \pi/4$ orientation is not affected by changes in defocus, as it occurs for all the other spatial frequencies in the complex plane. This means that when the restoration kernel (normally the cubic PSF at $w_{20} = 0$) is applied in the detected blur image, these spatial frequencies will be accurately recovered with the exact phase. However when defocus exceeds certain limit, the ends of the arc meet and nulls and phase reversals occur in the OTF. It is interesting to point out the series of anomalies or kinks that appear along the arc curve which cause the phasors to fold back into each other, reducing the overall length of the curve and generating such low MTFs. The magnitude of the kinks become more prominent as defocus is increased.

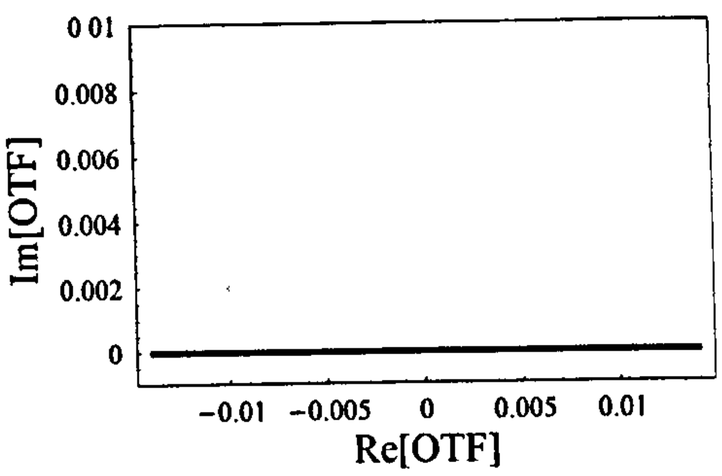

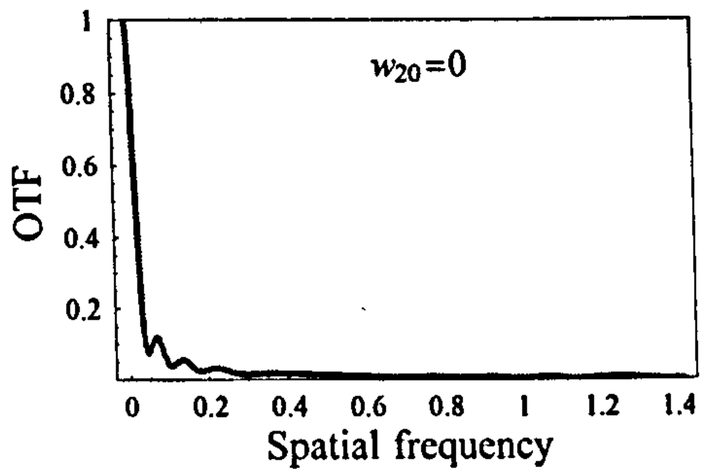

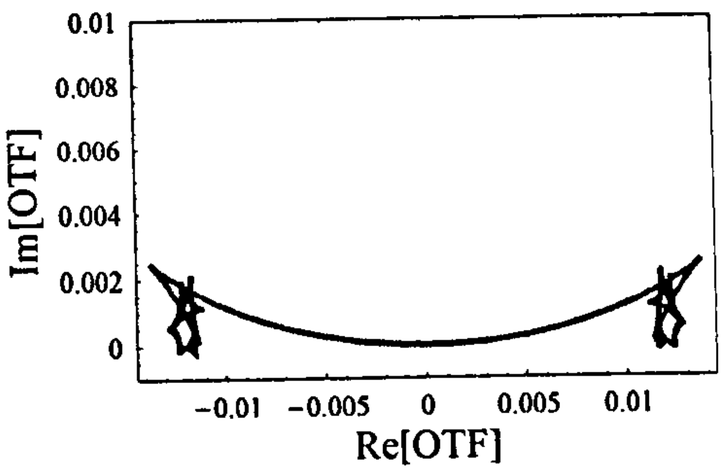

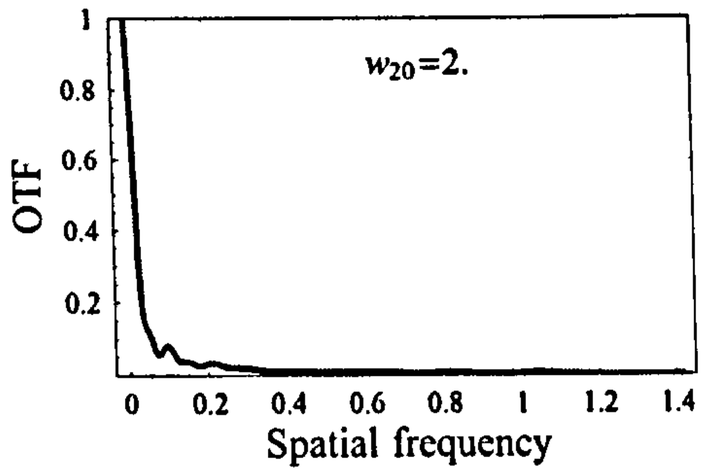

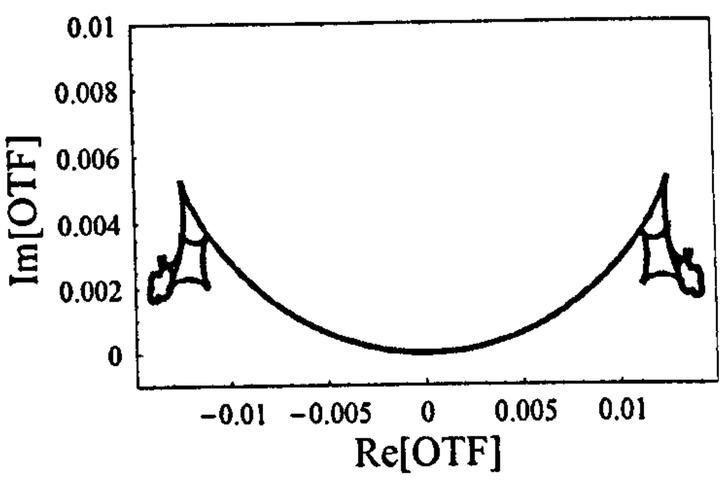

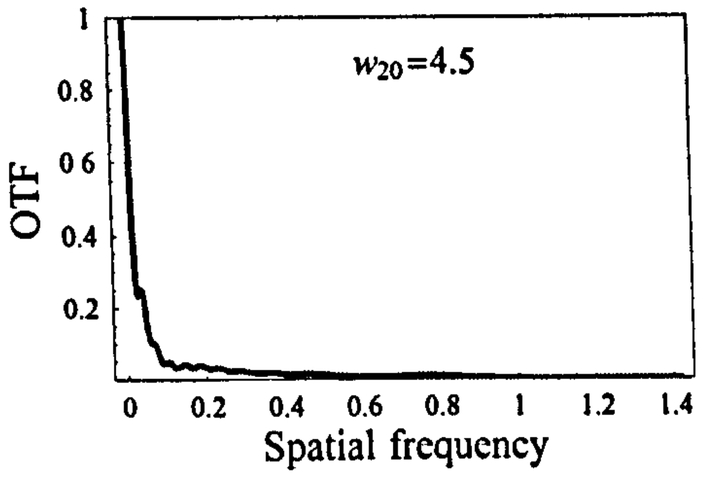

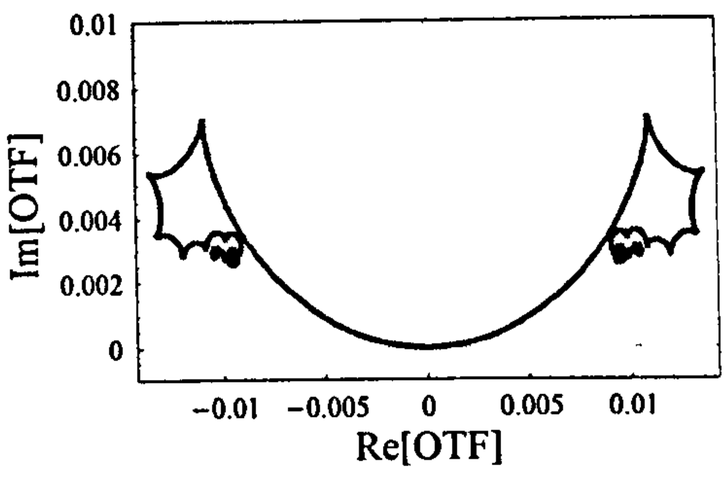

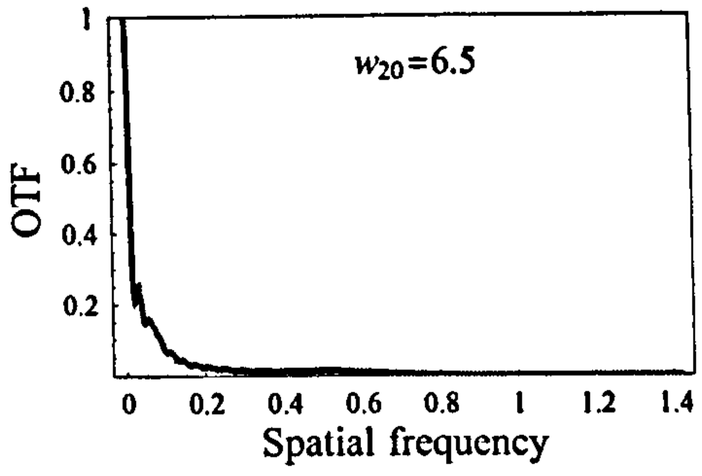

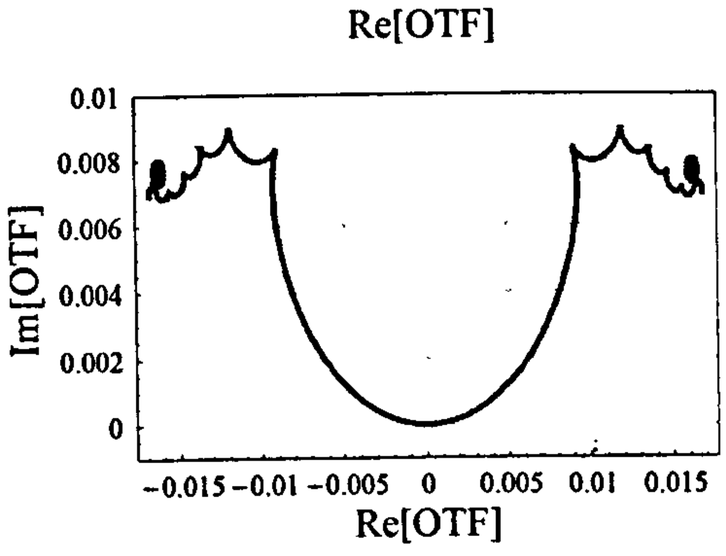

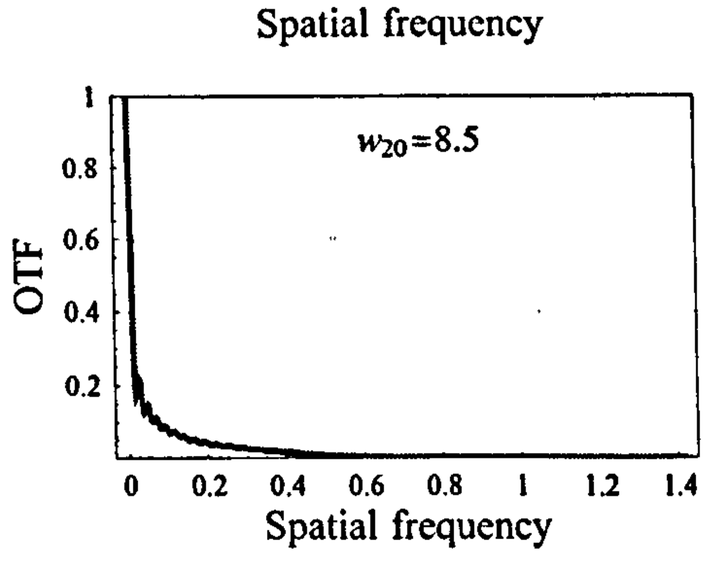

Figure 4.8: *(Left) Decomposition of the wavefront coding OTFs depicted as curves for* $\alpha = 5$ *and* $\nu = 0.25$ *lying on the* 45 *degree axis as defocus* w_{20} *increases. (Right) The corresponding MTFs along the* 45 *degree axis*

The curvature of the arc curves is readily calculated using the same method as for the 1D mask, thus applying Eq. (4-15) to Eq. (4-27) and Eq. (4-28) yields:

$$\kappa(x') = \frac{192\sqrt{2}\pi^2 w_{20}\alpha\xi^2|x'|}{|\sin[\text{sign}(x')x'12\pi\alpha\xi(2+\sqrt{2}x'-\sqrt{2}\xi)]|} \tag{4-29}$$

which is equally valid for $x' > 0$ and $x' < 0$ (hence the symmetry of the plots) and $-\sqrt{2} < \xi < \sqrt{2}$. It can be appreciated from the curvature expression that despite not obtaining phasor contributions along the 45 degree axis arranged in the manner of Cornu spirals, the arc curves still facilitate reduced sensitivity to defocus as the parameter α fixes the amount of kinks along the curve by means of the argument of the sine function in the denominator. Defocus aberration stretches out the kinked sections of the curve until defocus finally overcomes the cubic effect and a full arc circle is produced. This effect can be seen in the evolution of the curve in Fig. 4.8.

A similar analysis can be carried out with the spatial frequencies which fall on the other OTF diagonal. The phasor interferogram is calculated by substituting $\theta = 3\pi/4$ into Eq. (4-24) and calculating the overlap of two displaced pupil function, which yields

$$h(x, y, \xi, 0; 3\pi/4) = \exp\{-\text{i}2\pi\xi[-4w_{20}x + \sqrt{2}\alpha(3x^2 + 3y^2 + \xi^2)]\}. \tag{4-30}$$

Unfortunately, although it is possible to obtain analytical solutions for the phasor contributions and their plot curvatures for any spatial frequency along the 135 degree axis, the expressions become of significant length and complexity with several error function terms. These equations are not included here as very little mathematical manipulation can be performed; nevertheless the plots of the geometrical configuration of the phasor contributions have been produced, as shown in Fig. 4.9(right). This figure shows also a comparison of the three different type of curves generated by the decomposition OTF of a spatial frequency $\xi = 0.5$ with three different orientation in the scene: 0, 45 and 135 degrees from the horizontal axis. In contrast to the arc-type phasor diagram for spatial frequency falling on the 45-degree diagonal (centre column), the phasor contributions at 135 degrees depict a spiral similar to that obtained at 0 degrees (right column) and subject to the same wrapping and unwrapping mechanism described in the previous section when defocus is increased. Also note from the spiral drawing at 135 degrees that as the spiral unwinds due to defocus, fast changes in the phase of the spatial frequency take place. In spite of having two completely different representations of the decomposed OTF for 45

and 135 degrees, the former an arc, the latter a spiral with different properties, the distance between the curve ends (i.e. the MTFs) for both frequency orientations remains identical, but clearly phase effects are different.

We finish our study of the decomposition of the OTF of a cubic phase mask in 2D with the plots of the curvatures associated with the geometrical diagrams shown in Fig. 4.9, see Fig. 4.10. As we have demonstrated earlier, the curvature equation has provided a simple mathematical tool to characterise the spatial frequency performance of a wavefront coding system along the horizontal and vertical directions of the OTF. In this case, the curvature varies both linearly along the spiral arc-parameter x' and with defocus w_{20}, as shown in Fig. 4.10(left). Defocus simply displaces the offset of the linear curvature. The curvatures along the 45 and 135 degree OTF directions, Fig. 4.10(centre) and Fig. 4.10(right) respectively, distinctly account for the non-linear behavior of the phasor diagrams with respect to x' and w_{20} and the extremely low MTFs. Note that for these orientations, the curvatures are two orders of magnitude larger. Astonishingly, the analysis of the MTFs away from 0 or 90 degrees has been completely neglected in the literature; certainly, because of the much poorer behaviour outside the favourable directions.

Other rectangularly separable phase masks: high order polynomial $n > 3$ and logarithmic profiles

Encouraged by the results and elucidative physical insight provided by our unique method of OTF decomposition, we next investigate, in a qualitative way, several variations of rectangularly separable antisymmetric phase masks for alleviation of defocus aberration. The general phase profile of these masks is defined by a polynomial equation in normalised coordinates

$$\phi(x, y) = \alpha(\text{sign}(x)x^n + \text{sign}(y)y^n), \tag{4-31}$$

with the order n higher than cubic. As for the cubic phase mask, the parameter α controls the amount of wavefront modulation.

We have calculated the MTFs and geometrical representation of the contributing complex interferogram OTF components for a spatial frequency $\nu = 0.5$ and with the same phase strength $\alpha = 3$ for various values of defocus, see Fig. 4.11, Fig. 4.12, Fig. 4.13 and Fig. 4.14 with $n = 5, 7, 9, 11$ respectively. It is evident from the OTF decomposition figures that any phase mask with antisymmetric profile will reduce

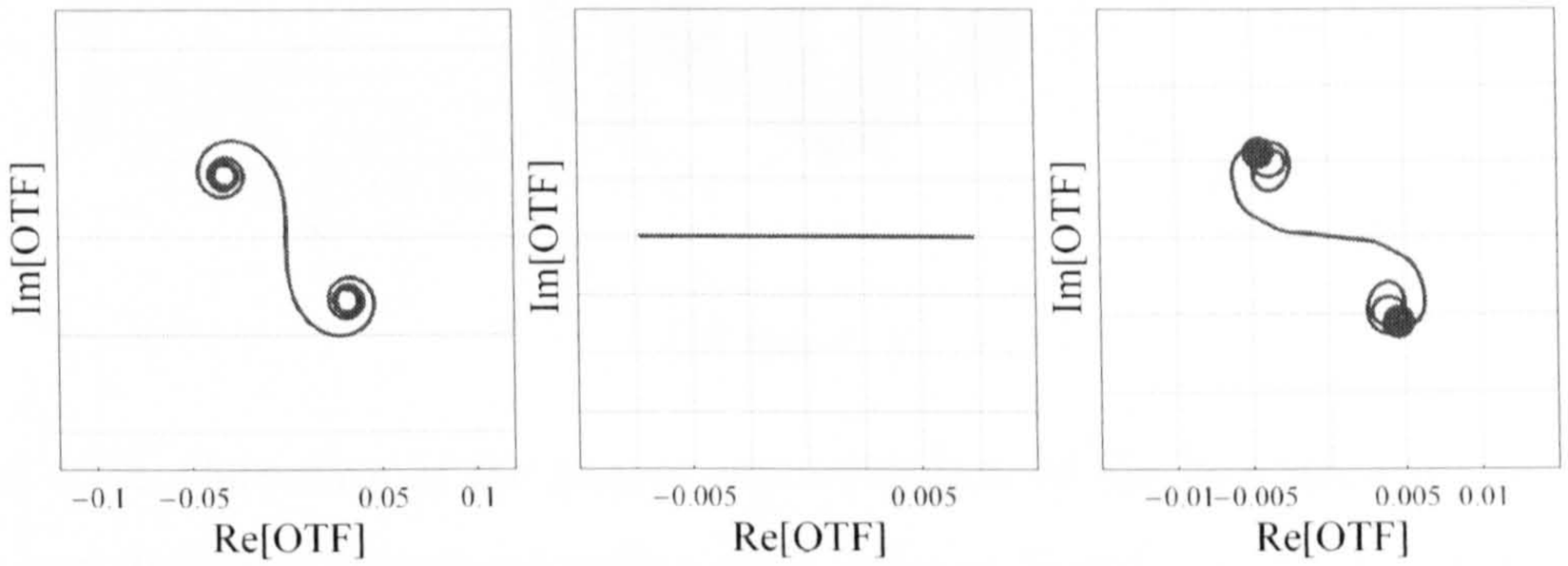

(a)$w_{20} = 0$

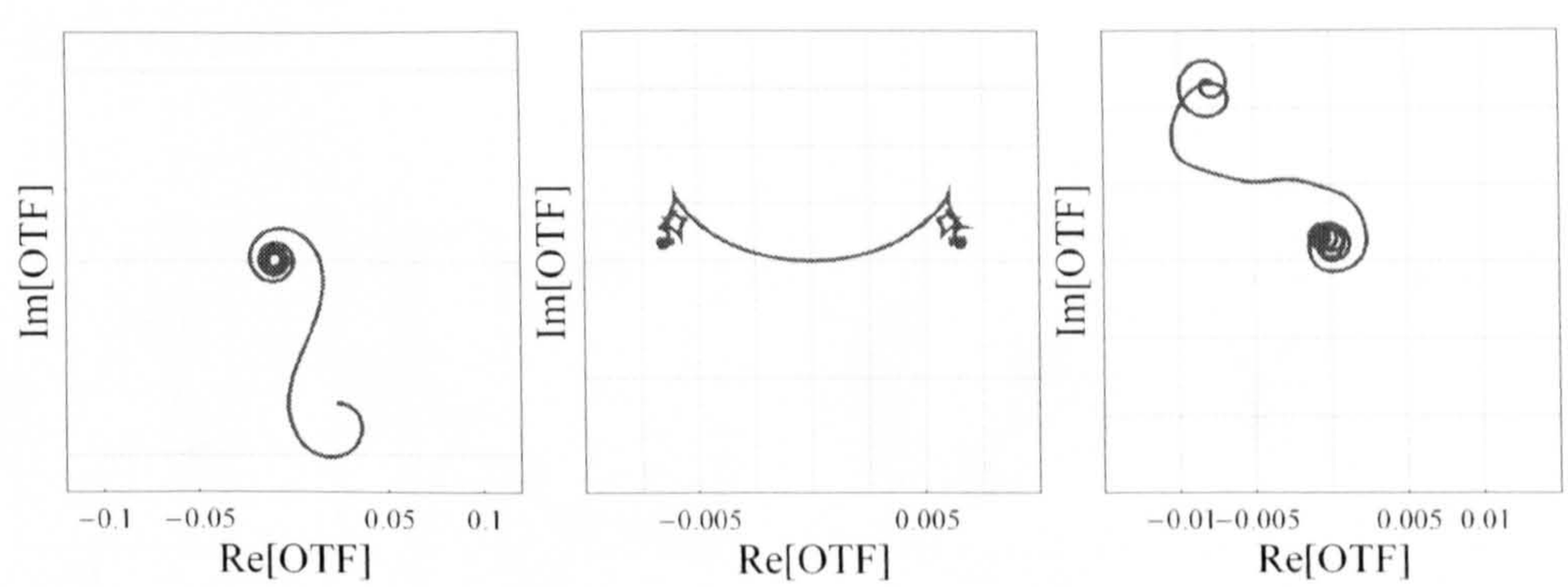

(b)$w_{20} = 4$

Figure 4.9: *Geometrical representation of the decomposition of an in-focus and defocused wavefront coding OTF for* $\alpha = 5$ *and* $\nu = 0.5$ *for three spatial frequency orientations: 0 degrees (left), 45 degrees (centre) and 135 degrees (right).*

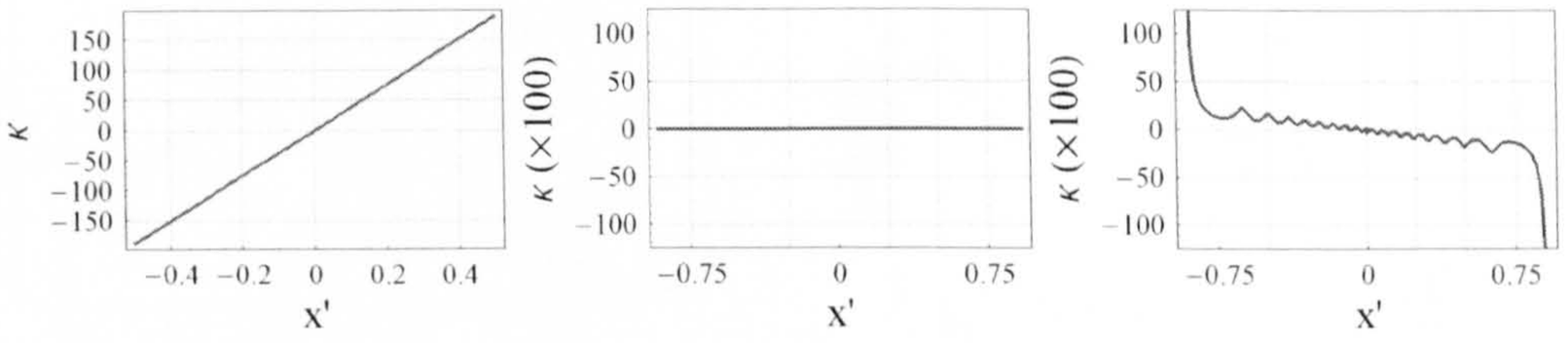

(a) $w_{20} = 0$

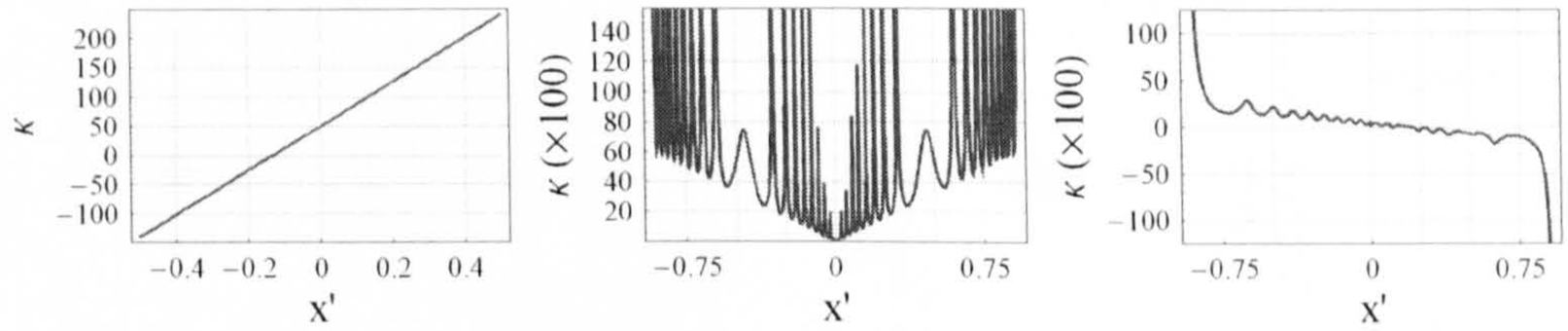

(b) $w_{20} = 4$

Figure 4.10: *Curvature of the phasor representation of the decomposition of an in-focus and defocused wavefront coding OTF for* $\alpha = 5$ *and* $\nu = 0.5$ *for three spatial frequency orientations: 0 degrees (left), 45 degrees (centre) and 135 degrees (right).*

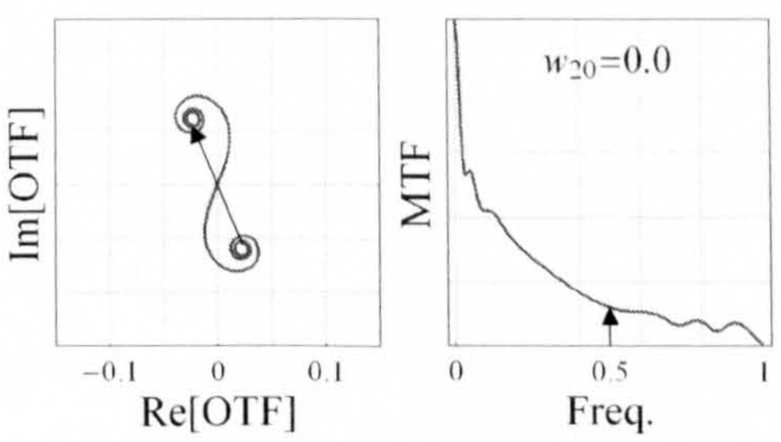

(a) $w_{20} = 0$

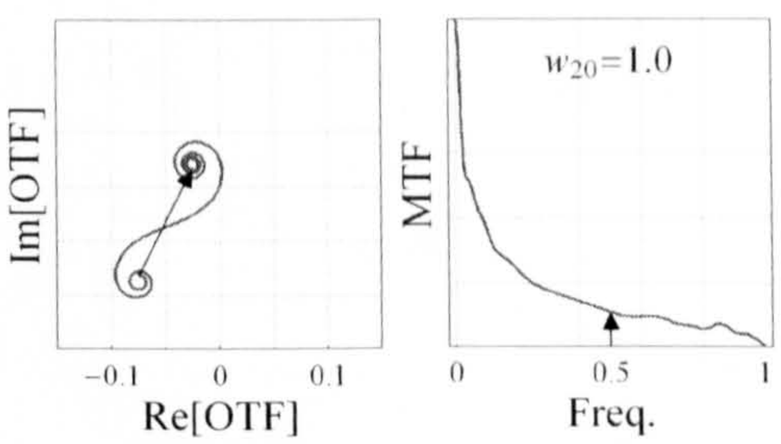

(b) $w_{20} = 2$

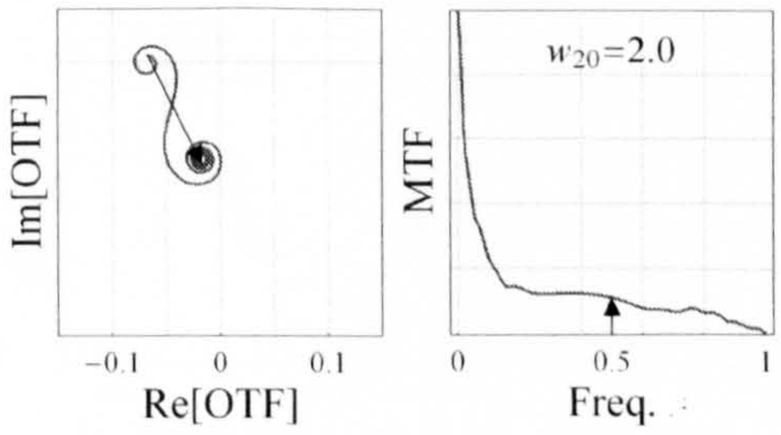

(c) $w_{20} = 4$

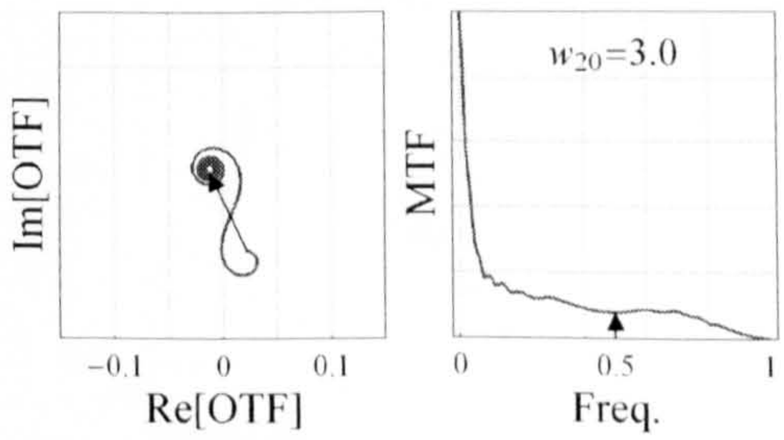

(d) $w_{20} = 6$

Figure 4.11: *Wavefront coding OTFs and MTFs depicted as spirals for a 5th-order phase mask with* $\alpha = 3$ *and* $\nu = 0.5$ *as defocus* w_{20} *increases. All parameters in units of wavelength.*

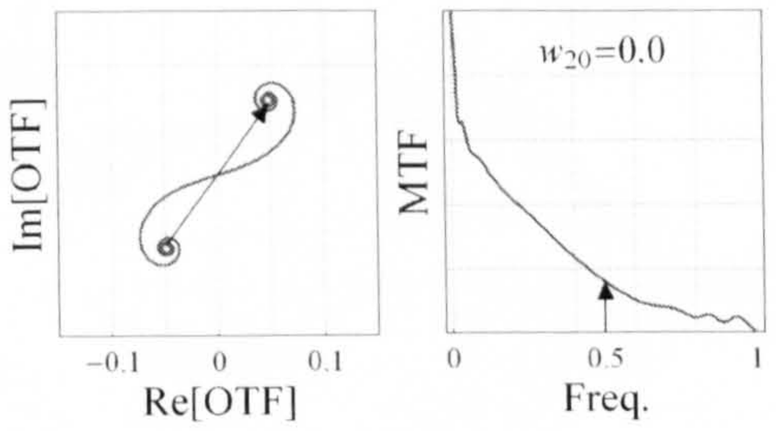

(a) $w_{20} = 0$

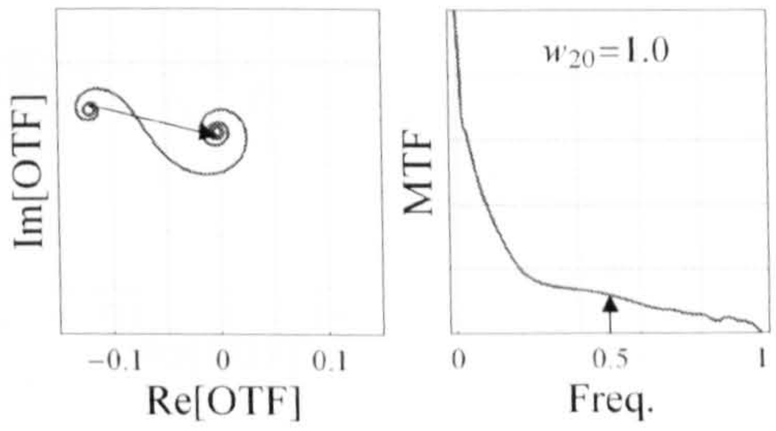

(b) $w_{20} = 2$

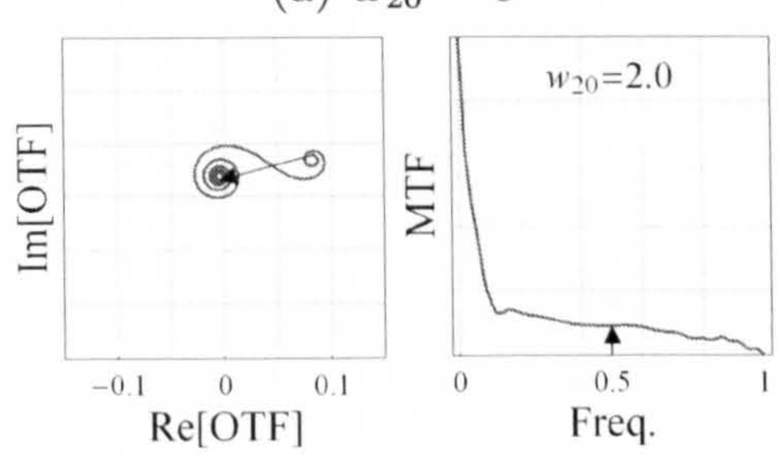

(c) $w_{20} = 4$

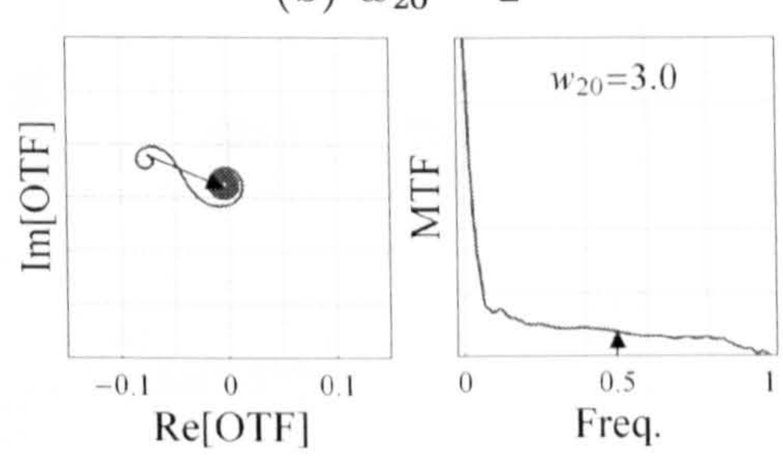

(d) $w_{20} = 6$

Figure 4.12: *Wavefront coding OTFs and MTFs depicted as spirals for a 7th-order phase mask with* $\alpha = 3$ *and* $\nu = 0.5$ *as defocus* w_{20} *increases. All parameters in units of wavelength.*

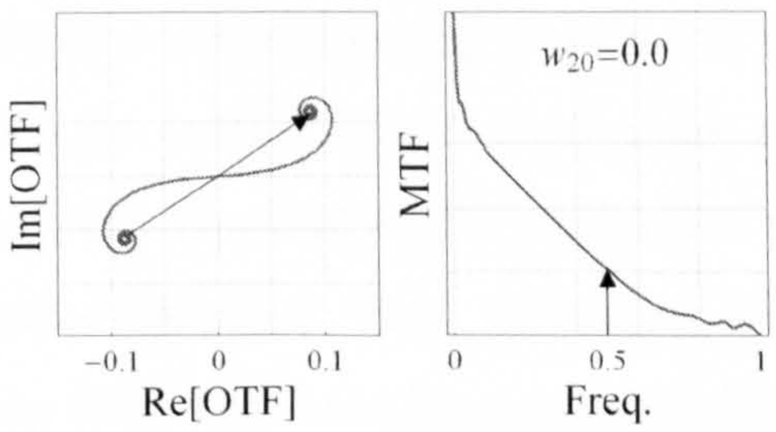

(a) $w_{20} = 0$

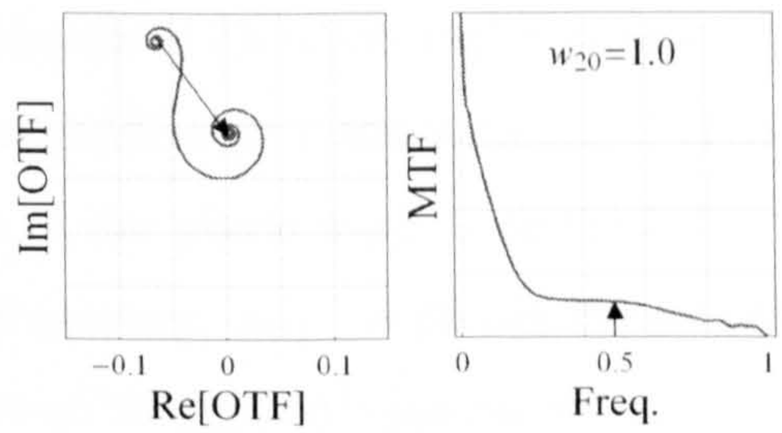

(b) $w_{20} = 2$

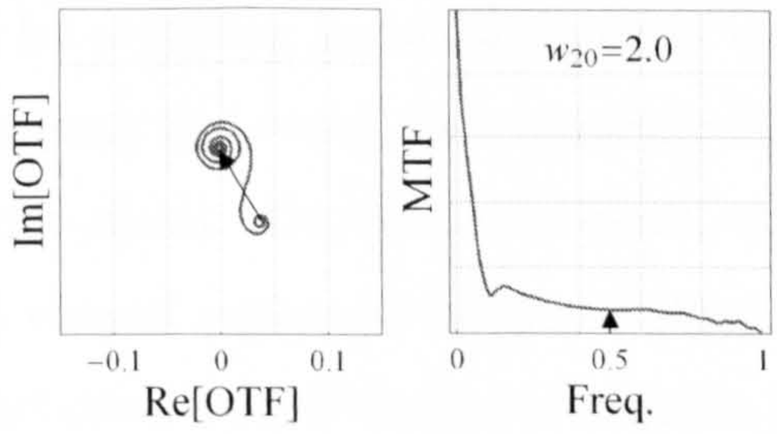

(c) $w_{20} = 4$

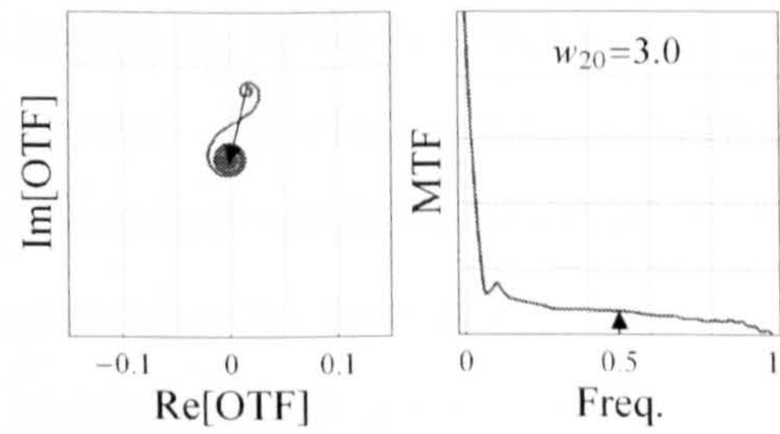

(d) $w_{20} = 6$

Figure 4.13: *Wavefront coding OTFs and MTFs depicted as spirals for a 9th-order phase mask with* $\alpha = 3$ *and* $\nu = 0.5$ *as defocus* w_{20} *increases. All parameters in units of wavelength.*

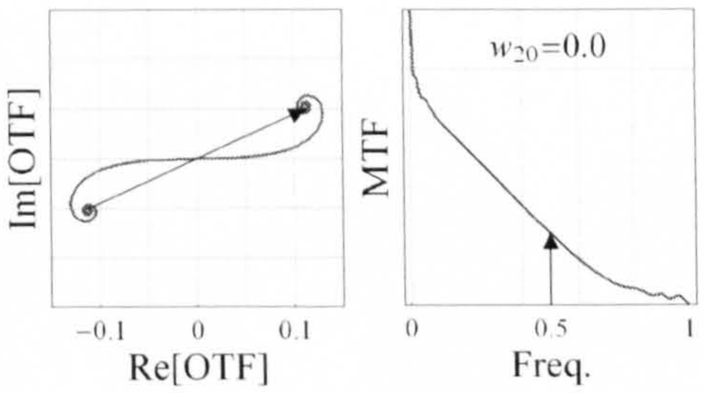

(a) $w_{20} = 0$

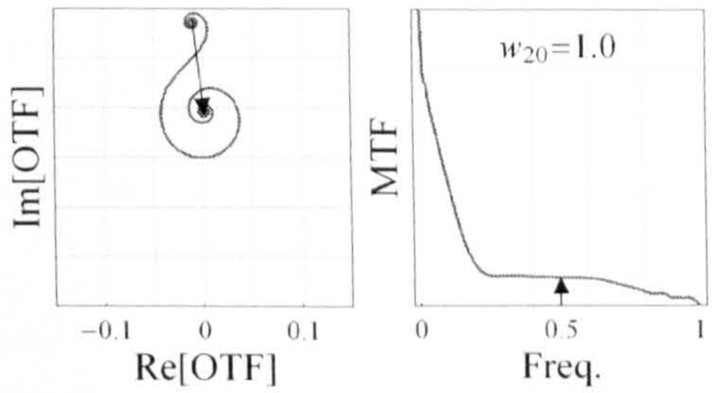

(b) $w_{20} = 2$

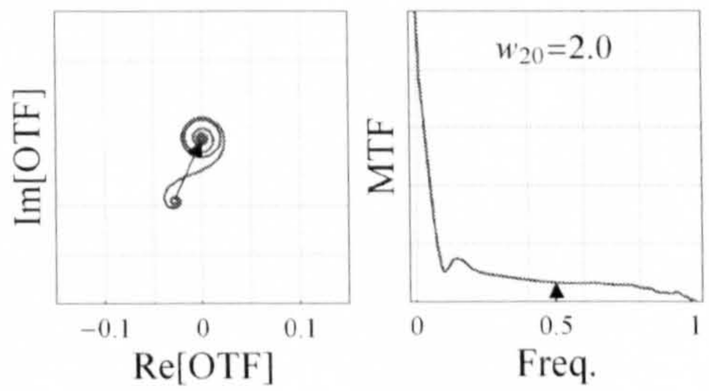

(c) $w_{20} = 4$

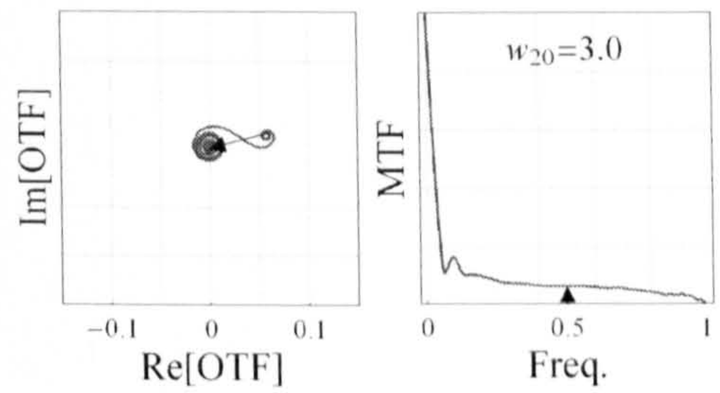

(d) $w_{20} = 6$

Figure 4.14: *Wavefront coding OTFs and MTFs depicted as spirals for a 11th-order phase mask with* $\alpha = 3$ *and* $\nu = 0.5$ *as defocus* w_{20} *increases. All parameters in units of wavelength.*

the variation of the MTFs and hence the PSFs of an optical system due to defocus aberration. By increasing the order of the polynomial for a constant maximum deviation, the central region of the phase mask expands over a larger area and becomes essentially constant whilst the active region of the phase mask is restricted to the edges of the pupil. Thus, for a given spatial frequency, only the phasor contributions of the OTF that have been generated by pairs of Young's slits placed outside the flat central region are modified by the phase mask. These *active* phasors are responsible for providing a certain degree of defocus invariance to the corresponding spatial frequency and reveal their existence by the presence of curled sections at both ends of the spiral. On the other hand, the phasor contributions originating from the flat central region are left unmodified and are subject to the full extent to defocus aberration. In the absence of defocus, these *passive* phasors are coherently added to compose the linear section of the spiral. In some way, by increasing the order of the polynomial it is possible to trade amount of defocus invariance for increased MTF height, which in turn drastically reduces the noise amplification introduced by the digital processing applied to recover ideal performance. This effect can be clearly observed in the figures Fig. 4.11 to Fig. 4.14. As the value of n grows, the in-focus

wavefront coding MTF gradually evolves into the characteristic triangular form of the diffraction-limited MTF, just suppressing the frequency response of the higher spatial frequencies which fall in the active region. In the light of the spiral argument, the increase in the order of the polynomial is followed by a further extension of the linear section of the spiral and hence a reduction of its curled extremes. The quadratic wavefront due to defocus introduces arcs of a circle which will modify the structure of the spiral in two steps:

1. The elongated linear section is rapidly curled into a circular form. This effect brings closer together the extremes of the spiral and explains the sudden drop that occurs in the MTF at low spatial frequencies due to a small amount of defocus. This phenomenon becomes more acute as the order of the polynomial increases.

2. At this point, the MTF height has stabilized across all the spatial frequencies and the tightening and loosening of the coils about the foci become the main mechanism to prevent nulls in the OTF and gain defocus invariance.

The last observation explains why the high-order MTFs become less affected by defocus after a certain defocus threshold have been attained. Additionally, our spiral representation provides a clear explanation of why the modulations in the magnitude of the MTF due to defocus are reduced when n increases: the curled ends of the spiral become smaller and their tightening and loosing hardly make a significant contribution to the height of the MTF.

To conclude this section, a spiral-based comparison of the various phase masks defined by n-order polynomials reveals that the optimal phase mask for defocus invariance is actually given by the original $n = 3$ cubic profile since the curvature of its associated spirals is always linear with defocus (only valid for spatial frequencies along the horizontal or vertical orientations). As a result, no sudden drops in the MTF will take place at low frequencies and all the phase mask power is entirely dedicated to the spiral wrapping and unwrapping process.

Logarithmic phase mask

Since the derivation of the cubic phase mask back in 1995, there have been many mathematical derivations of phase masks that allow extension of the depth of field.

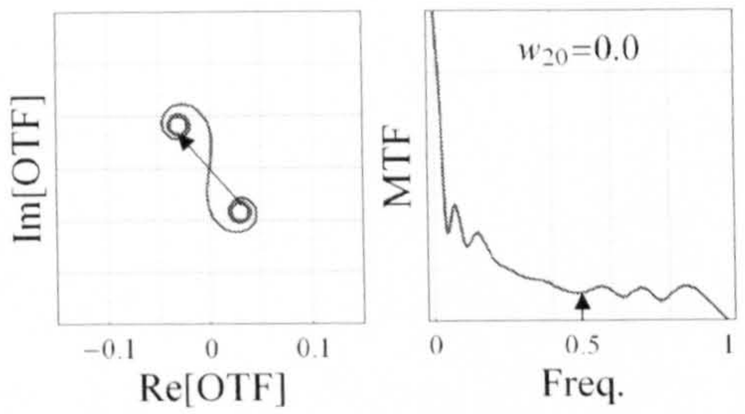

(a) $w_{20} = 0$

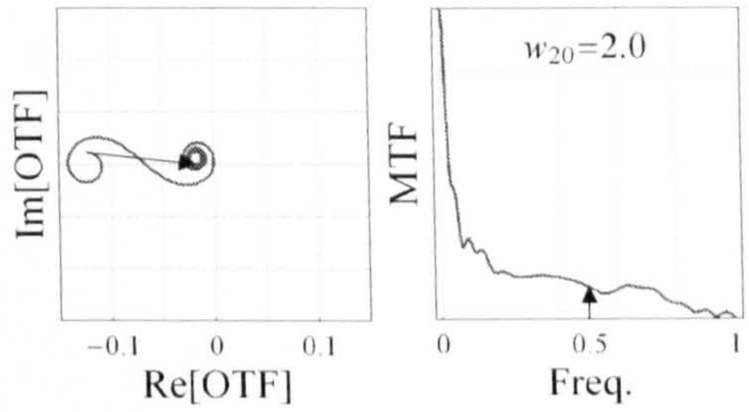

(b) $w_{20} = 2$

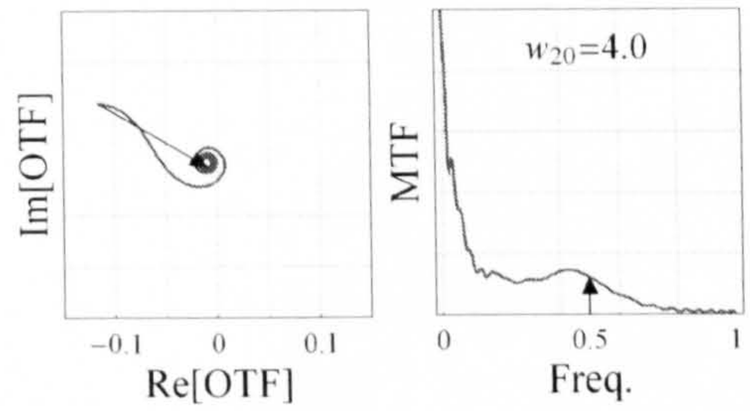

(c) $w_{20} = 4$

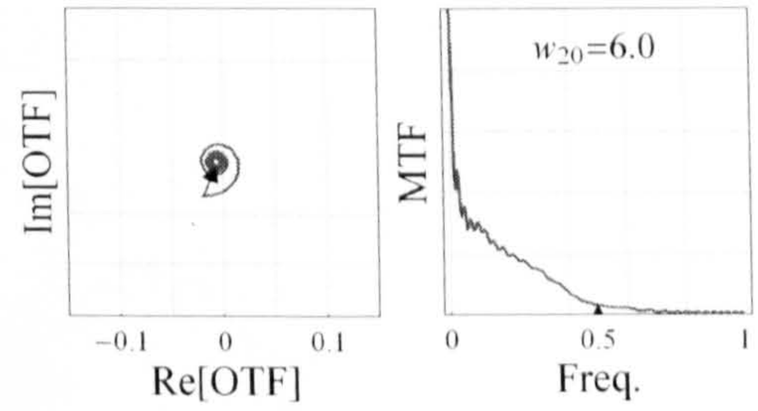

(d) $w_{20} = 6$

Figure 4.15: *Wavefront coding OTFs and MTFs depicted as spirals for a rectangularly separable logarithmic phase mask with an optical path difference equivalent to* $\alpha = 3$ *and* $\nu = 0.5$ *as defocus* w_{20} *increases. All parameters in units of wavelength.*

The search for new rectangularly separable phase profiles has provided with a great opportunity to supply the literature with countless derivations of phase masks that offer little or no improvement over the cubic mask. Moreover, the search has somehow been nourished by the lack of real understanding of the physical principles behind the MTF defocus-invariance process which, eventually, our decomposition of the OTF description has helped to comprehend. One of the main outcomes of our description is that *any* antisymmetric rectangularly separable phase mask improves the tolerance to defocus. Hence, an infinite number of profiles can be synthesized without taking into account optimum-phase considerations. A paradigm of this group of phase mask is the rectangularly separable logarithmic phase mask defined by [32]

$$f(x) = \text{sign}(x)\alpha x^2(\log|x| + \beta) \tag{4-32}$$

where x is the normalised coordinate and α and β control the amount of defocus invariance by means of the wavefront's peak-to-valley height. The phase mask in 2D is simply described by $\phi(x, y) = f(x) + f(y)$.

The performance of this phase mask in terms of MTF invariance due to defocus is illustrated in Fig. 4.15 and a comparison of the geometry of the spirals produced by

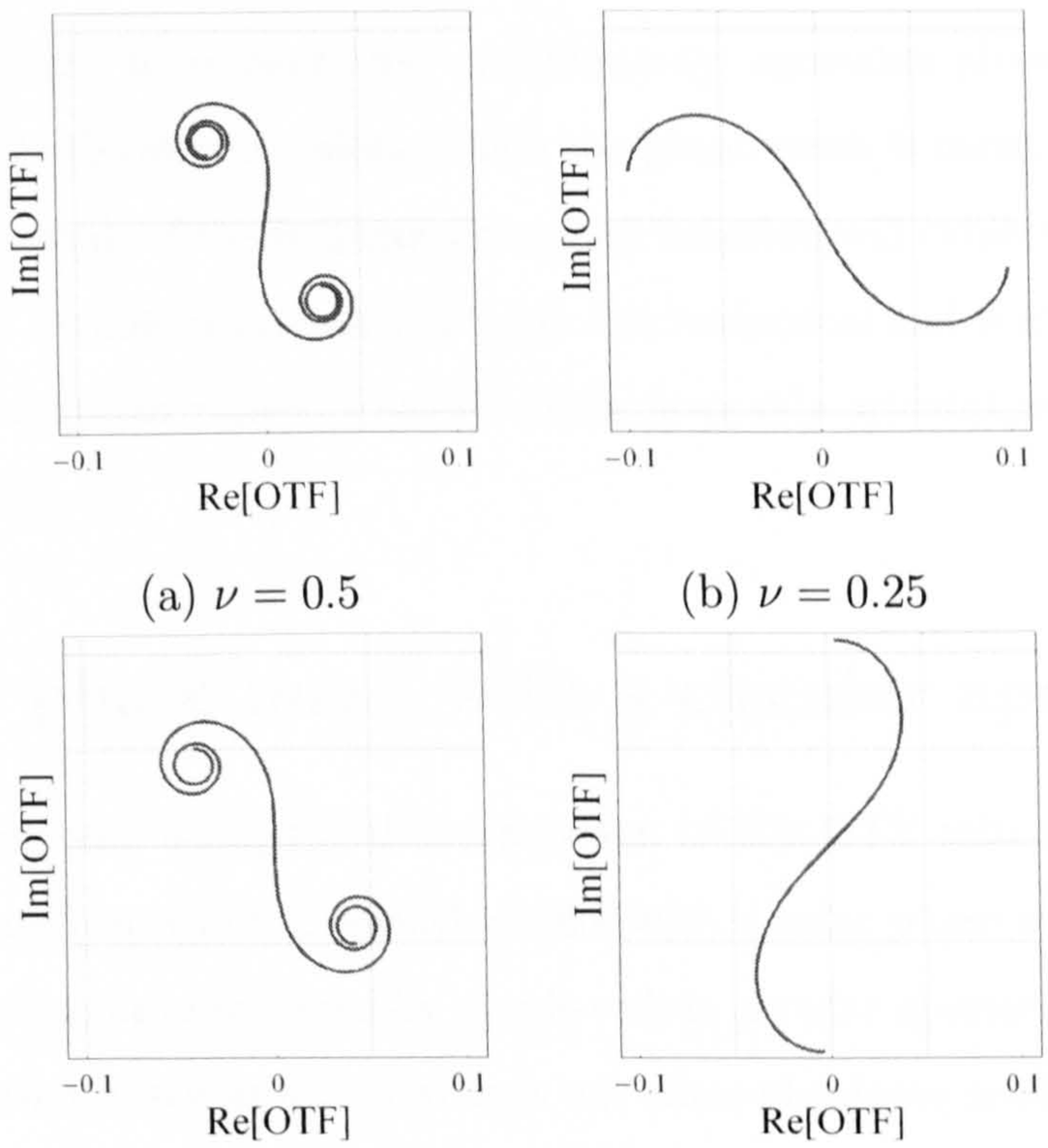

(a) $\nu = 0.5$ (b) $\nu = 0.25$

(c) $\nu = 0.5$ (d) $\nu = 0.25$

Figure 4.16: *Spirals for a rectangularly separable logarithmic phase mask (top) and a cubic phase mask with alpha* $= 3$ *(bottom). Both phase masks introduce the same optical path difference at the edges of the pupil (3 wavelengths).*

the cubic and logarithmic phase masks at spatial frequencies $\nu = 0.5$ and $\nu = 0.25$ is shown in Fig. 4.16. The cubic and logarithmic phase mask were designed to introduce the same wavefront distortion at the horizontal edge of the aperture (3 wavelengths). It is apparent from the figures that defocus-invariant performance between both masks is almost identical. The spiral diagrams are practically identical in both cases (apart from the offset angle of the phase which does not have any effect on the MTF height) and they exhibit the same amount of coiling in each ends of the spirals for the selected spatial frequencies.

It is important to remark that rectangularly separable phase masks always have one axis of antisymmetry along which the phase mask is constant. As a consequence, the magnitude of the frequency response function will exhibit two orthogonal preferred spatial frequency orientations (e.g. the horizontal and vertical axes) where it attains the maximum values. Outside these favorable orientations,the MTF will drop dramatically.

4 Cubic phase mask with a circular aperture

The previous analysis using the decomposition of the OTF into interferograms is applied to a Wavefront Coding optical system with a cubic phase mask in which the square aperture has been replaced by a unit-radius circular aperture. The geometrical complexity that arises in this case does not allow obtaining analytical expression for the OTF nor its amplitude and phase modulations from Eq. (4-3). However, it is possible to obtain an expression for the curvature of the spiral that provides some qualitative analysis. Likewise as for the square aperture, we choose the spatial frequencies along the horizontal or vertical cross section of the OTF ($\xi = 0$ or $\eta = 0$). The curvature of the spiral for a circular aperture is thus given by (see Appendix E for detailed derivation)

$$\kappa(x', \eta) = \frac{4\pi^2 \xi (w_{20} + 3\alpha x')}{\sqrt{|-1 + (|x'| + \xi)^2|}} \tag{4-33}$$

with $-1 + \xi \leq x' \leq 1 - \xi$. This expression shows that the curvature of the spiral for a circular aperture is no longer linear in x', as was shown for a square aperture, and increases to infinity as the length parameter x' approaches the end values at

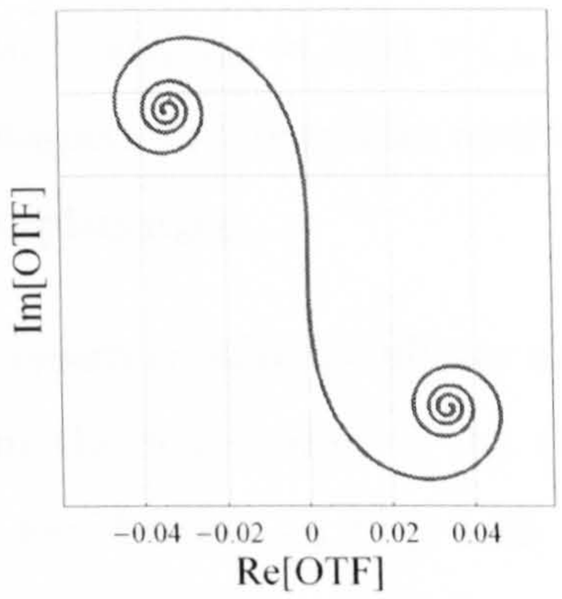

Figure 4.17: *Generalised spiral of a wavefront coding system with circular aperture. Normalised spatial frequency* $\nu = 0.5$ *and* $\alpha = 5$ *(in units of wavelength).*

$x' \to \pm(1-\xi)$ [†].

A generalised spiral for a wavefront coding circular aperture is shown in Fig. 4.17.It is actually this key circumstance that prevents us from obtaining analytical expressions for the mean OTF and modulations as we cannot take $x' \to \pm\infty$. In other words, the stationary phase approximation does not exist for the cubic phase mask with a circular aperture. Nevertheless, the expression for the curvature reveals two qualitative performance aspects:

1. Although the point of inflection ($\kappa = 0$) occurs at the same value of defocus

[†]The curvature of a spiral whose extreme point can be reached (in our case, when $x' = \pm(1-\nu)$) can be finite or infinite at the vertices. The most clear examples are the spirals described by polar equations such as $\rho = \theta^a$, which in parametric coordinates is given by

$$x(t) = t^a \cos(t),\ y(t) = t^a \sin(t),\ t \in [0, \infty).$$

Depending on the coefficient a, these spirals have finite or infinite curvature at the vertices $t = 0$. For these spirals, the curvature is

$$\kappa(t) = \frac{t^2 + a + a^2}{t^{a-1}(t^2 + a^2)\sqrt{t^2 + a^2}},$$

which, when $t \to 0$ is finite if $a \leq 1$ and infinite if $a > 1$. For instance, for $a = 2$, the spiral of equations

$$x(t) = t^2 \cos(t),\ y(t) = t^2 \sin(t)$$

has infinite curvature at the vertices. Note that the extreme point is reached when $t = 0$. What it actually happens for the curvature to be infinity is that the arc length tends to zero faster than the angle (the curvature measures the ratio between the derivatives of the radius and the angle, that's why a circumference has a constant curvature, for the arc length increases as constant $(1/\kappa)$ times the arc).

as for the square aperture $|w_{20}|_{max} = 3\alpha(1-\xi)$, the fall in the MTF is larger than the factor of 2 obtained for the square aperture because the curvature is no longer lineal with displacement.

2. Since the curvature increases rapidly to infinity along the spiral, it is expected that the modulation in the magnitude of the OTF varies less abruptly for increasing defocus, as can be seen in Fig. 4.18. Note that the MTF shows reduced modulation compare to the square aperture.

This suggests that the use of a cubic phase mask with a circular aperture can be implemented at the expenses of reducing the maximum tolerable defocus. On the other hand, a positive aspect has been gained: the magnitude of the modulations as the MTF decreases has become negligible.

5 Circular phase mask with radial symmetry

As we demonstrated in Chapter 3, radially symmetric quartic and logarithmic aspheric phase masks [34, 84, 40, 41], also enable defocus aberration mitigation. The performance in term of the MTF attained by these kinds of phase mask cannot equal that of the antisymmetric, but are suitable under modest amounts of aberrations and some times can be used without digital signal processing. We also showed that the amount of defocus tolerance in rotationally symmetric phase mask defines the practical cutoff frequency. Thus, increased tolerance to defocus will result in a reduced cutoff frequency and therefore large PSFs. In addition, the OTFs of rotationally symmetric phase mask can sometimes contain frequency bands of contrast reversal at low spatial frequencies and are only functional for either positive or negative values of defocus.

The decomposition of the OTF for the quartic phase mask shows clearly the functioning principles and limitations of rotationally symmetric masks, see Fig. 4.19. Similar results are obtained with the logarithmic aspheric mask derived by Chi *et al.* [40, 41] when it is designed to image objects placed somewhere between infinity and a certain minimum distance from the optical system. The quartic phase mask designed in this quoted example gives a practical defocus invariance for values ranging $0 < w_{20} < 3$ and for spatial frequencies, $\nu < 0.5$. As shown in Fig. 4.19, for a selected spatial frequency $\nu = 0.25$, the phasor contributions of the OTF are mapped

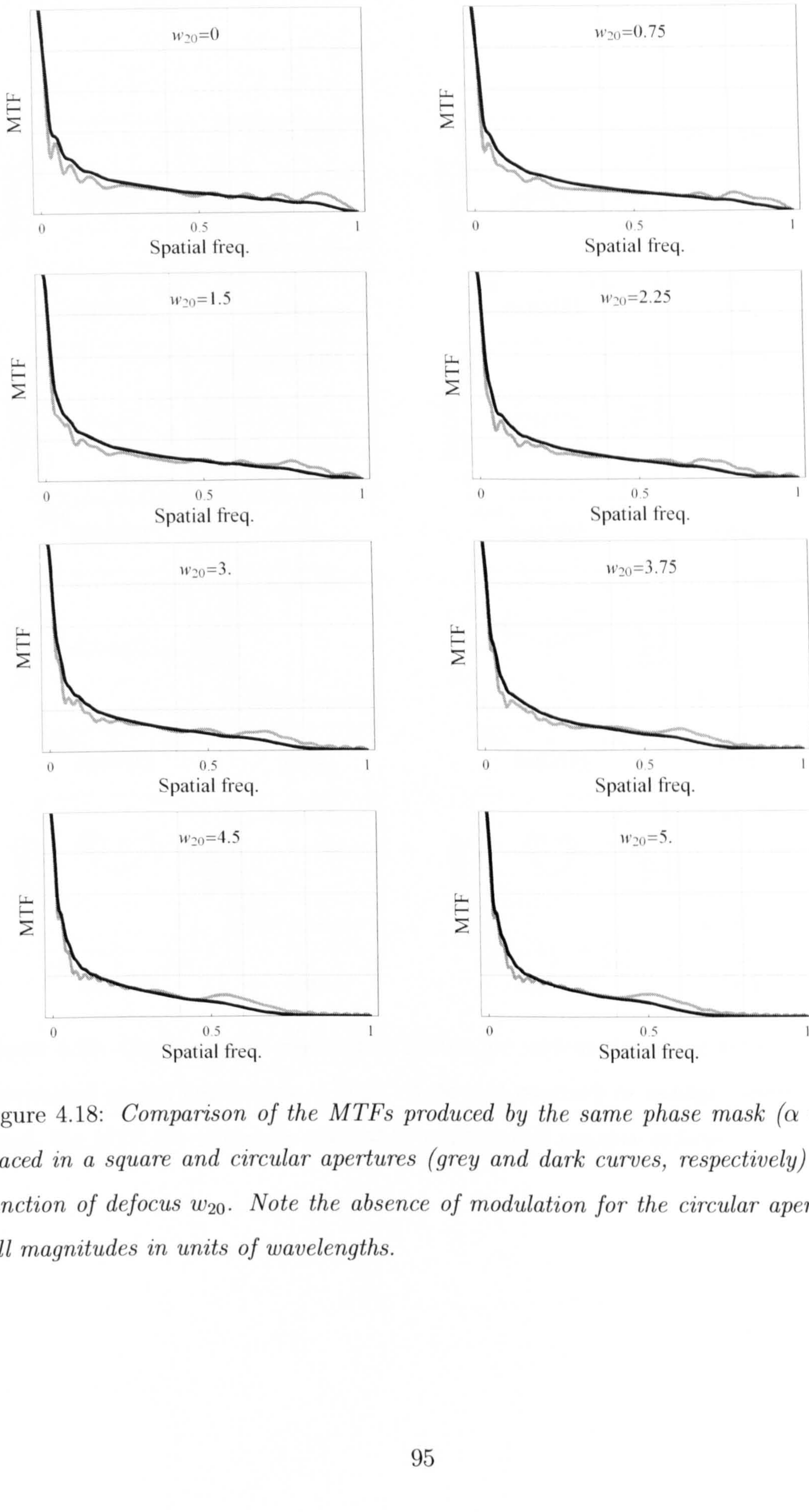

Figure 4.18: *Comparison of the MTFs produced by the same phase mask ($\alpha = 5$) placed in a square and circular apertures (grey and dark curves, respectively) as a function of defocus w_{20}. Note the absence of modulation for the circular aperture. All magnitudes in units of wavelengths.*

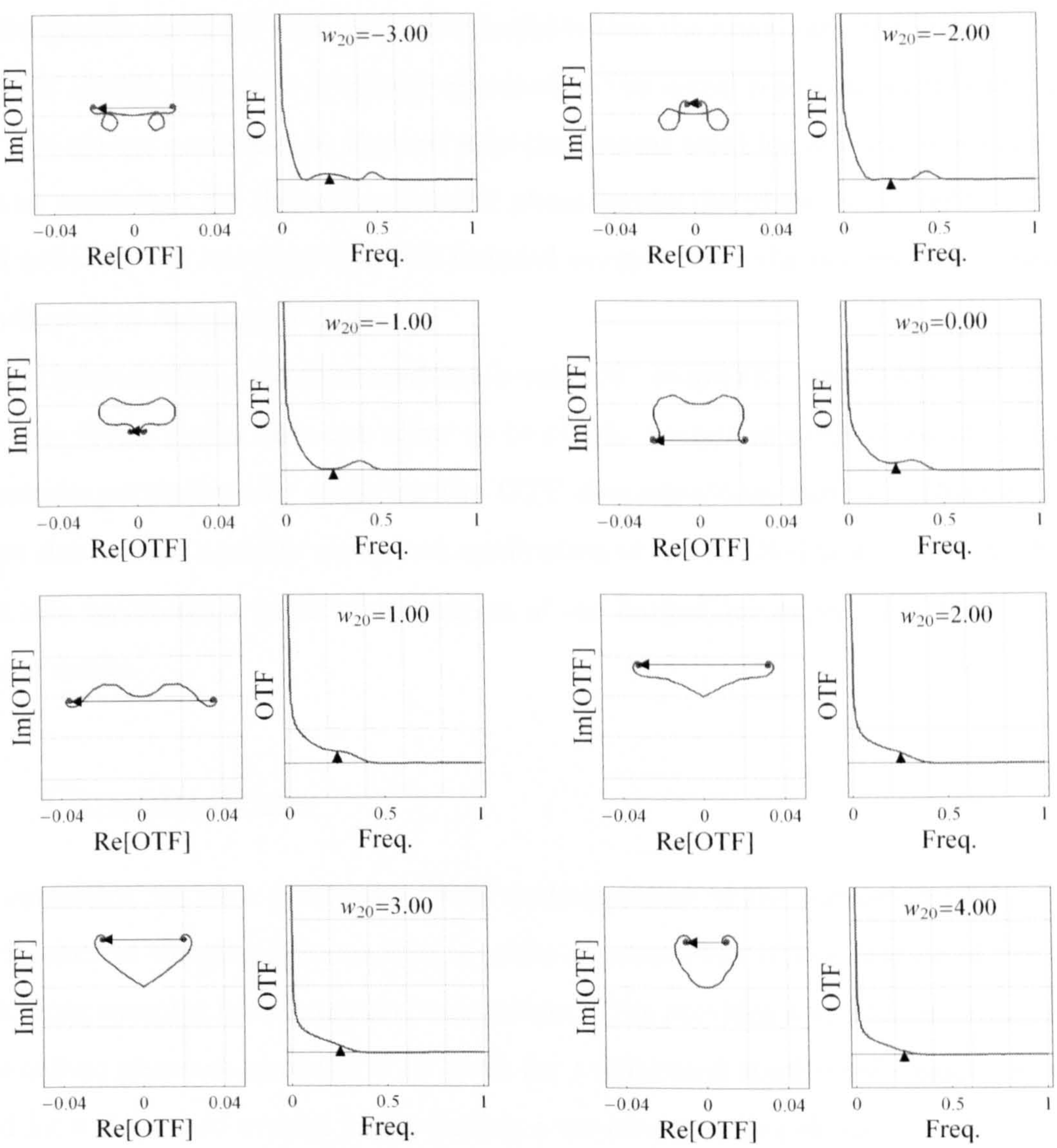

Figure 4.19: *Quartic OTFs depicted as spirals for various degrees of defocus at the normalised spatial frequency $\nu = 0.25$. Note that contrary to antisymmetric phase mask, the MTF are unequally affected by positive and negative defocus.*

into spirals which no longer counteract the effect of defocus by unwrapping one end and wrapping the other, as is the case for antisymmetric masks, but instead by wrapping in opposite direction. This effect results in a diminished range of defocus invariance in comparison to the cubic phase mask and produces OTFs which are not symmetrical under positive and negative values of defocus. An important advantage of the quartic mask (or any symmetric mask) is that the imaginary component of the OTF is always zero; this is clearly observed in the spiral representation where the OTF is always contained in the real axis (horizontal axis) for any value of defocus. Let us recall that for the antisymmetric phase masks the phase varies with defocus and artifacts are introduced in the restored image unless the deconvolution kernel is adjusted to the correct phase.

Unfortunately, the increased mathematical complexity associated with these circular phase masks does not allow us to obtain analytical expressions of the performance parameters by applying the OTF decomposition method. However, we have shown that a purely numerical application of the method is not only clarifying but also facilitates a quick identification of the limitations expected in this type of phase masks.

6 Conclusions

In summary, we have developed a new understanding of the formation of the OTF in incoherent imaging systems that involves a geometrical representation of the contributing complex interferogram components. This provides a lucid quantification of the salient parameters of the OTF both for a defocused traditional imaging system and for a defocused system incorporating a wavefront coding element. Features that are evident in the OTFs of wavefront-coded systems, such as amplitude modulation and the absence of nulls, have been explained analytically for the first time to our knowledge; thus the possibility of simple calibration has been introduced. It is noteworthy that the two-dimensional integral of the ambiguity function, as employed in Ref. [5] to synthesize the phase masks, can be effectively simplified to the equation for a straight line as shown in Eq. (4-17). We have also reported in terms of numerical simulations how the OTF decomposition method allows to explain the important differences and similarities between the radially symmetric and the antisymmetric wavefront coded phase masks.

Future exploitation potential for this OTF decomposition can be directed towards deigning a numerical tool to efficiently synthesize phase masks (perhaps in combinations with amplitude masks) for specific-purpose applications such as conformal optics where aberrations pose sometimes an insurmountable challenge to optical engineers.

Chapter 5

Detector sampling and restoration of wavefront coded images

Summary. In the first part of the chapter, we describe and analyze the performance of wavefront coding when additive white Gaussian noise is present at the detector. Numerical results of the noise amplification and simulated images will be presented. For a practical phase mask strength of $\alpha = 5\lambda$, the loss in signal-to-noise ratio after inverse filtering is 26dB. In the second part, we present a comprehensive study of the effect of detector sampling on wavefront coded systems. Two important results are obtained: aliasing artifacts are reduced by up to 20% in restored images and detector sampling does not compromise the restoration of wavefront coded images with improved depth of field.

1 Introduction

The effect of noise on image quality is an important issue especially when restoration of the detected or coded image is required to display the final image. The blurred image produced by the wavefront coded optics requires post-detection digital processing to remove the distortion and obtain the final image. Unfortunately, the use of the phase mask suppresses the magnitude of the OTF. Additionally, we have shown that antisymmetric phase masks distort the phase of the OTF, thus the digital processing must also be able to correct the phase of the spatial frequency components. Therefore, considerable noise amplification and presence of artifacts in the restored image are expected. In some applications such as thermal imaging, this inconveniences can be particularly relevant.

In the first half of this chapter, we investigate the restoration of images acquired

by an incoherent wavefront coding system and quantify the reduction in signal-to-noise ratio expected in the final images as a function of phase mask strength. We restrict our analysis to linear deconvolution filters due to their simplicity and computational efficiency. Linear filters also provide simple metrics to quantify noise amplification.

The second part of the chapter is dedicated to the study of detector sampling and averaging in the acquisition and restoration of wavefront coded images. To our knowledge, no work in this subject has been reported before. The second part is divided into three sections. In section 1, we summarize the essential information related to the sampling model that exists in the literature and obtain quality metrics that allow us to investigate the effect of sampling in a wavefront coding system and compare it with a traditional sampled imaging system. In section 2, we make use of an established method to depict the performance of a sampled wavefront coding system by representing the system output as the sum of two component images: one, an aliased component responsible for the frequency folding effect of sampling and another for the system low-pass filtering of image acquisition. Finally,the last section provides some conclusions.

2 Restoration of wavefront coded images

2.1 Deconvolution of noiseless image

The material in this section is the first step in studying restoration of wavefront coded images in the absence of noise. This allows us to isolate and evaluate the artifacts that appear in the image without interferences from noise amplification. It is well known that imaging through an incoherent shift-invariant optical system can be approximated as a linear operation given in the spatial domain by,

$$i(x,y) = h(x,y) \otimes o(x,y), \tag{5-1}$$

that is, the image $i(x,y)$ is the convolution of the object or scene $o(x,y)$ with the position-invariant point spread function $h(x,y)$ introduced by the optical system when noise is not considered. Since convolution in the space domain corresponds to a multiplication in the frequency domain, the imaging system can be simply

represented in the Fourier domain:

$$I(\xi,\eta) = H(\xi,\eta)O(\xi,\eta), \tag{5-2}$$

where the terms in capital letters are the Fourier transforms of the corresponding terms in Eq. (5-1). In particular, H is the optical transfer function (OTF) of the imaging system. The simplest approach to decoding or restorating of wavefront coded images is direct inverse filtering, where we compute an estimate of the Fourier transform of the object O' given by

$$O'(\xi,\eta) = I(\xi,\eta)F(\xi,\eta), \tag{5-3}$$

where $F(\xi,\eta)$ is the frequency response of the inverse filter. The inverse filter must be designed so as to restore the coded image to diffraction limited quality, therefore the OTF associated with diffraction-limited performance is included in the frequency response of the filter, more explicitly,

$$F(\xi,\eta) = \frac{H_{dl}(\xi,\eta)}{H_{pm}(\xi,\eta)}, \tag{5-4}$$

where $H_{dl}(\xi,\eta)$ is the in-focus diffraction-limited OTF of the optical system without phase mask, and $H_{pm}(\xi,\eta)$ is the in-focus OTF of the optical system with a phase mask at the aperture stop. Images of a spoke target and a natural scene (the picture of Lena) have been simulated for different values of defocus and a cubic phase mask parameter $\alpha = 5\lambda$, see Fig. 5.1 and Fig 5.2 respectively. In the left column of both figures, the images acquired with the conventional imaging system are displayed. Restored images obtained using the phase mask and post-detection inverse filtering are illustrated in the right column.

Lack of zeros in the in-focus wavefront-coding OTF allows us to apply a single inverse filter across the entire defocus range to decode the effects of the phase mask. Clearly, the restored images appear sharp and demonstrate an increased tolerance to defocus. It can also be observed that diffraction-limited performance is only achieved near the focal plane and, for increasing defocus aberration, artifacts become severe. The images contain ringing or replicas of edges, in particular along the x- and y-axis corresponding to the characteristic arms of the point spread function. Furthermore, the physical extent of the replicas across the image depends on the size of the point spread function and hence in the magnitude of the cubic parameter α. Additionally, the images are translated as a function of defocus following the caustic across the

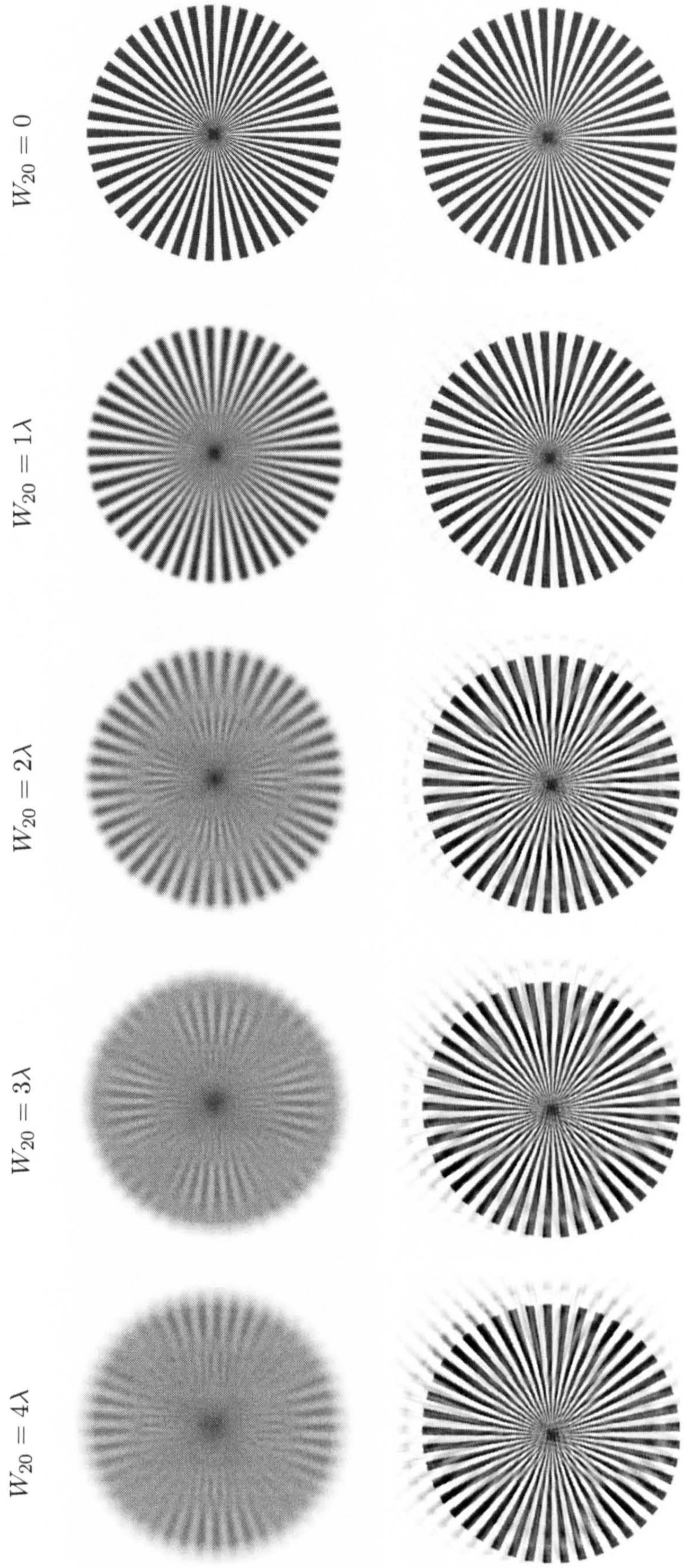

Figure 5.1: *Traditional (left) and restored wavefront coding (right) images of a spoke target for several defocus values and cubic phase mask with* $\alpha = 5\lambda$.

Figure 5.2: *Traditional (left) and restored wavefront coding (right) images of Lena for several defocus values and cubic phase mask with* $\alpha = 5\lambda$.

image focal plane. This effect was discuss in Chapter 2 when we derived the equation of the caustic and implies that objects with different defocus in a 3D scene will suffer transverse displacements in the decoded image according to their relative distance to the object focal plane.

The origin of the restoration artifacts lies in the discrepancy between the phase of the coding OTF and the phase of the decoding inverse filter as was demonstrated in Chapter 4 by means of the spiral representation. The cubic phase mask, while guaranteeing relative defocus invariance of the MTF, does suffer from the problem of having an extremely defocus-dependent phase for the OTF. Surprisingly, this important consideration is hardly mentioned in the literature of wavefront coding and, perhaps for that reason, restoration artifacts often go unnoticed.

Finally, the MTF corresponding to the cubic phase mask employed in the modeling ($\alpha = 5\lambda$) and the magnitude of the frequency response of the inverse filter are shown in Fig. 5.3 and Fig. 5.4 respectively. The filter shows amplification values that range from 1 to 6 in the horizontal (or vertical) frequency axes. We have also included 3D representations of the MTF and magnitude of the inverse filter to emphasize the significant amplification of the frequency components that occurs outside the horizontal and vertical frequency axis. For example, the amplification at diagonal frequencies reaches values of the order of 40. This feature is also evident for any antisymmetric phase mask defined by a rectangularly separable function (placed in a rectangular or circular aperture). Again, the literature devoted to wavefront coding only shows statistics relative to the most favourable horizontal and vertical axis of the MTF, where spatial frequencies are far less suppressed and an eventual noise amplification would be less detrimental.

As we will show, decoding will significantly reduce the signal-to-noise ratio across the image, affecting in particular all frequencies not aligned with main orthogonal frequencies axis. This reduction in the signal-to-noise ratio is one of the main disadvantages of wavefront coding systems and will be comprehensively assessed in the following section.

2.2 Deconvolution in the presence of noise

In real imaging systems, the detected scene is degraded by various sources of noise that arise during image acquisition. In this section we investigate the performance

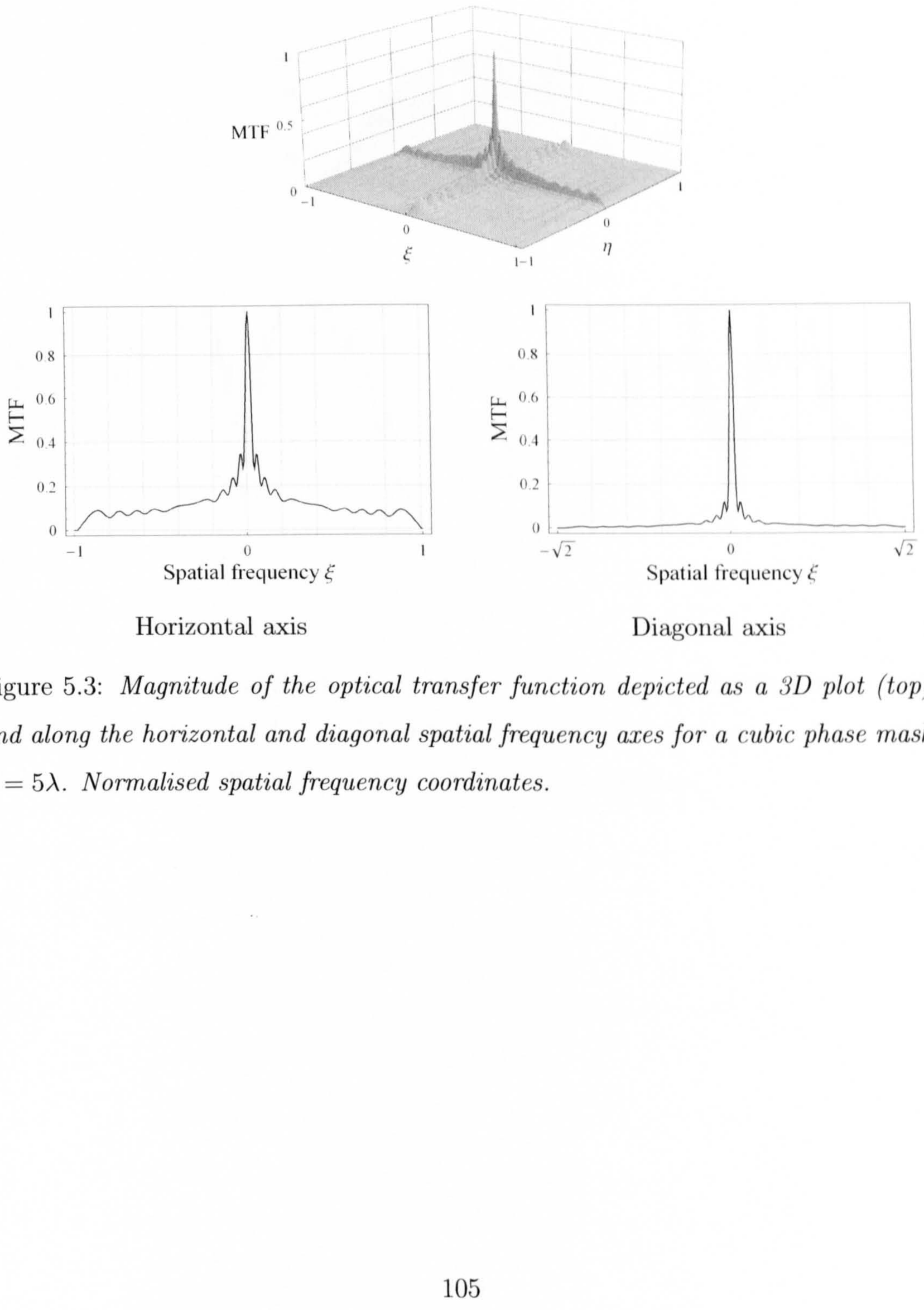

Figure 5.3: *Magnitude of the optical transfer function depicted as a 3D plot (top) and along the horizontal and diagonal spatial frequency axes for a cubic phase mask* $\alpha = 5\lambda$. *Normalised spatial frequency coordinates.*

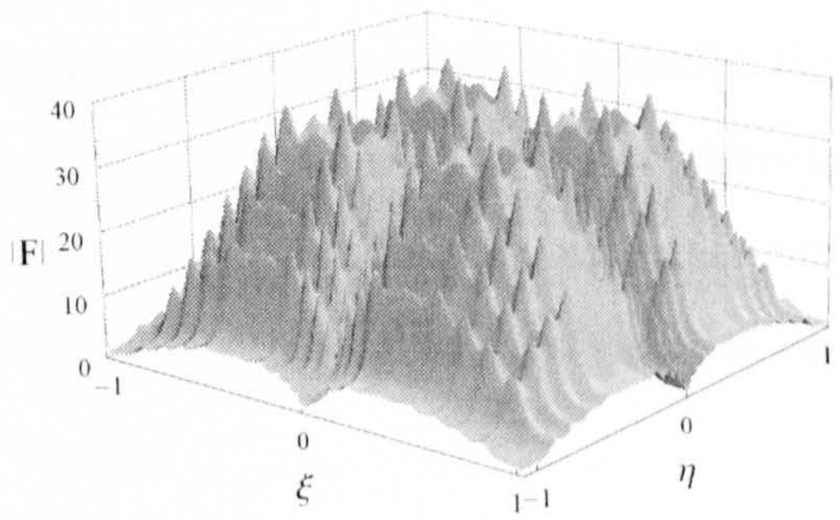

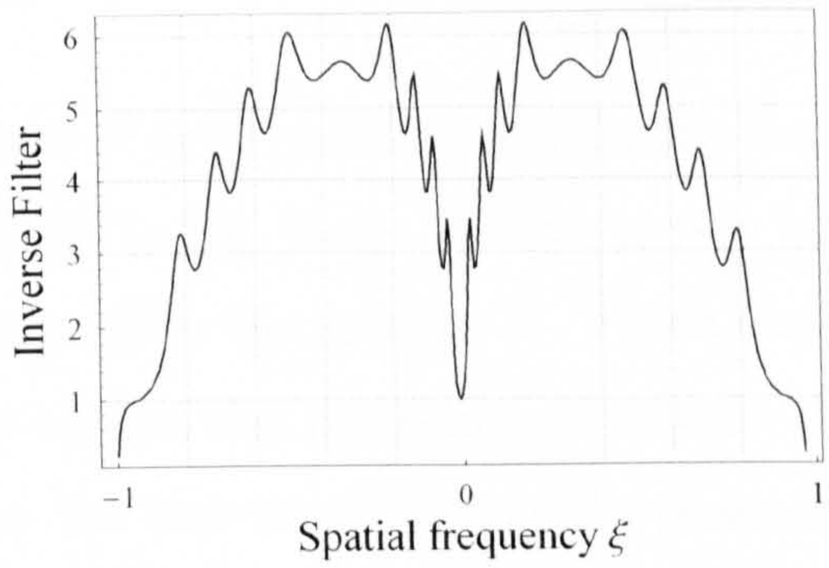

Horizontal axis

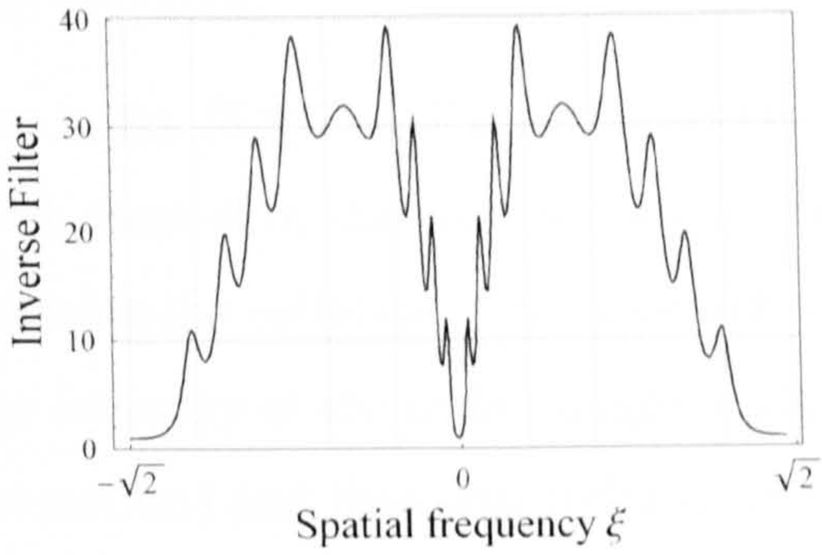

Diagonal axis

Figure 5.4: *Magnitude of the frequency response of the inverse filter depicted as a 3D plot (top) and along the horizontal and diagonal spatial frequency axes for a cubic phase mask* $\alpha = 5\lambda$. *Normalised spatial frequency coordinates.*

of a wavefront coding system when the statistical characteristics of noise are include in the restoration process. Let us recall that the dynamic range of many modern cameras allows for some loss of signal-to-noise ratio without severely damaging the inverse filtering.

In the presence of noise Eq. (5-2) becomes

$$I(\xi,\eta) = H(\xi,\eta)O(\xi,\eta) + N(\xi,\eta), \tag{5-5}$$

where $N(\xi,\eta)$ is the Fourier transform of the additive noise term. Because of its mathematical tractability, additive white Gaussian noise is employed throughout this work. This type of noise is generally used to describe thermal noise, which is produced by the thermal motion of the electrons in the detector and is particularly relevant in infrared imaging [85]. By following the same mathematical approach to noise-free images, the estimate of the Fourier transform of the object O'_n in the presence of noise now given by

$$O'_n(\xi,\eta) = O' + N(\xi,\eta)F(\xi,\eta), \tag{5-6}$$

where O' is the estimate of the noise-free object in Eq. (5-3) and F is the linear filter defined in Eq. (5-4). If noise is very large with respect to the intermediate coded image, then the product $N \cdot F$ can easily dominate the estimate. One approach to get around this problem is to assume that the intensity of the coded image is high (i.e. the blur introduced by the phase mask is modest) and that uncorrelated white Gaussian noise with zero mean and standard deviation σ_n is subsequently added. As we have shown in the previous section, all the components of the high-boost filter F are equal or greater than unity. Each component accounts for the amplification of the signal at a particular frequency and altogether represents the amount of noise amplification associated with the linear filter. It can be shown that the standard deviation of the amplified noise is calculated by multiplying the noise term σ_n by the noise gain G [86], hence

$$\sigma'_{noise} = G \cdot \sigma_{noise}; \tag{5-7}$$

under the noise assumptions stated above the noise gain is given by [78]:

$$G = \sqrt{\frac{1}{MN}\sum_{\xi=0}^{M-1}\sum_{\eta=0}^{N-1}|F(\xi,\eta)|^2} \tag{5-8}$$

where F is the $M \times N$ inverse filter given by Eq. (5-4) with $F(0,0) = 1$ to ensure that the zero spatial frequency components (energy of the image background) are

unchanged by the digital processing. The restored image will have a reduction of signal-to-noise ratio of $1/G$ with respect to the coded image. The reduction of SNR in the restored image is commonly expressed in decibels, thus

$$\mathrm{SNR}_{\mathrm{loss}} = -20 \log_{10} G. \tag{5-9}$$

In Fig. 5.5 we illustrate the SNR in the final image as a function of the wavefront retardation introduced by the cubic phase mask. Additionally, for comparison purposes, the SNR associated with the petal phase mask (described by $\theta(x,y) = \alpha(x^3+y^3)+\beta(x^2y+xy^2)$ [42]) is also shown in Fig.5.6. These graphs allow a straightforward appraisal of the maximum noise penalties expected for a specific phase mask power. As shown in Fig. 5.4, the dependence of the noise amplification on the orientation in the frequency domain requires the calculation of various statistics: the SNR loss was evaluated for the tangential (or sagittal) direction, for the diagonal and finally for the entire frequency space. For a cubic phase mask with $\alpha = 5\lambda$, the SNR is decreased by approximately 27dB along the diagonal and 10dB for the favourable tangential axes; overall, the SNR loss is 23dB. On the other hand, on average the overall SNR loss of the petal mask is 10dB greater than for the cubic (for the same wavefront distortion), though a more uniform noise amplification occurs across the frequency space.

Images of a spoke target acquired by an imaging system with a noisy detector and various degrees of defocus were simulated, see left column in Fig. 5.7. In the right column, the restored images acquired by an analogous imaging system with a cubic phase mask at the aperture stop are displayed. All the images, both coded and conventional, were detected with a SNR of 43dB. When the recorded SNR is of the order of 40 or 50 dB the noise is not visible in the image [87]. Certainly, the restored images achieve an extended defocus tolerance though at a significant cost in the SNR. A simple calculation reveals that the SNR of the restored images is 16dB, which corresponds to a SNR of 26dB. This measurement is in agreement with the value obtained for $\alpha = 5\lambda$ in Fig. 5.5.

Wiener filter

When additive noise dominates many different restoration algorithms can be employed to improve the SNR of these images. The reduction in noise is achieved at the expense of modification the system MTF. Therefore, a tradeoff arises between

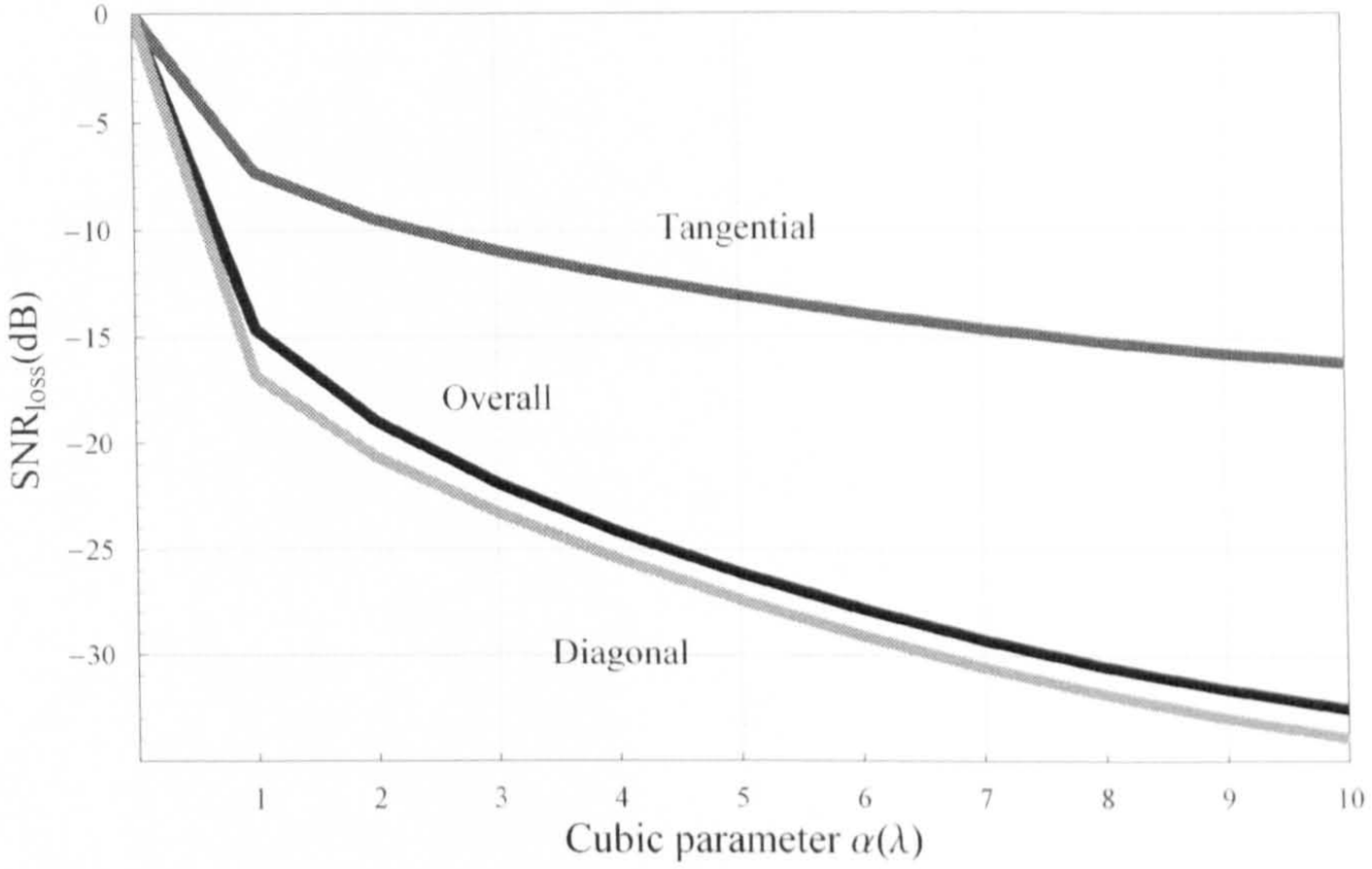

Figure 5.5: *Maximum expected loss in signal-to-noise ratio in the restored image as a function of cubic phase mask parameter α for all frequency components (black curve), horizontal or tangential components (dark gray) and diagonal components (light gray)*

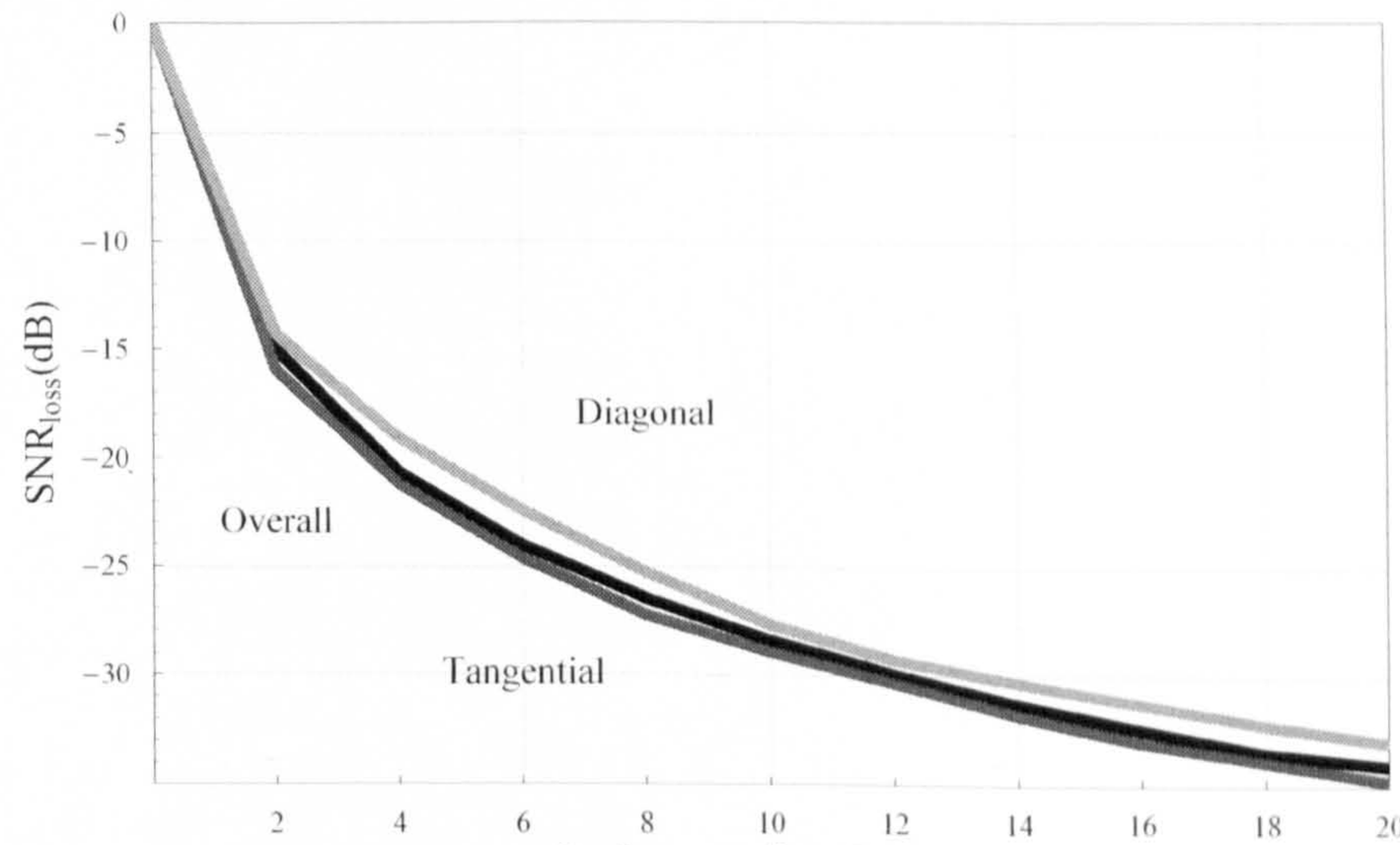

Figure 5.6: *Maximum expected loss in signal-to-noise ratio in the restored image as a function of the peak-to-valley optical path difference introduced by a petal phase mask for all frequency components (black curve), horizontal or tangential components (dark gray) and diagonal components (light gray)*

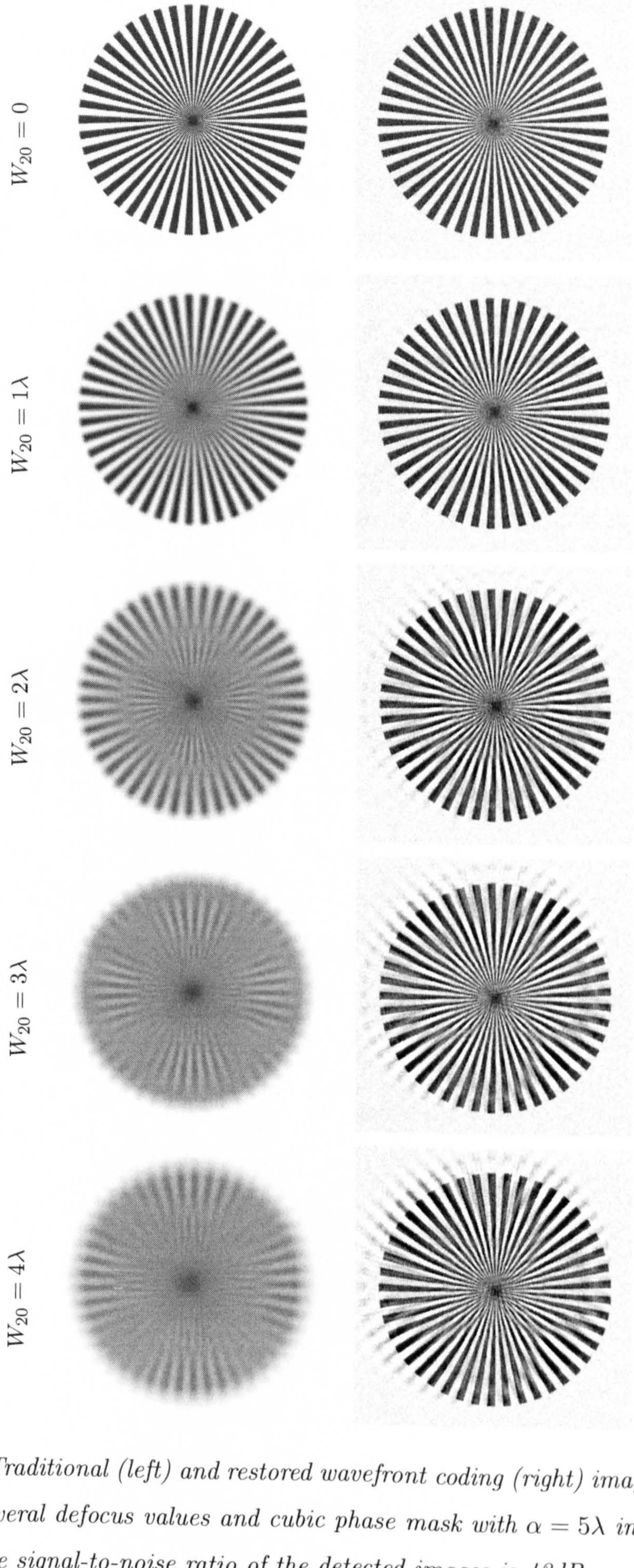

Figure 5.7: *Traditional (left) and restored wavefront coding (right) images of a spoke target for several defocus values and cubic phase mask with $\alpha = 5\lambda$ in the presence of noise. The signal-to-noise ratio of the detected images is 43dB.*

the biased and the noisy reconstruction. Wiener filters have been designed to find the optimum trade-off between noise and signal amplification [88, 89]. Direct linear algorithms such as the Wiener filter have been widely used to restore wavefront coded images because of computational efficiency and its importance for real-time implementation [5, 90]. Nevertheless, investigations with more computationally intensive iterative algorithms and non-linear techniques seeking to improve restoration fidelity have also been carried out [91, 92, 41]. In this thesis, we analyze the performance of the wavefront coding system with a simple Wiener filter under a given SNR estimate. It is beyond the scope of this thesis to research into more involved digital processing algorithms to improve restoration fidelity.

In practice, when dealing with white noise (i.e. the noise power spectrum is a constant), the frequency response of the Wiener filter can be approximated by,

$$F(\xi,\eta) = \frac{1}{H(\xi,\eta)} \frac{|H(\xi,\eta)|^2}{|H(\xi,\eta)|^2 + K}, \tag{5-10}$$

where K is a regularization parameter to adapt the response of the restoration filter and $H(\xi,\eta)$ is given by Eq. (5-4). The constant K is the ratio of the power spectra given by the inverse of the signal-to-noise ratio. The value of K can be chosen interactively to give the best visual results. This is the approach adopted here. Other methods, such as constrained least squares filtering provides improved results and requires only knowledge of the mean and variance of the noise.

When noise is dominant Wiener restoration produces more visually pleasing images as indicated in Fig. 5.8 for different values of SNR: 75 (37dB), 50 (34dB) and 25 (28dB). The inverse-filtered images are also shown for comparison. For low values of recorded SNR, the restored images are noticeable blurrier and less detail along the diagonals because of the characteristic signal suppression introduced by the cubic phase mask in these spatial frequencies. For high values of noise, these frequencies are well within the noise floor and the Wiener filtering washes them out. Similarly, this effect becomes more acute when raising the cubic parameter α, see Fig. 5.9 for $\alpha = 10\lambda$. Because Wiener filter has suppressed the high spatial frequencies responsible for the edge ringing from phase mismatch, the intensity of the artifacts in the restored images is much stronger in the case of noise free detected images than in the presence of noise.

We have demonstrated that one of the crucial limitations of wavefront coding is given by the amplification of noise, however recent and future improvements in

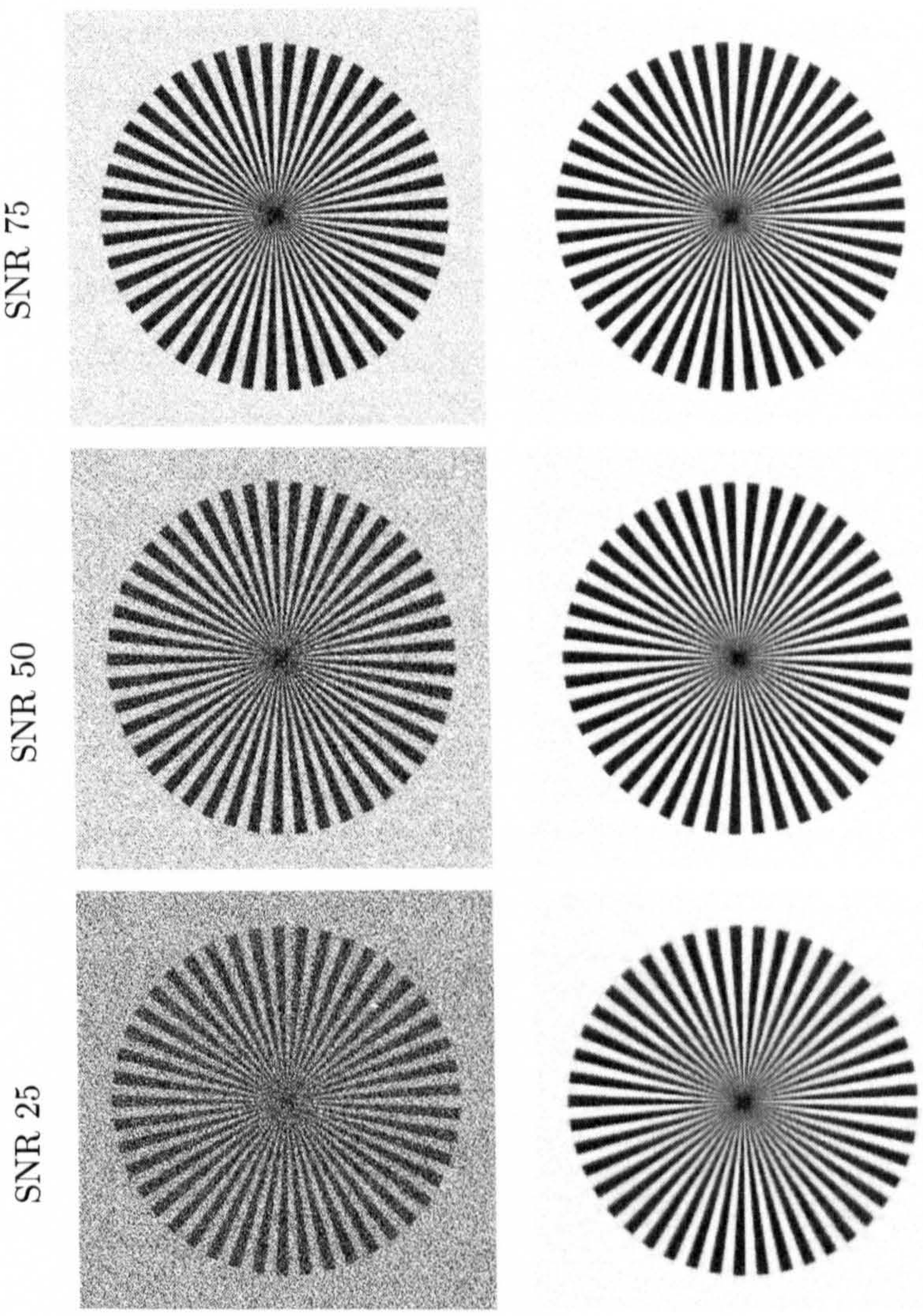

Figure 5.8: *Inverse (left) and Wiener (right) filtered images of an in-focus spoke target for several SNR and cubic phase mask with* $\alpha = 5\lambda$. *Note the degradation along the diagonal directions.*

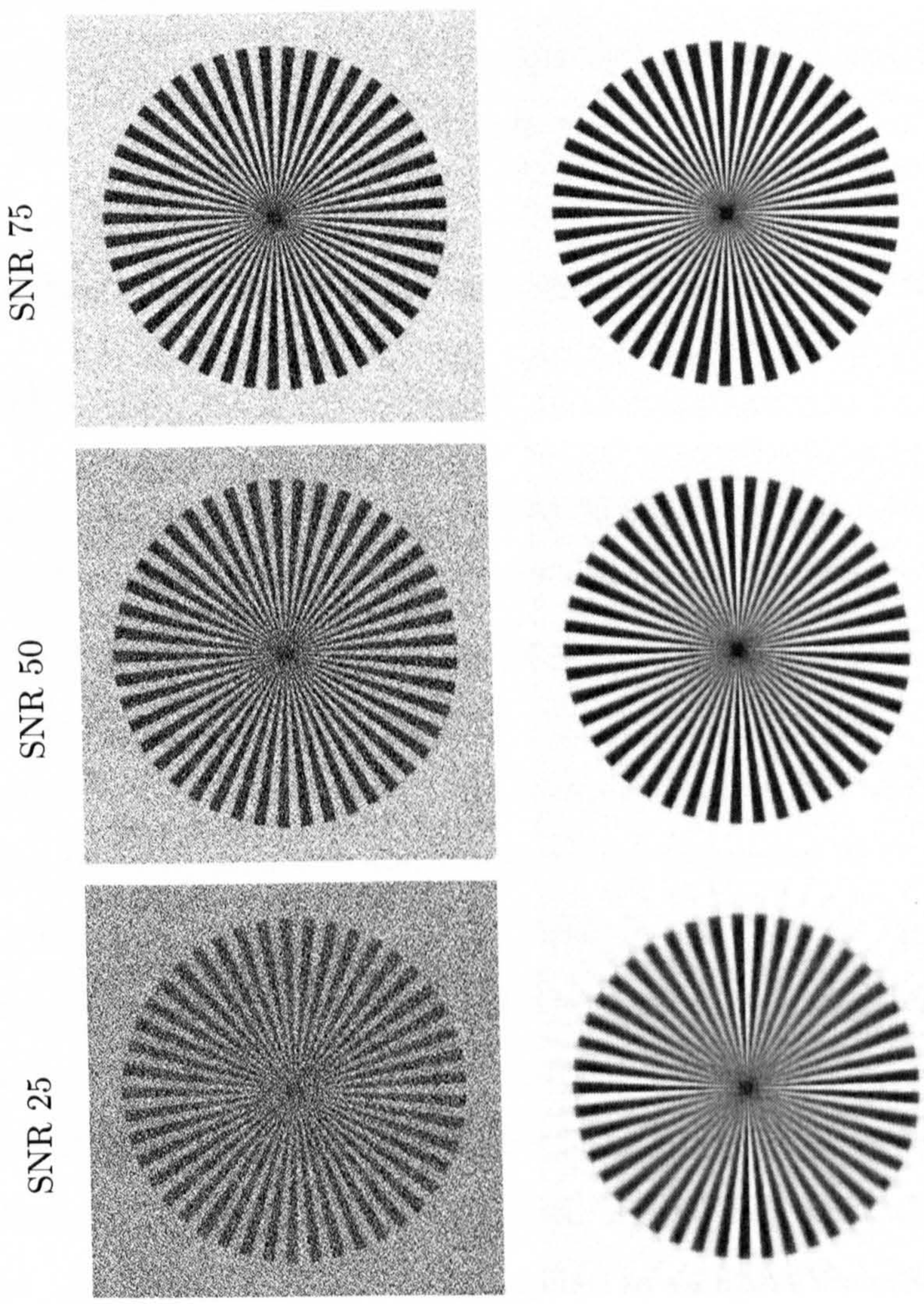

Figure 5.9: *Inverse (left) and Wiener (right) filtered images of an in-focus spoke target for several SNR and cubic phase mask with* $\alpha = 10\lambda$. *Note the degradation along the diagonal directions.*

detector sensitivity are expected to increase the potential and applications of wavefront coding. While the cubic phase mask enables an increased defocus tolerance, there remains a need to design phase masks which retain capacity to reduce defocus aberration while also ensuring less noise amplification. Other designs of rectangularly separable phase mask, such as logarithmic mask, have failed to offer improved noise performance with similar levels of defocus tolerance [32, 93]. Unfortunately, antisymmetric phase masks whilst providing the best defocus aberration mitigation, produce the higher noise amplification figures.

3 Detector sampling and averaging in wavefront coded imaging systems

The sampling and averaging effect that occurs in real detectors has been excluded by considering Nyquist-sampled point spread functions. In the second half of the chapter we investigate for the first time the nature and impact of aliasing in the restoration of wavefront coding systems.

The amount of aliasing in an image is dependent on the spatial frequencies that constitute the original scene and the sampling frequency of the detector. The capacity of a sampled imaging system to produce aliasing can be determined by imaging a scene that is uniform across all frequencies (i.e., a point source). This description is analogous to the traditional optical transfer function approach, where the characterization of the imaging system's response to a point source provides a good indication of the quality of images which can be expected under a variety of environments. A similar understanding applies to sampled imaging systems. We cannot know how each detail in the scene will be corrupted by the sampling process until the exact scene and its relative position to the detector are specified. Nevertheless, the tendency of the imager to corrupt scene details can be characterised. This is the approach adopted here too whereby the transfer function of a sampled wavefront coding system will be calculated.

Fourier transform theory has been used to describe and quantify sampling effects due to aliasing in a wavefront coding system. In particular, we have followed two excellent texts, Vollmerhausen *et al.*[94] and Boreman [95], as they provide a comprehensive analysis of Fourier theory applied to sampled aliased imaging sys-

tems. Additionally, for the correct and comprehensive simulation of sampled images we have followed a continuous/discrete model-based simulation by Park and Rahman [96] which characterises aliasing as an additive scene dependent noise and provides simple and practical metrics.

3.1 Transfer function of a sampled wavefront coded imaging system

The frequency response function of a sampled wavefront-coded imaging system can be derived by characterizing the system response to a point source. The method is very similar to that employed with continuous imaging systems, however the results are different because the sampled system is not *isoplanatic* or shift-invariant: the point spread function and its Fourier transform change with the relative positions of the point object to the sampling locations.

To simplify the mathematics, we restrict the study to a one-dimensional sampling process but the concept can be generalised to two dimensions. For most practical sampled imaging systems, the complete image formation of the point source by an array of discrete detectors may be separated into two components:

1. Pre-sample OTF, which is the product of the optics OTF $H_{opt}(\xi)$ and detector footprint OTF $H_{pix}(\xi)$, where ξ is the spatial frequency. Due to the finite extent of the detectors, the point spread function of the input optics is averaged over the pixel areas [97]; The OTF contribution of image averaging over pixels of finite dimension is well known. For a 1-D square pixel, the pixel OTF is a sinc function

$$H_{pix}(\xi) = \mathrm{sinc}(p\xi) = \frac{\sin(p\xi\pi)}{p\xi\pi}, \tag{5-11}$$

where p the full width of the pixel.

2. The sampling of this image. The sampling function can be represented by a Dirac comb function in which the distance between successive samples is given by X

$$\text{Ш}(x) = \sum_{n=-\infty}^{\infty} \delta(x - Xn). \tag{5-12}$$

The comb function is its own Fourier transform, where the spacing between

single pulses in the frequency domain is given by $f = 1/X$, thus

$$\text{Ш}(\xi) = \sum_{n=-\infty}^{\infty} \delta(\xi - n/X). \tag{5-13}$$

We assume that these three components H_{opt}, H_{pix} and Ш multiply in the frequency domain to yield an aggregate response function for the imaging and sampling process, which yields [94, 98]

$$R(\xi, \phi) = H_{pix}(\xi) \sum_{n=-\infty}^{\infty} H_{opt}(\xi - nf) \exp(in\phi), \tag{5-14}$$

where $H_{pix}(\xi)$ is the spatial frequency transfer function associated with a single pixel (footprint OTF) given in Eq. (5-11). The sampling process replicates $H_{opt}(\xi)$ at each integer n multiple of the sampling frequency $f = 1/X$. Each replicated spectrum varies in phase from the adjacent spectrum by the sample phase increment ϕ. Due to this phase variation, the sum in Eq. (5-14) is different for each value of ϕ and therefore $R(\xi, \phi)$ will depend on the relative position of the pre-sample point spread function and the sample points. Finally, the detected spectrum is the product of the replicated spectra multiplied by the footprint OTF $H_{pix}(\xi)$ centred at the spatial frequency origin.

From this mathematical description of the image-sampling process we can clearly identify two distinct parts in the sampled response function $R(\xi, \phi)$: a transfer function and an aliasing-related parameter, termed *spurious response* [99]. The transfer function or *baseband spectrum* corresponds to $n = 0$ and is independent on the sample spacing. The term *aliasing* refers to the overlap in the frequency domain between the spurious response and the baseband spectrum. The spurious response is the Fourier transform of the sampling artifacts and is found by multiplying the pixel OTF by all the replicates spectra except the one located at the origin ($n \neq 0$). In contrast to the baseband spectrum, the spurious response depends on both sample spacing X and phase ϕ. If the sampling frequency is small as normally occurs in thermal imagers, the spurious response term overlaps the baseband and becomes difficult to filter out. On the other hand, if the sampling frequency is high, the spurious response is located far from the baseband and in most situations it is simply filtered out by the pixel OTF. The spurious location-dependent phase dependence is responsible for the change in the intensity pattern of the spread function as the detector array is moved across the point source.

In this chapter, we consider a case study of a thermal imager with a cubic phase mask in the aperture stop and quantify the impact of sampling on the overall OTF performance, and in particular, the effect of aliasing on the ability of the wavefront coding system to mitigate defocus aberration. In this assessment, no post-detection display transfer functions such as the MTFs from the observer's eye and display monitor (cathode ray tube spot, LCD, etc.) are included. The same sampling model is performed on the thermal imager without the cubic phase mask and the results obtained from both schemes before and after post-detection digital signal processing are subsequently compared.

The thermal imager consists of a representative F/1.12 germanium optical system, 75 mm focal length and the primary operating wavelength is 10.5μm. The pixel size is $p = 25\mu$m and we assume a fill factor of 100% (i.e. sample spacing $X = p$). Consequently, the cutoff spatial frequency ($f_{cut} = 1/\lambda F/\#$) is 85 cycles/mm and the Nyquist frequency ($f_{nyq} = 1/2X$) of the detector is 20 cycles/mm. Thus, the cutoff frequency of the optics is about twice the sample frequency and the replicas centred on frequencies above the latter are practically filtered out by the pixel OTF since it becomes increasingly small at high frequencies. The amplitude of the optical transfer function, replicated spectra and pixel MTF of the thermal imager without and with a cubic phase mask are shown in Fig. 5.10(a) and (b) respectively. In this system, only the replicas with $-3 \leq n \leq +3$ in Eq. (5-14) contribute with sampling artifacts. Note that only the magnitudes are displayed in the figures but the phase must not be neglected when calculating the spurious response. The pictures in Fig. 5.10 show that due to the sub-Nyquist sampling of the IR detector the replicas are very close together and overlap severely, causing significant corruption of the information in the baseband. Furthermore, notice that the replicas $\exp(-i2\phi)$ and $\exp(-i\phi)$ in the negative frequency axis spread over the positive axis and *vice-versa*. A first examination of the suppressed wavefront-coded replicas in Fig. 5.10 may suggest that the presence of aliasing be greatly reduced with respect to the conventional imaging system. However, the wavefront coding transfer function still requires post-detection digital processing to restore the intermediate image to that of the sampled diffraction-limited system, thus increasing the area of overlap between the replicas and baseband spectra and therefore intensifying the aliased artifacts. Another important aspect to take into consideration in the wavefront coding system is that the antisymmetry of the phase mask function produces complex OTF adding

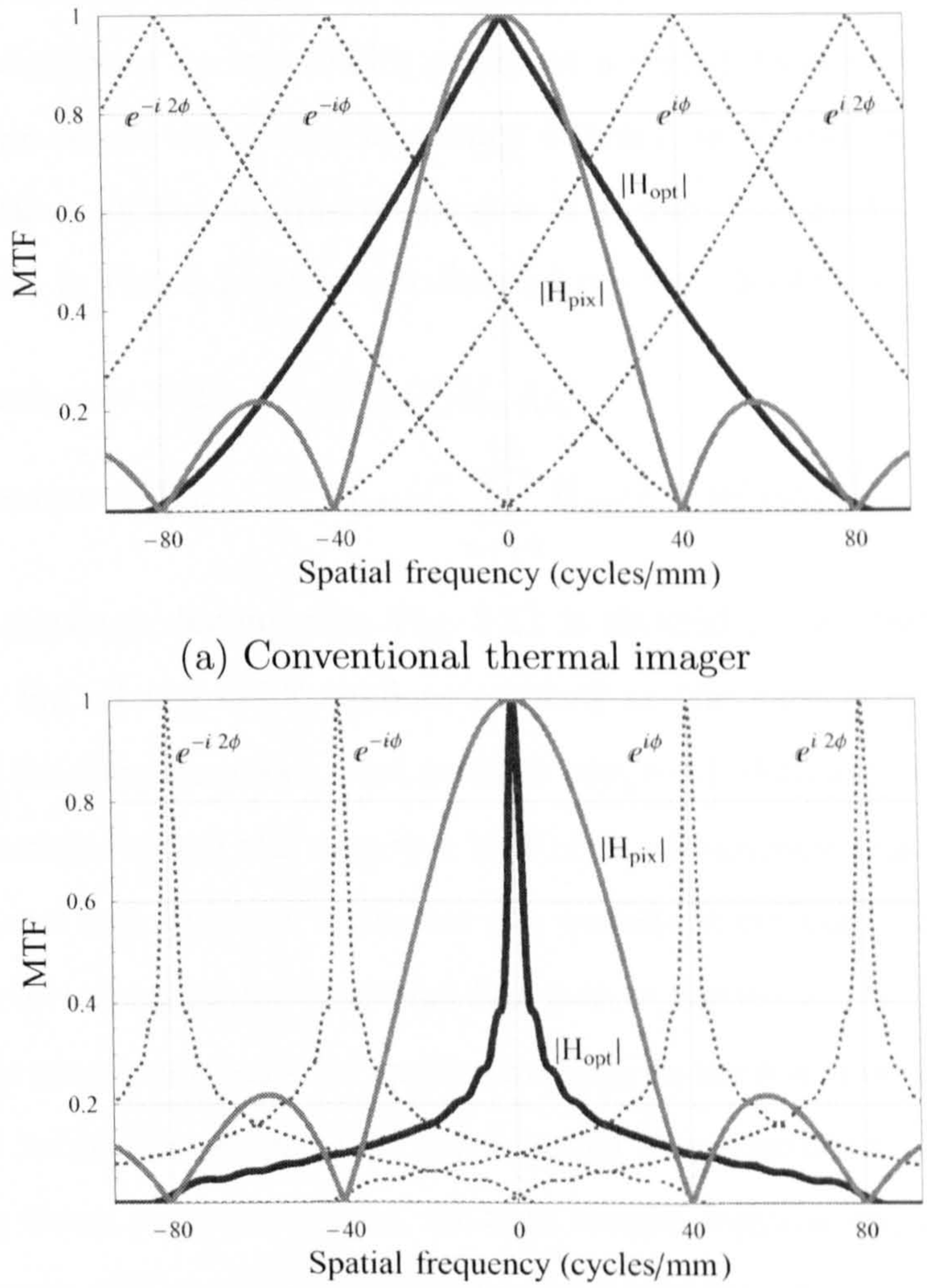

(a) Conventional thermal imager

(b) Thermal imager with cubic phase mask $\alpha = 5\lambda$

Figure 5.10: *Optics MTF (solid black curve), replicated spectra (dotted) and pixel MTF (solid gray curve) of a conventional thermal imager (a) and with a cubic phase mask $\alpha = 5\lambda$ prior to post-detection processing (b). Sampling causes the power spectrum to be periodic at every integer multiple of the sampling frequency of 40 cycles/mm.*

an extra frequency-dependent phase factor to the replicated spectra. Consequently, the amplitude of the entire response function $R(\xi, \phi)$ at any one frequency will not simply be the sum of the amplitudes of the individual terms but the complex summation of all terms, and the result will depend not only on sample phase ϕ but also on the amount of wavefront coding distortion α. As a result, the complex summation of wavefront coding OTFs produces a highly modulated and intricate spurious response across the spatial frequency domain, as illustrated in Fig. 5.11 for two arbitrary values of the sample phase $\phi = 0$ and $\phi = \pi/2$. The baseband and spurious response in Fig. 5.11 were calculated from Eq. (5-14), which yields

$$\begin{aligned} \text{Baseband: } B(\xi) &= H_{pix}(\xi) H_{opt}(\xi), \qquad (5\text{-}15) \\ \text{Spurious response: } S(\xi, \phi) &= H_{pix}(\xi) \sum_{n=-3}^{+3} H_{opt}(\xi - nf) \exp(in\phi), \text{ with } n \neq 0. \end{aligned}$$

The spurious response displayed in Fig. 5.11 is divided in two parts: one labeled with $\exp(+i\phi)$ for all the OTF replicas centred at the sample frequency on the positive half of the frequency axis, and another one, $\exp(-i\phi)$, for the corresponding OTF replicas centred along the negative half of the frequency axis. Let us remark that the baseband and spurious terms for the wavefront coding system in Fig. 5.11 relate to the detected coded point spread function at the sensor, and therefore post-detection image processing must be applied in order to draw a valid comparison with the traditional infrared system. Yet, some image characteristics can be explained from analyzing these response curves. At high spatial frequencies, greater than the Nyquist frequency (20 cycle/mm), the spurious response accounts for producing sharp edges and blocky pixels in the image. In the traditional system, the high frequency content of the spurious response is very large, meaning that the sharp pixel edges become much more visible than in the wavefront coded image prior to restoration, see Fig. 5.12. In the latter, the combination of the cubic phase mask OTF and pixel OTF lowers the transfer and spurious response attenuating the high frequency content and adding further blur to the image. When signal processing is applied on the coded sampled image to compensate for the effects of the cubic mask, the filtering magnifies simultaneously the system transfer and spurious response increasing the aliasing-related artifacts in the restored image. The absence of zeros in the cubic MTF allows the use of an inverse filter to recover a transfer function

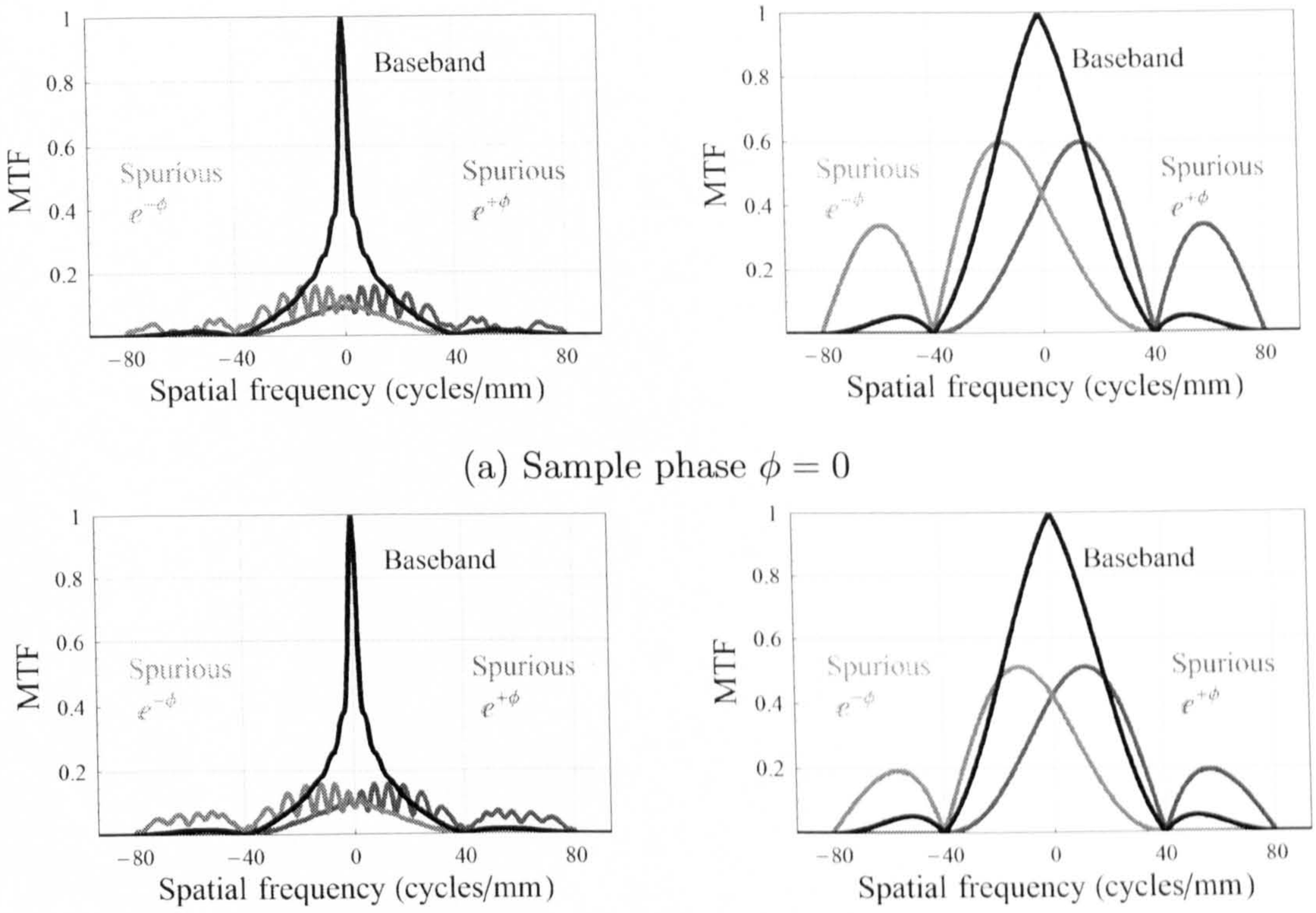

(a) Sample phase $\phi = 0$

(b) Sample phase $\phi = \pi/2$

Figure 5.11: *Magnitude of the transfer function (optics OTF and pixel OTF) and spurious response (replicated spectra and pixel OTF centred at the frequency origin) as a function of phase sampling for a wavefront coding system with a cubic phase mask* $\alpha = 5\lambda$ *(left) and traditional system (right) for two values of the sample phase. No post-detection digital processing has been applied.*

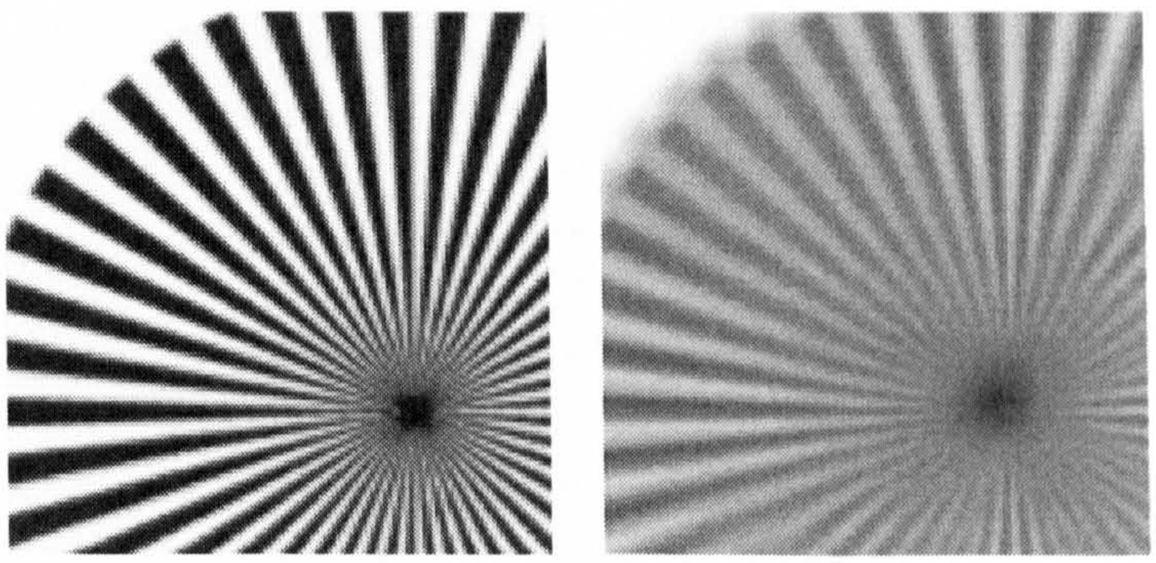

Traditional system Wavefront coding system

Figure 5.12: *Detected image with a sampled traditional optical system (left) and with a sampled wavefront coding system (right). Clearly, the significantly higher spurious response content of the traditional system compared to the wavefront coding system accentuates the blocky nature of the pixels.*

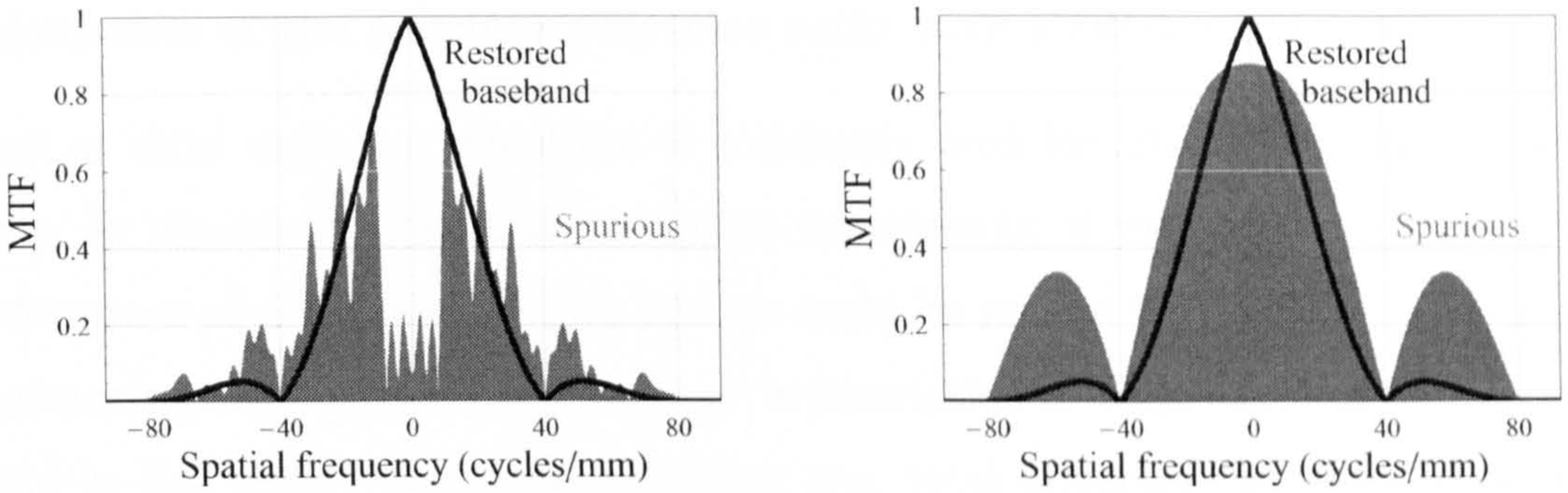

Figure 5.13: *Magnitude of the transfer function (optics OTF and pixel OTF) and spurious response (replicated spectra and pixel OTF centred at the frequency origin) for the IR wavefront coding system with a cubic phase mask $\alpha = 5\lambda$ after inverse filtering (left) and traditional IR system (right), for phase $\phi = 0$.*

identical to the sampled MTF of the traditional system, thus

$$\text{Restored baseband: } B'(\xi) = \frac{H_{dif}(\xi)}{H_{opt}(\xi)} B(\xi), \tag{5-16}$$

$$\text{Restored spurious response: } S'(\xi, \phi) = \frac{H_{dif}(\xi)}{H_{opt}(\xi)} S(\xi, \phi),$$

where H_{dif}/H_{opt} is centred at the spatial frequency origin and applied only for $-f_{cut} \leq \xi \leq f_{cut}$. With the aim of providing a clear analysis of aliasing effects no noise is considered in the model. Both restored baseband and spurious response of the wavefront coding system are shown in Fig. 5.11 for $\phi = 0$. Clearly, in spite of obtaining an identical baseband to that of the traditional system, the restored spurious response appears to have a significantly reduced impact upon the baseband spectrum, especially in the low spatial frequency region. As mentioned before, this is due to the highly variable phase introduced by the cubic phase mask across the spatial frequencies. Furthermore, any other antisymmetric phase mask, such as the petal-like phase mask, will produce the same effect: it is the rapid phase changes from adjacent spatial frequencies so characteristic of antisymmetric wavefronts that produce low spurious responses. One final aspect worth remarking is that the high-boost inverse filtering also modifies the phase of the net spurious response at any given spatial frequency. Hence, aliasing artifacts may also become present in areas of the restored image different from those of the conventionally acquired image.

Calculation of the spurious response ratio with a cubic phase mask

A set of three aggregate quantities is commonly used for aliasing evaluation purposes. In the course of several perception experiments, it was discovered that the performance of a sampled imaging system could be related to a ratio of integrated spurious response to baseband response. A description of these experiments can be found in Ref. [100]. The three quantities are: total integrated spurious response ratio (SRR), in-band spurious response ratio (SRR_{ib}) and out of band spurious response ratio (SRR_{ob}) [101]:

$$SRR(\phi) = \frac{\int_{-\infty}^{\infty} |S'(\xi,\phi)| \mathrm{d}\xi}{\int_{-\infty}^{\infty} |B(\xi)| \mathrm{d}\xi}, \tag{5-17}$$

$$SRR_{ib}(\phi) = \frac{\int_{-f_{nyq}}^{f_{nyq}} |S'(\xi,\phi)| \mathrm{d}\xi}{\int_{-\infty}^{\infty} |B(\xi)| \mathrm{d}\xi}, \tag{5-18}$$

$$SRR_{ob}(\phi) = SRR(\phi) - SRR_{ib}(\phi). \tag{5-19}$$

The area of the total spurious-response magnitude normalised to the baseband transfer function area is taken as a measure of image artifact content in the imaging process. SRR_{ib} takes into account the in-band aliasing, and it is defined as the area underlying the part of the spurious response falling inside the Nyquist frequency range normalised by the area of the entire baseband response. Typically, in-band aliasing accounts for degrading recognition performance to a large extent in a sampled imager *. The total and in-band spurious-response ratio (SRR) were calculated for the traditional and restored wavefront coding systems as a function of the sample phase ϕ, see Fig. 5.14. Depending on the phase and frequency content of the spurious signals, the SRR becomes destructive or constructive in nature and undergoes a series of changes in its magnitude. Yet, the SRR can be condensed into a single number in order to predict a good performance measurement by taking the average

*From Ref.[101]: Based on perception experiments, it appears that in-band aliasing has a strong affect on low-level discrimination tasks like hot-spot detection; out-of-band aliasing has only a minor impact on these tasks. For high-level discrimination tasks like target identification, however, out-of-band aliasing has a significant impact on performance, whereas in-band aliasing has a very minor affect. For intermediate-level discrimination tasks like target or character recognition, both in-band and out-of-band aliasing have a moderate impact on performance.

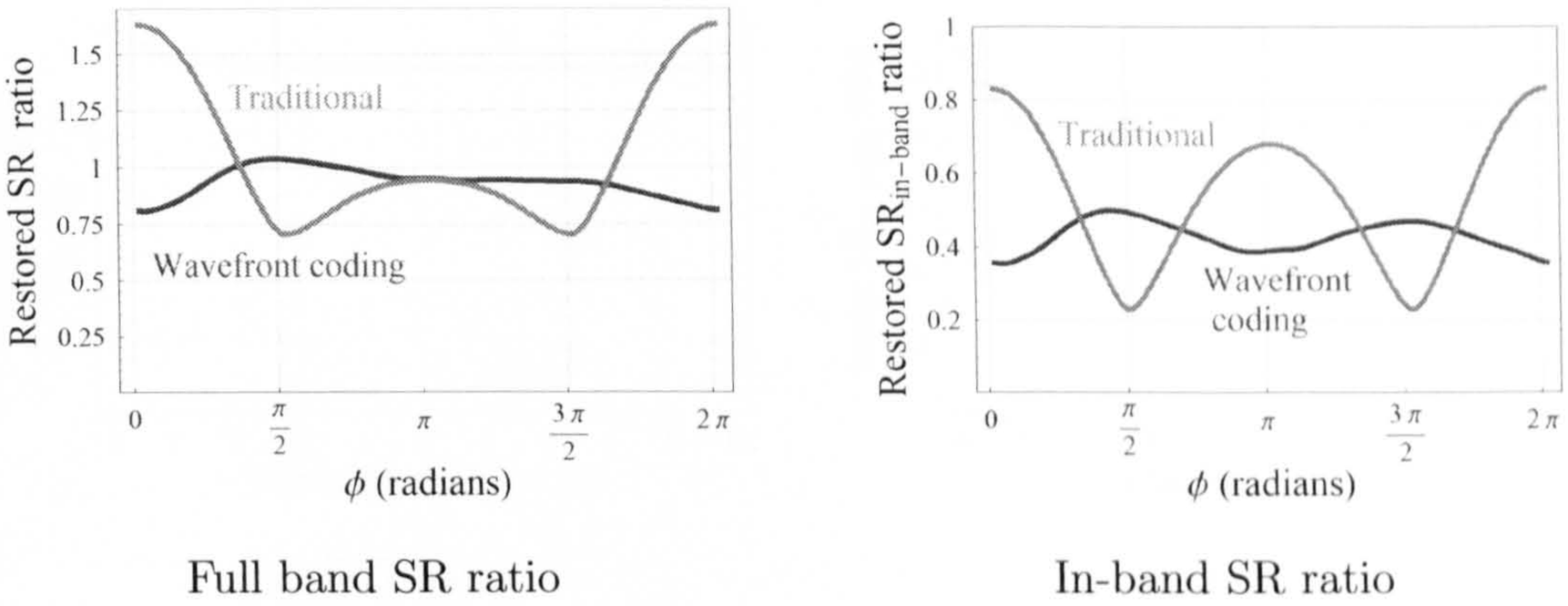

Full band SR ratio In-band SR ratio

Figure 5.14: *Magnitude of the total spurious response (left) and magnitude of the in-band spurious response (right), as a function of phase sampling ϕ for both traditional (grey curve) and restored wavefront coding systems (dark curve).*

across the sample phase $0 \leq \phi \leq 2\pi$ (this incurs no error for it is justified to perform an average MTF calculation over all relative positions of the image data with respect to the sampling sites [102]). The total SSR was calculated for the conventional system: 1.05 (in band SRR 0.54); and 0.94 (in band SRR 0.43) for the wavefront coding system after post detection processing. Thus, in principle, the use of a cubic phase mask with $\alpha = 5\lambda$ results in a reduction of in-band aliasing artifacts of up to 20%. The calculation of spurious response ratios was also extended to cubic phase masks with coding strengths $0 \leq \alpha \leq 10$. This is illustrated in Fig. 5.15, where both total and in-band spurious responses remain practically constant with α parameter. This suggests that beyond a certain rate of mask-induced phase change between adjacent frequencies, the number of destructive and constructive spurious events balances out and hence the SRR remains unchanged for any value of $\alpha > 1\lambda$.

The results presented in this section rely on the sampled transfer function to characterise the quality of the imaging system. Since, the sampling artifacts produced by an imaging system depend on the actual scene being imaged, we shall conclude the study in the last section with a numerical evaluation in which the frequency spectrum of a representative IR scene is considered.

Effect of aliasing on wavefront coding's defocus insensitivity

We have shown that detector sampling of wavefront coded point spread functions does not affect in a negative way the restoration process by which diffraction limited performance is subsequently recover. Furthermore, we have demonstrated that

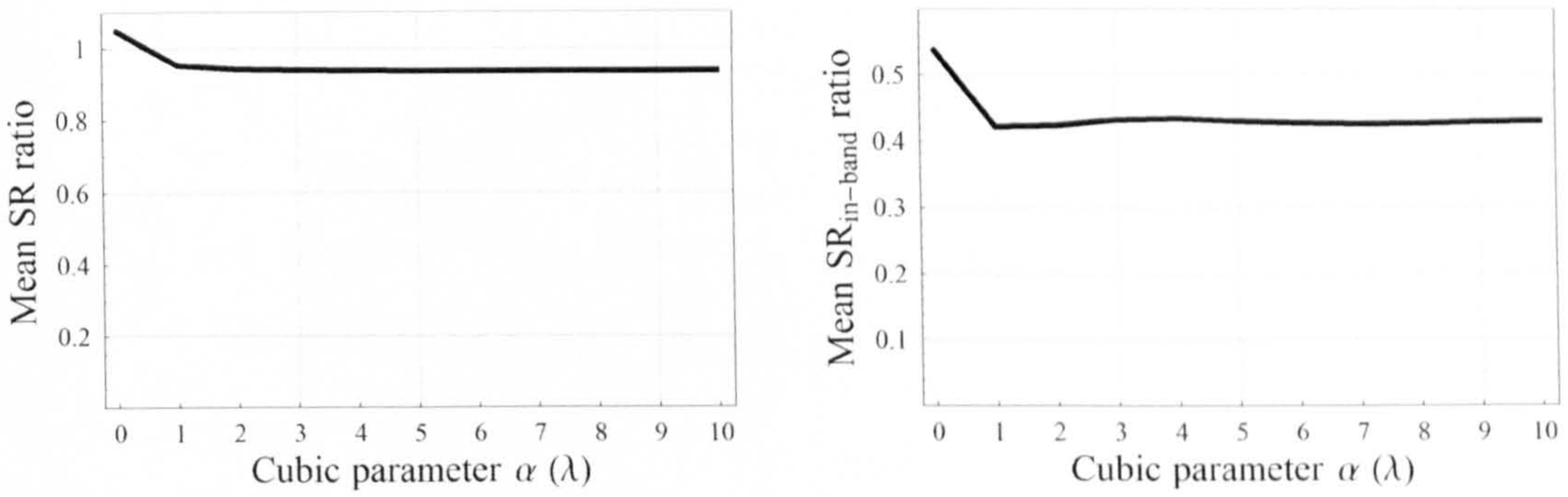

(a) Full band (b) In-band

Figure 5.15: *Mean magnitude of the spurious response for full band (a) and in-band (b) over the sample phase, as a function of the cubic phase mask parameter* α

wavefront coding enables reduced presence of aliasing artifacts in the restored images. In this section, the impact of sampling on wavefront coding's ability to mitigate defocus aberration is investigated.

We restrict the study to a cubic phase mask with $\alpha = 5\lambda$, although the results shown here can be extended to any antisymmetric phase mask, in particular to the family of cubic phase masks with different values of α. The detected (unprocessed) baseband and spurious response of a wavefront coding system were generated for a set of defocus coefficients W_{20} varying from 0 to 5λ. Subsequently, both coded transfer function and spurious response were inverse filtered using the cubic optical transfer function associated with no defocus. This process can be expressed mathematically by simply introducing the defocus variable W_{20} in Eq. (5-16), which yields

$$\text{Restored baseband: } B'(\xi, W_{20}) = \frac{H_{dif}(\xi)}{H_{opt}(\xi, W_{20}=0)} B(\xi, W_{20}), \quad (5\text{-}20)$$

$$\text{Restored spurious response: } S'(\xi, \phi, W_{20}) = \frac{H_{dif}(\xi)}{H_{opt}(\xi, W_{20}=0)} S(\xi, \phi, W_{20}).$$

The result of restoring the baseband $B'(\xi, W_{20})$ with the in-focus OTF is identical to that of a non-sampled imager (let us recall that a sampled system has the same baseband as a non-sampled system[†]). The inverse filtering of the defocused basebands introduces identical phase and magnitude mismatches at exactly the same spatial frequencies as the non-sampling situation. Thus, detector sampling does not

[†]In the literature, it is common to include the pixel OTF in the baseband of a non-sampled imager. Sampling only refers to the replication of the transfer function and not to the blurring by the pixel OTF.

undermine wavefront coding's capability to alleviate defocus aberration whatsoever, nor improves it. This is illustrated in Fig. 5.16, where the restored basebands as a function of defocus exhibit the characteristic magnitude modulations and high-frequency decline as the non-sampled MTFs. The magnitude of the baseband is plotted up to the Nyquist frequency. Also shown in Fig. 5.16 is the inverse-filtered spurious response as a function of defocus. Clearly, the spurious response becomes progressively suppressed as increasing defocus degrades the high spatial frequencies subsequently mirrored under the Nyquist band. This is an expected result since aliasing artifacts are reduced in magnitude with defocus due to the suppression of high spatial frequencies. The variation of the total and in-band spurious response ratio with defocus is depicted in Fig. 5.17. The mean of the spurious response ratio was calculated across a sampled phase space $0 \leq \phi \leq 2\pi$.

3.2 Quantitative evaluation of sampled images with wavefront coding

To complete our study on sampling and its effect on wavefront coded imaging systems, we make use of a comprehensive sampling simulation to process various scenes in a way that enables the baseband and spurious components of the sampled images to be isolated and displayed unequivocally [96]. The model considers aliasing as a scene-dependent additive noise and provides metrics to quantify its extent. Additionally, by displaying the aliased component of the sampled images, the model allows a qualitative assessment of aliasing as noise.

Two representative scenes have been selected because of their distinct and illustrative frequency content: a synthetic spoke target and an ordinary thermal imaging picture, shown in Fig. 5.18. These scenes will be imaged by the same thermal imager described before (25μm pixels, F/1.12 optics with 75mm focal length).

To accurately represent the practical performance of the sampled imager, the sampling OTF is included in the performance modeling. The sampling MTF arises from the consideration that typical scenes, in particular natural scenes, have no net alignment with the sampling locations. Therefore sampling by a 2-D array of finite-size pixels involves two distinct modulation transfer function contributions: one for the spatial averaging process associated with the pixels, given by Eq. (5-

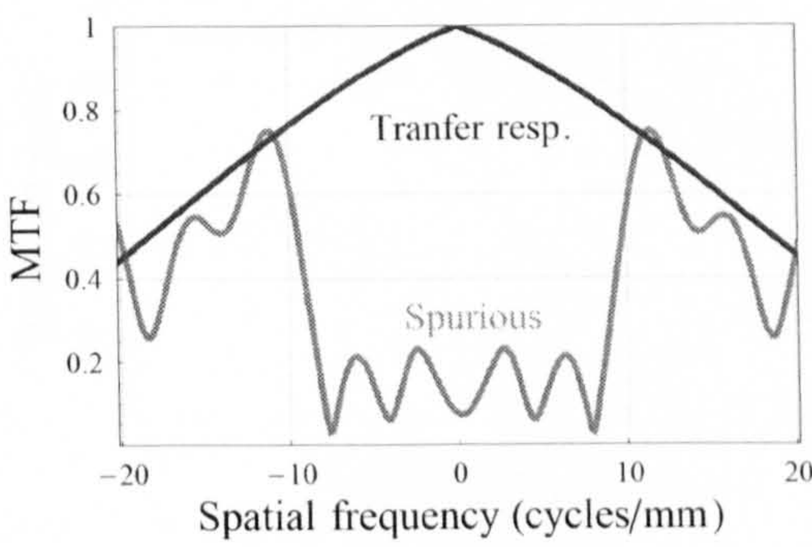

(a) $W_{20} = 0$

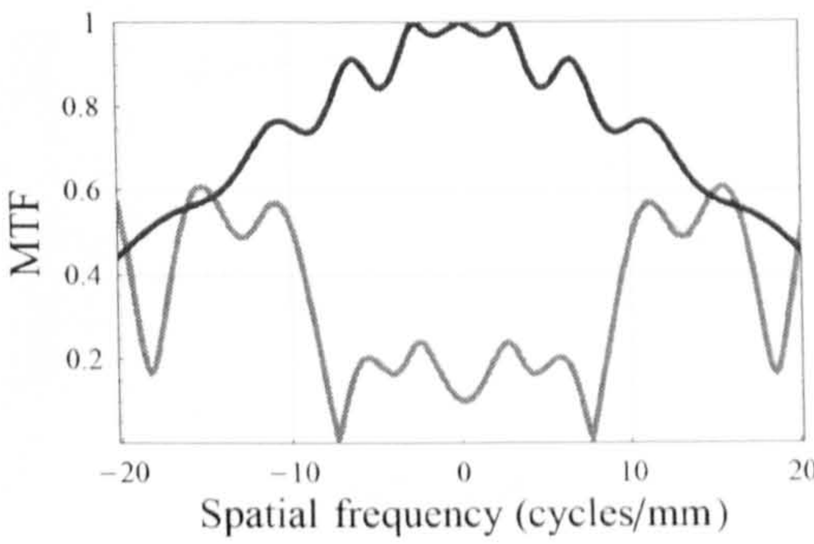

(b) $W_{20} = 1\lambda$

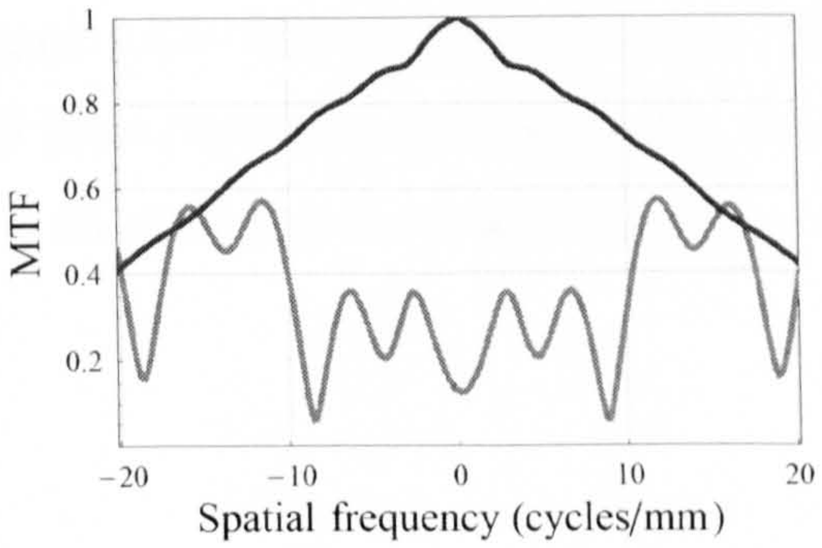

(c) $W_{20} = 2\lambda$

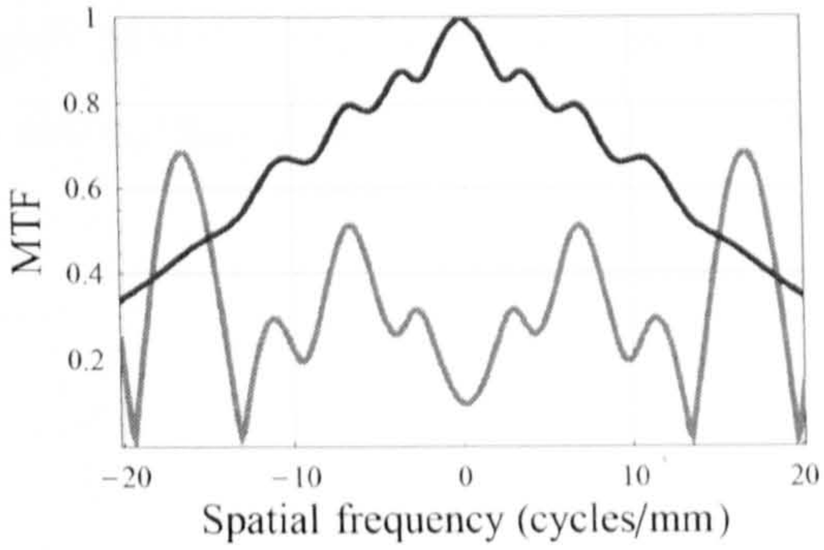

(d) $W_{20} = 3\lambda$

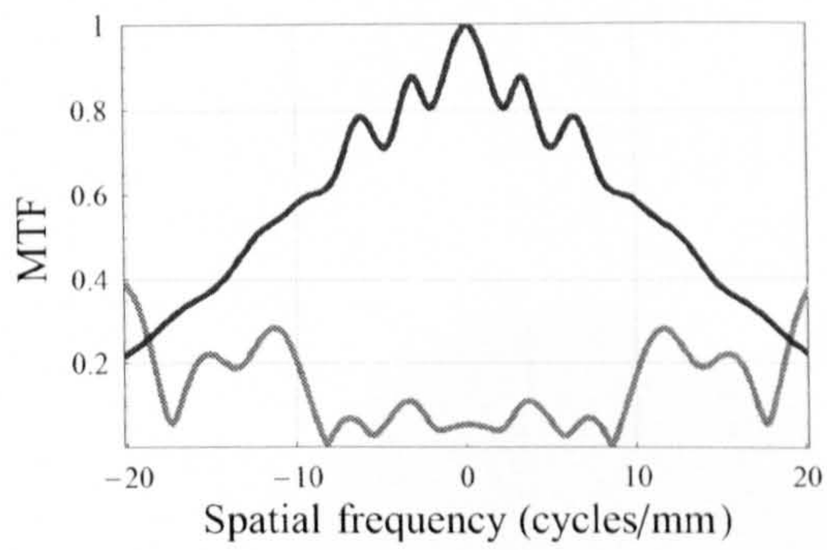

(e) $W_{20} = 4\lambda$

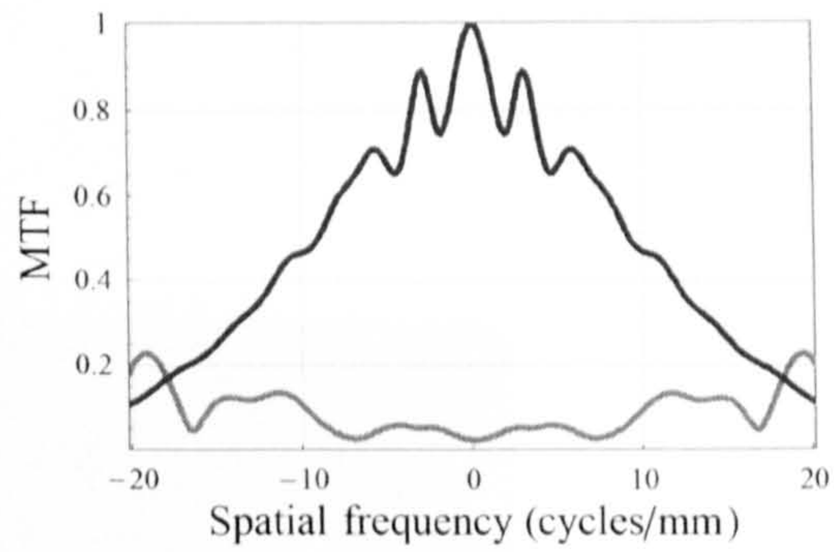

(f) $W_{20} = 5\lambda$

Figure 5.16: *Magnitude of the transfer response and spurious response for a wavefront coding system with a cubic phase mask* $\alpha = 5\lambda$ *after post-detection image processing for various amounts of defocus* W_{20}. *Magnitude displayed up to the Nyquist frequency* $20 cycles/mm$.

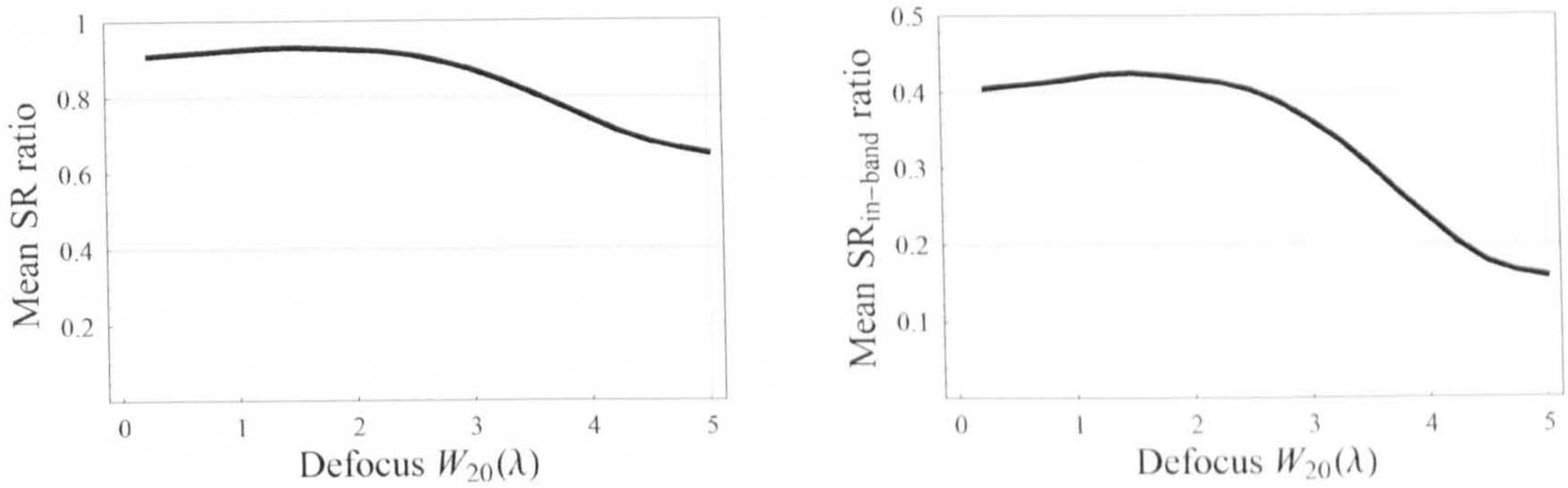

Full band SR ratio In-band SR ratio

Figure 5.17: *Mean magnitude across the sample phase of the spurious response for full band (left) and in-band (right), as a function of the defocus coefficient* W_{20} *for* $\alpha = 5\lambda$ *after post-detection image processing.*

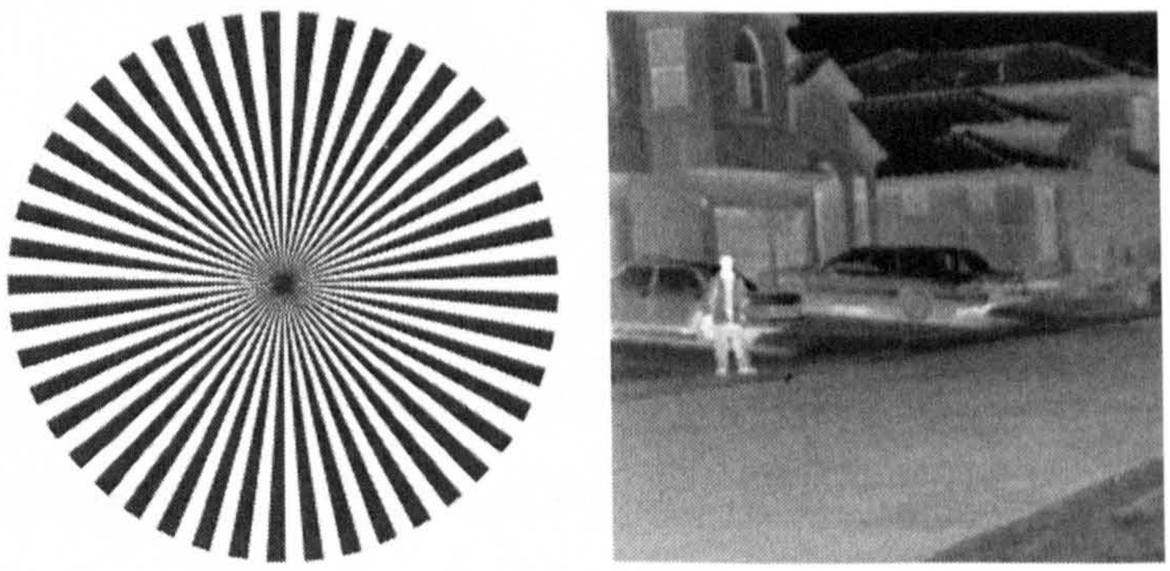

(a) Spoke target (b) IR scene

Figure 5.18: 1280×1280 *pixel high-resolution scenes for sampling model*

11), and one for the sampling process associated with the finite spacing between samples [103, 104]. Park *et al.* [102] perform an average MTF calculation over all relative positions of the image data with respect to the sampling sites. This statistical approach performs an average of the shift-variant image quality that is seen in sampled data systems to define a shift-invariant average sampling MTF. Thus, it can be demonstrated that the sampling MTF is a sinc function, with first zero equal to the inverse of the sampling interval. For a 100% fill factor, the sampling MTF equals the pixel MTF. We assume that these two MTFs multiply to yield an aggregate.

To simulate aliasing properly, it is required to allow for significant energy well beyond the sampling passband. This is achieved by choosing high-resolution images several times larger than the detector size. Super-resolution scenes of a spoke target and IR image with 1280×1280 pixels are used to synthesize the corresponding 640×640 continuous scenes. The continuous scenes are employed as inputs to a simulation of the image quality produced by a focal plane array with a maximum of 320×320 pixels (for practical and computational reasons a detector with $2^N \times 2^N$ pixels is preferred, thus a 256×256 detector is modeled instead by cropping the images). Post-detection digital processing is applied only to the sampled wavefront coded images and no random noise is introduced. The digital processing restores the wavefront coded baseband to match exactly the baseband of the traditional system. The baseband spectrum of the image after restoration is given in discrete components by:

$$B_i'[k_m, k_n] = \frac{H_{dif}}{H_{opt}} \times (H_{pix}^2 H_{opt} O[k_m, k_n]), \tag{5-21}$$

where O represents the spectrum of the object or high-resolution scene, the pair $[k_m, k_n]$ corresponds to a spatial frequency coordinate and H_{pix}^2 combines the sampling and pixel MTFs (i.e. 100% fill factor). The first factor in the equation accounts for the inverse restoration. The rest of the functions have been defined previously. The aliasing noise component is calculated by adding replicas of the imaged scene shifted at multiples of the sampling frequency f

$$S_i'[k_m, k_n] = \frac{H_{dif}}{H_{opt}} H_{pix}^2 \sum_{l=-3}^{+3} G[k_m - lf, k_n - lf] \text{ with } l \neq 0, \tag{5-22}$$

with $G[k_m, k_n] = H_{opt}[k_m, k_n] O[k_m, k_n]$. By considering aliasing as scene-dependent additive noise, we can express the final sampled image as the sum of two terms B_i'

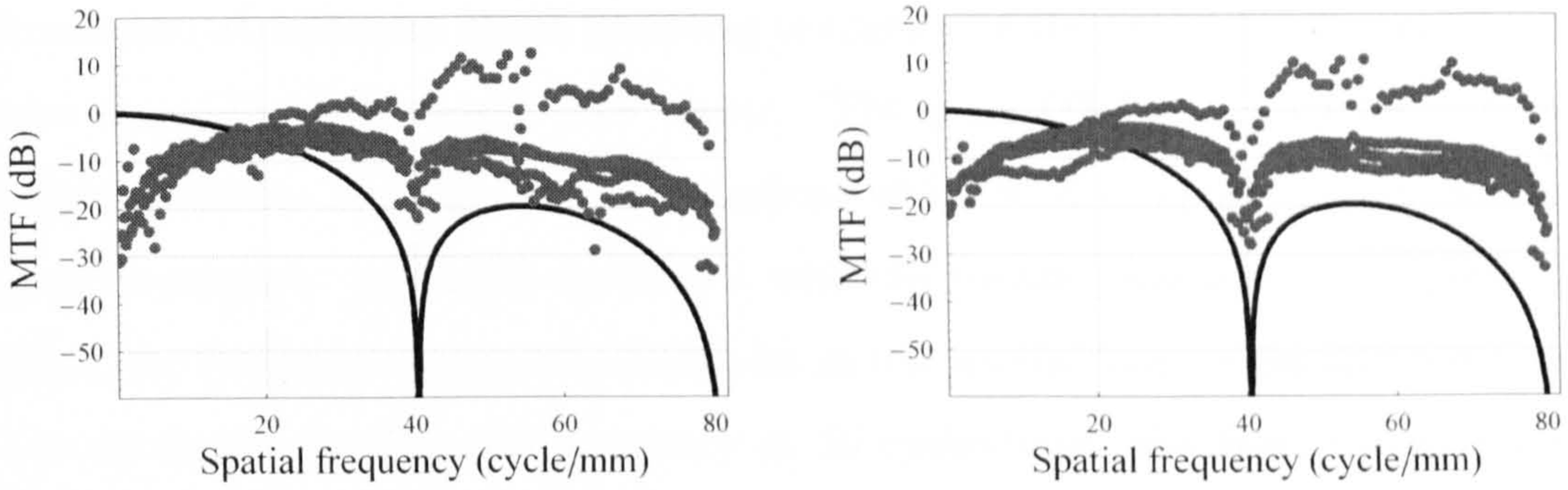

Wavefront coding system | Traditional system

Figure 5.19: *Magnitude of the baseband spectrum ratio B_i'/O (solid) and aliasing component ratio S_i'/O (dotted) of the spoke target imaged by the wavefront coding system (left) and traditional system (right).*

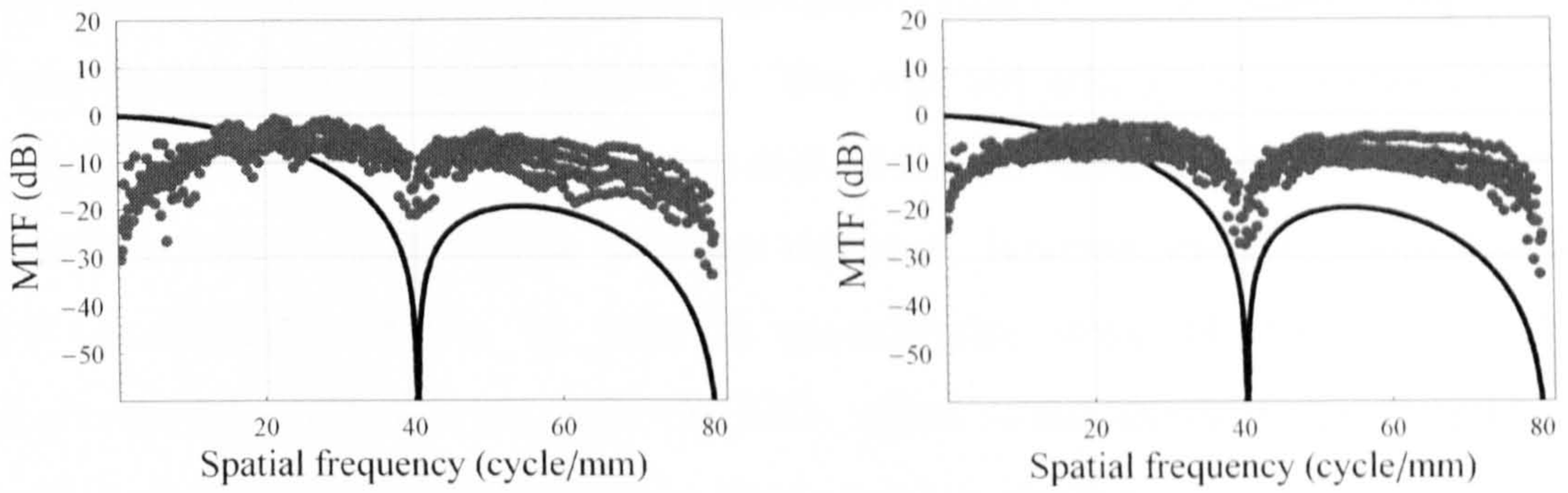

(a) Full band | (b) In-band

Figure 5.20: *Magnitude of the baseband spectrum ratio B_i'/O (solid) and aliasing component ratio S_i'/O (dotted) of the IR scene imaged by the wavefront coding system (left) and traditional system (right).*

and S_i'. The extent of aliasing can be quantified by comparing both terms referenced to the input scene:

$$\frac{B_i'[k_m, k_n]}{O[k_m, k_n]} \text{ and } \frac{S_i'[k_m, k_n]}{O[k_m, k_n]}, \tag{5-23}$$

which can be calculated only if $O[k_m, k_n] \neq 0$. In some way, the magnitude of these ratios represents the inverse of a frequency-dependent signal-to-noise ratio.

The quantitative evaluations of the spoke target and IR scene are illustrated in Fig. 5.19 and Fig. 5.20 respectively. The left column in the figures corresponds to the wavefront coded system, the right column to the traditional system. The solid dark curve represents the magnitude of the baseband ratio B_i'/O in decibels. Likewise, the gray dots map the magnitude of the aliasing ratio S_i'/O. Note both ratios

become zero at multiples of the sampling frequency of the detector (40 cycles/mm) where the nulls of the pixel OTF occur. The pixel OTF fails to filter out the spurious response because the MTF replicas which lead to spurious response are at low frequencies. In perfect agreement with the results presented in the previous section, the baseband response is dominant at low spatial frequencies and continues so up to almost the Nyquist frequency at 20 cycles/mm. For frequencies greater than the Nyquist frequency, the aliased ratio is manifestly dominant. Due to the coarse sampling of the detector the aliased component of the output image is very substantial. A closer investigation of the aliased component curves of the sampled images reveals two important features that are consistent with our expectations: 1. The mean of the aliased component (given by $S_i'[0,0]$, at the frequency origin) from the restored wavefront coded images is diminished relative to the aliased component of the traditionally acquired images, 2. The restored aliased components appear much more irregular and dispersed as a result of the increased number of destructive and constructive events in the spurious response, however the net effect results in lower aliasing artifacts. In order to quantify the extent of aliasing we make use of *signal-to-aliased-noise ratio* (SANR), which is analogous to the concept of signal-to-noise ratio for characterizing image quality; similarly, low values represent a significant aliasing component. The ratio is given by the variance of the scene's baseband over the variance of the aliased component,

$$\text{SANR} = \frac{\sigma_b}{\sigma_s}, \tag{5-24}$$

with,

$$\sigma_b^2 = \sum_{k_m \neq 0} \sum_{k_n \neq 0} |B_i[k_m, k_n]|^2, \tag{5-25}$$

and

$$\sigma_s^2 = \sum \sum |S_i'[k_m, k_n]|^2. \tag{5-26}$$

This metric was applied to both wavefront coded and traditional images and its results are displayed in Table 5.1. These figures correspond to SANR of sampled images acquired in the absence of defocus. Note that wavefront coded images show a reduction in SANR between 13% and 20% when compared to the traditional images, as predicted when we derived the transfer function of a sampled wavefront coding imager. It is interesting to note that prior to restoration the wavefront coded

	Traditional SANR	Wavefront coding SANR
Spoke target	28	32
IR scene	42	52

Table 5.1: *Signal-to-aliased-noise ratio of two scenes being imaged by a traditional and a wavefront coding system after restoration. Wavefront coding decreases the aliased-noise components in the restored images.*

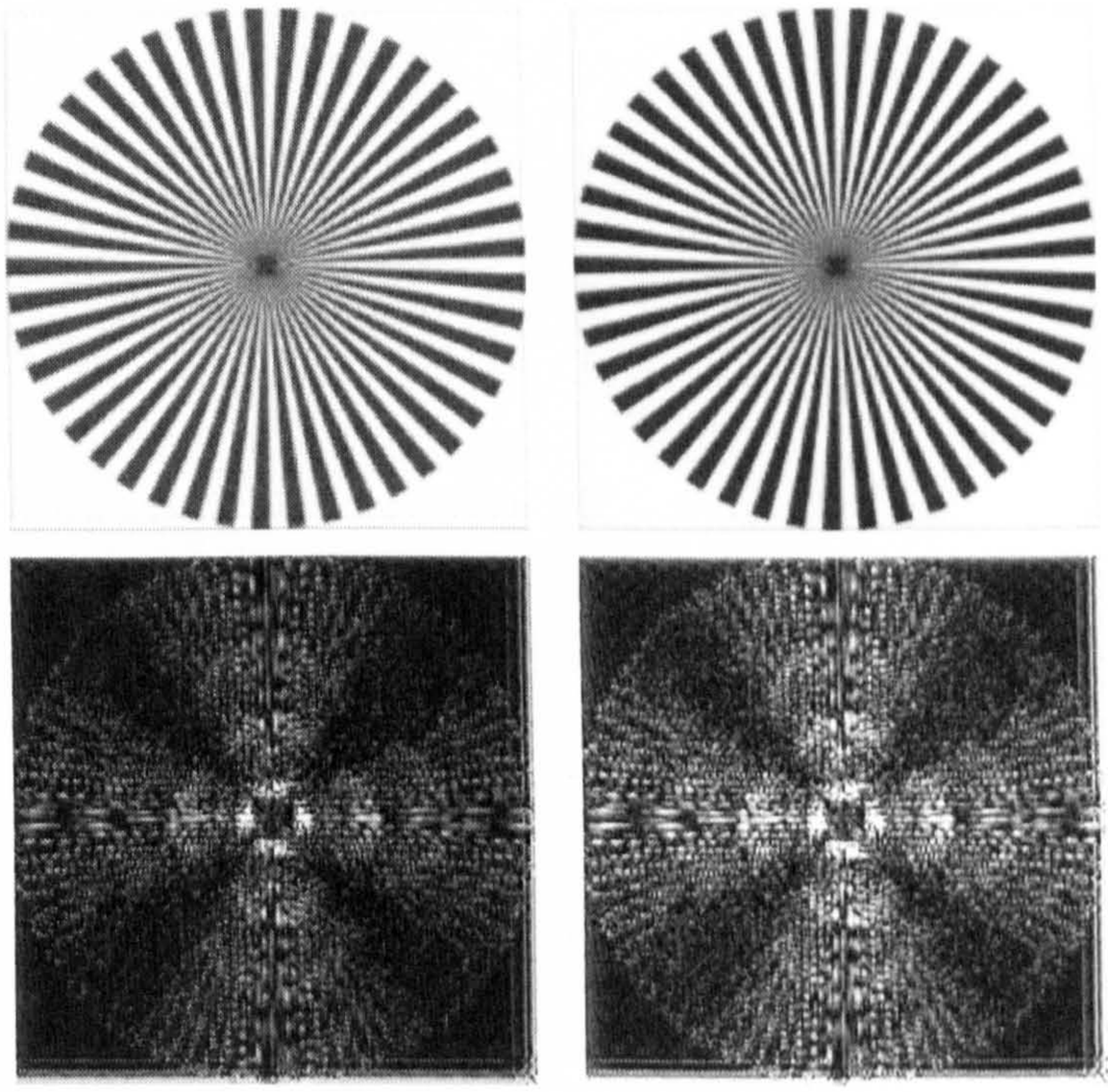

Wavefront coding Traditional

Figure 5.21: *(Top) Final output images of the spoke target and (bottom) their corresponding aliased components for the wavefront coding and traditional systems. Wavefront coded image obtained after inverse restoration. The aliased component of the traditional system is more evident.*

images presented a SANR=170 due to the defocus-invariant blurring introduced by the phase mask.

The assessment of the impact of aliasing on the recovery of the coded scene data must also be based on visual inspection of the restored images. Figures 5.21 and 5.22 illustrate the inverse filtered images of the spoke and IR scene respectively together with the images acquired with the conventional system. Clearly, post-detection inverse filtering has been able to decode and restore the images to diffraction-limited

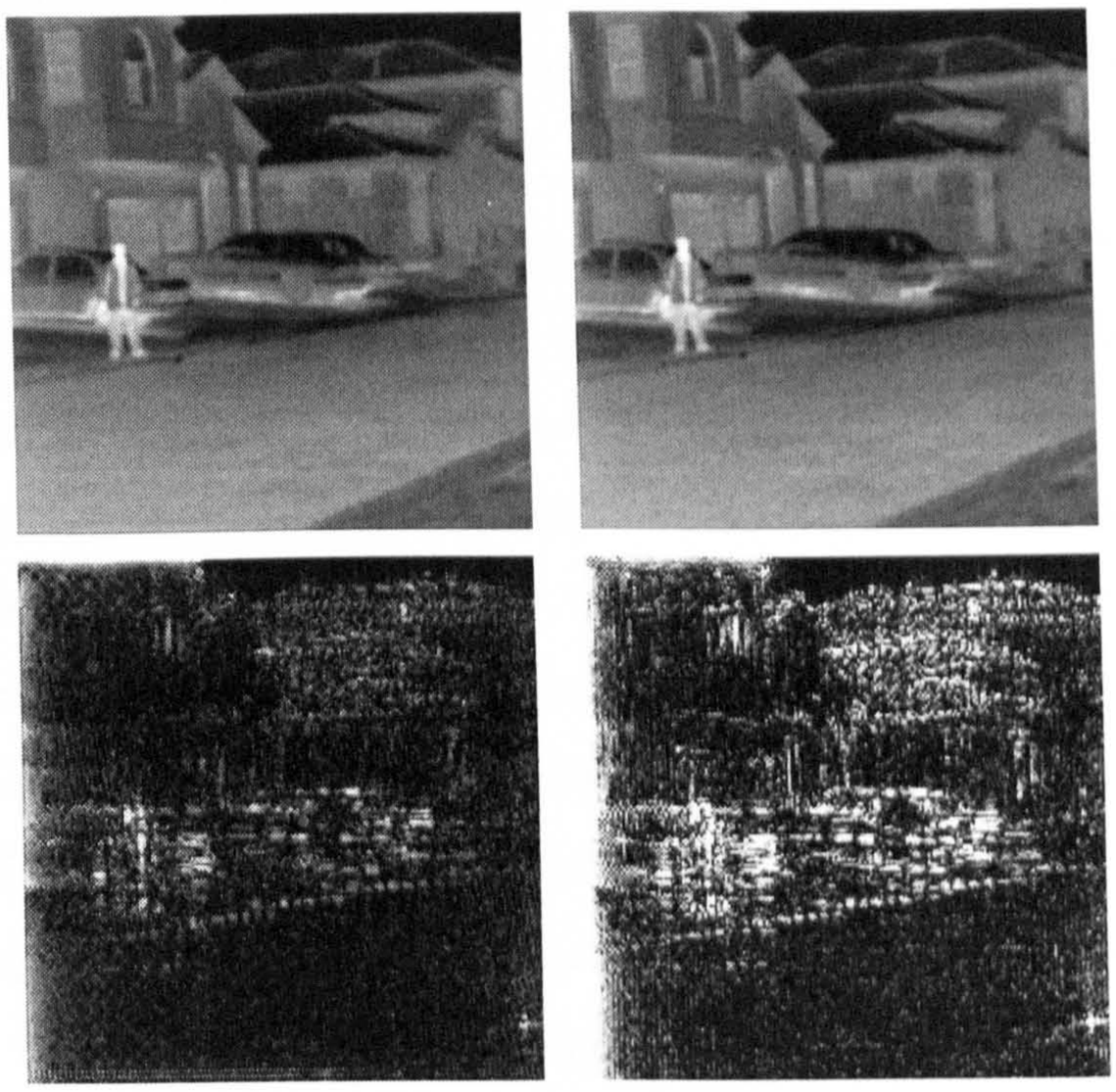

Wavefront coding Traditional

Figure 5.22: *(Top) Final output images of the IR scene and (bottom) their corresponding aliased components for the traditional and wavefront coding systems. Wavefront coded image obtained after inverse restoration. The aliased component of the traditional system is more evident.*

quality in spite of all the intricate sampling interferences that take place and corrupt the desirable baseband content: no difference can be observed between the decoded and conventional images.

The sampling model followed here allows us to synthesize and present the aliased component of the output image in an unequivocal way. For example, also shown in Fig. 5.21 and 5.22 are the scene-dependent aliased components for each of the output images. In all cases, wavefront coding has decreased the contrast of the spurious components and the reduction in SANR is apparent. Note that, the contrasts in the density maps has been enhanced with respect to the input scene for displaying purposes.

Finally, we conclude this quantitative and qualitative assessment of sampled images taking into account the combined action of defocus aberration and wavefront coding. The spoke target was imaged in the presence of defocus $W_{20} = 2\lambda$ with and without the cubic phase mask inserted in the system. These pre-sample images were subsequently sampled by the detector, and in the case of the coded image, deconvolved using the in-focus optical transfer function. The output images are displayed in Fig. 5.23 and their magnitude baseband and aliasing component ratios in Fig. 5.23. It is evident from analyzing these figures that wavefront coding maintains its capability to mitigate defocus aberration in sampled imagers. The minor artifacts visible in the restored image correspond to phase mismatches between the deconvolution kernel and convolution OTF, and have been reported in this chapter also for non-sampled imagers. In contrast to the standard sampled image where there exists significant blur, phase reversals and nulls within the Nyquist passband (see Fig. 5.23), the image from the cubic-phase-mask system is essentially unaffected and no nulls can be found within the Nyquist passband. In terms of the signal-to-aliased-noise ratio, the restored image achieves a SARN of 35 (compare with a SANR of 32 in-focus) due to the MTF magnitude disparity between the deconvolution kernel and convolution OTF. Finally, the SANR for the defocus standard image is 635, as both baseband and spurious response degrade by defocus blur.

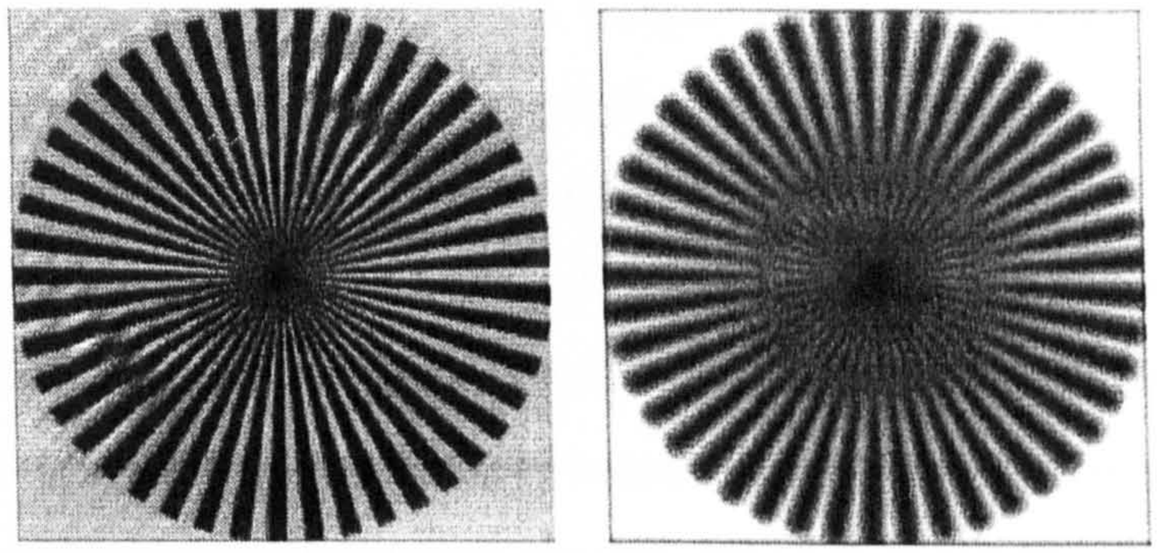

Wavefront coding system Traditional system

Figure 5.23: *Output sampled images of a defocused spoke target corresponding to the wavefront coding system after restoration (left) and the traditional imaging system (right).*

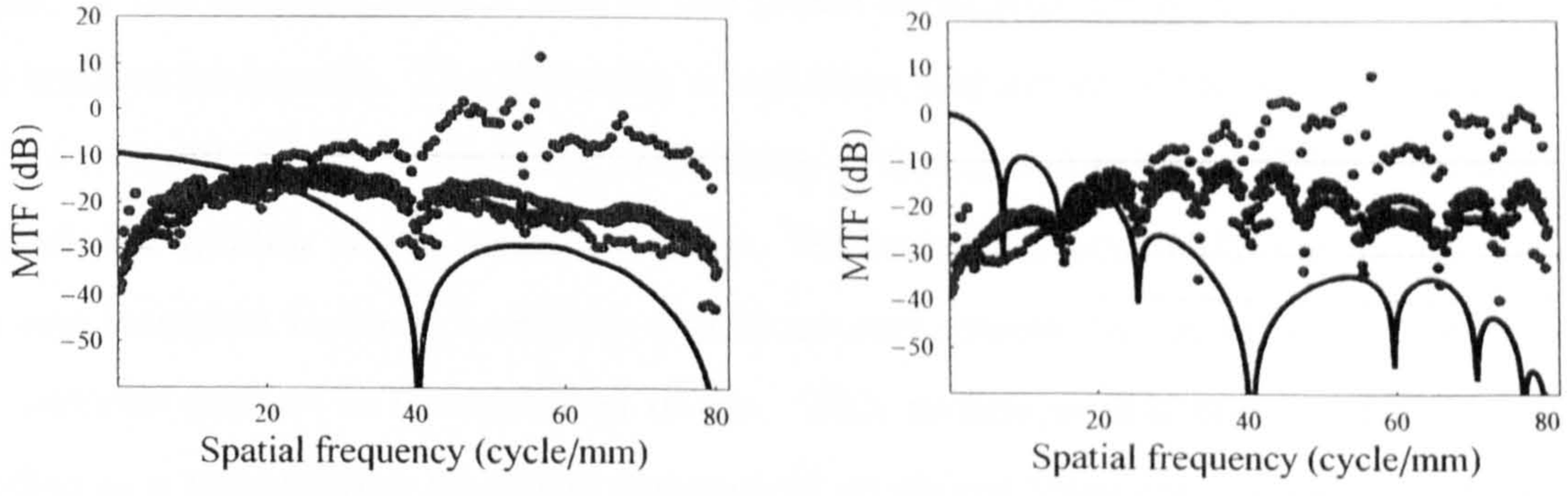

(a) Full band (b) In-band

Figure 5.24: *Magnitude of the baseband spectrum ratio B_i'/O (solid) and aliasing component ratio S_i'/O (dotted) of the defocused spoke targeted. (Left) Wavefront coding system, (right) traditional system.*

4 Conclusions

We have evaluated the performance of the wavefront coding technique by means of the noise amplification in the restored image. Numerical modeling with cubic and petal phase masks indicates that the reduction in the signal-to-noise ratio can be a serious limiting factor in the practical implementation of this technique. The noise amplification is fundamentally dependent on the shape and surface sag of the phase masks. In rectangularly separable antisymmetric phase masks such as the cubic, the noise amplification is notably larger for spatial frequencies outside the tangential and sagittal axis. In general, for any value of the cubic parameter α, the noise penalty outside the favourable axis is at least a factor of 10 greater. Thus, for a viable use of wavefront coding, a careful study of the tradeoff between aberration mitigation and noise amplification must be performed for each specific system. The results shown here correspond to a representative wavefront coding system and are aimed at providing a general demarcation of the maximum noise levels expected in the restored image after simple inverse filtering. The use of more sophisticated postdetection processing algorithm will certainly improve the signal-to-noise ratio of the restored image. More work remains to be done in the search for decoding techniques with reduced noise gain.

We have also reported the presence of artifacts (ringing or replica of most of the edges) in the restored images due to the phase mismatch between the convolution and restoration kernels. The intensity, orientation and extent of the artifacts depend on the strength of the phase mask and degree of defocus aberration. These artifacts degrade the quality of the resulting image. Yet recent research [105] has shown that one can interpret them as a defocus signature and remove by iteratively estimating the defocus present in the restored image. This technique has the potential to be applied as a range finder since the distance of an object from the optical system can be deduced from the optical set up and the estimated defocus work.

Finally, a comprehensive and rigorous assessment of the effect of detector sampling on wavefront coding performance has been carried out for the first time. The results showed a decrease in aliasing artifacts of 15% in the restored image when compared to a traditional optical system. More importantly, we have also demonstrated that detector sampling does not prevent from decoding the detector image to diffraction-limited (sampled) quality.

Chapter 6

Experimental realizations and applications of wavefront coding

Summary. Experimental realization in the visible band of a wavefront coding system is reported. A cubic phase mask was manufactured in fused silica and employed in combination of post-detection digital signal processing to extend the depth of field of a conventional imaging system. Three potential applications of wavefront coding are also explored: 1. As an electro-optic protection measure by means of reducing and compressing the peak intensity in the image plane of a visible-band imager. Numerical and experimental validation is presented. 2. As a tool to correct thermally induced defocus aberrations in infrared imaging systems. An exhaustive modeling and analysis of the use of wavefront coding in a germanium IR imaging system subject to an operating temperature range from $-20°C$ to $+70°C$ was performed. An athermalised wavefront coding system with $\alpha = 4\lambda$ and noise gain of a factor 2 was accomplished. 3. As a means of reducing system complexity whilst maintaining image quality. This enables the use of simple, low-cost, light-weight lens systems. We present for the first time an experimental application where wavefront coding alleviates aberrations across the field of view of an uncooled LWIR optical system formed by F/1, 75mm focal length germanium singlet and a 320x240 detector array with 38-micron pixel.

1 Experimental realization of wavefront coding

We report experimental proof-of-concept realization of wavefront coding to obtain extended depth of field by means of modifying a conventional incoherent optical system with a cubic phase mask plate placed at its aperture stop. Several cubic phase masks were manufactured by Dr. Mohammed Taghizadeh and his collaborators at

the Physics Department of Heriot-Watt University. A number of images using the manufactured cubic phase masks have been acquired at different defocus position and subsequently inverse filtered. The restored images showed an increased depth of field. The price for this extended performance is noise amplification in the restored image relative to a perfectly focused image.

These experiments are performed in the visible spectrum. In this way, it enables a risk reduced appraisal of wavefront coding prior to a more costly implementation in the long-wave infrared band, as we have done at the end of the Chapter. In the visible spectrum, we can readily carry out a series of experiments to evaluate the artifacts in the digitally processed image, the effect of detector sampling, the signal-to-noise ratio along various directions of the restored image (due to the cubic nature of the phase mask), the practical range over which the wavefront coded PSF remains invariant, etc.

In the next section, the characteristics of the phase masks are described together with a short account of the current manufacturing techniques currently available for fabricating these antisymmetric optical elements. In the second section, the experimental set-up and apparatus used are explained. Finally, the restored images are displayed.

1.1 Manufacture of the cubic phase mask

The manufactured cubic phase mask is antisymmetric and rectangularly separable with an active region of 20×20 mm on a fused silica substrate. The peak-to-valley height in the substrate is 13.8 microns which introduces an optical path difference of 10 wavelength at $\lambda = 0.6328\mu$m (i.e. $\alpha = 2.5\lambda$). The cubic masks can be produced by a continuous refractive surface relief profile. The difficulty in manufacturing is due to the antisymmetry of the surface and the large depth required. The continuous phase profile was quantized to 64 discrete phase levels as illustrated in Fig. 6.1. The error introduced in the OTF by this quantization can be neglected (PSF's root-mean square error less than 1%). The quantization of the mask to a 64-level was shaped by a reactive ion etching process and lacked antireflection-coated surfaces. Because of the large amount of depth required, the manufacture process is difficult and requires high precision machining. It is possible to reduce the depth to etch by introducing a linear phase term given by $(x+y)$. The additional linear term has no effect on the

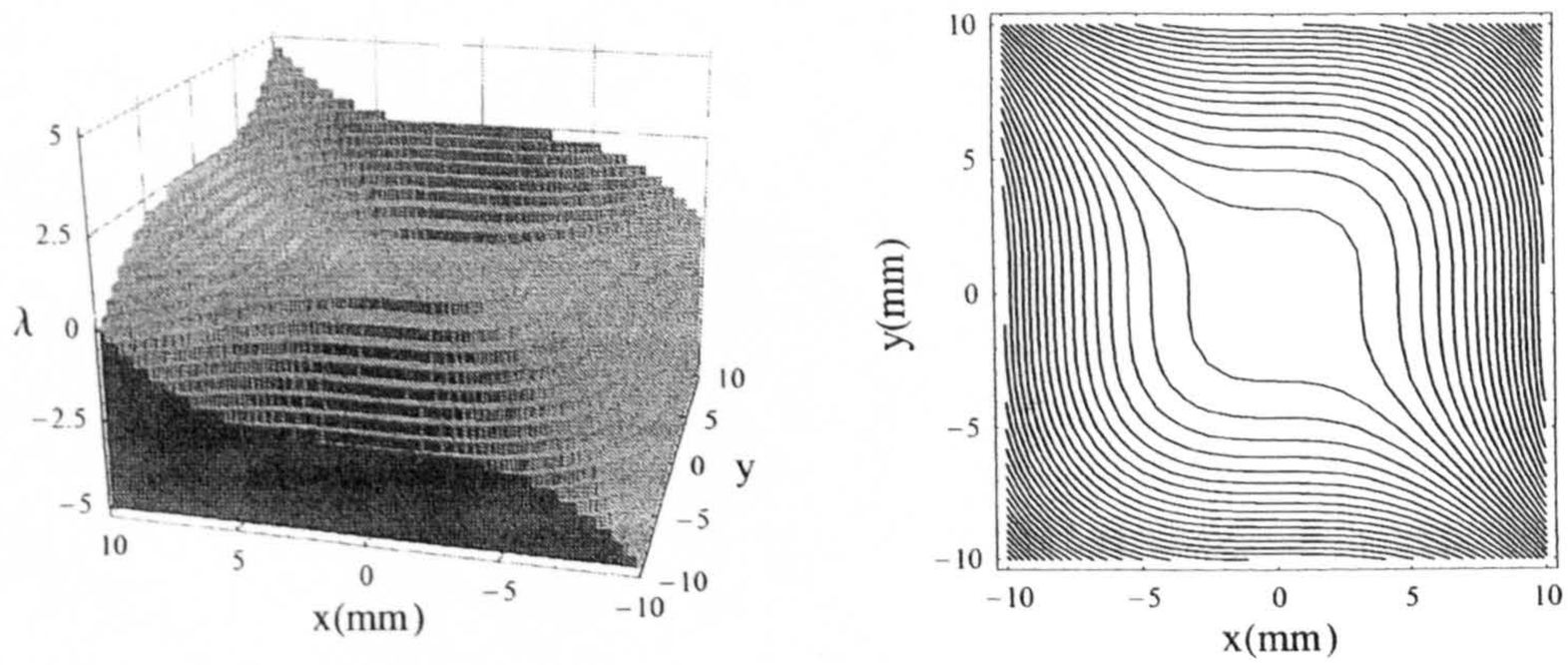

Figure 6.1: *Manufactured cubic phase mask with 64 levels of quantization.*

OTF of the system as previously discussed in the derivation of the cubic phase mask in Chapter 2. More appropriate methods exist to manufacture such asymmetric elements. Magnetorheological finishing is a modern polishing technique that uses a controlled magnetorheological fluid as a polishing tool [106]. This technique is able to grind and polish precision glass aspheres with 400 microns of deviation to $\lambda/4$ in 30 minutes. Aspherical lenses and phase masks can also be manufactured with conventional techniques such as high-precision diamond machining and moulding. Single-point diamond turning has traditionally been useful for producing diffractive and aspheric optics for the infrared region [107]. Generating antisymmetric optical surfaces is possible with multi-axis machining systems, which permit 3D flycutting for freedom shaping. Recent developments in the stability and control system of single-point diamond turning machines have allowed the production of surfaces that meet the demands of the visible spectrum with precision level of less than 0.15 microns of form accuracy and 5 nanometers of surface roughness. However, the manufacturing of small numbers of optical elements by diamond machining is costly. On the other hand, plastic injection moulding technology has been developed for the low cost market (mobile phone cameras, digital cameras, etc) with accurate surface precision. The main competitive advantage of this glass is associated with the fact that even very complex surfaces such as the non-rotationally symmetric phase mask can be produced directly by moulding, eliminating the costly polishing or single point diamond turning used for other lens material.

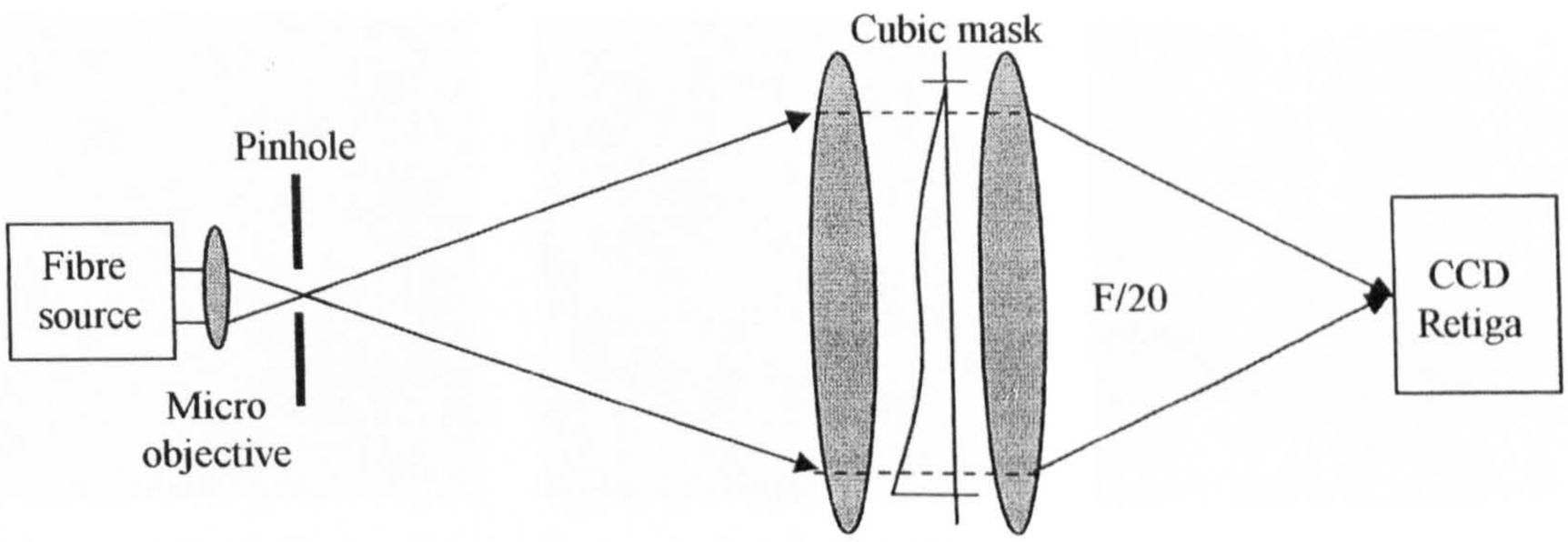

Figure 6.2: *Experimental setup of a focus-invariant wavefront coded imaging system. The cubic phase mask is placed at the aperture stop of a two-lens imaging system. Front and rear focal length is* $f = 400mm$.

1.2 Experimental measurement of the wavefront coded PSF

An experiment was arranged to measure the PSF of the cubic phase mask. The first part of these experiments was to collect images of the PSF of the system at different values of defocus. The experimental setup is illustrated in Fig. 6.2. A broadband fibre-optic light source was spatially filtered using a 5-micron pinhole. The system aperture stop was a 20x20mm square aperture placed at 400mm to the right of the pinhole. The cubic phase mask was placed in a mount inserted in the aperture stop. This mount also allowed precise rotational alignment of the mask, in order to match the CCD pixel array x and y axes with the cubic phase mask rectangular axes. The compound lens systems were placed right next to the aperture stop, performing as a $F/20$ system (along the sides of square aperture). The image was formed on a CCD detector at the focal plane of the compound lens. A QImaging Retiga 1300c CCD camera provided a maximum of 12 bits of dynamic range for subsequent digital filtering. The sampling effects of the CCD optical detector are also important to consider. Assuming a 100% fill factor, the pixel size of the CCD determines the sample rate of the image capturing process. Given the size of the pixels in the CCD (in this case, 6.7-micron width) and the slow optics used in the experiment, the image is Nyquist sampled ($\nu_{Nyquist} = 75$cycles/mm). When used with diffraction-limited optical systems, the CCD detector of the camera determines the spatial-frequency cut-off of the entire system. This frequency cut-off will be the limiting factor in the resolution of the images. The first part of these experiments, after setup and alignment of the optical system, was to collect images of the PSF of

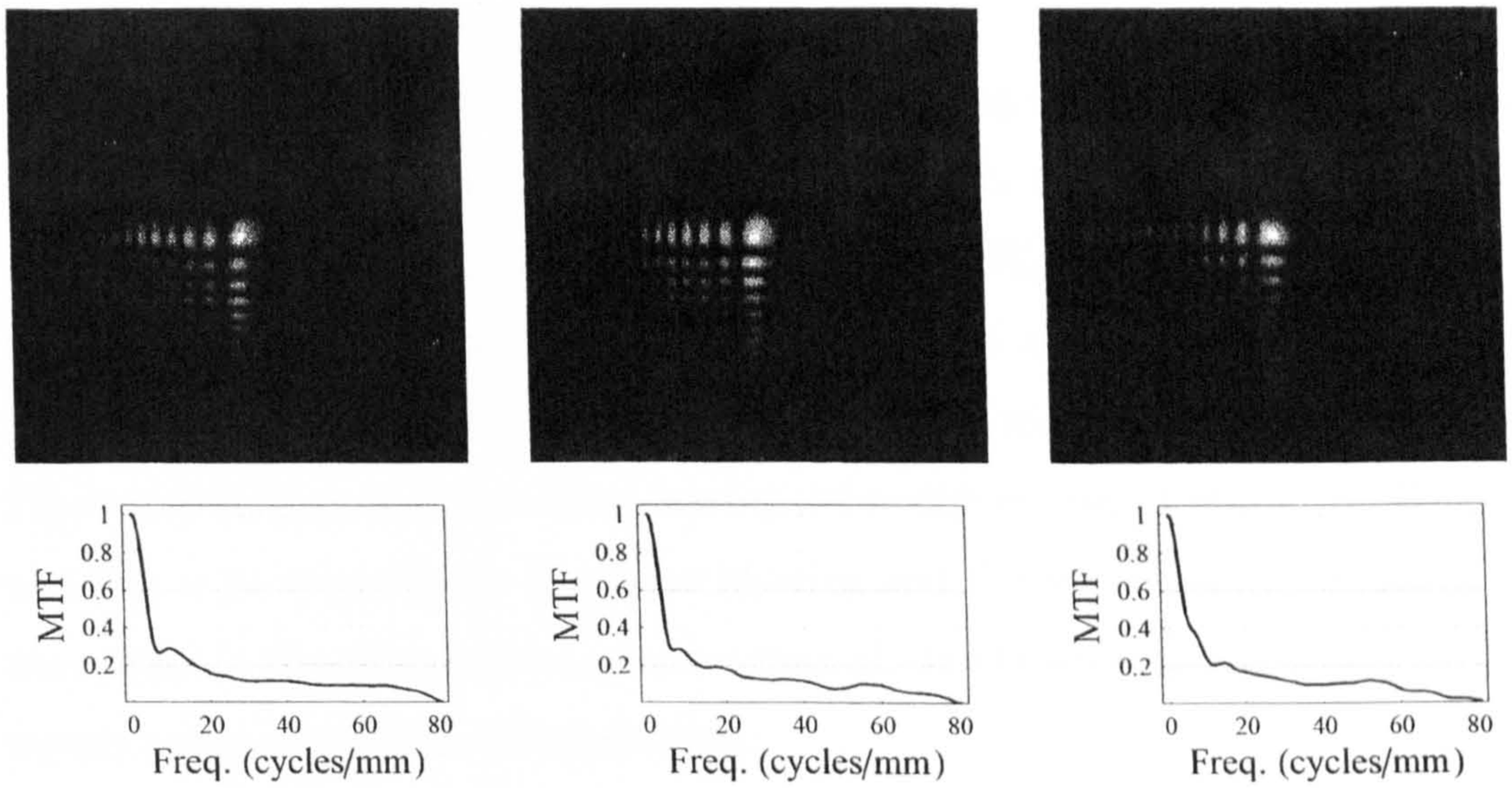

Figure 6.3: *Experimental PSFs (top)and MTFs (bottom) of a $F/20$ wavefront coding system for various degrees of defocus. The PSF density plots have been compressed to improve display.*

the system at different values of defocus. Fig. 6.3 shows the experimentally acquired PSFs and calculated MTFs (along the tangential axis) of the focus-invariant system in focus, at 0.75 and 1.5 wavelengths of defocus. The defocused PSFs were obtained by moving the camera either in front the back focal plane. The OTF of the system was calculated from the measured 2D PSF and used to calculate the inverse filter that was later applied to the images. It can be observed from Fig. 6.3, that the MTF height decreases at higher spatial frequencies when defocus is introduced as predicted in Chapter 4.

1.3 Acquisition and restoration of images

The experiments to collect images were carried out using the wavefront-coded system setup shown in Fig. 6.2. The pinhole mount was replaced by an extended object such as a spoke target, which was uniformly illuminated with white light from a fibre-optic light source. Images of the spoke target with several values of defocus were taken with and without the cubic phase mask at the aperture stop. To measure the degree of defocus accurately, we fixed the target at the object focal plane and

displace the detector along the image focal plane*.

The effect of defocus on the conventional imaging system with a 20-mm square clear aperture is shown by the experimental results in the right column of Fig. 6.4. The best focus position corresponding to a value of $W_{20} = 0$ results in the sharply focused image. Moderate defocus corresponding to a defocus value $W_{20} = 0.5\lambda$ results in the blurred image of Fig. 6.4(b). Finally, the severely defocused images Fig. 6.4(c) through to Figure 18(e) correspond to defocus values $W_{20} = 1\lambda$, $W_{20} = 1\lambda$ and $W_{20} = 3\lambda$ respectively. Excessive blurring and the well-known phase reversal of the spokes in the defocused image are apparent. In the severely defocused images is clearly apparent the loss of information.

When the cubic phase mask is inserted at the aperture stop, it produces a considerable difference in the optical performance, compare to the previous conventional clear aperture optical system. The detected image appears highly blurred but practically unchanged for a relatively large displacement of the detector. The detector is placed at the same on-axis positions as before and images are acquired for each defocused location.

The recorded images were Wiener filtered using the previously measured in-focus PSF to yield the images shown in the right column of Fig. 6.4(c). Clearly wavefront coding has enabled sharp images to be recovered for a wide range of values of defocus. The image quality for moderate and severe defocus is clearly improved, although some artifacts are evident. Note that, in contrast to the conventional system, there are no phase reversals across the images for most of the defocus range as discussed in our previous work.

Wiener filtering was applied to the detected images to avoid magnification of the system noise, especially in areas of low signal-to-noise ratio. The digital filter was applied to provide an overall optical transfer function that approximates the ideal transfer function of a diffraction-limited system. The filter was calculated by dividing the ideal triangular OTF by the cubic phase mask OTF. The Wiener scalar coefficient K in Eq.(5-10) representing the ratio of noise power to signal power was determined by trial to yield best results in terms of root-mean-square error with respect the in-focus image. The value of $K = 0.00024$ for a cubic parameter $\alpha = 2.5\lambda$ was found so that the noise in the image is reduced without a considerable

*A relative displacement δz of the detector from the image plane results in defocus aberration with coefficient $W_{20} = \delta z/8F/\#^2$, where $F/\#$ is the f-number of the optical system.

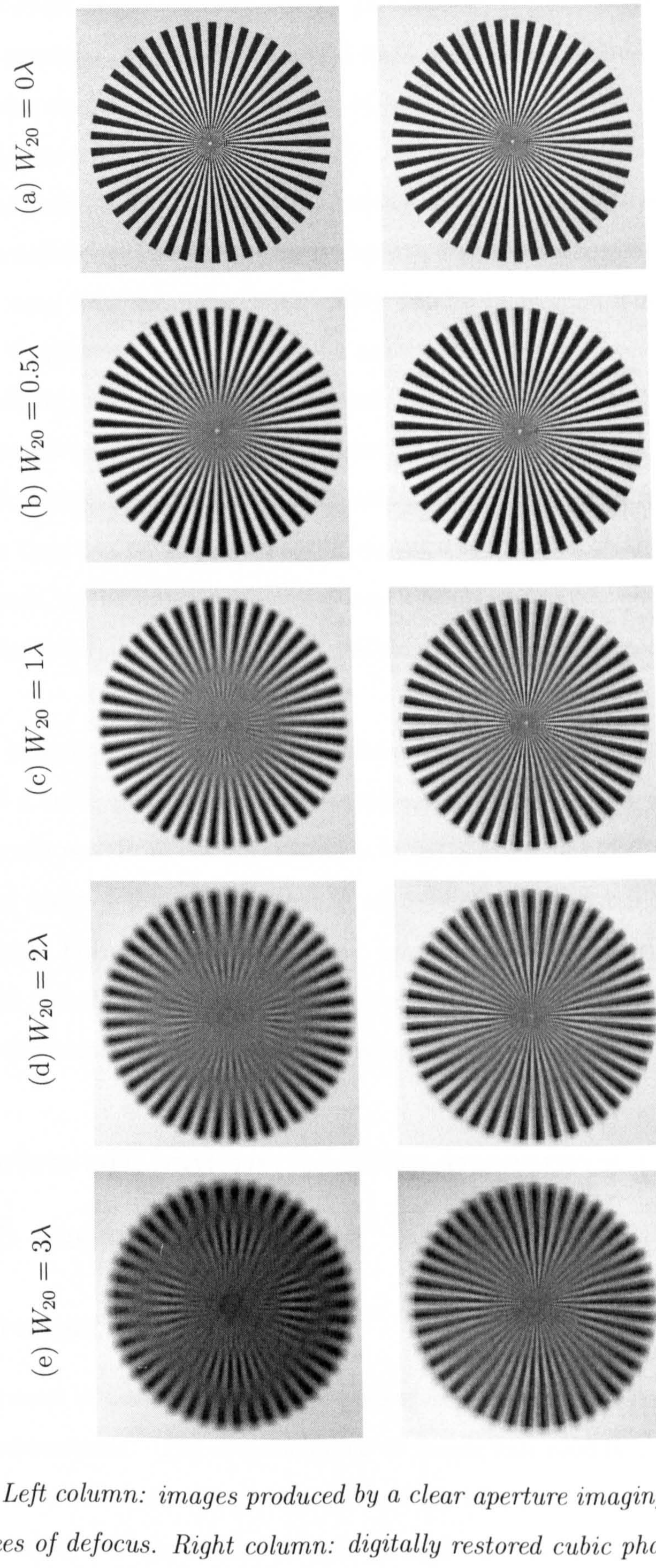

Figure 6.4: *Left column: images produced by a clear aperture imaging system for different degrees of defocus. Right column: digitally restored cubic phase mask images using a Wiener filter.*

lost in the contrast of the restored image. In addition, the extra dynamic range of the detector employed in the experimental implementation resulted in high values of signl-to-noise ratio and allowed the use of a single Wiener filter in the decoding of the cubic phase mask images.

Finally, the imperfections in the reconstructed images are caused mainly by the extreme values of defocus that suppress the spatial frequencies outside the horizontal and vertical axes into the noise floor. This results in a greater loss of contrast for diagonal frequencies as can clearly be seen in Fig. 6.3 (d)-(e). Unfortunately, this effect will be present in any phase mask with only one axis of antisymmetry. Phase masks with more than one radial direction of constant optical path difference tend to develop more uniform noise amplification across the spatial frequency space. Phase effects that can be so prominent in deconvolved wavefront-coded images are barely apparent in the images presented here because the high spatial frequencies responsible for these edge effects (replica and ringing) were attenuated by the Wiener algorithm.

These experimental realizations demonstrate an increased defocus tolerance by means of a cubic phase mask and postdetection digital signal processing. The performance of a wavefront coding system in terms of MTF and PSF obtained during the modeling stage of this project were in agreement with the experimental results presented here. Future work on this area, and which is beyond the scope of this thesis, should include a study into more elaborated digital deconvolution algorithms to reduce noise amplification in the restored images.

2 Electro-optical protection measures (EOPM) with wavefront coding

2.1 Introduction

The employment of lasers to neutralize optical and infrared imaging systems relies on two considerations: The directionality of lasers can readily enable the transmission of intense radiation to the detector plane of a remote imaging system and secondly, imaging sensors at visible and infrared wavelengths can be damaged or dazzled (jammed) with relatively low radiation intensity. Wavefront coding offers an important opportunity to counter the above: the potential to reduce the peak

intensity in the image of a point source whilst minimizing the reduction in image quality.

The salient aim of the work described in this section is an assessment of the feasibility of using wavefront coding in the reduction and compression of the peak intensity in the image plane of a visible-band imager. The main objectives are to quantify the reductions in peak intensity and the associated performance cost in terms of image signal-to-noise ratio so as to enable an assessment of the merit for further research in this area.

2.2 Theoretical attenuation of the peak intensity

A necessary feature of wavefront coding is that the PSF is broadened across an increased number of detector pixels, such that for illumination by a point source, peak intensity is reduced. As a corollary, image contrast is also reduced. Subsequent to inverse filtering, contrast and peak intensity is restored in the recovered image; that is to say, wavefront coding compresses the dynamic range of light intensities at the detector, whilst digital restoration decompresses the range of intensities in the image. It can be appreciated that wavefront coding can be used to increase dynamic range in the image beyond that of the detector. The magnitude of these improvements is greatest for an isolated point source as is encountered when a laser is imaged or in astronomy as will be demonstrated in the next section.

In Fig. 6.5 are shown three-dimensional representations of PSFs obtained at the focal plane of an optical system in which cubic or generalised phase masks (such as petal phase mask, see Ref.[42]) with increasing phase retardation have been inserted. As previously stated, the wavefront coding PSFs are spread over a larger area, that is more pixels, in comparison with that of a conventional system.

Let us recall that the petal phase mask is described by $\theta(x, y) = \alpha(x^3 + y^3) + \beta(x^2y + xy^2)$ and it was presented in Chapter 5. In a conventional, diffraction-limited system, light is focused into the Airy disk, which is generally matched with the detector so that most of the power incident at the pupil-plane of the imager will be coupled into a single pixel. The peak intensity at the detector is therefore reduced for the same total optical throughput. The calculated attenuation of the PSF peak intensity at the focal plane as a function of the peak-to-valley phase retardation parameters for both cubic and petal phase masks is shown in Fig. 6.6 and Fig. 6.7

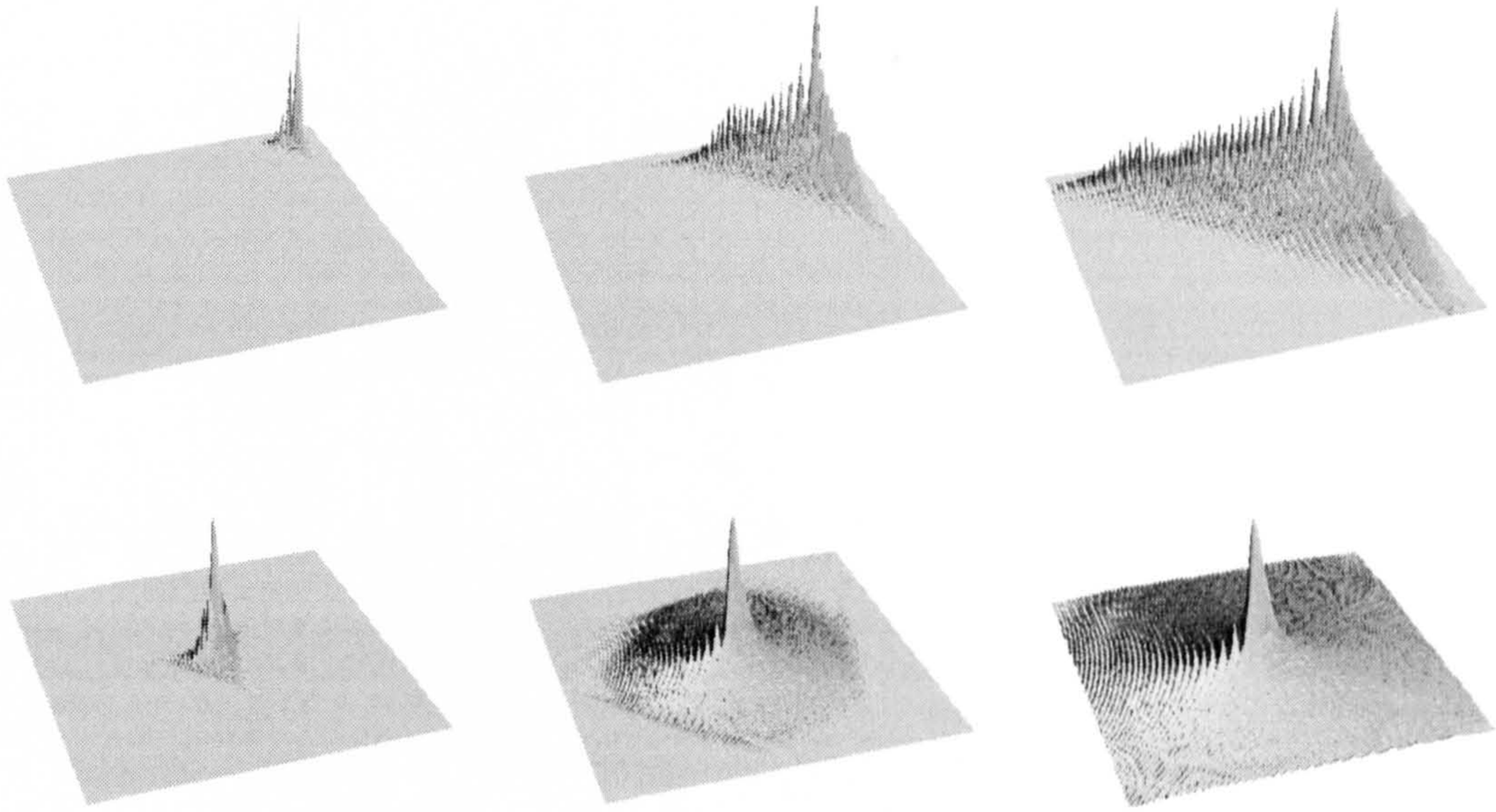

$OPD_{max} = 2\lambda$ $OPD_{max} = 10\lambda$ $OPD_{max} = 20\lambda$

Figure 6.5: *Three-dimensional intensity distribution of the point spread function for a cubic phase mask (top) and petal phase mask (bottom), for increasing values of phase retardation. The PSFs energy was varied in order to maintain a maximum intensity value of 1. The area shown in each plot remains constant.*

respectively. The attenuation of the peak intensity is given by the ratio of the PSF maximum intensity of a diffraction-limited optical system divided by the PSF maximum intensity of the same optical system in which a wavefront coding phase mask was inserted. The effects of sampling and pixelation have not been included in this analysis. In addition, the peak attenuation has been calculated for a cubic phase mask placed in a circular aperture. Nevertheless, a better attenuation is attained with a rectangular aperture. From the computations, a significant reduction of the PSF peak intensity can be obtained even for moderate values of peak-to-valley optical path difference. For instance, a circular cubic phase mask with peak-to-valley phase retardation of 10λ, which corresponds to $\alpha = 5\lambda$, allows an attenuation of a factor of almost 35. On the other hand, the use of a petal phase mask with the same amount of optical path difference achieves a reduction of a factor of 100.

The most important criterion from a users perspective is not the peak-to-valley path difference introduced by the phase mask, but the cost in terms of imaging performance associated with the compression of laser light intensity; that is, it is important to consider the ability of the wavefront coding phase masks to reduce the peak intensity together with the noise amplification introduced during the restora-

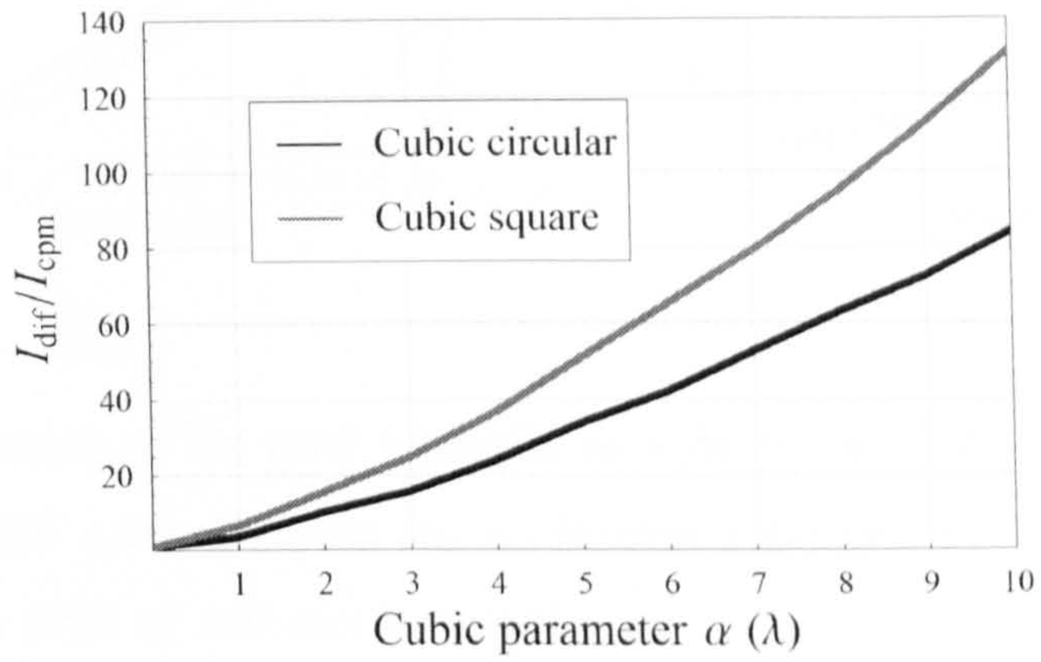

Figure 6.6: *Theoretical reduction of the peak intensity as a function of the parameter α introduced by the cubic phase mask. The intensity reduction was calculated for circular and square apertures.*

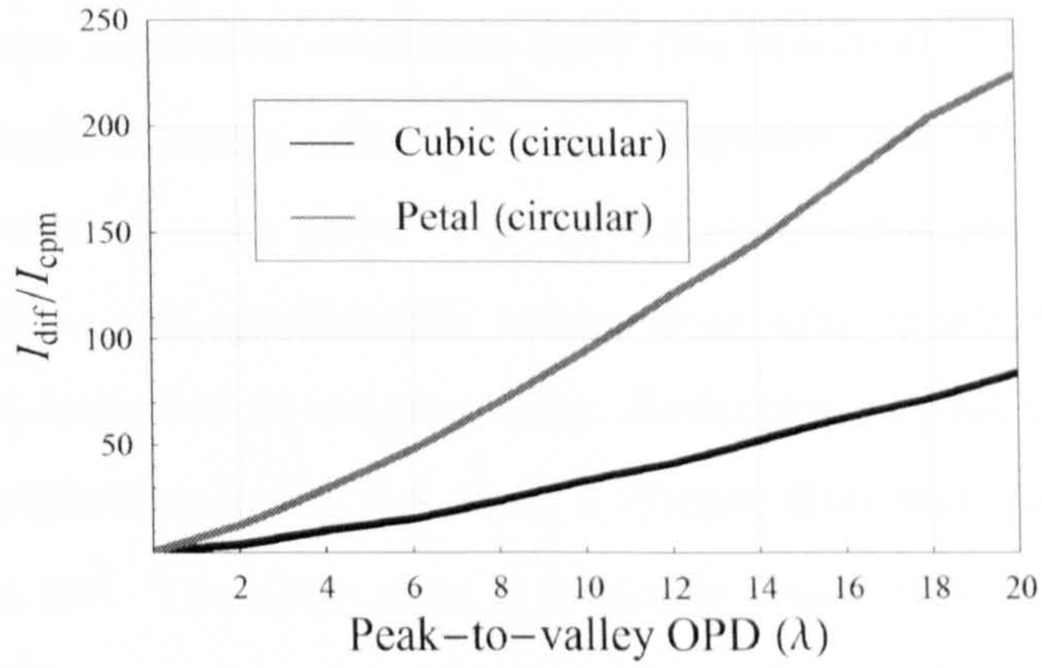

Figure 6.7: *Theoretical reduction of the peak intensity as a function of the peak-to-valley optical path difference introduced by a circular cubic and petal phase masks.*

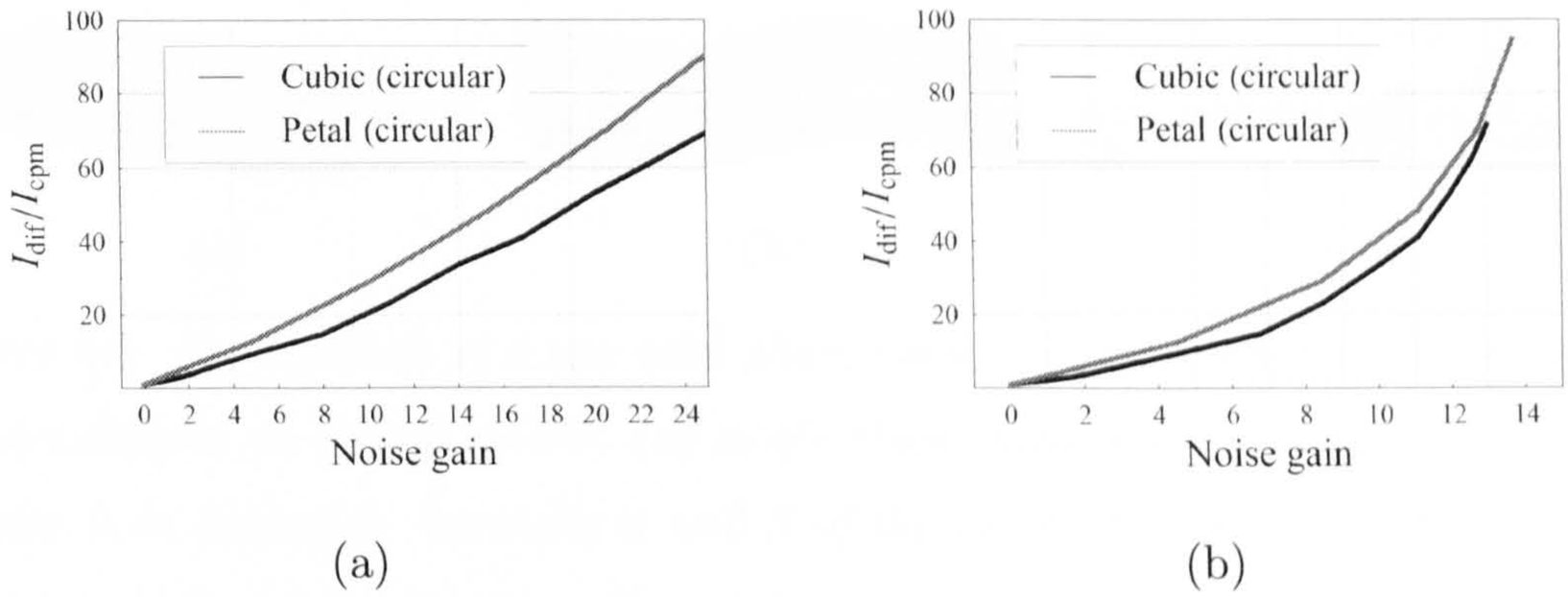

Figure 6.8: *Reduction of the peak intensity as a function of the noise amplification in the restored PSF after applying (a) an inverse filter and (b) a Wiener filter. In the latter case, a SNR of 100 was assumed.*

tion process. Without considering the effect of detector sampling, the wavefront coded PSF is deconvolved so that the restored PSF becomes the diffraction-limited Airy disk (inverse filter).

In general, the signal-to-noise ratio of the deconvolved image will be different from that of the original. The variation of the amplification of the noise (that is reduction in SNR) with degree of suppression of point source intensity is summarized in Fig. 6.8. This shows that for equal SNR gain the suppression of point-source intensity is typically a factor of 2.6 greater than the noise amplification for the cubic mask and a factor of about 3.5 greater for the petal mask. For the use a simple neutral density filter this factor would be unity (for detector-noise limited imaging), so this overly simplistic result offers a modest improvement of a factor of about 4 over a simple neutral density filter. Further improvements can be achieved: The use of a Wiener filter will significantly reduce noise amplification whilst incurring, typically, minimal reduction in image quality. Reduction in peak intensity is plotted against noise amplification in Fig. 6.8 when a Wiener filter is employed and the SNR at the detector is 100. The noise gain is typically about 60% of that exhibited by an inverse filter. The use of more sophisticated non-linear filters have been claimed to offer further improvements. Based on the above arguments, it is probable that further work will produce reductions in point-source intensity to about ten times more than the reduction in SNR.

(a) (b) (c)

Figure 6.9: *Combination of a two-petal phase mask to control the amount of wavefront coding in an optical system, (a) single phase mask where the values of α and β have been magnified, normally α and β of the order of microns, (b) position of cancelation of wavefront coding effect, (c) maximum wavefront coding effect.*

Phase mask of variable strength

The use of wavefront coding requires a trade-off between reduction in peak laser intensity and reduction in the signal-to-noise ratio; that is, the greater the improvement in EOPM parameter, the greater will be the reduction in the SNR. We describe here a novel solution to this problem. Clearly active optics techniques can be used to implement the wavefront coding mask in an agile way so that EOPM could be employed to protect imagers only when most needed and the reduced SNR can be tolerated. At other times wavefront coding could be reduced or removed so that the maximum SNR could be obtained but with reduced EOPM. Wavefront modulation techniques currently employed in adaptive optics (deformable mirrors, liquid crystal modulators) could enable agile deployment of wavefront coding, however the technique described here offers a more convenient, low-cost route to agile implementation of wavefront coding at all imaging wavelengths. The technique may be used with the generalised (petal) wavefront coding mask. To enable agile implementation two such wavefront coding masks are introduced into the pupil plane of an imager such that one is fixed and the other rotated about its axis as depicted in Fig. 6.9. In Fig. 6.9(a) is shown a single wavefront coding phase plate, whilst in Fig. 6.9(b) is shown two phase plates combined with the lower phase plate rotated 120° about its axis such that the depressions of one phase plate coincides with the peaks of the other and the overall phase plate introduces no net phase modulation and wavefront coding is absent. In Fig. 6.9(c) the lower phase plate is rotated such that the depressions and peaks on each phase plate coincide and the net phase modulation is twice that of a single phase plate in isolation. The petal form is retained at all intermediate rotations and therefore the amplitude of phase modulation introduced by this compound system can be continuously varied between these two extremes

to enable real-time trade of EOPM against SNR according to operational requirements. This implementation offers the potential for the agile introduction of EOPM with negligible performance penalty.

2.3 Experimental realization of the peak compression

An experimental realization was arranged to determine the reduction of the peak light intensity when the cubic phase mask is employed. The experimental setup is equivalent to the one used in the previous section and is illustrated in Fig 6.2.

There are two scenarios that are of interest: firstly, when the scene is dominated by a laser source and secondly, when the laser source is contained within a representative scene dominated by edges (hence, with Fourier spectrum similar to 1/frequency). The former case corresponds to, for example, laser illumination from an empty sky.

First scenario

In Fig. 6.10 the scene is dominated by a laser source, and shows in (a) the noisy image detected when the manufactured cubic wavefront coding mask is used with a square aperture, with $\alpha = 2.5\lambda$ and a SNR of 790, where SNR is defined as the peak pixel value divided by the standard deviation of the background noise[†]. When inverse filtering is performed onto the detected image of a point object, a diffraction-limited PSF image was obtained as shown in Fig. 6.10(b). The central peak is now a sinc^2 function and the SNR is increased to 3500. In this case the inverse filter provides more amplification of the point source than it does of the white noise and for this type of target the output SNR will always be higher than the input SNR.

It can be observed from Fig. 6.10(a) and (b) that a experimental peak attenuation of a factor of 19.9 is obtained, in accordance with the predicted theoretical results (a factor of 20.5)[‡].

[†]The 12-bit cooled Retiga camera provided 4096 gray levels with a noise standard deviation of 5, thus SNR is 820

[‡]Another method to assess the reduction factor of the peak intensity consisted in measuring the maximum exposure time at which the PSF peak intensity attained the detector's maximum saturation level for both the wavefront coding and standard systems. The ratio between the two exposure times gave an estimation of the distribution of energy across the surface of the detector. For the standard system, the maximum intensity level after 2.72 milliseconds of exposure time was 4047, near saturation. Preserving the same experimental conditions, the cubic phase mask was

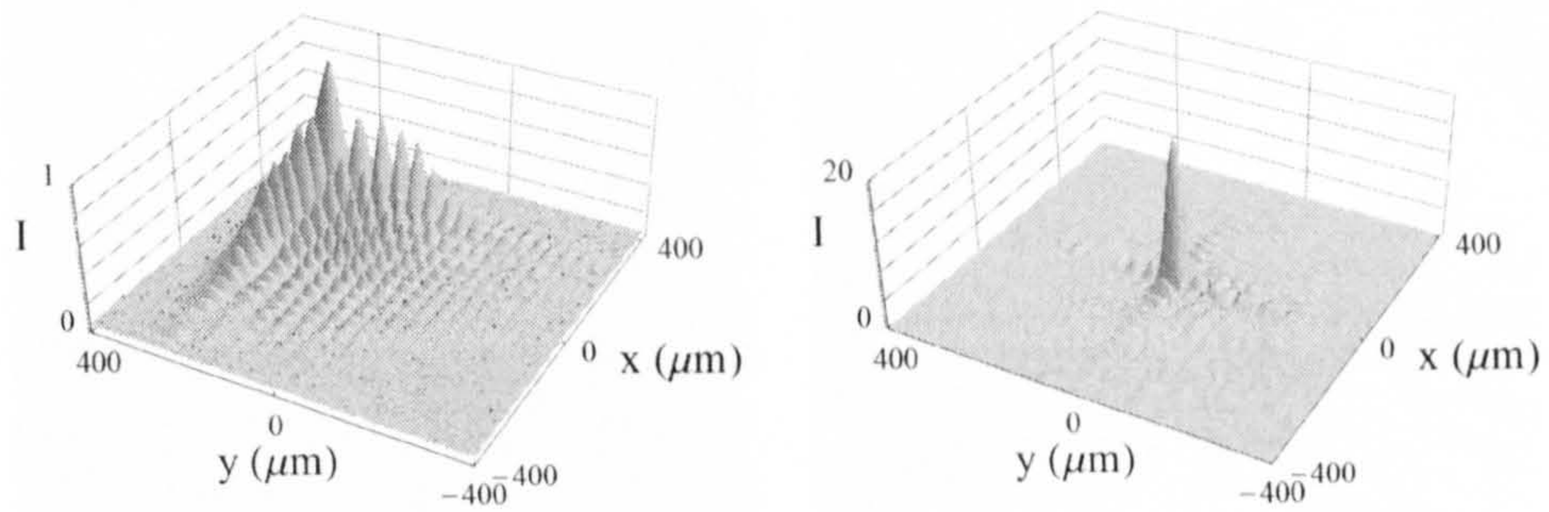

(a) (b)

Figure 6.10: *(a) Detected image for a square cubic phase mask with $\alpha = 2.5\lambda$ and detected signal-to-noise ratio of 790 (58 dB) and (b) deconvolved image; SNR is 3500 (70 dB).*

Second scenario

In the second scenario a more typical image containing the intense point source within an image containing edges we see a different behavior and this is illustrated by the images in Fig. 6.11. The scene, a spoke target with an aperture in it, was placed precisely on the laser point source. A 0.9 mW laser diode of wavelength 632.8 nm was filtered using a 5-micron pinhole. Light emerging from the pinhole went through the opening and was imaged by the optical system. The diameter of the laser spot in the plane of the optical lens was 2.6 m. A fibre-optic light source illuminated the spoke target uniformly. Fig. 6.11(a) represents the recorded image at the detector using the manufactured square cubic phase mask. Note that the peak intensity of the laser light has been sufficiently suppressed to approximately the same intensity level as the scene. The inverse filtered image is shown in Fig. 6.11(b) and demonstrates a reduced SNR of 10. Horizontal profiles of the line containing the peak of the imaged laser spot in Fig. 6.11(a) and (b) are shown in Fig. 6.11(c) and (d). This clearly shows that whereas the laser spot is discernable in the detected image it is detectable with a high SNR in the inverse-filtered image. It is clear from the images in Fig. 6.11 that if we define the SNR in the detected image as the peak detected signal for a point source to the standard deviation of the noise, then wavefront coding increases the SNR, however if the SNR in the detected image is

placed in the aperture stop. After 53.47 milliseconds the maximum intensity level reached 4050. The ratio between the two exposure times gave a factor of about 19, which is in agreement with the previous experimental result.

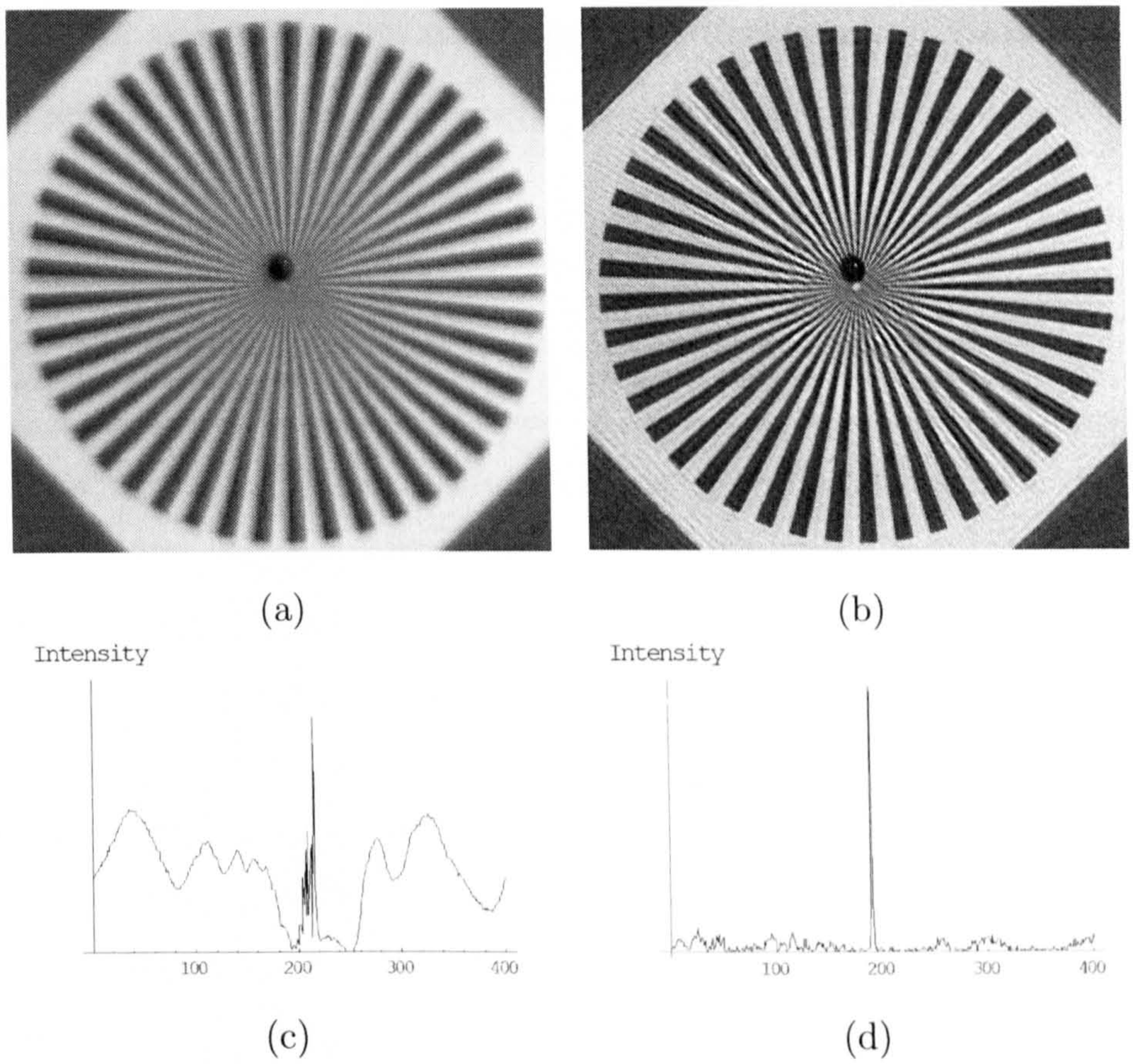

Figure 6.11: *Depiction of the different gain mechanisms for a point source and edges. (a) shows the image of this scene recorded with a wavefront coding mask with* $\alpha = 2.5\lambda$ *and a SNR of 790. (b) Shows the deconvolved image, (c) is a horizontal profile through (a) along the line containing the laser source and (d) shows a horizontal profile through (b).*

defined as the ratio of the intensity step at an edge (contrast) to the noise, then the SNR is reduced by wavefront coding.

Probably of greater interest is the change in the SNR when recording extended scenes and in this case, as described above, edges are not modified in magnitude whilst the noise is increased and this results in the observed reduction in SNR.

In summary, wavefront coding offers scope for reduction in laser intensity at the detector and there is the potential to provide an order of magnitude improvement in SNR over the simplest option of simply inserting a neutral density filter into the optical path. Of specific interest is the potential for using two wavefront coding elements, as discussed in the pervious section, to enable agile implementation of wavefront coding and hence of trade off of SNR reduction against protection. The set of images presented here shows a possible application of a wavefront coding

optical system, and they clearly demonstrate its effectiveness in the attenuation of the peak intensity.

3 Athermalization of infrared imaging systems

A prominent feature of wavefront coding is that it enables some of the burden for image formation to be shifted from a requirement for high-performance, high-cost imaging lenses to high-performance, low-cost postdetection digital processing. This is particularly pertinent to thermal imaging. The requirement for high sensitivity demands fast optics that employ not only multi-element aspheric lenses for aberration control but also expensive infrared transmissive material such such as germanium and gallium arsenide, which are expensive and tend to introduce additional chromatic- and thermal-related defocus. As we demonstrate in the next section, the ability of wavefront coding to mitigate aberrations can especially be used to reduced and overcome thermal defocus problems. It can also be applied for achromatization of thermal imagers with chalcogenides (GASIR) but due to noise issues, we suggest chromatic aberration be corrected with other well-established techniques, such as diffractive optics, that have a significantly lower impact on the detected image [108, 109].

3.1 Concept of thermal defocus

It is well known that thermal defocus exhibits a real problem in thermal imagers [110, 111]. Conventional infrared optical materials have large variations in index of refraction with temperature. For example, the variation of refractive index with temperature for germanium is over 100 times that of common optical glasses. This complicates the design and fabrication of simple optical systems that can operate reliably over even a small range of temperatures.

Athermalization is the correction of the effect of focus shift with temperature. Active temperature control for IR imaging systems increases the cost, size, and weight of IR imaging systems. The concept of designing optical systems insensitive to temperature is not new: Grey applied the idea as early as 1948 [112]. Since then, many mechanical and optical methods have been tried to accomplish athermalization [113, 114, 115, 116, 117, 118]. These include using a combination of optical materials with different refractive optics, using temperature sensors to actuate motors which move the lenses axially to the require positions, using optical mounting materials that differentially expand with temperature so as to compensate the changes in optical properties. Since the aberrations that arise by temperature changes are

mainly defocus aberration, wavefront coding offers the potential to be used on its own or in combination with the mentioned athermalization methods to control the temperature effects.

To quantify the effect of temperature, we consider a simple IR germanium optical system. Because the effect of temperature in the index of refraction of germanium is an order of magnitude greater than the effect on the thickness and radius, we can consider without large error, only "thin" lenses. The thermal defocus over a temperature change of ΔT for a lens element of effective focal length f is [116]

$$\Delta f = -\delta f \Delta T, \tag{6-1}$$

where δ is analogous to a *focal length expansion coefficient* which characterises the change of converging power of the lens with respect to temperature. The thermal constant δ for the material is given by

$$\delta = \frac{\mathrm{d}n/\mathrm{d}T}{n-1} - \alpha, \tag{6-2}$$

with n the refractive index of the material and α the expansion coefficient. For a germanium system with a 75-mm-focal length at 20°C and a ±40°Ctemperature range, the focal shift is 0.38 mm. This thermal focal shift Δf corresponds to a defocus aberration,

$$W_{20} = \frac{\Delta f}{2}\left(\frac{1}{2F/\#}\right)^2, \tag{6-3}$$

where $F/\#$ is the f-number. A thermal focal shift of 0.37 mm in an $F/1$ infrared optical system introduces a defocus aberration coefficient W_{20} of 4.5λ, with an operating wavelength of 10.5μm. Furthermore, if we allow a maximum of defocus aberration of $W_{20} = \lambda/4$, i.e. in agreement with the Rayleigh criterion, the maximum allowable temperature change is less than 3°C.

This significant performance limitation motivated us to design a wavefront coding long-wave IR thermal imager. The focus-invariant feature of wavefront coding jointly with digital decoding offers the potential to implement athermal, diffraction-limited IR imaging using simple and low-cost optics. In this section, we explore the use of a cubic phase mask and signal processing as an athermalization technique in a practical IR optical system in which no thermal compensation has been included.

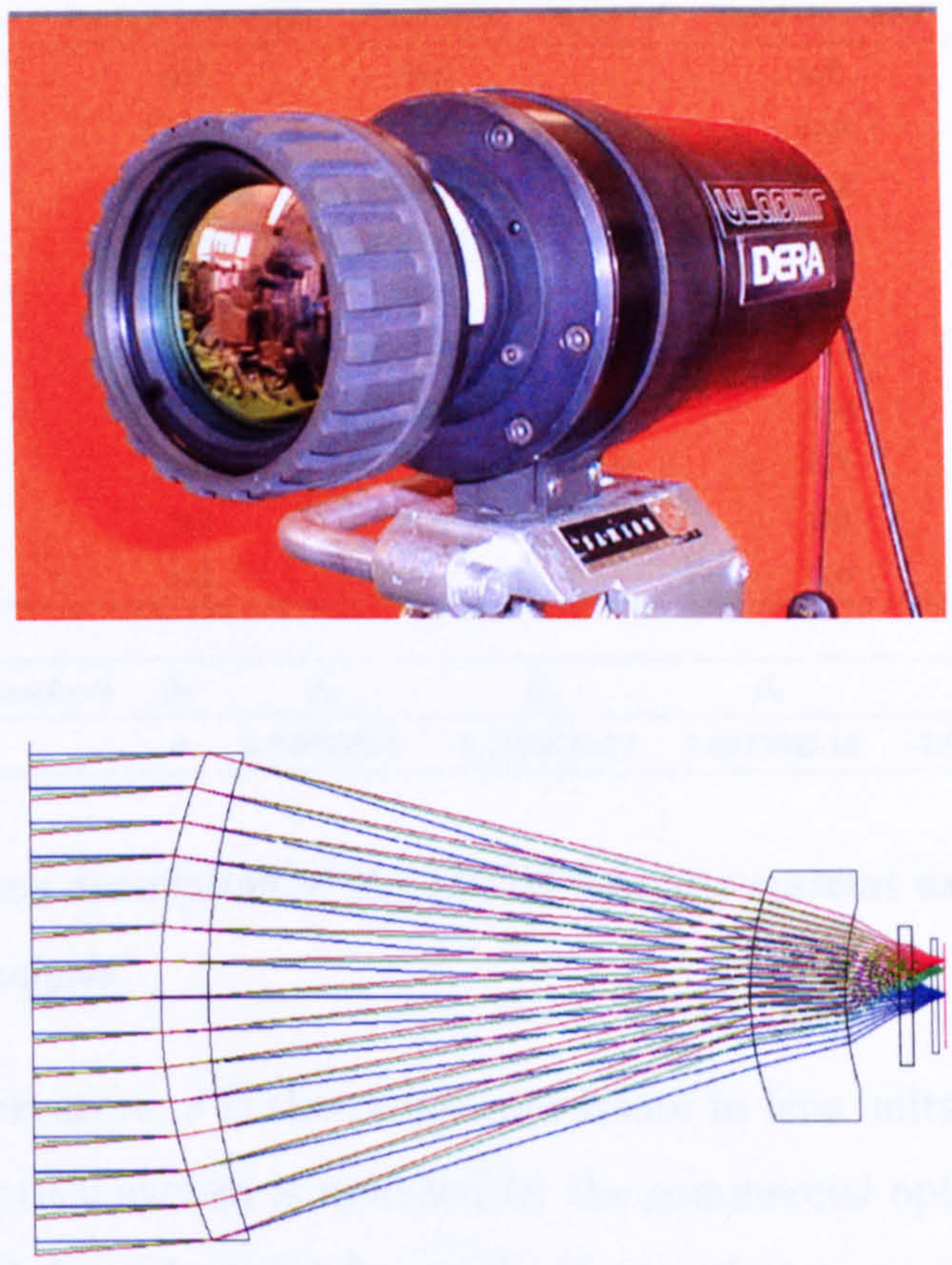

Figure 6.12: LWIR *imaging system and the corresponding Zemax diagram used in the wavefront coding implementation.*

3.2 IR optical system and detector modeling

System overview

The desired goals for this IR system are an $F/1$ system with a 75-mm focal length and a 12×9 degrees of field of view, as shown in Fig. 6.12. The operating wavelengths are $8-12\mu$m and the system is designed to be diffraction limited at 20°C. The optical material used in this design is germanium. Our aim is to maintain the optical performance over the temperature range: -20°C to $+70$°C. The optical system is based on the Petzval configuration, which includes an aspherical front element and a thick spherical germanium meniscus element. The detector window is also made of germanium and the mounts are made of aluminum. The complete optical characteristics for the optical system are given in Table 6.1. The back surface of the front element is an even asphere which is described by the common expression

$$z = \frac{cr^2}{1+\sqrt{1-(1+k)c^2r^2}} + \beta_1 r^2 + \beta_2 r^4 + \beta_3 r^6 + \beta_4 r^8 + \beta_5 r^{10}, \qquad (6\text{-}4)$$

Surface	Radius curvature	Thickness	Material	Semi-diameter	Conic
Obj.	Inf.	Inf.		Inf.	0
Stop	94.800	7.50	Ge	37.5	0
2*	119.703	83.94		36.8	0
3	50.680	14.80	Ge	19.0	0
4	51.061	8.38		14.3	0
5	Inf.	2.00	Ge	10.6	0
6	Inf.	3.00		10.4	0
7	Inf.	1.00	Ge	8.7	0
8	Inf.	1.01		8.6	0
Ima.	Inf.			8.0	0

*Even Asphere	β_1	β_2	β_3	β_4	β_5
	0	2.34049E-8	-5.79050E-12	7.82778E-15	-2.53723E-18

Table 6.1: *The lens description of the* LWIR *imaging systems used in the wavefront coding system analysis.*

where c is the curvature, r is the radial coordinate in lens units and k is the conic constant. The optical system is modeled by the commercial optical design package Zemax. The field-dependent weights in the Zemax design vary linearly from 1 on-axis to 0.5 off-axis. The wavelength-dependent weights are set at 0.5 for 8 and 12 μm and at 1 for 10.5μm. The thermal coefficient of expansion (TCE) for aluminum within the goal temperature range is 23.0×10^{-6} and is introduced in the TCE cell of the Zemax model. This optical system images with high quality across the entire field of view and over the entire LWIR spectrum. For example, the optical path difference (OPD) variation across the field of view is less than $\lambda/4$. Thus, for clarity, the optimization of the wavefront coding optical system is performed taking into account only the on-axis MTFs. However, the PSFs across the entire field of view will be displayed.

The system uses a resistive bolometer focal plane array detector with $25 \times 25\mu$m pixel size. The fill factor is assumed to be 100% (i.e. the pixels are close packed). The pixel size corresponds to a Nyquist frequency of 20cyc/mm. The MTF associated with the detector array is illustrated in Fig. 6.13 and its contribution to the final MTFs is considered in the modeling and optimization of the system. Consequently, all following MTFs plots only show modulation up to the detector spatial frequency limit. A detailed derivation of the detector MTF is presented in Appendix F.

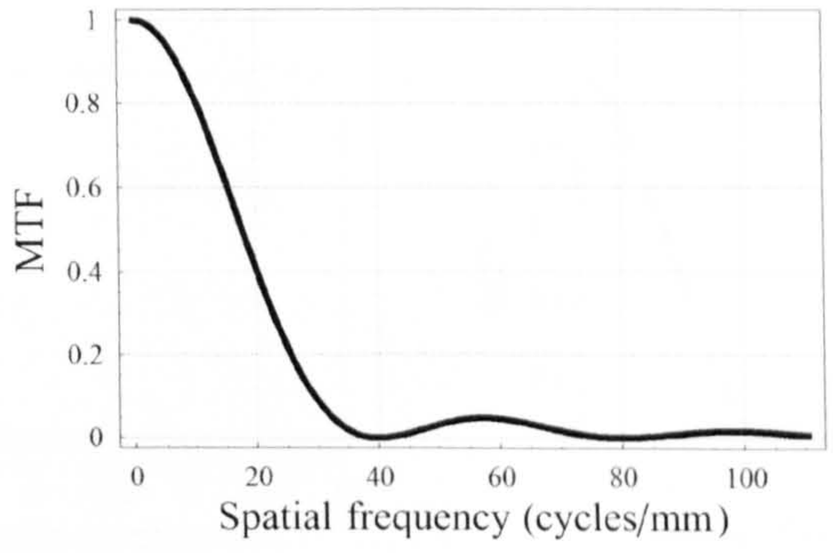

Figure 6.13: *MTF for a focal plane array detector with 25μm pixel pitch and 100% fill factor.*

Imaging performance with temperature: MTFs and PSFs

The fast speed of the optics, the simple aluminum housing and the germanium lenses make the performance of the traditional system extremely sensitive to temperature variation. The performance, as measured by the MTFs, is shown in Fig. 6.14. These MTFs include the detector MTF. At the designed temperature the traditional thermal imager achieves practically diffraction-limited performance. With a temperature change of only $\pm 5^{o}$C, the image quality becomes degraded. With temperature changes of the order of $\pm 10^{o}$C, the MTFs drop dramatically and nulls become present within the band pass. This results in a notably defocused system with loss of image information and contrast. For greater variations of temperature, the imaging performance is highly degraded. The sampled PSFs of the traditional system are shown in Fig. 6.15 as a function of temperature and for several image height positions. Note that these PSFs are essentially invariant across the detector. The sampled PSF at $+70^{o}$C is similar to that at -20^{o}C. With the help of the Zemax analysis toolbox, the amount of defocus present in the PSFs at both ends of the temperature range was calculated. The defocus coefficient W_{20} varies from -3.4λ (-20^{o}C) to $+4.2\lambda$ ($+70^{o}$C). It is evident that this infrared system requires thermal stabilization in order to operate even over a useful range of temperatures. Certainly, one might think of another alternative method such as using only post-detection signal processing in the traditional infrared optical system together with a temperature sensor inserted [81]. The sensor would enable determination of the appropriate PSF to be employed as inverse filter so the image could be restored for all temperatures. However, the corresponding MTFs would contain zeros which

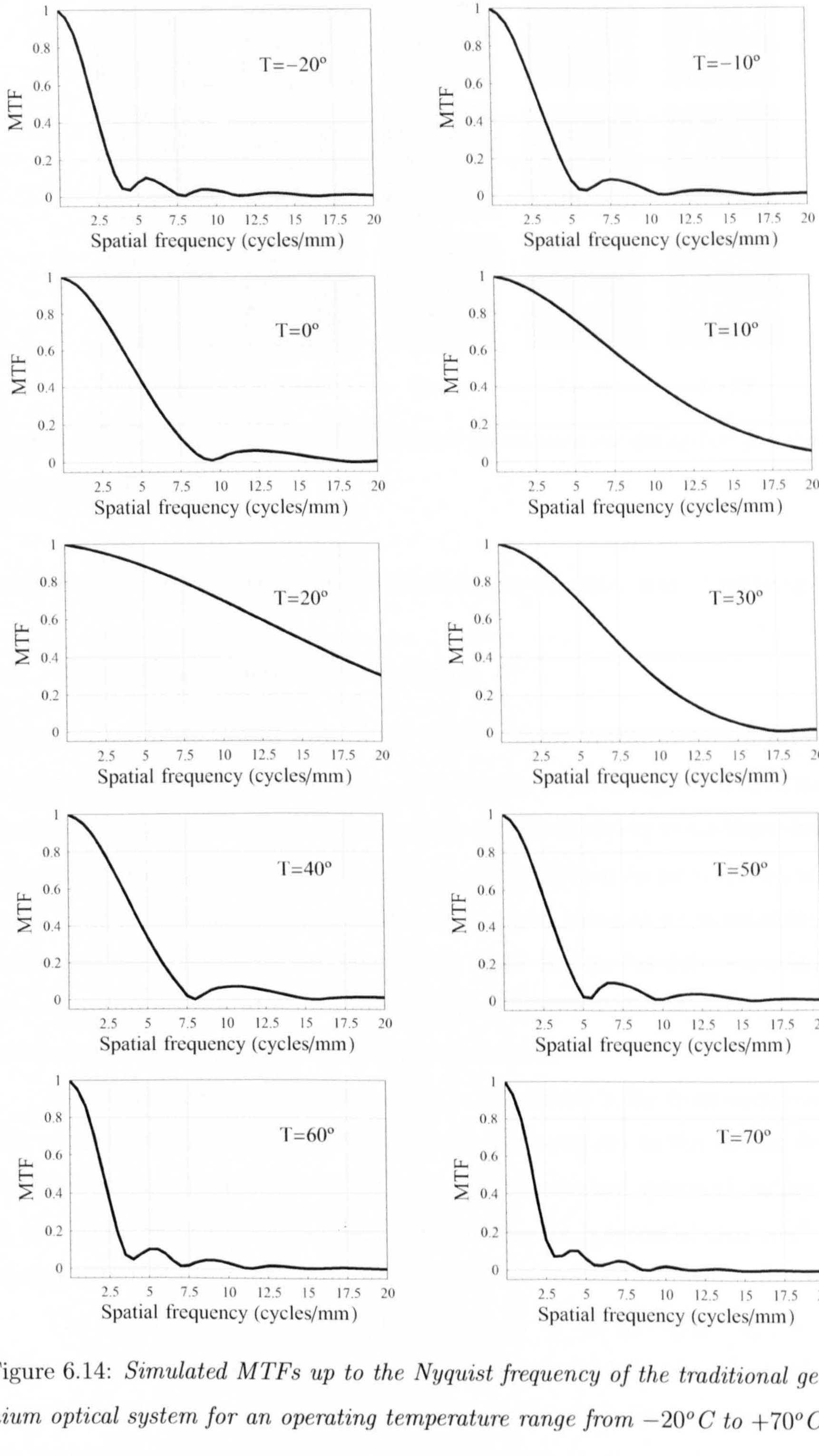

Figure 6.14: *Simulated MTFs up to the Nyquist frequency of the traditional germanium optical system for an operating temperature range from* $-20^{o}C$ *to* $+70^{o}C$.

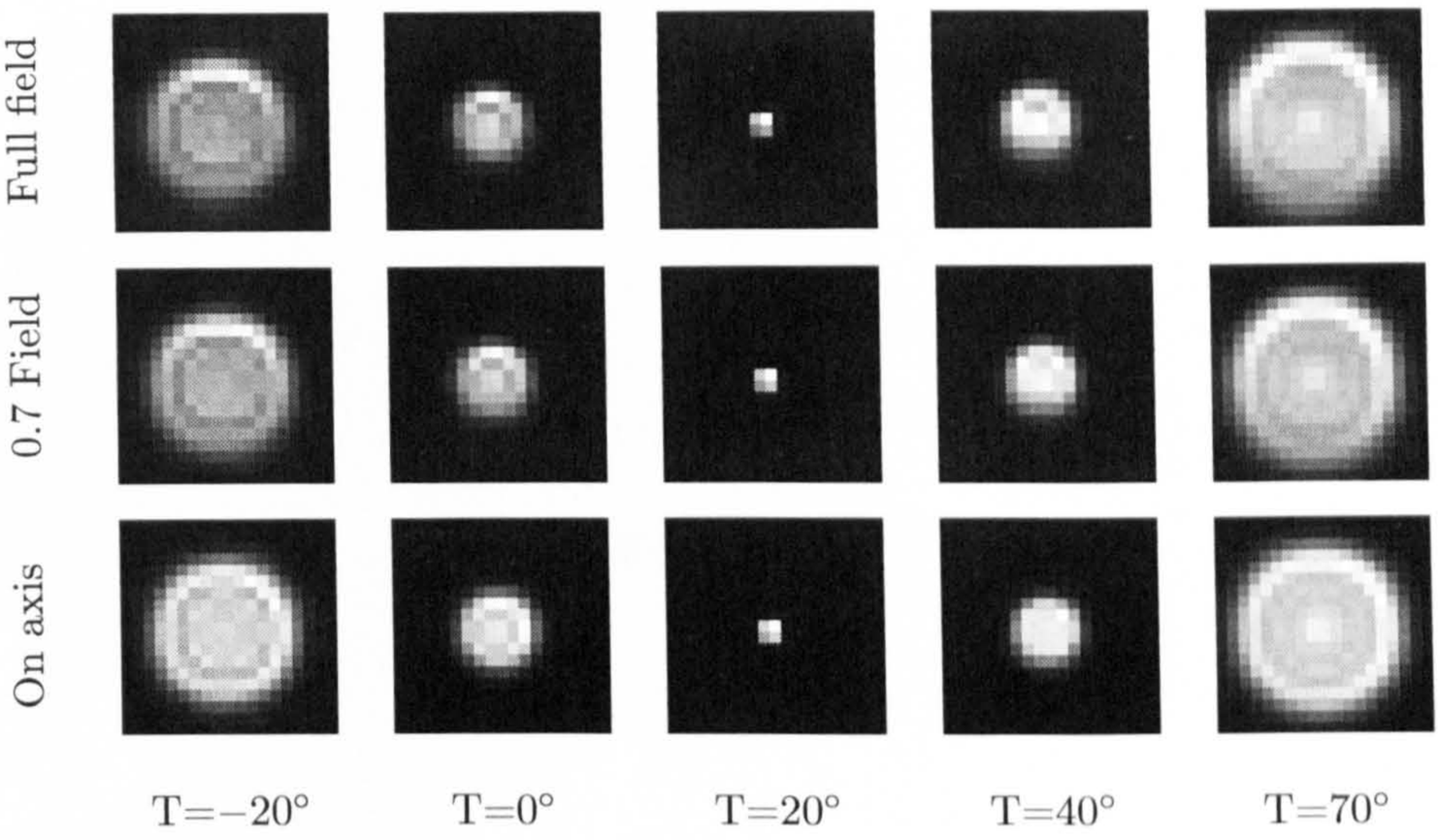

Figure 6.15: *Simulated PSFs of the traditional germanium optical system for various operating temperatures.*

would yield loss of information or infinite noise amplification in the final image.

3.3 Wavefront coding IR system

Antisymmetric phase masks such as the cubic or petal enable to reduce the effect of thermal defocus in the IR system. The election of an adequate antisymmetric phase mask for this application is dictated not only by its ability to alleviate thermal defocus but, to a greater extent, its impact on the signal-to-noise ratio of the restored image. The level of noise is particularly relevant with low-cost uncooled detectors; hence, care must be taken when choosing the mask. For similar defocus mitigation, the cubic phase mask produces a lower noise amplification than the petal mask [119], and therefore the cubic is selected for this application.

A cubic phase mask with parameter α is introduced in the front surface of the first optical element (surface 1 in Table 6.1). With respect to the Zemax design, the cubic element is implemented by changing the *standard spherical* surface 1 to an *extended polynomial* surface which allows adding the polynomial term $\alpha(x^3+y^3)$ directly onto the spherical sag.

The degree of athermalization is determined by the strength α of the cubic phase mask. Acceptable athermalization performance can be achieved according to the noise amplification and temperature range trade-off set by the requirements of the application. In the next section, a type of system optimization based on metrics

such as the MTF and noise amplification is performed to determine an optimum cubic phase mask.

Optimum value of α

The degree of athermalization to be achieved must be balanced against the reduction in the signal-to-noise ratio incurred by inverse filtering. Three figures of merit specific to this IR imaging system are selected in order to obtain an optimum value of α:

- The MTF of the wavefront coding system does not have nulls within the band pass and throughout the entire operating temperature range.
- The noise amplification after inverse filtering is minimum.
- The insensitivity of the MTF with temperature is maximum.

The last two points are explained in more detail as follows. A simple inverse filtering F is considered, which is given in the spatial frequency domain by

$$F(\nu, \alpha, T) = \frac{MTF_{dl}(\nu)}{OTF(\nu, \alpha, T)} \tag{6-5}$$

$OTF(\nu, \alpha, T)$ is the appropriate optical transfer function recorded with the cubic phase mask at a given temperature T (i.e. the inverse filter kernel is varied with temperature), and MTF_{dl} is the sought modulation transfer function, normally the transfer function of a diffraction limited imaging system. The system specifications required a restored MTF at the Nyquist frequency of 0.5 for all the temperature range. Based on the inverse filter of Eq.(6-5), the noise gain is calculated across the entire temperature range and its mean value computed for each value of α. Thus, the mean noise gain in decibels units is described by the following expression:

$$\overline{NG_{dB}}(\alpha) = \frac{1}{M} \sum_{T=T_0}^{T_{M-1}} -20Log_{10} \left(\frac{1}{N} \sum_{\nu=\nu_0}^{\nu_{N-1}} |F(\nu, \alpha, T)|^2 \right)^{1/2}, \tag{6-6}$$

where $T_0 = -20°\text{C}$, $T_{M-1} = +70°\text{C}$, $\nu_0 = 0\text{cyc/mm}$ and $\nu_{N-1} = 20\text{cyc/mm}$. A minus sign is introduced to represent the noise gain as a loss of signal-to-noise ratio.

A criterion to measure the MTF invariance with temperature is also produced. It employs the relative variation between the thermally in-focus MTF and thermally out-of-focus MTF as a metric of temperature insensitivity. We can express this

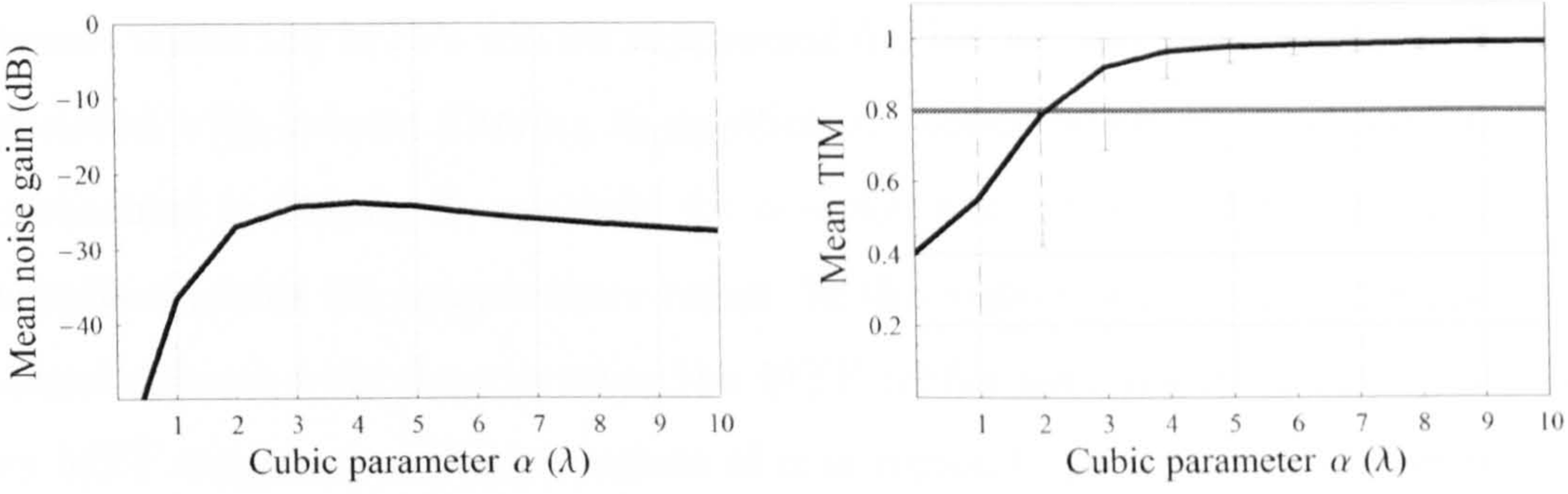

Figure 6.16: *(a) Mean noise gain as a function of cubic parameter α (the negative sign represents loss of signal-to-noise ratio); (b) Mean temperature invariance metric (TIM) as a function of cubic parameter α. The error bars represent the dispersion of TIM across the temperature range for each alpha (only phase masks with TIM > 0.8 are considered).*

variation as the area under the out-of-focus MTF surface divided by the area under the in-focus MTF surface of the wavefront coding IR system. For each value of α, the mean across the entire temperature range is calculated, thus

$$\overline{TIM}(\alpha) = \frac{1}{M}\frac{1}{N}\sum_{T=T_0}^{T_{M-1}}\sum_{\nu=\nu_0}^{\nu_{N-1}}\frac{MTF(\nu,\alpha,T)}{MTF(\nu,\alpha,T')}, \tag{6-7}$$

where T' denotes the designed temperature at $+20^{\circ}$C.

The signal-to-noise ratio penalty can be understood from Fig. 6.16(a). The figure shows the variation of the mean noise amplification with α. To enable comparison, the MTF has been fully recovered to achieve near diffraction-limited MTF (by varying the inverse kernel with temperature), so that for small values of α, the increasing suppression of MTF with increasing temperature is manifested as increasing noise gain. The interpretation of the figure is illustrated by the following example. If wavefront coding is not used, then defocus introduced by thermal drift will suppress the MTF and some temperature-dependent restorations will produce infinite noise gain, as shown for $\alpha = 0$. For $\triangle T$ greater than $\pm 8^{\circ}$C, the defocus is sufficient to introduce zeros in the MTF and the noise amplification is infinite. If wavefront coding is used, the noise gain performance is distinctly classified into three regions: A. $0 < \alpha < 3$, B. $3 \leq \alpha < 5$ and C. $5 \leq \alpha < 10$. In region A, certain degree of athermalization is achieved, particularly for $\alpha = 2\lambda, 3\lambda$, but this only occurs for temperatures near the nominal. As the temperature approaches the

extreme values the MTFs will be suppressed further so that the noise amplification associated with inverse filtering is significant. Lower levels of noise amplification are obtained in Region B, specially for $\alpha = 4\lambda$, were thermal defocus is optimally neutralised across the temperature range. In this region, wavefront coding prevents thermal defocus from deteriorating the MTF whilst avoiding introducing unnecessary MTF suppression. Higher values of α in region C produce excessively reduced MTFs in which thermal defocus becomes practically a secondary effect. Unwanted wavefront coding power is present and noise gain starts to increase.

In combination with the noise gain plot, the mean temperature invariance metric (TIM) is illustrated in Fig. 6.16(b). For each mean TIM, its set of values or distribution is represented with error bars. Only those values of α with set of TIM values greater than 0.8 meet the temperature invariance requirements of the wavefront coding IR system. The value 0.8 was selected from the traditional IR system by taking into account the MTF variation for a temperature change of (+8°C) from the nominal. This temperature corresponds with the first manifestation of a null in the traditional MTF.

In summary, our numerical study shows that the best α for an optimum athermalization of the IR system is $\alpha = 4\lambda$. This value is introduced in the Zemax model to obtain the necessary data to produce athermalised MTFs and sampled PSFs. The MTFs of the wavefront coding IR optical system as a function of temperature before and after post-detection digital signal processing are shown in Fig. 6.17. Note that the athermalised MTFs contain no nulls and are very similar to each other throughout the operating temperature range in contrast to the traditional MTFs. After applying a single inverse filter, the upper set of MTFs is produced, which closely match the diffraction-limited performance over then entire temperature range. Note that the filter applied is the same for all the MTFs. The inverse filter was calculated from of the wavefront coding MTF at the nominal temperature (+20°C) so as to restore the MTFs to diffraction-limited quality with a modulation of 0.5 at the Nyquist frequency.

The sampled PSFs as a function of temperature before and after post-detection digital signal processing are shown in Fig. 6.18 and Fig. 6.19 respectively. It is interesting to observe in Fig. 6.18 the temperature-related displacement of the cubic PSFs following the characteristic parabolic caustic; which was the subject of extended analysis in Chapter 2. Apart from the translation, note that the PSFs bear

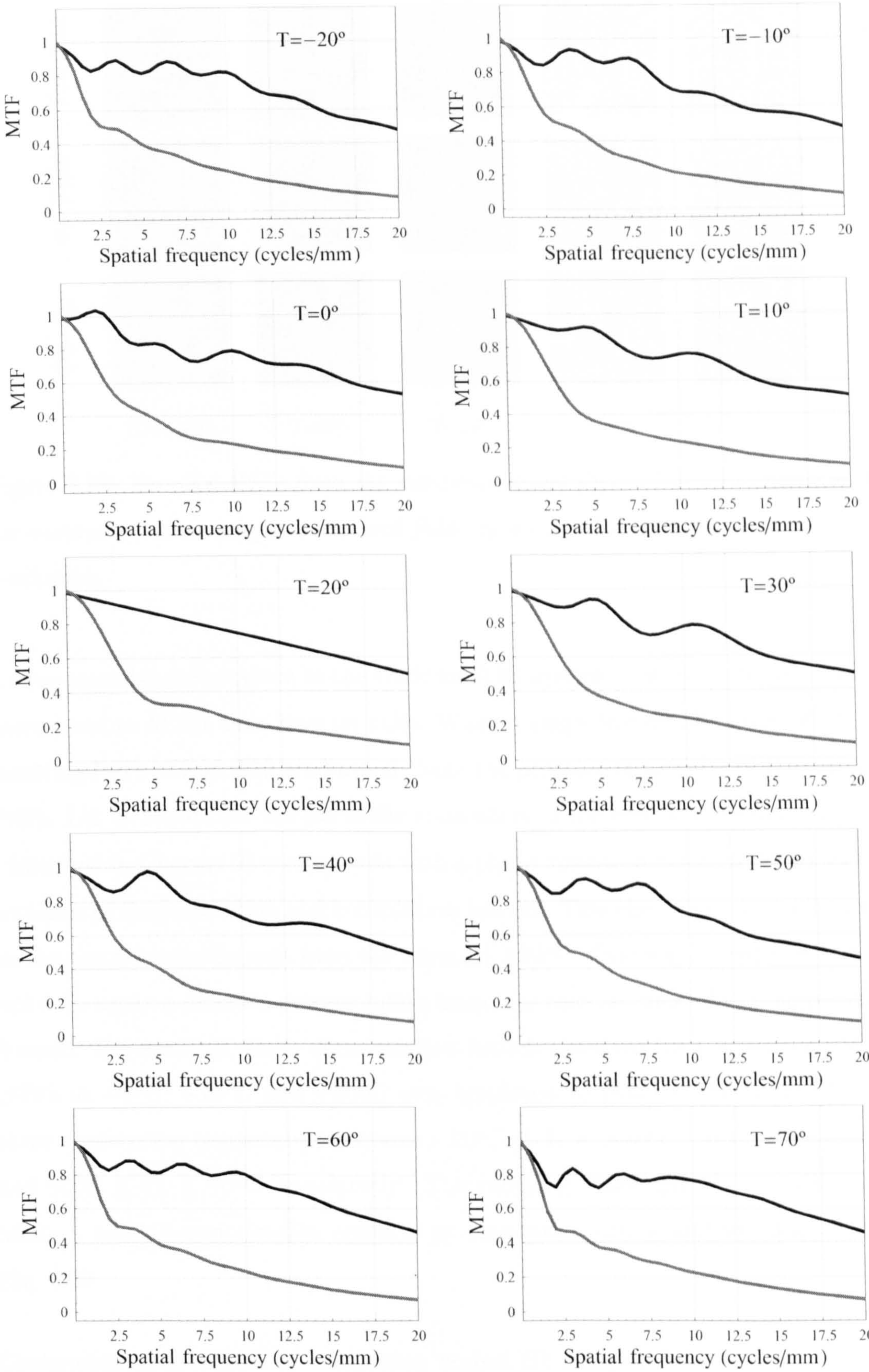

Figure 6.17: *MTFs from the wavefront coding thermal imager with* $\alpha = 4\lambda$ *for various ambient temperatures before (gray) and after (black) applying post-detection digital processing.*

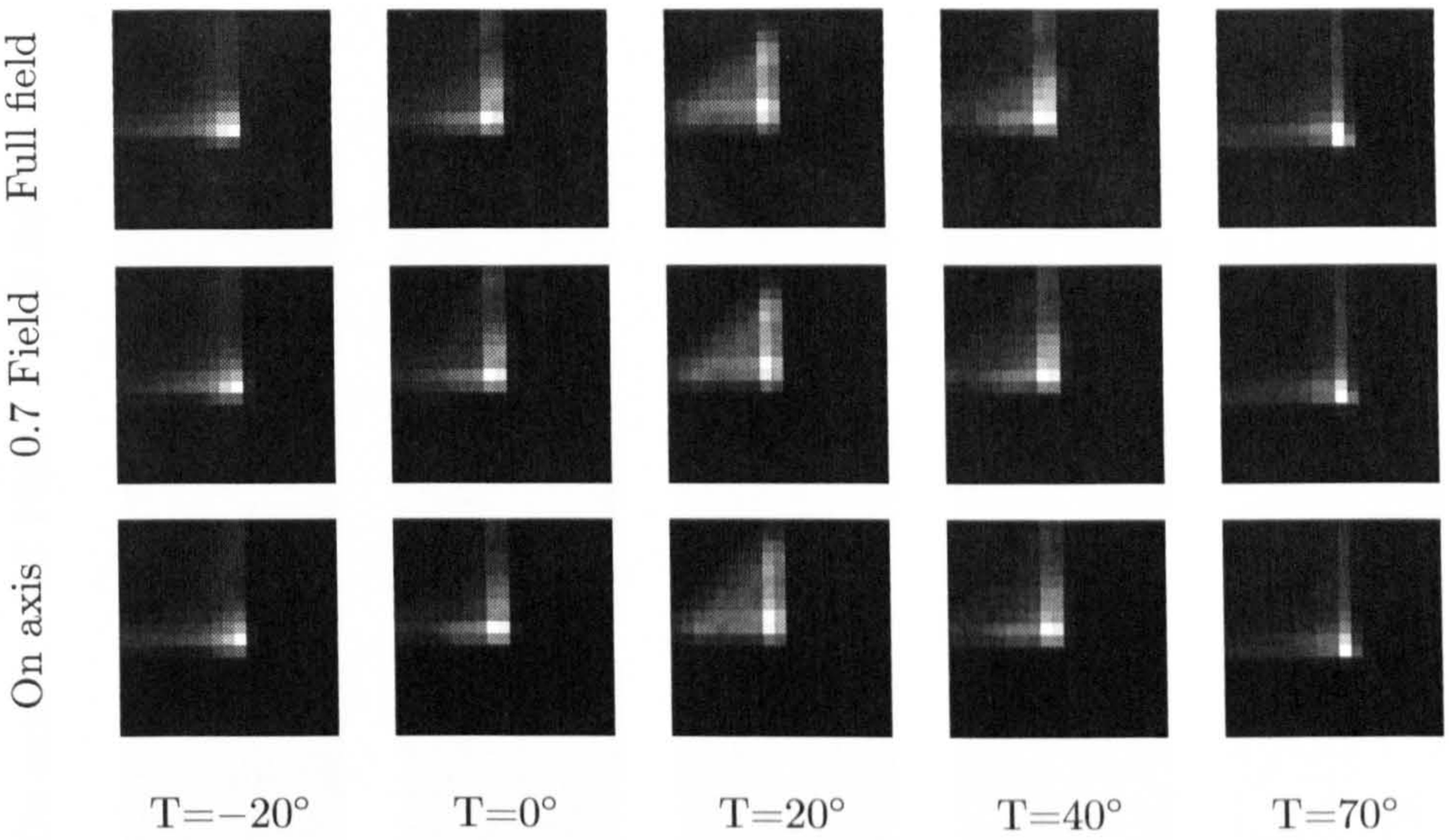

Figure 6.18: *Sampled PSFs from the wavefront coded thermal imager with* $\alpha = 4\lambda$ *for various ambient temperatures and fields of view before applying post-detection processing.*

a close resemblance compare to the traditional IR system. Furthermore, these PSFs correspond to MTFs that have no nulls. When a single inverse filter is applied, the resulting PSFs of Fig. 6.19 are formed. Note the presence of artifacts in the restored PSFs. Let us recall that the parabolic translation of the PSF with thermal defocus (described in Chapter 2) corresponds with a phase mismatch between the frequency response of the restoration and convolution kernels. This effect becomes more acute as the temperature departs from the nominal +20°C. One way to reduced this effect is to apply a different deconvolution kernel for each segment of the temperature domain. For example, three deconvolution kernels obtained from wavefront coding OTFs at −5°C, +25°C and +55°C were employed to restored the cubic PSFs at three consecutive temperature sections $-20°\text{C} \leq T_1 < +10°\text{C}$, $10°\text{C} \leq T_2 < 40°\text{C}$ and $40°\text{C} \leq T_3 \leq 70°\text{C}$ respectively. The resulting PSFs, practically diffraction-limited, present unnoticeable artifacts or restoration errors and are displayed in Fig. 6.20.

Computer simulation of wavefront coded IR images

A more subjective perception of the wavefront coded IR system performance is achieved by examining the simulated images. For a correct simulation of a sampled IR imaging system, a continuous/discrete model is the appropriate choice. This

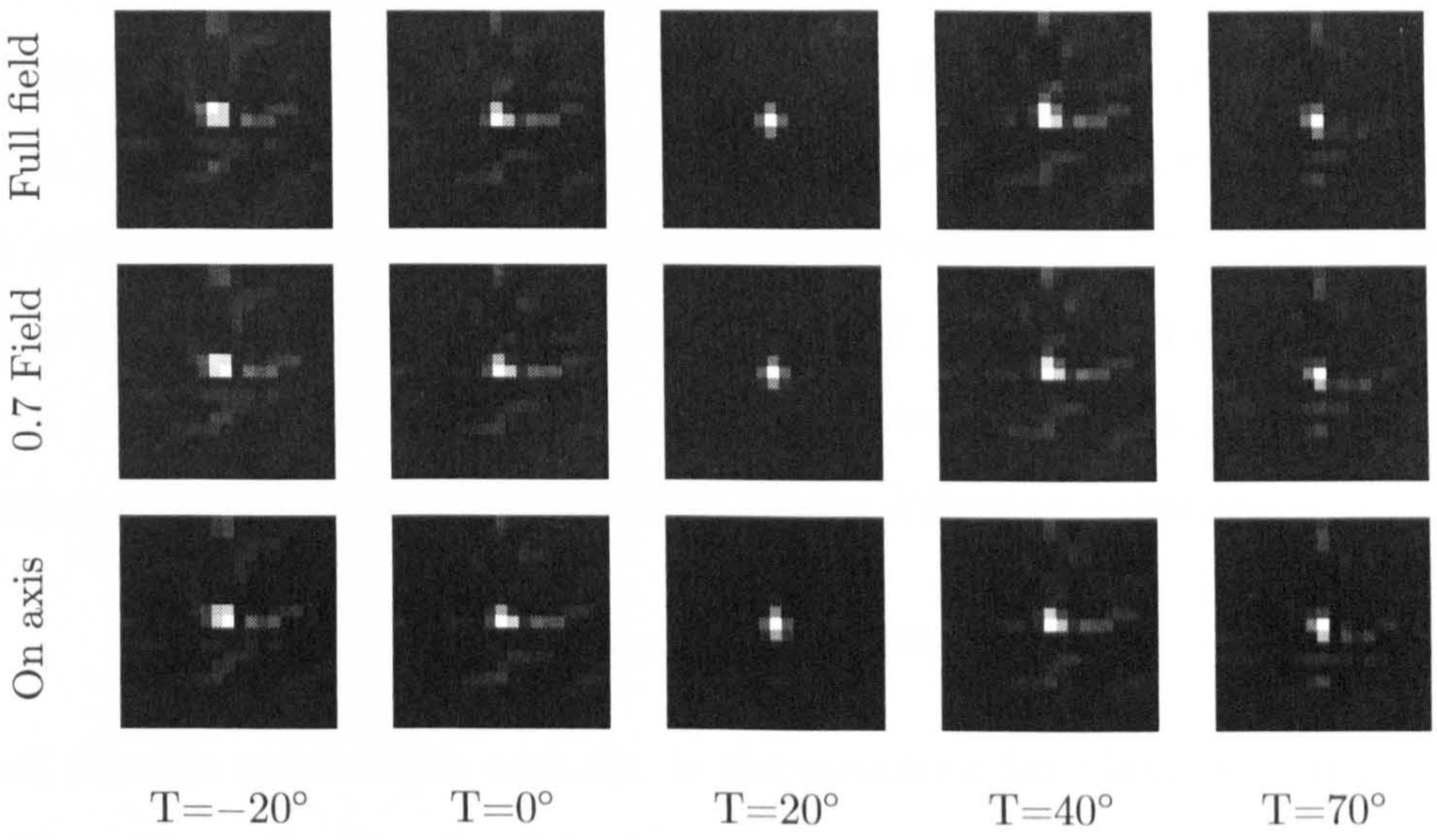

Figure 6.19: *Sampled PSFs from the wavefront coded system for various ambient temperatures after applying post-detection processing with only a single inverse filter (from nominal temperature at +20°).*

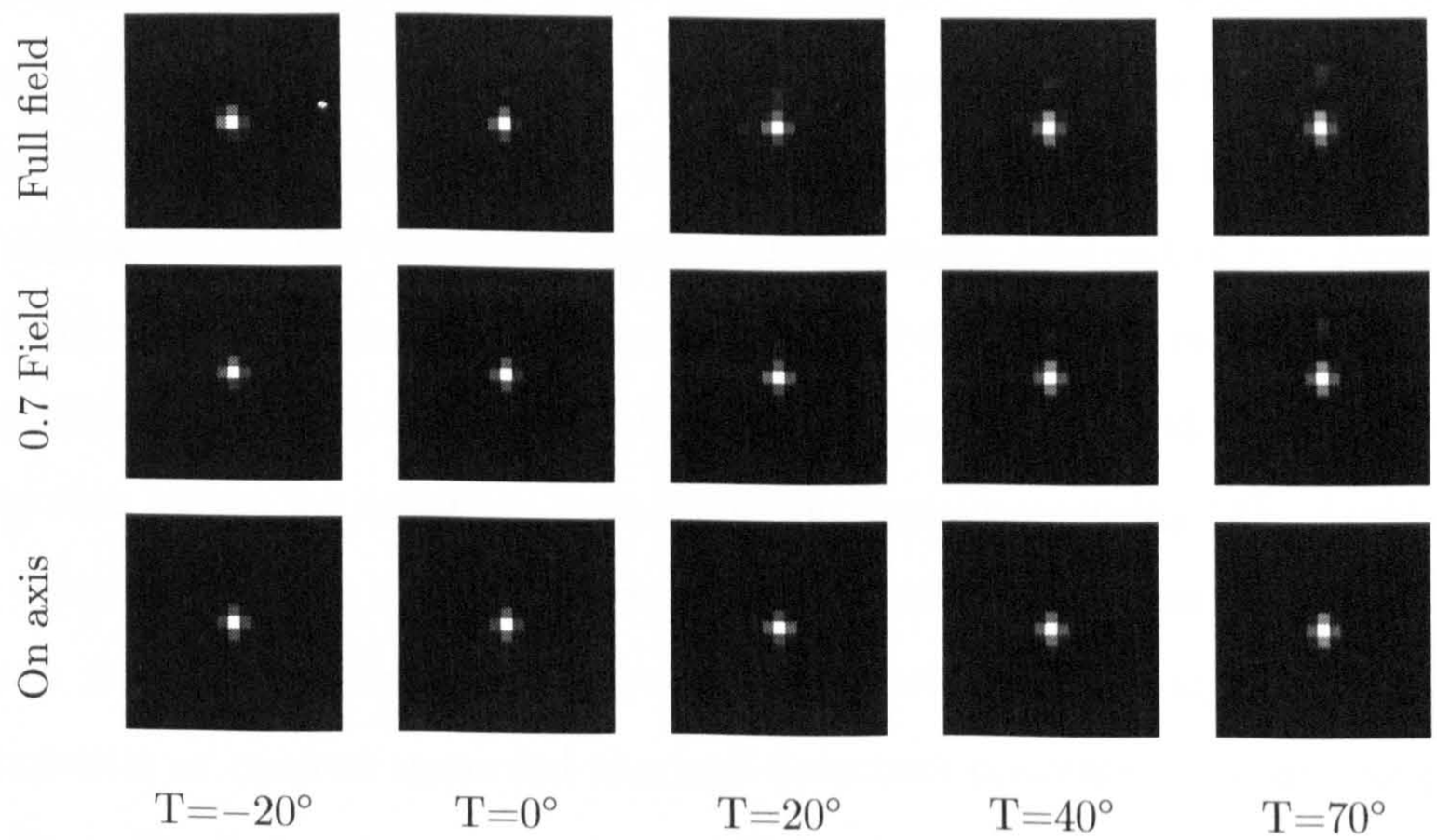

Figure 6.20: *Sampled PSFs from the wavefront coded system for various ambient temperatures after applying post-detection processing using three inverse filters across temperature range.*

model was developed by Park *et al.* [96] and it will be used in this section. Briefly, the model can be summarized as follows: The input o is the projection of a continuous scene onto the imaging system. The scene is blurred by convolution with the wavefront coded point spread function h_{opt} and the detector point spread function h_{det}. A detail derivation of the PSFs that successively formed h_{det} can be found in Appendix F. The blurred image is then sampled to produced an $M \times N$ digital image i_d. Additive random noise n from the detector electronics is also introduced. This image acquisition model is described by the following equation:

$$i_d = [o \otimes h_{opt} \otimes h_{det}] \times \text{⊥⊥⊥⊥} + n, \tag{6-8}$$

where $\otimes$ denotes convolution and ⊥⊥⊥⊥ is the sampling function. A digital deconvolution filter f is applied to the digital image i_d to produced a restored digital image $i_r = i_d \otimes f$. The sampling models the continuous/discrete conversion inherent to any sampled imaging system. The image acquisition models the optics low-pass filtering and phase mask coding whilst the image restoration simulates the wavefront decoding.

The detector characteristics are also taken into account. We assume here a focal array with 256×256 pixels and pixel pitch of 25μm. The noise equivalent temperature difference (NETD) is 100 mK, which corresponds to the current state-of-the-art uncooled IR detector [85]. The noise is assumed to be additive, normally distributed with standard deviation given by the NETD. The detected signal-to-noise ratio is set at 100 (40dB) by scaling the intensity contrast of the scene.

Until now researchers have stressed the use of direct linear methods such as the Wiener filter, to restore wavefront coded images because of good computational efficiency that allows for real-time post-detection signal processing [90]. Additionally, linear filtering provides straightforward merit functions to assess the noise amplification in wavefront coded imaging systems. The relatively low signal-to-noise ratio characteristic of current uncooled thermal detectors prevents us from using an inverse filter. For instance, a simple inverse filter that restores the athermalised MTF to diffraction-limited performance (0.5 at the Nyquist frequency) amplifies the underlying noise by a factor of 24. The magnitude of the frequency response of this inverse filter is shown in Fig. 6.21. The filter contains amplification values that range from 1 to 7 in the horizontal frequency axis and from 1 to 80 in the diagonal axis. Clearly, a noise-suppression linear filtering technique such as the Wiener filter

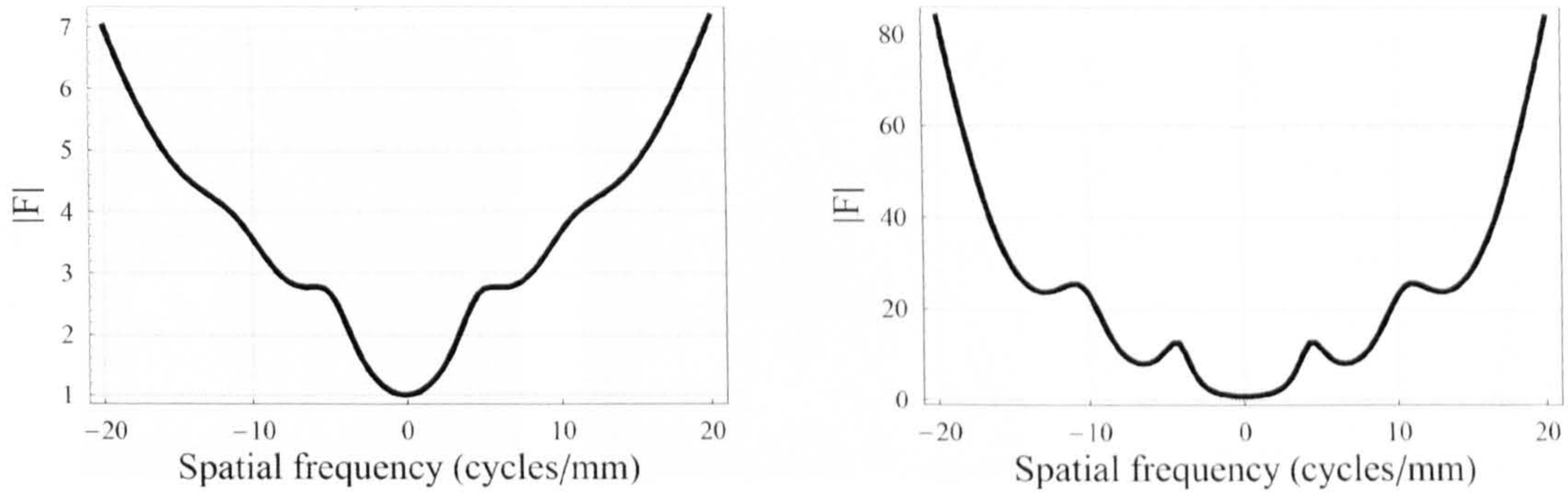

Figure 6.21: *Magnitude of the frequency response of the inverse filter up to the Nyquist frequency along the horizontal (left) and diagonal (right) spatial frequency axes.*

is required.

Three different restoration schemes with Wiener filters have been applied to the wavefront coding IR images in order to improve image quality and reduce artifacts:

- Scheme 1. For the entire temperature range, the images are deconvolved with a single Wiener filter which is calculated from the OTF at the nominal temperature.

- Scheme 2. Three Wiener filters calculated from the OTFs at -5°C, $+25$°C and $+55$°C were applied to images acquired at $-20°\text{C} \leq T_1 < +10°\text{C}$, $10°\text{C} \leq T_2 < 40°\text{C}$ and $40°\text{C} \leq T_3 \leq 70°\text{C}$ respectively.

- Scheme 3. Nine Wiener filters are employed throughout the temperature domain. Each filter is applied to images acquired within ten degrees.

The last two schemes require a temperature sensor incorporated in the thermal imager. In Figs. 6.22, 6.23 and 6.24, we display the restored images for the three deconvolution schemes respectively. For comparison, we also exhibit next to the restored images the images acquired by the traditional IR system with no athermalization present. Note the visually superior image quality attained by the wavefront coded system at the extremes of the operating temperature range.

Artifacts are particularly apparent in Figs. 6.22 due to the rapid phase variations in the wavefront coded OTF with thermal defocus. The artifacts tend to vanish from the images as the phase mismatches between the OTF and deconvolution kernels are minimized by restoring with more phase-coupling kernels. This can

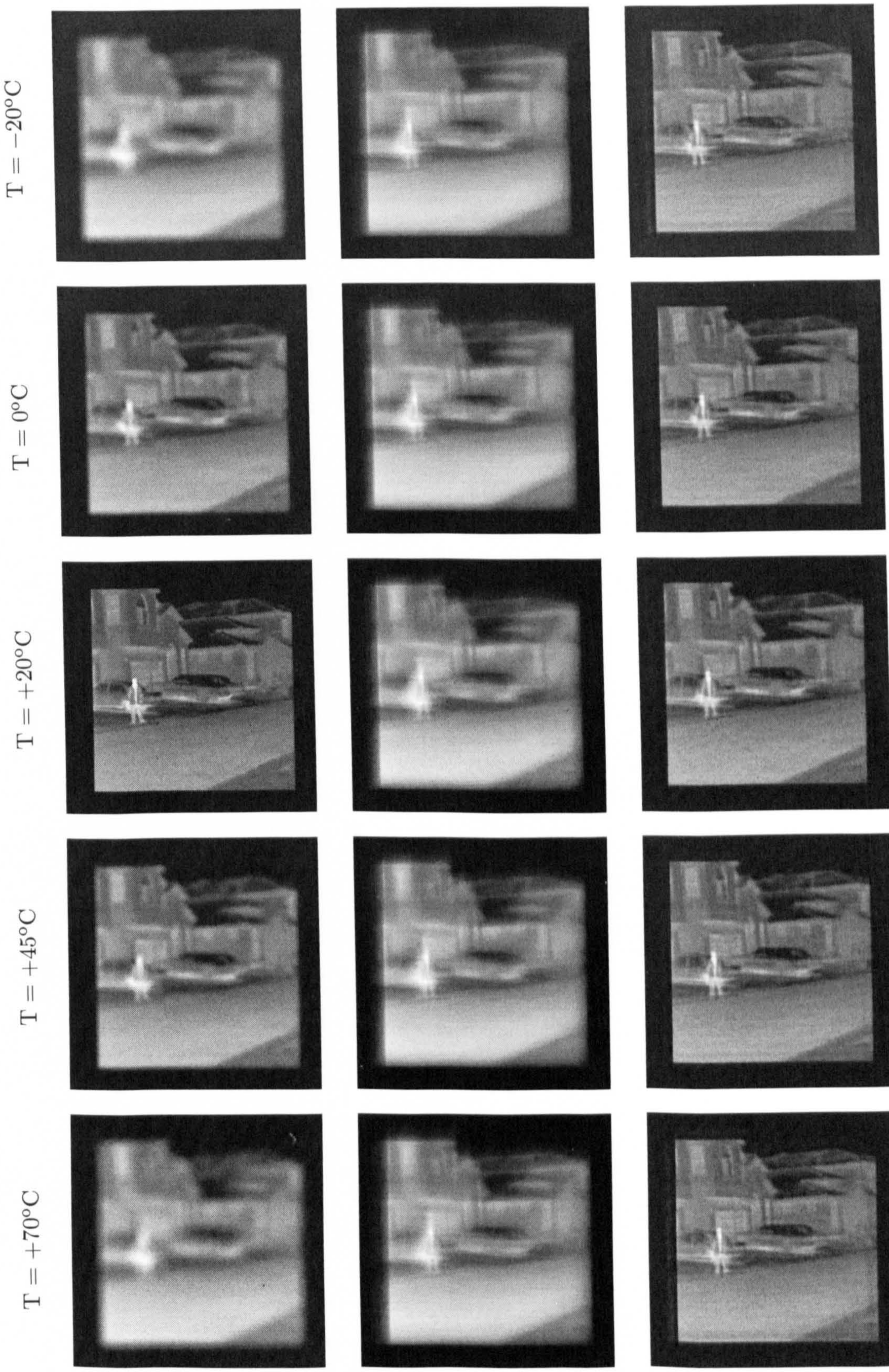

Figure 6.22: *Scheme A. Simulated images for the traditional IR system (left), raw wavefront-coded images (centre) and after Wiener restoration with a single filter applied across the entire temperature range (right).*

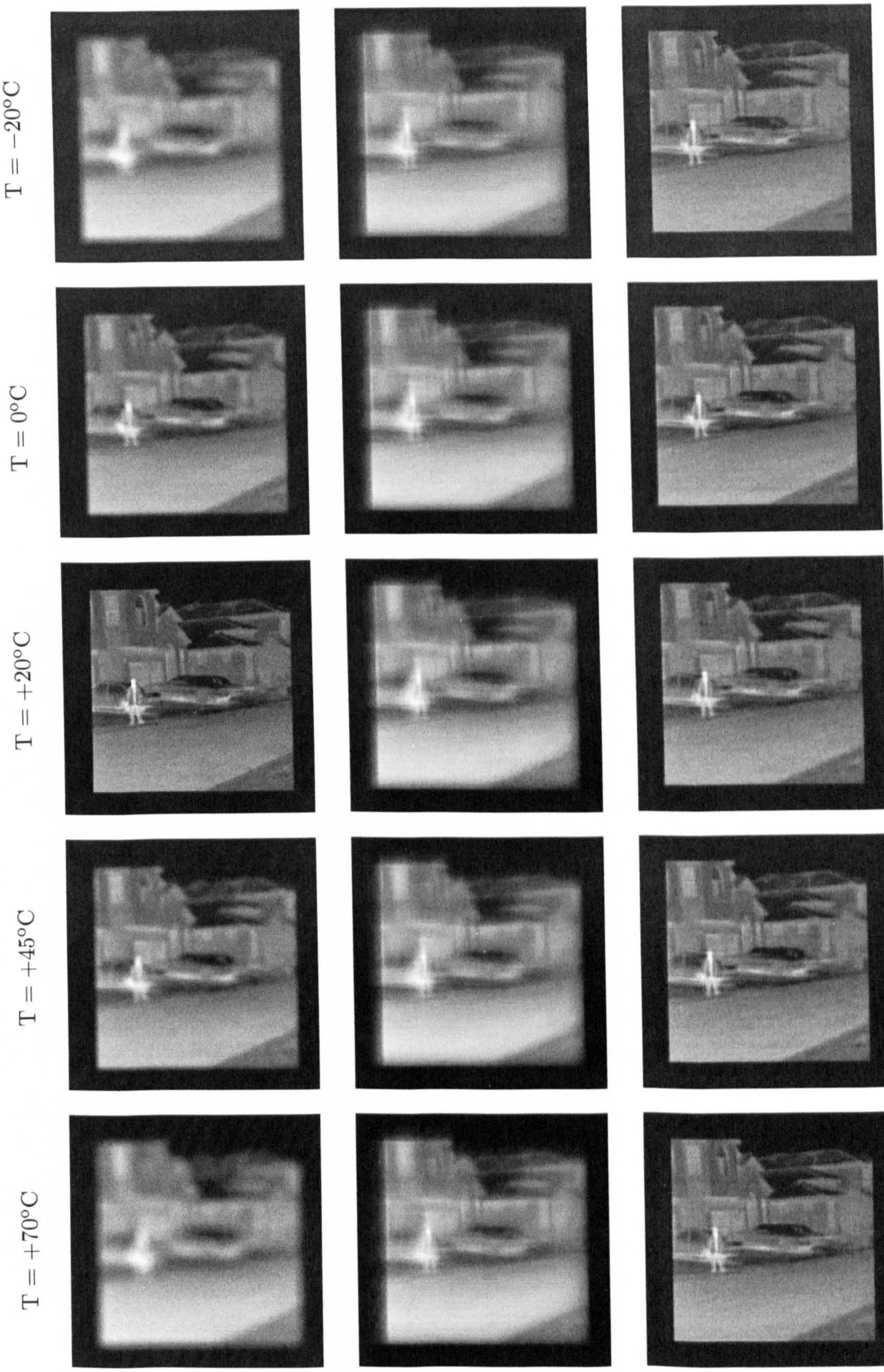

Figure 6.23: *Scheme B. Simulated images for the traditional IR system (left), raw wavefront-coded images (centre) and after Wiener restoration with three filters applied across the entire temperature range (right).*

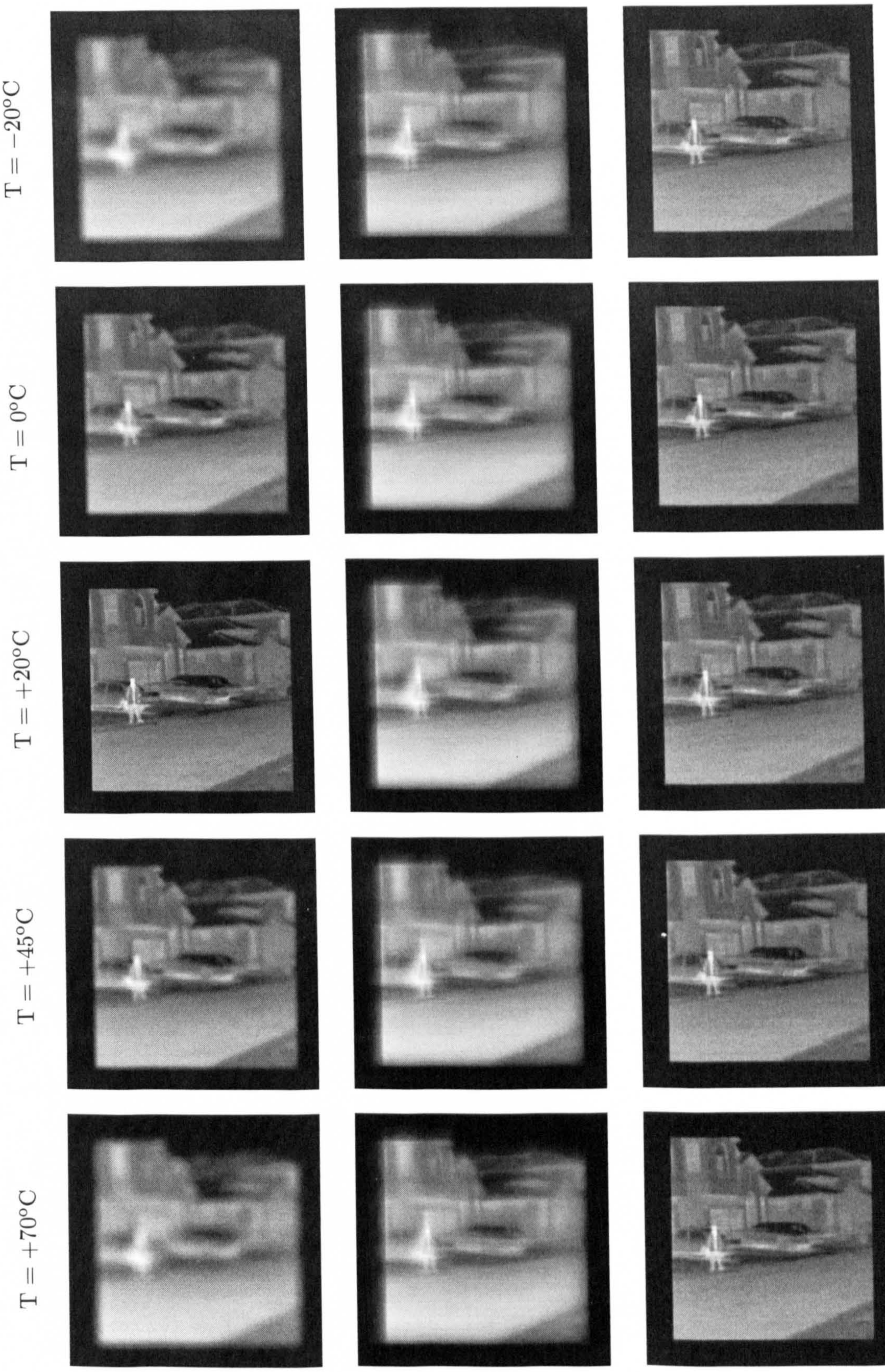

Figure 6.24: *Scheme C. Simulated images for the traditional IR system (left), raw wavefront-coded images (centre) and after Wiener restoration with nine filters applied across the entire temperature range (right).*

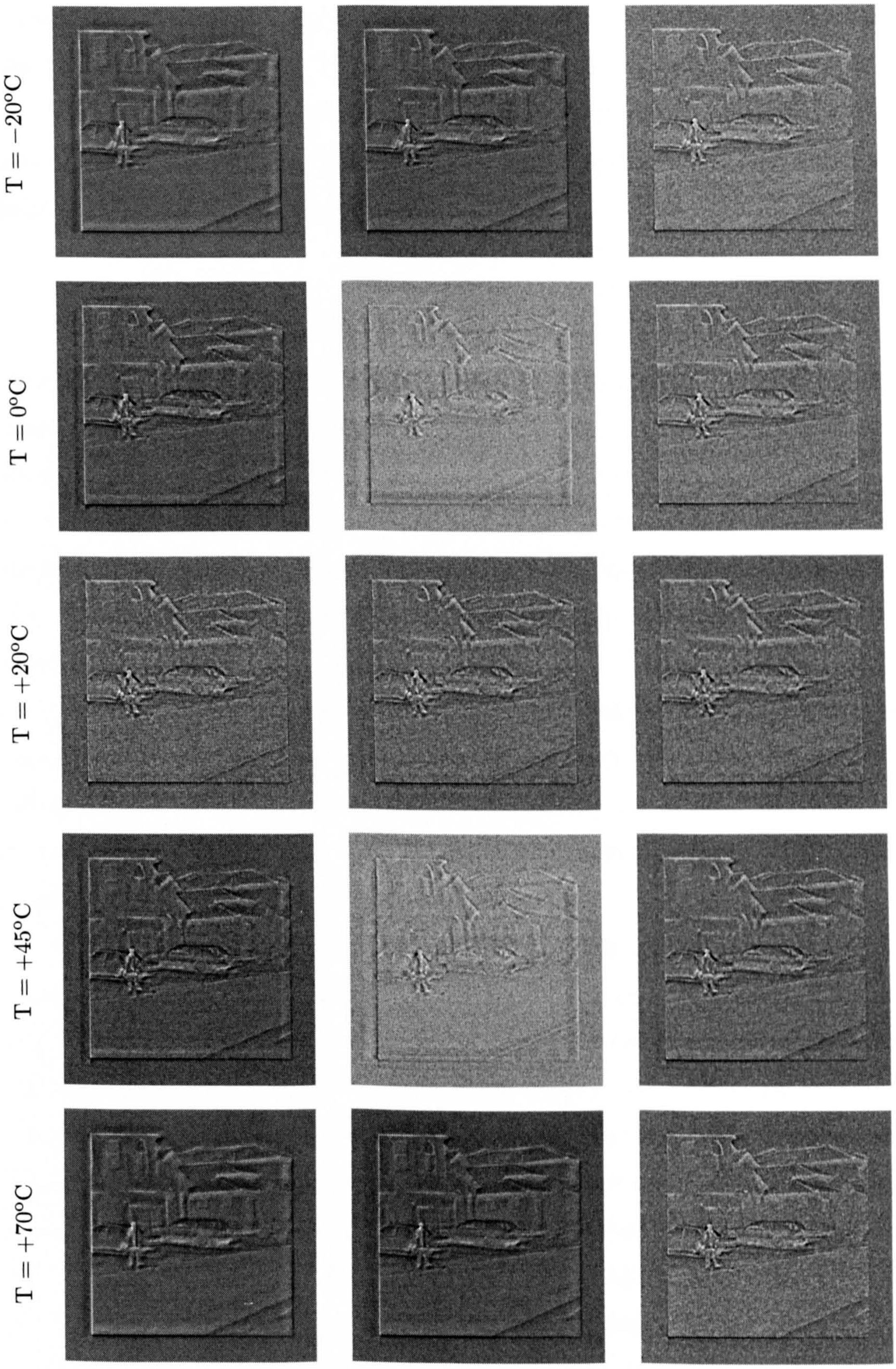

Figure 6.25: *Simulated difference image (True scene minus restored image) across the operational temperature range for the three restoration scheme reported in this work. The signal-to-noise ratio of the pre-restored images is 40dB.*

be clearly seen in Fig. 6.23 and Fig. 6.24 where the number of filters used is greater than 1.

Visual perception can only provide a qualitative appraisal. We therefore use a more objective metric such as the root mean squared error (RMSE) over the whole image. The RMSE per pixel is defined as

$$\text{RMSE} = \sqrt{\frac{1}{N^2}\sum_{i=1}^{N}\sum_{j=1}^{N}\left(O[i,j] - I[i,j]\right)^2} \tag{6-9}$$

where the image is a $N \times N$ pixel array, O is the model scene and I the restored image. Pixel locations in the image are given by $[i,j]$. We use the RMSE as a metric to compare the different restoration schemes with respect to each other and the object. In Fig. 6.25, we display the difference images, each formed by subtracting the restored image from the true object, for the three restoration methods suggested here. The amount of RMSE in the Wiener-restored images averaged out across the operating temperature range for the A, B and C deconvolution methods is 3.8%, 2.7%, and 2.3%, respectively. The same metric was calculated for traditional system without athermalization and an error of 8.5% was obtained. Thus, the wavefront coding IR system with any of the restoration schemes outperforms the traditional IR system, a fact that is also corroborated by the visual appearance of the various images.

In summary, we have demonstrated with this study that wavefront coding can be certainly used as an adequate athermalization technique by carefully balancing the trade-off between noise amplification and wavefront-coded distortion required to extend the usable temperature range of the IR system. We have shown that wavefront coding enables enhanced image quality across the entire temperature range whilst reducing system complexity and cost. Improvements in the post-detection digital processing (eg. increased number of deconvolution kernels throughout temperature range and use of non-linear filtering techniques) will help reduce the noise amplification and obtain restored images with fewer artifacts. Future advancements in detector sensitivity will reduce system noise in uncooled detectors and will provide greater scope for the use of wavefront coding in low-cost thermal imager whilst maintaining current performance levels.

4 Optimised thermal imaging with a singlet and wavefront coding

The potential of wavefront coding as a joint optimization of optics and electronics increases the degrees of freedom of traditional optical design and therefore overcomes the usual tradeoff encountered in optical systems: high performance is achieved at the expense of increasing lens complexity, optical element counts and cost. In the work presented here, we consider the possibility of using wavefront coding to reduce the lens count of a traditional two-element infrared imaging system whilst maintaining high optical throughput and acceptable image quality. The new wavefront coding optical system combines a singlet with a phase mask inserted in the front surface and benefits from low weight and low cost optics. The actual construction of this optical system was carried out by Qioptiq (formerly Thales Optronics), UK. The experimental performance studies took placed at FLIR, Sweden, who kindly offered their facilities and a LWIR uncooled detector. The post-detection digital restoration was performed in collaboration with Saab Bofors Dynamics, Sweden.

4.1 Modeling of the wavefront coding singlet

The initial IR optical system consisted of two elements made of germanium, F/1, with an effective focal length of 75 mm and field of view of 12×9 degrees. The operating wavelengths were $9 - 12\mu$m. The lens was based on the Petzval configuration, which included an even asphere in the second surface of the front element.

This two-element IR system was then reduced to a single element by removing the rear meniscus that acted as a field flattener. The new optical system formed by the singlet is shown in Fig. 6.26 and its optical specification is displayed in Table 6.2. The front and rear surfaces of the singlet were re-optimised with Zemax in order to preserve the f-number and focal length of the previous system. The singlet was corrected from coma and spherical aberration (by bending the lens and using an even asphere), but its optical performance (MTF, PSF and optical path difference) across the field of view was greatly limited by astigmatism and field curvature. Further re-optimization was carried out to try to improve the imaging performance of the IR singlet; however unavoidable astigmatism and field curvature remained present. The singlet on-axis MTF performance was diffraction-limited but rapidly decreased

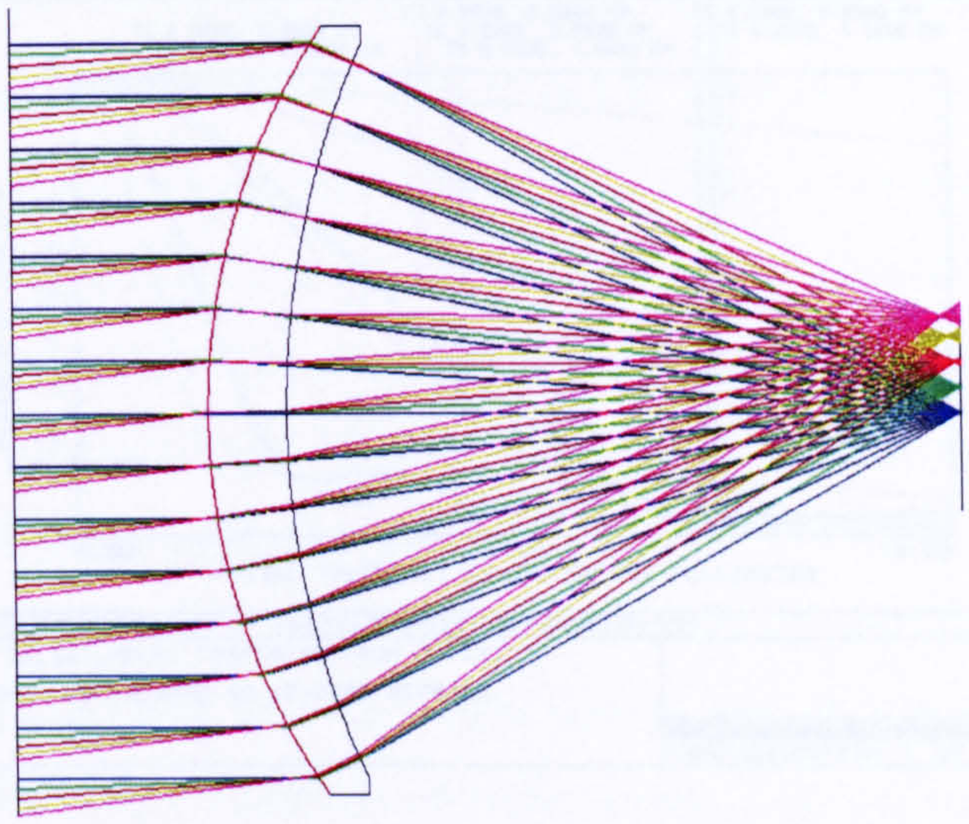

Figure 6.26: *Singlet layout made of germanium, effective focal length f=75 mm, F/1, field of view of* 12×9 *degrees. Note the off-axis performance limited by aberrations (mainly astigmatism and field curvature).*

Surface	Radius curvature	Thickness	Material	Semi-diameter	Conic
Obj.	Inf.	Inf.		Inf.	0
Stop	Inf.	1		37.5	0
2	69.964	8.00	Ge	39.24	0
3*	92.791	68.56	Ge	37.44	0
Ima.	Inf.			10	0

*Even Asphere	β_1	β_2	β_3	β_4
	0	3.9707E-8	3.2738E-12	6.0239E-16

Table 6.2: *Singlet optical specifications.*

even for narrow fields of view. At the edge of the vertical and horizontal fields of view the optical path different showed a maximum wavefront error of 10 and 18 waves respectively ($\lambda = 10.5\mu$m).

At this stage of the project, the goal is set to correct up to 6 waves of aberration. This amount of wavefront aberration corresponds to the optical path difference (OPD) at a half field of view (FoV) of about 3.5 degrees. In terms of detector area, only the PSFs within a 4.5 mm half-width square are corrected. The variation of the MTF of the singlet with FoV is illustrated in Fig. 6.27, in which the MTFs exhibit multiple zeros and astigmatism is clearly present for there is a large disparity between the sagittal and tangential MTF. The MTFs are displayed up to the Nyquist frequency of the detector (10 cycles/mm). The target specification required that the

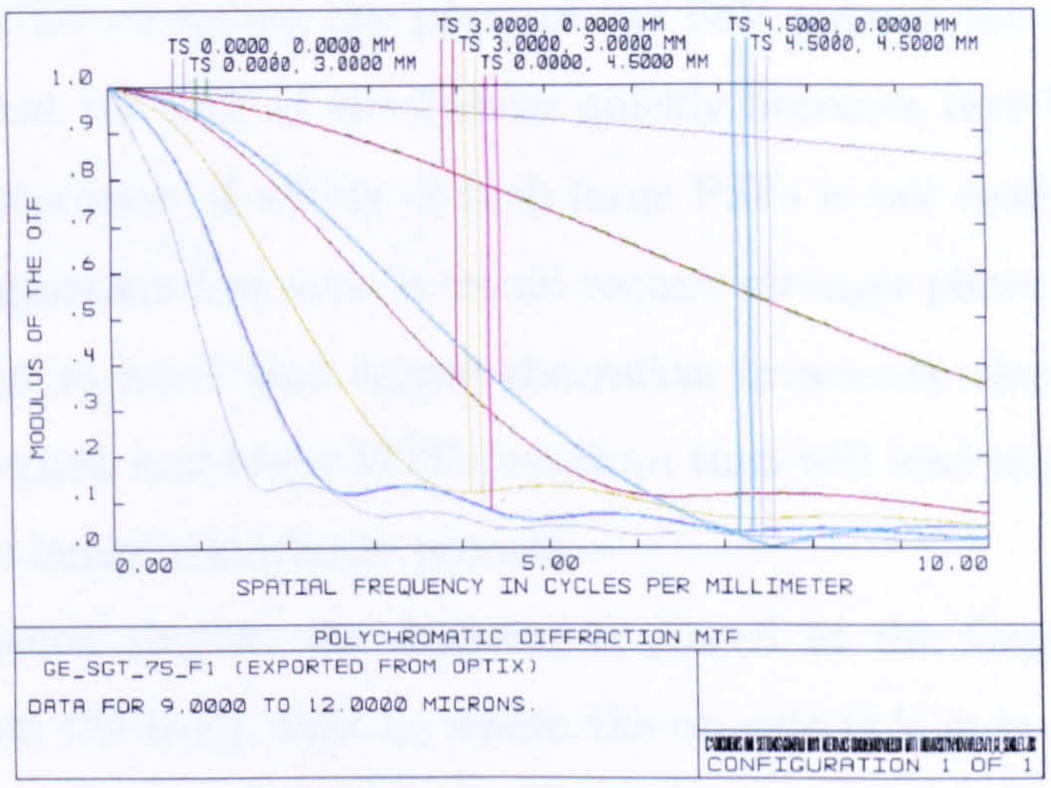

Figure 6.27: *MTF performance for various FoV ranging from 0 to 7.5 degrees for the IR singlet. Note the presence of zeros and the mismatch between the sagittal and tangential MTFs due to astigmatism.*

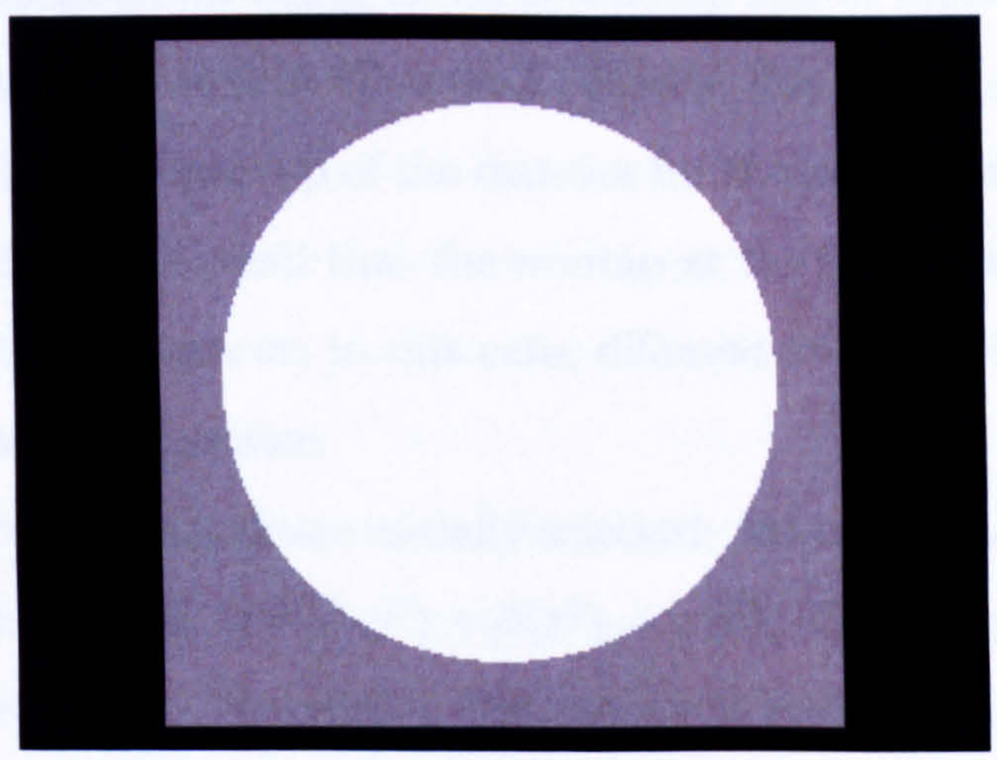

Figure 6.28: *Area of the detector (black), area of PSF invariance and aberration mitigation (in white). In grey is the region where a shift-variant PSF deconvolution technique can be applied to recover parts of the image.*

phase mask must be able to alleviate the effect of aberrations across the FoV ranging from 0 up to 7 degrees. Fig. 6.28 shows the actual area of the detector array (in black), the area in white represents the region where the phase mask PSFs remain practically invariant and where the aberrations have been corrected. The radius of the white circle is 4.5mm. Between these two regions there exists a square region, in gray, in which the variation of the PSFs with FoV is sufficiently small to enable the application of deconvolution techniques that correct for the spatially varying PSF.

The reason for excluding the parts of the FoV outside the above mentioned gray square is that the PSF of the system quickly becomes very large, of order of millimeters. Restoration of effects of such large PSFs is not easily dealt with. To increase the astigmatism-free area, it would require stronger phase masks. However, it should be kept in mind that larger aberration invariance also leads to greater deconvolution kernels and lower MTFs which in turn will lead to greater noise amplification in the image restoration process.

In the original singlet, the detector is placed at the Gaussian focal plane (68.5368mm from the lens), that is, where the on-axis FoV is in sharp focus, thus its optical path difference OPD=0λ. At this image position, the FoV at the outer edge suffers a maximum OPD=6λ. For an optimum aberration correction with the phase mask, the detector plane is moved towards the lens to 68.3043 mm. In this position, the OPD across the field of view is balanced with values ranging from -3λ to $+3\lambda$. The justification for doing an OPD balance can be found in more detail in the caustic analysis presented in Chapter 2. Briefly, this action places the detector in a position at which the overlap of the caustics for the on-axis and extreme-off-axis FoV is maximized. Let us recall that the overlap at the image plane of the caustics for different object positions or, in this case, different fields of view determines the amount of aberration invariance.

Two types of phase mask are initially selected: the cubic phase mask $\alpha(x^3+y^3)$ and the petal phase mask $\gamma(x^3+y^3)+\beta(x^2y+xy^2)$. For an optimum aberration mitigation $\gamma=-3\beta$ [42]. We employ the numerical optimization feature provided by Zemax to calculated the optimum values of α or β and γ so that the merit of function is minimized. A similar procedure was applied to the optimization of a logarithmic phase mask in Ref. [32]. The merit function contains three distinctive sections:

1. The first section is defined as the difference between the MTFs at various spatial frequencies of a comprehensive set of FoV and the on-axis MTF. If this part of the merit function is minimized, the MTFs will be very similar and astigmatism will be reduced.

2. The second section is defined as the difference between on-axis MTF and a diffraction-limited MTF with a modulation of 0.5 at the Nyquist frequency. If this part of the merit function is minimized, the height of the MTFs will have

the highest possible values.

3. Finally, the third part sets a constrain on the merit function so no nulls become present in the wavefront coding MTFs up to the Nyquist frequency.

Basically, the minimization of our merit function yields the highest value of the MTFs for a wavefront coding singlet that is invariant with field of view. The calculated optimum values of the petal phase mask are $\gamma = 0.009779\lambda$ and $\beta = -0.030530\lambda$. Note that these parameters describe wavefront distortion directly, not surface deformations. In terms of surface relief $\gamma_s = 9.78\mu$m and $\beta_s = -30.53\mu$m which results in a peak-to-valley height of 29.34μm in a germanium substrate.

Unfortunately, the cubic phase mask is unable to correct the aberration of the fields of view that fall outside the favourable axis of the phase mask. Furthermore, for these fields, the cubic mask fails to remove the nulls in the MTFs, as illustrated in Fig. 6.29(a). Increasing the value of α does not solve the problem but aggravates it by bringing down the MTFs of these fields of view. It becomes apparent that the cubic phase mask cannot cope with aberrations whose point spread functions are not rotationally symmetric or structured along the tangential and sagittal directions where the cubic phase mask attains the highest aberration insensitivity. This effect can be clearly observed in Fig. 6.30. The PSFs at FoV (0mm,0mm) and (4.5mm,0mm) are unaffected by astigmatism, however at (3mm,3mm) the characteristic L-shaped of the cubic PSF has disappeared. The aberration associated with the PSF at (3mm,3mm) produces nulls in the MTF. This effect can be understood from the our decomposition of the wavefront coding OTF along the diagonal axis presented in Chapter 4: the spiral-like structure that allows aberration tolerance is barely present at the diagonals and thus any aberration with distinctive degradation on these frequencies will not be affected by the mask. This behaviour is not only limited to the cubic phase mask but to any rectangularly-separable antisymmetric phase mask. As a result, the cubic phase mask was eliminated for manufacture.

The effect of the petal phase mask in the MTF of the optical system is illustrated in Fig. 6.29(b). When the designed petal phase mask is inserted into the system, the MTFs remain essentially constant and identical to each other. Note that these MTFs have no zero values and astigmatism has been effectively removed. This is in contrast to the MTF performance of the singlet alone. The field-invariant MTFs allows the applications of a simple single inverse digital filter within the PSF

invariance region and the system would be restored to an almost diffraction-limited performance. It can be observed that the field invariant imaging performance is accompanied with a reduction in the magnitude of the MTFs in comparison with the on-axis in-focus performance of the IR singlet. This drop in the signal height represents significant noise amplification in the digitally processed image. The suppression in the MTFs is determined by the strength of the PPE phase mask given by the parameters α and β. As we will see in the next sections, restoration algorithms must be chosen accordingly in order to prevent noise amplification to unacceptable levels.

4.2 Experimental realization of the wavefront coded IR singlet

Manufacture of the petal phase mask

The germanium aspherical singlet with the specifications described in Table 6.2 was manufactured by single point diamond machining. Our collaborators from Qiopitq had the phase mask manufactured at Cranfield University, UK.Despite the difficulties and challenges involved in the manufacturing process, the produced phase mask presented very little deviation from the originally designed phase mask. The physical peak-to-valley distance of the manufactured phase mask is 24 microns, which is slightly less than that of the designed mask (28 microns). This small reduction in the phase height results in a small loss of aberration tolerance, thus fields of view near the edge at 4.5mm become in some way affected by the weaker manufactured phase mask. Fig. 6.31 shows a comparison of the interferograms generated by the designed and manufactured phase masks. It can be observed that a minor deformation from the ideal shape was introduced during the manufacturing process.

In addition to manufacturing three petal phase mask with a peak-to-valley height of 24 microns, another three petal phase mask with identical shape but with less surface peak-to-valley sag ($\approx$ 16 microns) were manufactured. This mask corresponds to approximately 3 waves of aberration correction. The phase masks were not incorporated into the singlet surface in order to reduce cost (only one singlet had to be made) and manufacturing complexity. In practical terms, the separation of the phase mask and singlet has a negligible effect on the outcome of the experiment. In addition, fabrication of several masks allowed us to select the most accurately-made

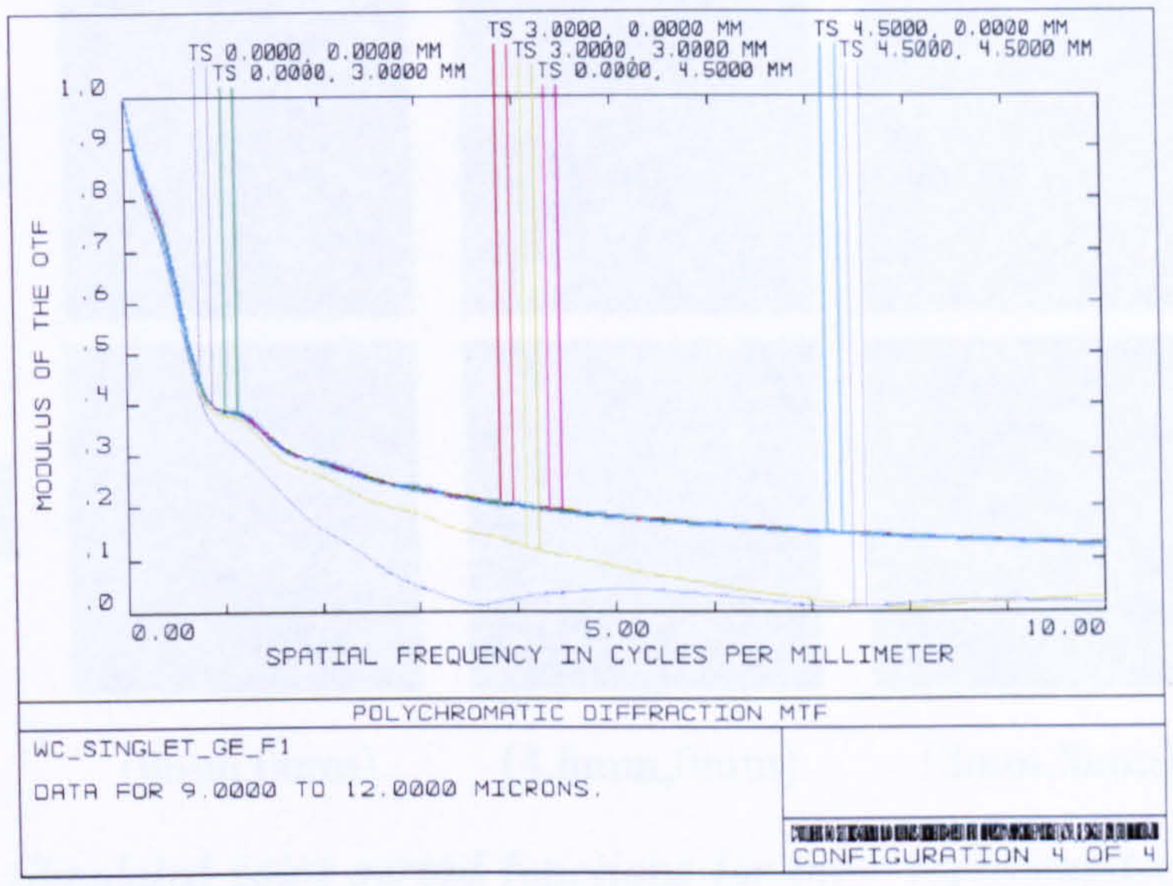

(a)

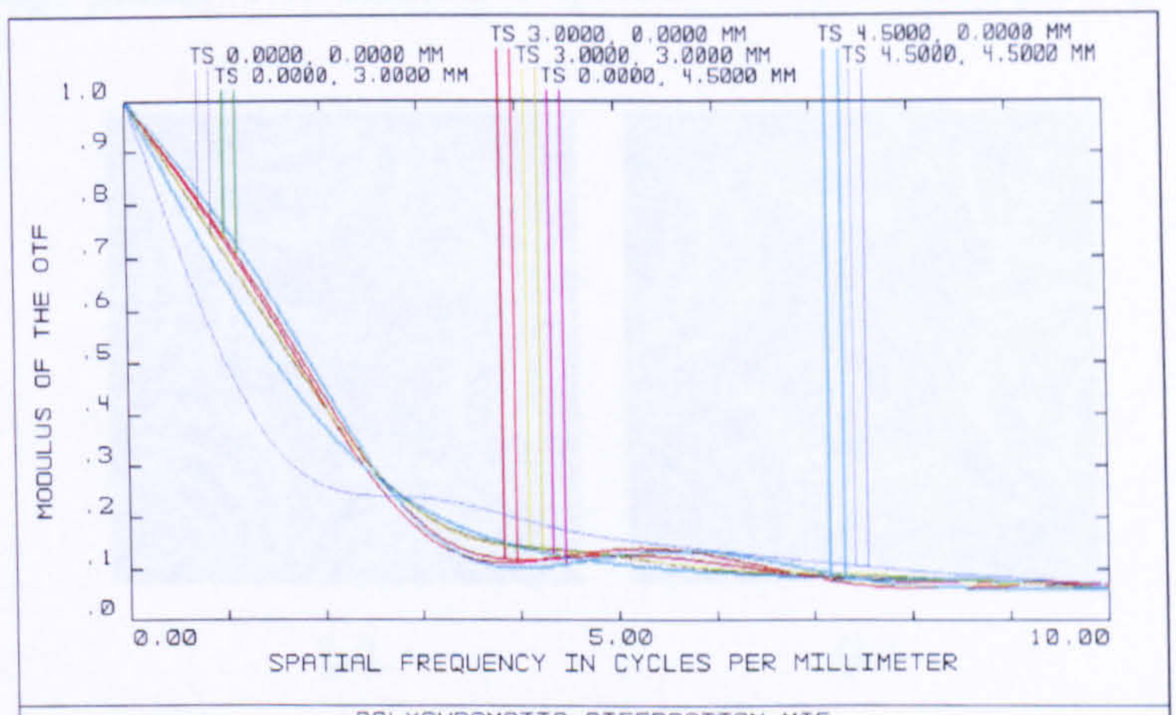

(b)

Figure 6.29: *MTF performance up to the Nyquist frequency for various FoV for IR singlet with (a) cubic phase mask and (b) petal phase mask after optimization.*

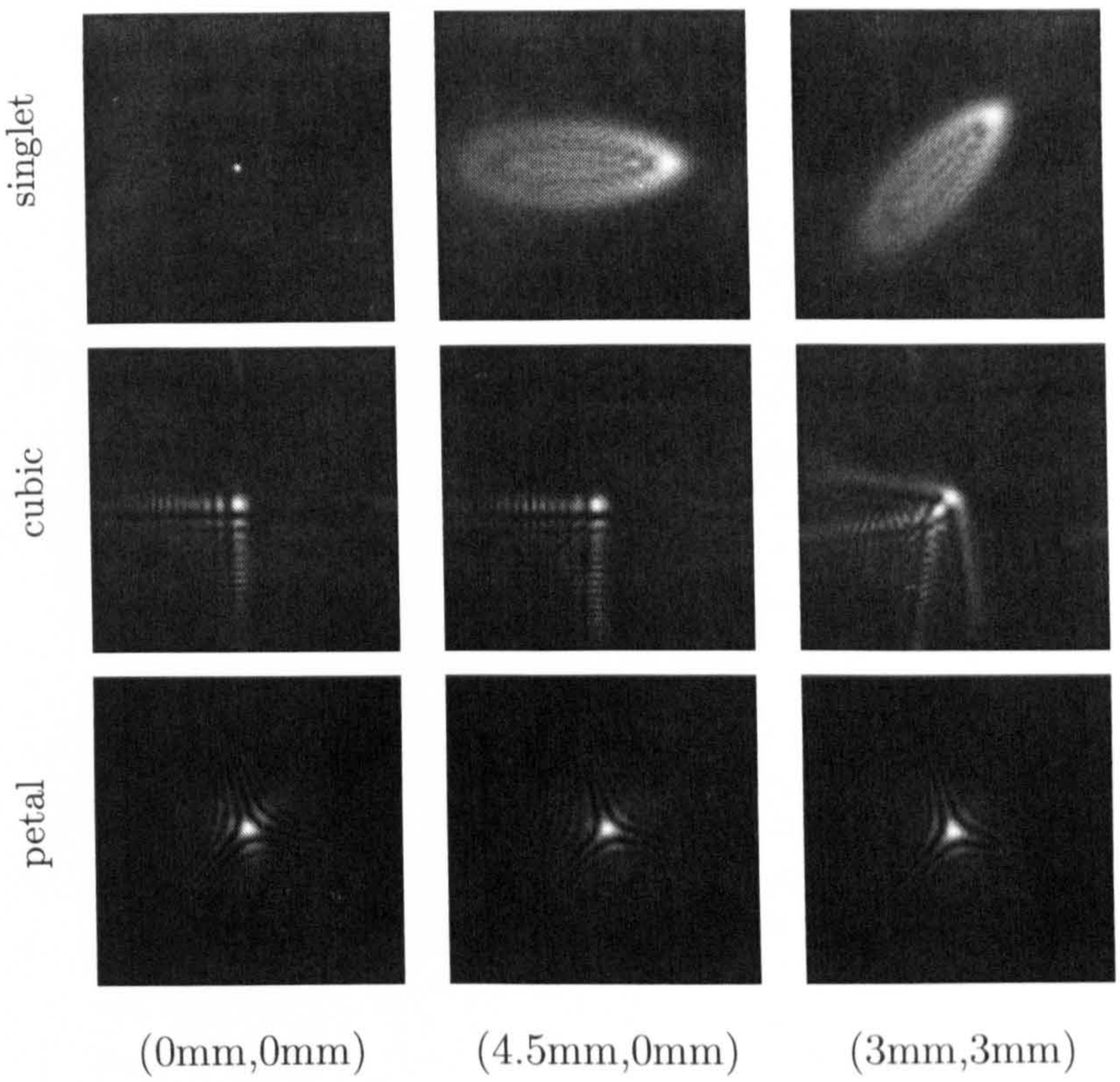

Figure 6.30: *Simulated point spread functions for three representative fields of view across the image plane. The detector is placed at the on-axis focal plane.*

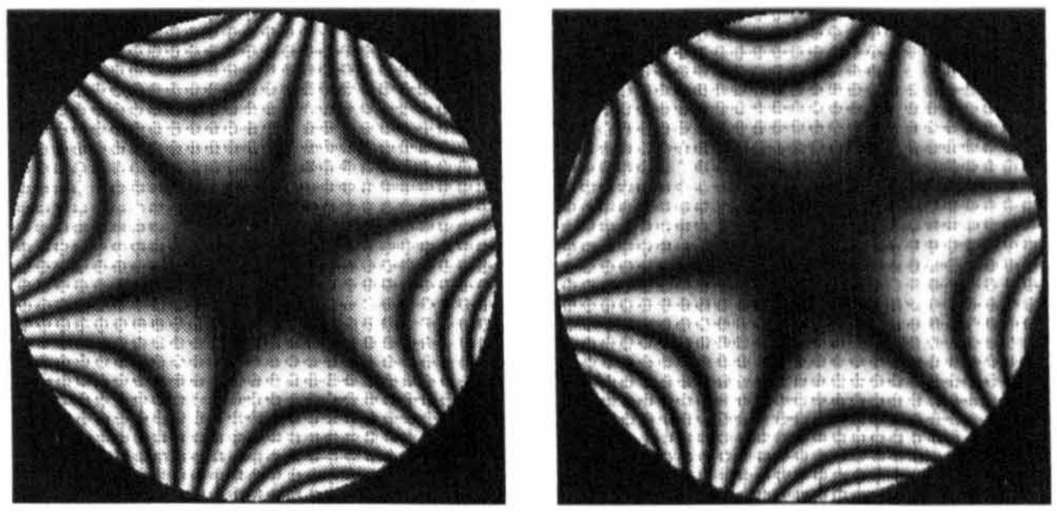

Figure 6.31: *(a) Wavefront interferograms produced by the designed phase mask and (b) by the Zernike polynomial fitting of the manufactured phase mask. The root-mean-square error of the fitting is less than 2.9%.*

mask and increase the probability of producing a successful experimental realization.

Image restoration and results

The inclusion of a PPE element blurs the image in a well known way. The PSF of the optical system is, as mentioned above, approximately shift-variant. Especially towards the edges of the FoV, the PSF changes rapidly. Due to the spatial

variation of the optical PSF, it is not possible to use a single deconvolution kernel for restoration of the whole encoded image. In the central part of the FoV, where the optimised phase mask has reduced the astigmatism of the singlet and hence the PSF is practically constant, deconvolution can actually be expected to yield an acceptable restoration. In this section, we briefly describe the image restoration approach. It is beyond the scope of this thesis to describe in detail the Van Cittert and Lucy-Richardson deconvolution algorithms, the interested reader can refer to Refs.[4, 120]. Amritpal Singh, from Saab Bofors Dynamics (Sweden) was responsible for the decoding and execution of image inversion based on the data provided by us.

To deal with shift-variant blur one must look at how blur is introduced in the image. The blurring of an image can be described as an integral equation. Below is an integral equation of the first order, also called the Fredholm integral of the first kind:

$$i(s) = \int h(s,t)o(t)\mathrm{d}t + n, \tag{6-10}$$

The detected image i is formed by the original image o and the blurring function h, (s,t) are 2-D spatial coordinates and n is an additive noise term. The aim is to recover the image o or a close estimate from the knowledge of i and h. The solution to the general integral-equation can be significantly more difficult than deconvolution.

A Van Cittert method supplemented with an interpolation scheme to control the shift-variant PSFs is firstly used to estimate the image o. Van Cittert is a straight-forward iteration scheme with no difficulties of implementation. The method is formulated in matrix-form:

$$x^n = x^{n-1} + \kappa(b - Hx^{n-1}) \tag{6-11}$$

where x is the estimate of the original image, b is the blurred image, H is the PSF matrix and κ is the relaxation factor that weighs the difference of the observed image and the output at $n-1$. The images, originally of size $m \times n$, are reshaped into column-vectors of size $mn \times 1$. H is a matrix of size $mn \times mn$ where each row corresponds to the PSF in one point in the image plane. The calculation is iterated until an image with sufficient quality is produced. Suppression of noise is handled by stopping iterations early, before the noise is amplified to unacceptable levels.

The problem is that the PSF is not known at every pixel in the image, every row of H is not known, and it varies over the image plane. This calls for some kind of interpolation which is what the interpolation-scheme mentioned above performs.

As a reference a well known deconvolution method, namely the Lucy - Richardson deconvolution (LRD) algorithm [121] is also used during evaluation. Because the LRD algorithm selected for this application is shift-invariant, we employ a sample of the PSFs from the centre of the image since that is the area of most interest and it is where the PSFs were optimised. The LRD iterations are defined as:

$$x^n(s) = x^{n-1}(s)\left(H(s) \otimes \frac{b(s)}{H(s) \otimes x^{n-1}(s)}\right) \tag{6-12}$$

where $\otimes$ denotes convolution and s is a spatial coordinate.

The PSFs, used in the restoration process, are calculated by modeling the manufactured singlet and phase mask in Zemax. By simulating the manufactured optical elements in Zemax, we are able to increase the accuracy and reliability of the restoration process. In order to model the manufactured phase mask in Zemax a Zernike polynomial fitting based on experimental interferometric measurements obtained from the germanium phase mask is used. Further details of the Zernike fitting and coefficient values can be found in Appendix G. The Zernike coefficients obtained in the fitting generated a new phase mask whose root-mean-square error with respect to the real manufactured phase mask resulted to be less than 2%. This minute error was assumed to be negligible as can be observed from the comparison of the Zernike-fitted MTF in Fig. 6.32 and the originally designed MTF in Fig. 6.29(b). Both MTFs are practically identical. For practical reasons, it is not possible to provide the restoration algorithm with PSFs at each image pixel. Instead the PSFs are calculated at certain field intervals as shown in Fig. 6.33. It shows the regions where the PSFs remain insensitive to off-axis aberration (area of radius 4.5mm) and where aberration outweighs the wavefront coding action. The filter response of the PSF at points situated between field intervals is approximated through a linear interpolation between the four nearest known PSF samples.

In the experimental setup an uncooled IR detector array with 320x240 pixels and a pixel size of 38 microns is placed at the optimal image plane. The total FoV of the system is 9.2 by 7 degrees. The operating wavelengths were 9-12μm. There was a light snow fall during the imaging session, resulting in rather small scene contrasts. Examples of the resulting images are shown in Fig. 6.34. Stationary scenes of a building were imaged both with and without the phase mask. In these figures we also show the results of the restoration using the Van Cittert algorithm, which takes into account the spatial variation of the PSF. As a reference, we also

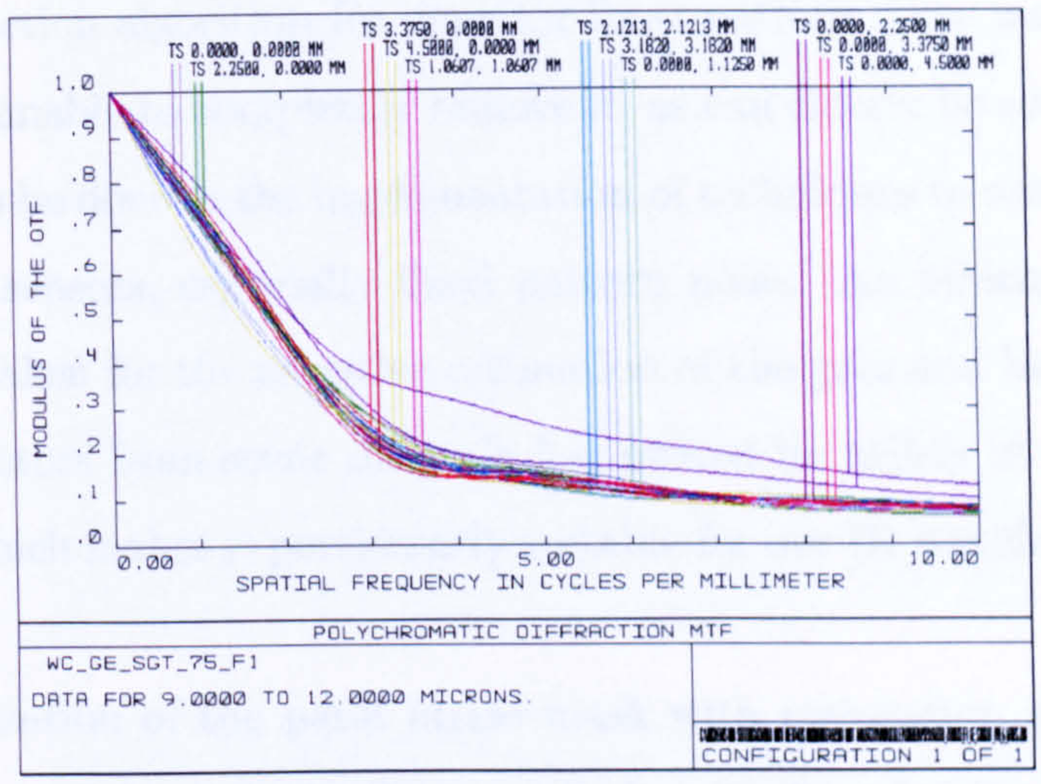

Figure 6.32: *MTF performance for various fields of view for the singlet with Zernike polynomial fitting based on the manufactured phase mask. The difference with the originally designed MTF is negligible.*

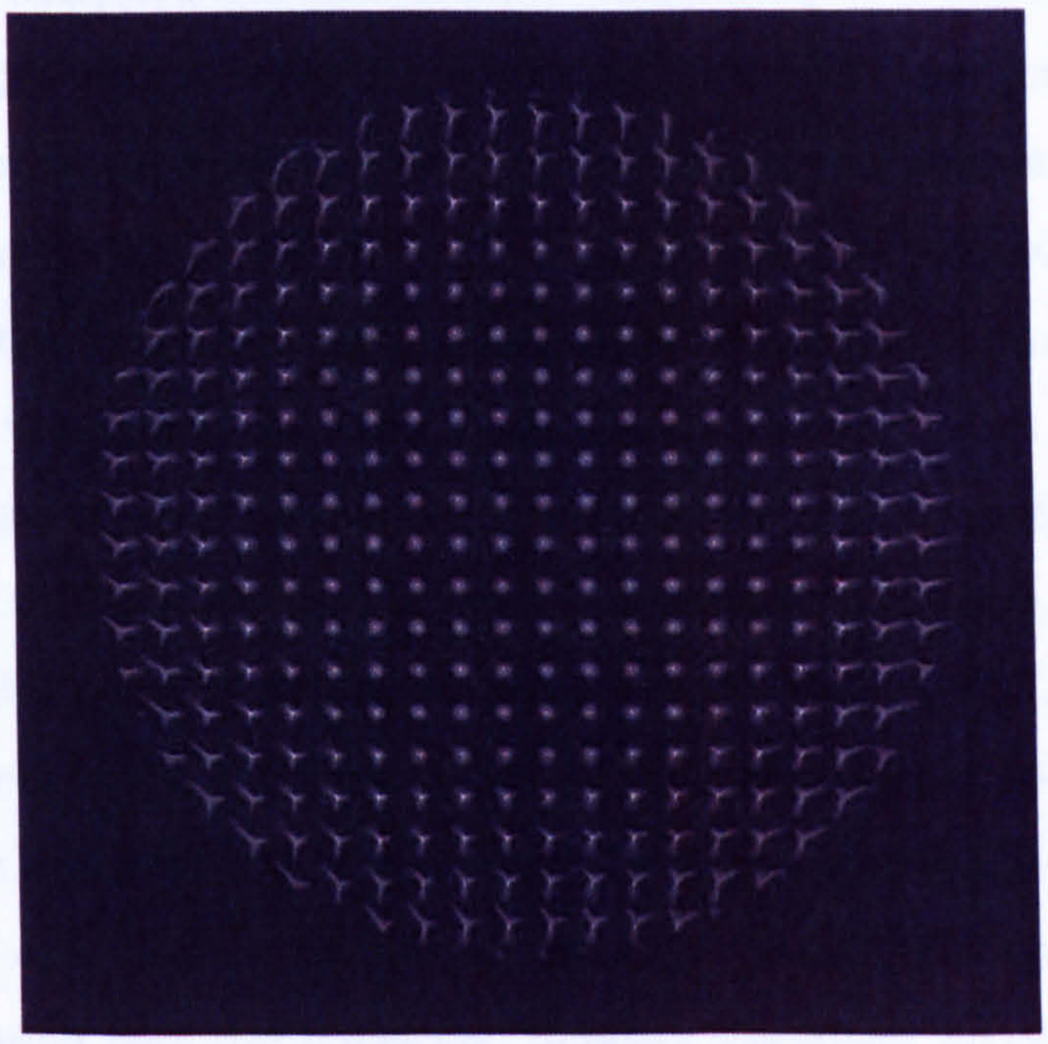

Figure 6.33: *PSF samples at a number of points in the image plane. The image is created by convolving a scene formed by dirac functions with the PSF produced by the manufactured phase mask.*

show the results of restoration with LRD, which only uses the central PSF. A non uniformity correction algorithm for detector fixed pattern noise was applied on the images but was unable to completely remove it, as can clearly be seen in the images. Work remains to be done in the implementation of techniques to mitigate the impact of noise in real sensors, especially fixed pattern noise. An interesting study [122] has been undertaken for the adaptive estimation of the gain and bias nonuniformity in infrared detectors from scene data. It has proved its utility in mitigating fixed-pattern noise which makes it particularly suitable for our IR wavefront coded image.

Joint utilization of the petal phase mask with restoration algorithm such as the Van Cittert and Lucy-Richardson methods, clearly enhances the imaging performance across the field of view, as it can be observed in From Fig. 6.34. We judge that the image quality after restoration is still superior in all of the considered cases to that produced with only a single element. Unfortunately the restoration process also amplifies noise and thereby lowers the signal-to-noise-ratio (SNR). We should note here that the uncooled detector in combination with the weather conditions leads to excessive amounts of fixed pattern noise, which is exaggerated in the restoration process. A better non-uniformity correction and/or higher contrast input images can be expected to yield even better restored images, with respect to image detail and SNR. To some extent, the noise can be reduced in the restored images by adaptive image processing, such as a Wiener filtering or wavelets based noise reduction algorithms. Lucy-Richardson deconvolution works surprisingly well in the central part of the FOV and exhibit moderate noise amplification. Towards the edges of the field of view LRD is not able to deblur the images, see Fig. 6.34(b). The Van Cittert algorithm, taking into account the varying PSF, performs better towards the edges of the FOV but results in somewhat higher noise amplification. The lower noise amplification in the Lucy-Richardson restoration is partly due to the fact that it only deals with a rather nice, i.e. small, PSF and partly because the implementation uses regularization, between iterations, to suppress noise. At the time being, the Van Cittert implementation has no regularizing mechanisms and also deals with rather large PSFs at the edges of the FOV.

To conclude, we have described what we believe is the first experimental realization of the potential of using a phase mask together with digital signal processing to reduce the number of optical elements and mitigate aberrations in an IR imaging

(a)

(b)

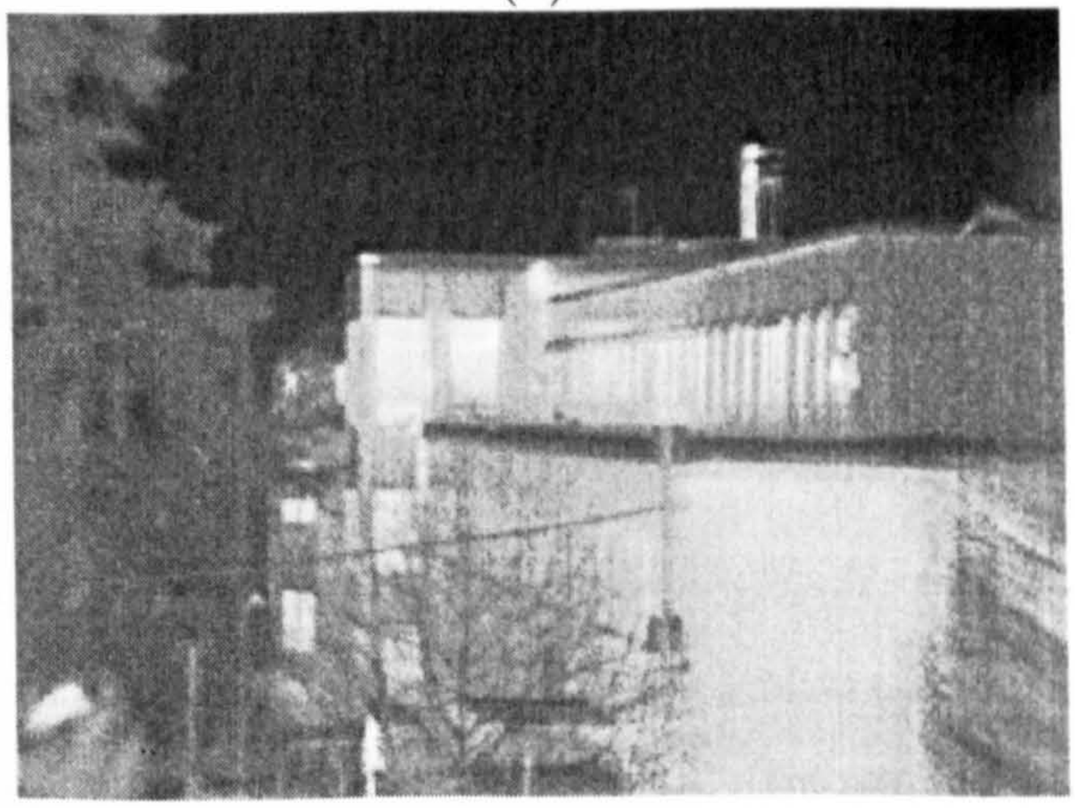

(c)

Figure 6.34: *(a) Image taken with only the singlet at the best on-axis focus, (b) wavefront coded image after Lucy-Richardson deconvolution, utilizing only the central PSF and (c) wavefront coded image after Van Cittert shift-variant restoration.*

system. To avoid the effect of thermal defocus, as it is the case with all germanium made optics, future work should include manufacture of a wavefront coded singlet from chalcogenides, with the encoding phase function incorporated into the front surface. In this case, the manufacturing of the singlet will benefit from low-cost moulding techniques.

5 Conclusions

Three simulated and experimental examples of the benefits of wavefront coding technique have been reported: the reduction of peak intensity at the detector when the imager is illuminated with laser light (EOPM), the athermalization of a complete IR optical system subject to a temperature range of −20°C to +70°C and an experimental IR system where the number of optical elements was decreased by a factor of two while maintaining imaging performance. The performance improvements attained by wavefront coding are balanced by significant increase in the system noise. Future work shall investigate in a comprehensive manner several iterative deconvolution technique for real phase encoded images in order to suppress noise and image artifacts, principal limitations of this technique.

The use of wavefront coding for electro-optical protective measures could be the subject of follow-on work, such as the reduction in the intensity of the optical retro-reflection. An additional consideration is that, in the case of the petal mask, wavefront coding could be an agile protective measure: varying between zero effect and maximum effect by the simple axial rotation of an optical element.

As a final comment, the manufacture of the asymmetric elements employed during these experiments is not unproblematic, but the major problems appear to be solved. Masks have been manufactured by Qioptiq (UK) for use in infrared systems using diamond machining. At Heriot Watt University, we have manufactured visible masks using reactive ion etching on glass. In future work, moulding and magnetorheological finishing may also be used. In summary, wavefront coding appears to offer significant potential in the three application presented here.

Chapter 7

Conclusions and future work

This thesis reports an investigation into the physical principles and potential applications of wavefront coding. The technique has been developed to mitigate the impact of optical aberrations in incoherent imaging systems. It employs phase masks and post-detection digital signal processing to achieve tolerance to aberrations which could not be attained by traditional imaging systems whilst maintaining their diffraction-limited resolution.

We have presented a review of the theory of wavefront coding and derived mathematical expressions of the phase masks that allow an increase in the tolerance to third order aberrations such as defocus, astigmatism and coma. This theoretical work required a series of numerical studies and simulations which included an understanding of the principles of diffraction and image recovery, as well as the necessary mathematical tools to evaluate integrals and perform computer-modeling of the diffraction phenomena.

In Chapter 2, we have evaluated the integral of the ambiguity function within the stationary phase approximation to obtain a rectangularly separable cubic phase mask suitable for the alleviation of defocus aberration. In a parallel study based on a purely geometrical optics description of the phenomenon, we have shown that rectangularly separable antisymmetric phase masks of polynomial degree equal or near cubic are the optimum when the optical system suffers from defocus aberration. In contrast to the mathematical complexity of integral equations, the geometrical optics approach offers analytical equations and clear and useful picture of the encoding process which may be potentially employed to design new phase mask for specific applications.

Antisymmetric phase masks are efficient in reducing the sensitivity to aberrations but their manufacture is in general problematic and costly. An attractive alternative for less-demanding applications that offers the advantage of low cost manufacture can be attained with rotationally symmetric phase masks. For this reason, in Chapter 3, we have minimised an asymptotic expansion of the integral of the variation of the Strehl ratio to design a quartic filter that achieves insensitivity to astigmatism and coma aberrations while enhancing the tolerance to defocus.

One of the most important outcomes of this thesis has been the development of a new understanding of the formation of the optical transfer function in incoherent imaging systems. The novel approach, presented in Chapter 4, is based on a geometrical analysis of plane curves and has been shown to provide by simple means an evaluation method of wavefront coding and a unique insight into its physical principles. This method offers an important tool for evaluation of phase masks against specific aberration.

The performance of the wavefront coded phase masks has been investigated by means of merit functions based on the modulation transfer function, point spread function and Strehl ratio. We have shown that the increased tolerance to aberrations is accompanied by a significant reduction in the signal-to-noise ratio and artifacts in the digitally restored image. We have shown in Chapter 5 that noise amplification is probably the most important factor when designing wavefront coding systems. We have extended earlier incomplete studies of the noise levels to include not only the tangential and sagittal axes (most favourable) but the entire spatial frequency domain for the cubic and petal phase masks. The metrics that quantified the noise gain were generated from the entire wavefront coded MTFs. A study of the noise amplification that separates a certain signal space of higher MTF values from a certain noise space of lower MTF remains to be done.

We have shown that the phase of the optical transfer function of antisymmetric phase masks varies rapidly with increasing aberration. The disparity between the phase of the convolution and deconvolution kernels during the inverse filtering lies at the origin of the presence of artifacts in the restored image. Unless the deconvolution kernel is adjusted, the artifacts become apparent. A more complete figure of merit that contains not only the magnitude of the wavefront coding OTF, but its phase (of greater importance in enhancing aberration tolerance) would be very relevant to explore in future work.

The majority of electronic imaging systems are undersampled, and this leads to aliasing. Until now, the sampling effect of the detector had been neglected in all wavefront coding analysis by assuming that the cut-off frequency of imaging systems was determined by the optical system only. In Chapter 5, we have provided a comprehensive performance model in order to characterise the sampling artifacts (aliasing) as fixed-pattern noise. We have demonstrated that the complex nature of the wavefront coded OTF results in a reduced aliasing component compared to a traditional sampled imaging system. Furthermore, the restoration of wavefront coded images is not compromised by detector sampling.

The thesis is also motivated by the implementation of wavefront coding to reduce the cost of military and commercial thermal imagers. The development of uncooled detectors has allowed a greatly decrease cost of the detector but the optics will increasingly dominate the cost of thermal imaging systems. We have demonstrated that by employing wavefront coding and post-detection signal processing, physical and mechanical parts can be removed in favour of low-cost electronics. An extensive assessment through numerical simulations and optimisations of the use of wavefront coding as an athermalization technique was reported in Chapter 6. Despite high levels of noise amplification, we have demonstrated that overall image quality was significantly improved from just ±10°C to ±50°C, so that the thermal imager could be operated in a more realistic temperature range and with decreased system complexity. A further investigation into deconvolution algorithms to reduce noise amplification in this particular application is necessary. More sophisticated image processing including non-linear algorithms and iterative methods need to be considered in the future to improve image quality.

The work reported in this thesis aims to provide future research with a comprehensive framework from which to develop the wavefront coding methodology of jointly designing the components of an imaging system. This methodology will be incorporated into specialized software that allows to model the components of the imaging system (optical elements, phase masks, detector architecture, noise model, image processing and observer) as well as provide figures of merit based on the objectives of a particular system or imaging application. The modeling will include optimisation of the system variables (e.g. shape and strength of the phase mask) in order to minimize the cost functions and achieve the final imaging system.

This thesis has not been restricted only to theoretical or modeling work. Sev-

eral experimental realizations of wavefront coding systems have been implemented. In Chapter 6 we have reported the first wavefront-coded single-element thermal-imaging lens which provides an image sharpness across the field of view equal to one employing a traditional two-element system. In collaboration with our partners, we have achieved a 40% reduction in physical components and weight, and therefore a large reduction in cost and simplified assembly with greater tolerances.

Our research into wavefront coding shows how combining optical and digital processing provides an extra degree of freedom that can offer improved imaging performance across a wider range of conditions and at reduced cost. It is not a panacea, however; aberration-free imaging offers the ultimate in performance, but for many applications in which aberrations are present, whether due to a requirement to image objects in depth or to limitations in lens complexity, wavefront coding offers an additional parameter to be included within the design trade-off space.

Appendix A

Stationary phase approximation

The stationary phase method originated in the interference principle of water waves and formulated in more general terms by Kelvin [56]. In the last decades, work on diffraction and other problems has caused the method to be extended to multiple integrals.

According to Huygens' principle the field diffracted by an aperture is obtained by adding the contributions of an infinitive number of secondary waves, one from each point in the aperture. Mathematically, this sum is expressed as a diffraction integral. By evaluating the diffraction integral asymptotically, one can show that only a few of the secondary waves mentioned above contribute significantly to the diffractive field [60]. This observation forms the physical basis for the use of the method of stationary phase in solving diffraction integral.

In this appendix, we describe some of the fundamental concepts of this subject and provide the equations that allow us to evaluate analytically the various one- and two-dimensional diffraction integrals encountered throughout this thesis.

Consider a one-dimensional integral of the form

$$J = \int_{x_1}^{x_2} f(x) \exp(\mathrm{i}k\phi(x))\mathrm{d}x, \tag{A-1}$$

where the phase function $\phi(x)$ is a real-valued function, the amplitude function $f(x)$ may be complex and $k = 2\pi/\lambda$ is the wave number. If k is sufficiently large, as it is the case in the optical domain, the integral in Eq. (A-1) may be evaluated asymptotically as $\lambda \to 0$. For large k, the integrand $\exp(\mathrm{i}k\phi(x))$ oscillates so rapidly compared to f(x) that cancelation occurs, except in the immediate neighborhoods of a stationary point $x = x_s$ at which $\phi'(x) = 0$, and boundary points x_1 and x_2. Thus, the main contribution to the integral in Eq. (A-1) comes from infinitesimally

small regions around the stationary points. In practice, integrals may contain more than one stationary point. If the stationary points are close together or near the boundary regions, the mathematical expressions become complicated and out of the scope of our work. Therefore, we restrict our research to derive phase filters in Chapter 2 and 3 to the simple case of an isolated stationary point, that lies inside the integration domain but far from its boundaries. Following the procedure by van Kampen [123, 124], we may expand $\phi(x)$ in a Taylor series about the stationary point x_s at which $\phi'_{x_s} = 0$ to obtain

$$\phi(x_s) = \phi(x_s) + \phi'(x_s)(x - x_s) + \frac{1}{2}\phi''(x_s)(x - x_s)^2 + \cdots \tag{A-2}$$

By replacing the Taylor expansion of ϕ up to the second order in Eq. (A-1) and taking into account that $\phi'_{x_s} = 0$, we obtain

$$J \sim \exp\left[ik\phi(x_s)\right] f(x_s) \int_{-\infty}^{\infty} \exp\left[\frac{1}{2}ik\phi''(x_s)(x - x_s)^2\right]. \tag{A-3}$$

The introduction of infinite limits of integration is justified since x_s is an isolated stationary point, far from the boundaries x_1 and x_2. The Gaussian integral in Eq.(A-3) can be evaluated analytically (see Ref.[125] or Ref.[72] for further details) which yields

$$J \sim \exp\left[ik\phi(x_s)\right] f(x_s) \sqrt{\frac{2\pi}{k\left|\phi''(x_s)\right|}} \exp\left(i\mu\frac{\pi}{4}\right), \tag{A-4}$$

with $\mu = \mathrm{sign}\phi''(x_s)$. This last equation represents the main term of the contribution to J corresponding to the stationary point $x = x_s$, assuming a certain degree of smoothness in ϕ and f.

The same approach can be adopted when optical diffraction is described by a two-dimensional double integral of the type

$$J = \int\int_A f(x, y) \exp(ik\phi(x, y))\mathrm{d}x\mathrm{d}y, \tag{A-5}$$

where the phase function $\phi(x, y)$ is a real-valued function, the amplitude function $f(x, y)$ may be a complex-valued function and A is the area of the aperture. In the same fashion as for the one-dimensional problem, if k is large enough, the leading contribution to the integral J occurs when the phase ϕ is stationary, i.e.

$$\left.\frac{\partial\phi}{\partial x}\right|_{x_s} = \left.\frac{\partial\phi}{\partial y}\right|_{y_s} = 0. \tag{A-6}$$

with (x_s, y_s) the stationary point. For an isolated interior stationary point, the expression for J becomes

$$J \sim \frac{2\pi\sigma}{k|H(x_s, y_s)|^{1/2}} f(x_s, y_s) \exp\left[ik\phi(x_s, y_s)\right], \tag{A-7}$$

where $H(x,y)$ is given by

$$H(x,y) = \frac{\partial^2\phi}{\partial x^2}\frac{\partial^2\phi}{\partial y^2} - \left(\frac{\partial^2\phi}{\partial x \partial y}\right)^2, \tag{A-8}$$

and

$$\sigma = \begin{cases} 1 & \text{if } H(x_s,y_s) < 0 \\ +\mathrm{i} & \text{if } H(x_s,y_s) > 0, \quad \partial^2\phi/\partial x^2 > 0. \\ -\mathrm{i} & \text{if } H(x_s,y_s) > 0, \quad \partial^2\phi/\partial x^2 < 0 \end{cases} \tag{A-9}$$

These last three equations are also used in the second part of Chapter 3 to derive the central intensity of the point spread function of an optical system with a phase mask.

Appendix B

Ray trace equations of an imaging system with a cubic phase mask

In contrast to a perfect optical system where all the rays come to focus at the same image point on the optical axis, a wavefront coding system deflects the rays so that they cross the optical axis at different locations. However, note that any ray transmitted by cubic phase mask will intersect at some point with the remainders. Two rays emerging from the exit pupil at p_1 and p_2 will cross each other when $f(x_{12}, p_1) = f(x_{12}, p_2)$; this condition is met when

$$x_{12} = \frac{M(p_1, p_2)}{N(p_1, p_2)}, \tag{B-1}$$

After lengthy mathematical manipulation, we obtain M and N

$$M(p_1, p_2) = \frac{\alpha\,(p_2^3 - p_1^3)}{R^3} - \frac{3\alpha p_1\,(p_1^2 - d_i^2)}{R^3 + 3\alpha p_1\sqrt{d_i^2 - p_1^2}} + \frac{3\alpha p_2\,(p_2^2 - d_i^2)}{R^3 + 3\alpha p_2\sqrt{d_i^2 - p_2^2}} \tag{B-2}$$

and

$$N(p_1, p_2) = \frac{1}{p_2\left(\frac{3\alpha p_2}{R^3} + \frac{1}{\sqrt{d_i^2 - p_2^2}}\right)} - \frac{1}{p_1\left(\frac{3\alpha p_1}{R^3} + \frac{1}{\sqrt{d_i^2 - p_1^2}}\right)}. \tag{B-3}$$

The exact expression for the caustic curve in parametric format produced by a cubic phase mask is given by

$$\begin{aligned} C_x(p) &= f(\lim_{\delta p \to 0} \frac{M(p, p+\delta p)}{N(p, p+\delta p)}, p) \\ C_y(p) &= \lim_{\delta p \to 0} \frac{M(p, p+\delta p)}{N(p, p+\delta p)} \end{aligned} \tag{B-4}$$

evaluating further, yields

$$C_x(p) = -\frac{1}{R^6\left[d_i^2R^3 + 6p\alpha\left(d_i^2 - p^2\right)^{3/2}\right]}\times$$
$$\left\{3p^2\alpha\sqrt{d_i^2-p^2}\left[\left(4R^6 + 9p\alpha\sqrt{d_i^2-p^2}R^3 - 9p^4\alpha^2\right)p^2 + \left(9p^4\alpha^2 - R^6\right)d_i^2\right]\right\} \tag{B-5}$$

$$C_y(p) = d_i + \frac{\alpha p^3}{R^3} + \frac{1}{R^3 + 3p\alpha\sqrt{d_i^2-p^2}}\left[3p\alpha\left(p^2 - d_i^2\right) + R^3\sqrt{d_i^2-p^2}\,C_x(p)\right]$$

The approximation of the caustic curve by a parabola assumes that there is a linear relationship between $C_x(p)$ and the exit-pupil coordinate p of the transmitted ray. Thus, we generate a power series expansion for $C_x(p)$ about the point $p = 0$ up to the first order term, which results

$$C_x(p) = d_i - \frac{6d_i^2\alpha}{R^3}p + \mathrm{O}[p]^2\,, \tag{B-6}$$

rearranging and defining $\delta x = C_x(p) - d_i$ as the displacement along the optical axis relative to the image plane, we obtain a linear approximation between p and δx

$$p \approx \frac{R^3}{6d_i^2\alpha}\delta x, \tag{B-7}$$

which is a valid approximation when $\alpha << R^2/6d_i$. The range of validity has been obtained by considering that the higher order terms in Eq. (B-6) when p take its maximum value at the edge of the pupil $p = R$ should be neglected, thus

$$\frac{6d_i^2\alpha}{R^2} >> \mathrm{O}[R]^2\,. \tag{B-8}$$

The final step requires substituting Eq. (B-7) into $C_y(p)$ given in Eq. (B-5). This results in an elaborated expression which contains high order term in δx. By expanding the expression into a Taylor series and extracting only the terms in δx that form a pure parabola we obtain the equation for the parabolic caustic near the image plane, finally

$$C(\delta x) = \frac{R^3}{12d_i^3\alpha}\delta x^2 \tag{B-9}$$

for a $F/\#$ optical system focusing at an object in the far distance, the caustic can be rewritten

$$C(\delta x) = \frac{1}{96F/\#^3\alpha}\delta x^2. \tag{B-10}$$

This can be approximated by a parabola, a the caustic is linear in p

$$L(\alpha) = \frac{-180\alpha^3 \left(d_i^2 - R^2\right)^3 - 2R^2\alpha d_i^2 \left(12R^4 - 19d_i^2R^2 + 6d_i^4\right)}{36\alpha^2 \left(d_i^2 - R^2\right)^3 - R^4 d_i^4} \tag{B-11}$$

$$L(\alpha) \approx \alpha \left(\frac{24R^2}{d_i^2} - 38 + \frac{12d_i^2}{R^2}\right) \tag{B-12}$$

As an example, the ends of the caustic for $\alpha = 10\lambda$ correspond to defocus values $W_{20} \approx \pm 27\lambda$. This amount of defocus is much larger than what the phase mask can tolerate and it indicates that the invariance region must be constrained into a small domain near the image plane.

$$L_s(\alpha) = -\frac{6\alpha \left(R^2 - d_i^2\right) R^2}{R^4 + 9\alpha^2 \left(R^2 - d_i^2\right)} - 2\alpha \tag{B-13}$$

$$L_s(\alpha) \approx \alpha \left(\frac{6d_i^2}{R^2} - 8\right) \tag{B-14}$$

Appendix C

Patent situation of wavefront coding technology

This research project has been fully funded by QinetiQ Ltd. Our industrial sponsor has shown special interest on commercial exploitation of wavefront coding and requested an evaluation of the existing intellectual property on this technology. A brief review is included in this appendix.

CDM Optics Inc. (E. R. Dowski and T. W. Cathey) has been granted several US and international (WO) patens in relation to Wavefront Coding optical systems. In 2005, OmniVision Technologies, one of the world's leading suppliers of CMOS image sensors, signed an agreement to acquire all of the outstanding securities of CDM Optics, Inc. Omnivision Technologies aims to be able to reduce the overall cost of an auto-focus and zoom camera module while reducing the reliability issues and supply limitations associated with current mobile phone camera module systems. Their main market is concentrated in the low-cost, mass-production applications such as mobile phones and web cams.

The most significant patents granted to CDM Optics Inc. on the field are given by:

1. US 5,748,371, Extended depth of field optical systems, May 1998.

2. US 6,021,005, Anti-aliasing apparatus and methods for optical imaging, Feb. 2000.

3. US 6,069,738, Apparatus and methods for extending depth of field in image projection systems, May 2000.

4. US 6,525,302, Wavefront coding phase contrast imaging systems, Feb. 2003.

5. US 6,842,297, Wavefront coding optics, Jan. 2005.

6. US 6,873,733, Combined wavefront coding and amplitude contrast imaging systems, Mar. 2005.

7. US 6,911,638, Wavefront coding zoom lens imaging systems, Jun. 2005.

8. US 6,940,649, Wavefront coded imaging systems, Sep. 2005.

In general, these patents contain two main claims by the inventor:

- The mathematical functions that describe the shapes of the Wavefront Coding optics.

- The apparatus of a wavefront coded imaging system: optical system, phase mask which modifies the OTF and post detection processing to inverse the effect of the coding.

1 Phase mask profiles

The main characteristic of these phase functions is their asymmetry. Our studies [58] have shown that the most suitable phase form for increasing the defocus tolerance is given by an odd function $f(x) = -f(-x)$, the same is applied to non-rectangularly separable masks.

Another family of phase masks, and also covered by patents, includes antisymmetric phase forms that leave the central group of rays passing trough the masks unmodified. By not modifying the central rays of a wavefront coded imaging system, it is possible to achieve higher MTFs and more control of defocus and defocus-related aberrations.

2 Apparatus and methodology

The intellectual property of the Wavefront Coding patents is not only restricted to the shape of the coding elements but to the methodology or apparatus of a wavefront coded imaging system. The methodology, which involves a traditional optical system, wavefront coding optics and a post processing element, becomes

therefore the strong nucleus of the patents and it is clearly an important part of the claims, eg:

"We claim:

wavefront coding optics between the object and the detector;

said wavefront coding optics being constructed and arranged to alter an optical transfer function of the lens system in such a way that the optical transfer function is substantially less sensitive to focus related aberrations than an unaltered optical transfer function, wherein the wavefront coding optics alters the optical transfer function substantially by affecting phase of light transmitted by the optics; and a post processing element for processing the image captured by the detector by reverse altering the optical transfer function accomplished by the optics.

The apparatus of claim 1, wherein the wavefront coding optics are integrally formed with at least one of the lenses"

Note that the claim mentions the optical transfer function so as to be insensitive to focus related aberrations. This statement is not precisely correct and unequivocal since it is only the magnitude of the optical transfer function the one that remains practically invariant to the effect of defocus and not the phase. We have demonstrated [58] that the phase term of the transfer function is highly changeable with defocus.

The IP covers all possible optical arrangements and substrates on which the phase mask can be implemented. There is no prior art about an imaging method which consists in distorting, with intention and in a specific way, an optical wavefront followed by applying post detection processing to undo the alteration. The claims are only restricted to Wavefront Coding phase masks that produce optical transfer functions less sensitive to defocus related aberrations. Phase masks which produce modulation transfer functions invariant to other aberrations are not mentioned.

Appendix D

Amplitude and phase modulation of the OTF

To calculate the amplitude and phase modulation of the OTF from the geometry of the spiral, it is necessary to obtain the normal to the curve in the complex plane, which by definition is

$$n(r') = \mathrm{i}\frac{\mathrm{d}L(r')}{\mathrm{d}r'} = \frac{\mathrm{i}}{2}\exp[\mathrm{i}4\pi\nu(\alpha\nu^2 + 2w_{20}r' + 3\alpha r'^2)], \tag{D-1}$$

whilst the radius of curvature at any point of the spiral is given by the inverse of the curvature κ

$$R(r') = \frac{1}{\kappa} = \frac{1}{16\pi\nu(w_{20} + 3\alpha r')}. \tag{D-2}$$

Combining Eq. (D-1) and Eq. (D-2), we obtain the relative oscillation $m(\nu)|_{\pm}$ of each end of the spiral with respect to their foci:

$$m(\nu)|_{\pm} = R(\pm(1-\nu)) \cdot n(\pm(1-\nu)). \tag{D-3}$$

The projection operation in the complex plane is given by the real component of the Hermitian product between the mean OTF $\langle H(\nu)\rangle$ and the combined modulations from both extremes of the spiral as given in Eq. (D-3), which yields

$$M_{\parallel}(\nu) = \mathrm{Re}\left[\left(m(\nu)|_{+} - m(\nu)|_{-}\right) \cdot \left(\langle H(\nu)\rangle^{*}/|\langle H(\nu)\rangle|\right)\right] \tag{D-4}$$

where $*$ denotes complex conjugate. By substituting Eq. (D-3) and Eq. (4-13) into Eq. (D-4) and making use of trigonometric identities, the amplitude modulation

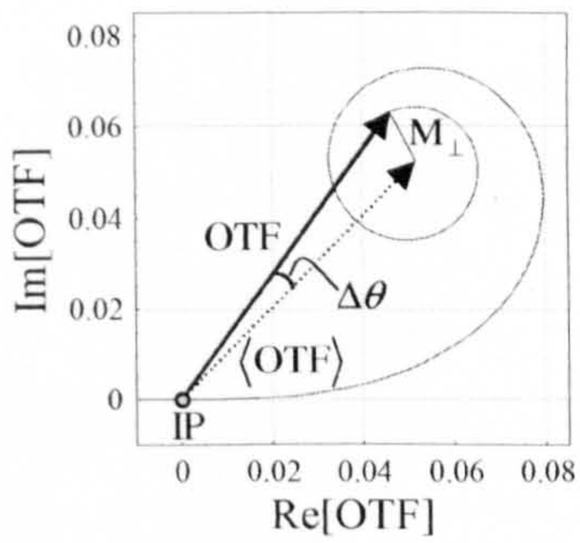

Figure D.1: *Diagram showing the relationship between the phase modulation of the OTF with defocus and its geometrical representation at one end of the spiral.*

obtained from summing both contributions is

$$M_{\parallel}(\nu; w_{20}, \alpha) = \frac{1}{16\pi\nu}\left(\frac{\cos\{(4\pi\nu/3\alpha)[w_{20}-3\alpha(1-\nu)]^2+(\pi/4)\}}{w_{20}-3\alpha(1-\nu)}\right.$$
$$\left.-\frac{\cos\{(4\pi\nu/3\alpha)[w_{20}+3\alpha(1-\nu)]^2+(\pi/4)\}}{w_{20}+3\alpha(1-\nu)}\right). \quad \text{(D-5)}$$

The modulation orthogonal to the mean OTF, $M_{\perp}$, is a measure of the amplitude of the phase modulation and is readily obtained by replacing the cosine by a sine function in Eq. (4-19). This trigonometric replacement implies simply a rotation of 90 degrees in the modulation, from parallel to orthogonal. In terms of the phase angle $\Delta\theta$, it is possible to obtain an expression taking into account the geometry relationships in the diagram shown in Fig. D.1. Thus, considering small phase angles so that $\tan\Delta\theta \sim \Delta\theta$, we obtain

$$\Delta\theta \approx \frac{M_{\perp}}{\langle H(\nu)\rangle/2}$$
$$= \frac{\sqrt{3\alpha\nu}}{2\pi\nu[w_{20}-3\alpha(1-\nu)]} \times \sin\left\{\frac{4\pi\nu}{3\alpha}[w_{20}-3\alpha(1-\nu)]^2+\frac{\pi}{4}\right\} \quad \text{(D-6)}$$

Appendix E

OTF decomposition for a circular aperture with cubic phase mask

The expression for the interferogram phasor representing a pair of Young's slits on the horizontal (or vertical) axis of a circular aperture with a cubic phase mask is substituted into the two-dimensional version of Eq.(4-3), which yields

$$L(x',\xi,\eta=0)=\frac{2}{\pi}\int_0^{x'}\sqrt{1-(x+\xi)^2}\exp\left\{4i\pi\xi\left[2w_{20}x+\alpha\left(3x^2+\xi^2\right)\right]\right\}, \quad \text{(E-1)}$$

for $0<x'<1-\xi$, and

$$L(x',\xi,\eta=0)=\frac{2}{\pi}\int_0^{x'}2\sqrt{1-(x-\xi)^2}\exp\left\{4i\pi\xi\left[2w_{20}x+\alpha\left(3x^2+\xi^2\right)\right]\right\} \quad \text{(E-2)}$$

for $-1+\xi<x'<0$. The complex decomposition of the OTF for the spatial frequency ξ is obtained by plotting the variation of $L(x',\xi,0)$ as x' varies from $-1+\xi$ to $1-\xi$. The curvature of the spiral is readily calculated using the same process as for the 1D phase mask, thus applying Eq.(4-15) to Eq.(E-1) and Eq.(E-2) we obtain after lengthy mathematical manipulation,

$$\kappa(x',\eta)=\frac{4\pi^2\xi(w_{20}+3\alpha x')}{\sqrt{|-1+(|x'|+\xi)^2|}} \quad \text{(E-3)}$$

which is valid for $-1+\xi<x'<1-\xi$.

Appendix F

Detector MTF

The one-dimendional MTF of a staring-focal-plane-array imaging system is given by

$$\mathrm{MTF}_{FPA}(\xi) = \mathrm{MTF}_{footprint}(\xi) \times \mathrm{MTF}_{samp}(\xi), \tag{F-1}$$

where $\mathrm{MTF}_{footprint}$ accounts for the finite-size of the detector elements and MTF_{samp} relates to a spatially averaged transfer function that is inherent in the sampling process itself by assuming that the scene being image is randomly positioned with respect to the sampling sites [95]. This random alignment corresponds to the situation where a natural scene is imaged with an ensemble of individual alignments. Thus, the sampling MTF is the average over all the possible MTFs[102]. However, this sampling MTF does not contribute in a MTF-measurement setup where the test target is aligned with the sampling sites because the central assumption in its derivation is the random position of any image feature with respect to the sampling sites. Because typical test procedures rule out the sampling MTF from contributing to the measurements is often forgotten in a system analysis. Nevertheless, as it is the case in our simulations, when the scene being image has no net alignment with respect to the sampling sites, the sampling MTF will contribute in practice and should thus be included in our system performance modeling.

An average sampling MTF in one dimension can be defined as

$$\mathrm{MTF}_{samp}(\xi) = |\mathrm{sinc}(\xi x_{samp})| = \left|\frac{\sin(\pi\xi x_{samp})}{\pi\xi x_{samp}}\right|, \tag{F-2}$$

where the x_{samp} is the centre-to-centre spacing between the pixels.

The one dimensional footprint MTF is given by

$$\mathrm{MTF}_{footprint}(\xi) = |\mathrm{sinc}(\xi w)| = \left|\frac{\sin(\pi\xi w)}{\pi\xi w}\right|, \tag{F-3}$$

where the w is the size of the pixel detector.

In the modeling of the uncooled FPA detector, we assume a pixel size of $w = 25\mu$m with a 100% fill factor, from which it follows that $x_{samp} = w$. These parameters were later substituted in Eq.(F-1) to simulate the MTF of the IR uncooled detector, see Fig. 6.13.

Appendix G

Zernike polynomial fitting of the manufacture phase mask

This surface *Zernike fringe phase* is well suited to modeling system aberrations for which measured interferometer data is available. The surface phase is given by

$$\Phi = \Sigma_i^N 2\pi A_i Z_i(\rho, \varphi), \tag{G-1}$$

where N is the number of Zernike coefficients in the series, A_i is the coefficient on the i^{th} Zernike fringe polynomial, ρ is the normalised radial ray coordinate and φ is the angular ray coordinate. This particular set of Zernike polynomials is sometimes called the *University of Arizona* notation.

The Zernike coefficients all have units of waves and a number $N = 36$ was used in the phase mask modeling. Only the Zernike coefficient different from zero as shown: $Z_1 = 0.032$, $Z_2 = -0.372$, $Z_3 = 0.306$, $Z_4 = 8E-3$, $Z_5 = 0.34$, $Z_6 = 1.074$, $Z_7 = 0.035$, $Z_8 = 0.094$, $Z_9 = -0.08$, $Z_{10} = 2.119$, $Z_{11} = -3.251$, $Z_{12} = 0.06$, $Z_{13} = 0.049$, $Z_{14} = -0.036$, $Z_{15} = 7E-3$, $Z_{17} = -0.065$, $Z_{18} = -0.114$, $Z_{19} = 0.02$, $Z_{20} = -0.045$, $Z_{21} = 0.034$, $Z_{22} = -8E-3$, $Z_{23} = 0.011$, $Z_{24} = 6E-3$, $Z_{25} = -3E-3$, $Z_{26} = 0.019$, $Z_{27} = 0.032$, $Z_{28} = -1E-3$, $Z_{29} = -0.041$, $Z_{30} = -0.012$, $Z_{31} = 0.021$, $Z_{32} = 2E-3$, $Z_{33} = -5E-3$, $Z_{34} = 4E-3$, $Z_{35} = 7E-3$ and $Z_{36} = -9E-3$.

References

[1] J. N. Mait, R. Athale, and J. van der Gracht. Evolutionary paths in imaging and recent trends. *Opt. Express*, 11:2093–2101, 2003.

[2] R. E. Fischer. Bending to demand. SPIE*'s* OE *magazine*, pages 25–27, April 2004.

[3] W.T. Cathey, B.R. Frieden, W.T. Rhodes, and C.K. Rushforth. Image gathering and processing for enhanced resolution. *J. Opt. Soc. Am. A*, 1:241–249, 1984.

[4] R.J.Hanish. Image restoration for the Hubble Space Telescope. *Proc. SPIE*, 2198:1349–1356, 1994.

[5] E. Dowski and T. W. Cathey. Extended depth of field through wavefront coding. *Appl. Opt.*, 34:1859–1866, 1995.

[6] R. M. Matic and J.W. Goodman. Optical preprocessing for increased system throughput. *J. Opt. Soc. Am. A*, 6:428–440, 1989.

[7] M. Descour and E. Dereniak. Computed-tomography imaging spectrometer: experimental calibration and reconstruction results. *Appl. Opt.*, 34:4817–4826, 1995.

[8] Omnivision Technologies. Omnivision introduces first truefocus camera using patented wavefront coding technology, available from `http://www.ovt.com`.

[9] W. J. Smith. *Modern optical engineering.* McGraw-Hill, New York, 2000.

[10] H. H. Hopkins. The frequency response of a defocused optical system. *Proc. Phys. Soc. London A*, 231:91–103, 1955.

[11] H. H. Hopkins. The use of diffraction-based criterion of image quality in automatic optical design. *Opt. Acta*, 13:343–369, 1966.

[12] K. Strehl. Investigations in optics with special reference to the spectroscope. *Zeitfür Instrumkde*, 22:213, 1902.

[13] A. Maréchal. Thesis. *Uni. Paris*, 1948.

[14] Lord Rayleigh. Investigations in optics with special reference to the spectroscope. *Philos. Mag.*, 8:261, 1879.

[15] H. Bartelt, J. Ojeda-Castaneda, and E. E. Sicre. Misfocus tolerance seen by simple inspection of the ambiguity function. *Appl. Opt.*, 23:26932696, 1984.

[16] G. Häusler. A method to increase the depth of focus by two step image processing. *Opt. Commun.*, 6:38–42, 1972.

[17] W. T. Welford. Polychromatic axial behavior of aberrated optical systems: Wigner distribution function approach. *J. Opt. Soc. Am.*, 50:749–753, 1960.

[18] J.T. McCrikerd. Coherent processing and depth of focus of annular aperture imaginery. *Appl. Opt.*, 10:2226–2230, 1971.

[19] T.-C. Poon and M. Motamendi. Optical/digital incoherent image processing for an extended depth of field. *Appl. Opt.*, 26:4612, 1987.

[20] H. H. Hopkins. The disturbance near the focus of waves of radially non-uniform amplitude. *Proc. Phys. Soc. London Sect. B*, 62:22–32, 1949.

[21] G. Indebetouw and H. X. Bai. Imaging with fresnel zone pupil masks: extended depth of field. *Appl. Opt.*, 23:4299–4304, 1984.

[22] M. Mino and Y. Okano. Improvement in the OTF of a defocused optical system through the use of shaded apertures. *Appl. Opt.*, 10:2219–2225, 1971.

[23] J. Ojeda-Castaneda, R. Ramos, and A. Noyola-Isgleas. High focal depth by apodization and digital restoration. *Appl. Opt.*, 27:2583–, 1988.

[24] J. Ojeda-Castaneda, P. Andres, and A. Diaz. Annular apodizers for low sensitivity to defocus and to spherical aberration. *Opt. Lett.*, 11:487489, 1986.

[25] J. Ojeda-Castaneda and L. Berriel-Valdos. Zone plate for arbitrarily high focal depth. *Appl. Opt.*, 29:994–997, 1990.

[26] J. Ojeda-Castaneda, L. R. Berriel-Valdos, and E. L. Montes. Spatial filter for increasing the depth of focus. *Opt. Lett.*, 10:520–522, 1985.

[27] J. Ojeda-Castaneda, E. Tepichin, and A. Diaz. Arbitrary high focal depth with finite aperture. *Opt. Lett.*, 13:183185, 1988.

[28] J. Ojeda-Castaneda, E. Tepichin, and A. Pons. Apodization of annular apertures: Strehl ratio. *Appl. Opt.*, 27:51405145, 1988.

[29] S. Sanyal and A. Ghosh. High focal depth with quasi-bifocus birefringent lens. *Appl. Opt.*, 39:2321–2325, 2000.

[30] S. Sanyal and A. Ghosh. High tolerance to spherical aberrations and defects of focus with a birefringent lens. *Appl. Opt.*, 41:4611–4619, 2002.

[31] W. T. Cathey, E. R. Dowski, and A. R. FitzGerrell. Optical/digital aberration control in incoherent optical systems. *SPIE*, 2730:120–126, 1995.

[32] S. S. Sherif, W. T. Cathey, and E. R. Dowski. Phase plate to extend the depth of field of incoherent hybrid imaging systems. *Appl. Opt.*, 43:2709–2721, 2004.

[33] A. Castro and J. Ojeda-Castaneda. Asymmetric phase masks for extended depth of field. *Appl. Opt.*, 43:3474–3479, 2004.

[34] S. Mezouari, G. Muyo, and A. R. Harvey. Amplitude and phase filters for mitigation of defocus and third-order aberrations. *Proc. SPIE*, 5249:238–248, 2004.

[35] D. Zalvidea and E. E. Sicre. Phase pupil function for focal depth enhancement derived from a wigner distribution function. *Appl. Opt.*, 37:3623–3627, 1998.

[36] E. Ben-Eliezer, Z. Zalevsky, E. Marom, and N. Konforti. All-optical extended depth of field imaging system. *J. Opt. A*, 5:164–169, 2003.

[37] E. Ben-Eliezer, E. Marom, N. Konforti, and Z. Zalevsky. Radial mask for imaging systems that exhibit high resolution and extended depths of field. *Appl. Opt.*, 45:2001–2013, 2006.

[38] S. Mezouari and A. R. Harvey. Phase functions for the reduction of defocus and spherical aberration. *Opt. Letters*, 28:771–773, 2003.

[39] J. Ojeda-Castaneda, L. E. A. Langrave, and H. M. Escamilla. Annular phase-only mask for high focal depth. *Opt. Lett.*, 30:1647–1649, 2005.

[40] W. Chi and N. George. Electronic imaging using a logarithmic asphere. *Opt. Lett.*, 26:875–877, 2001.

[41] W. Chi and N. George. Computational imaging with the logarithmic asphere: theory. *J. Opt. Soc. Am. A*, 20:2260–2273, 2003.

[42] S. Prasad, T. C. Torgersen, V. P. Pauca, R. J. Plemmons, and J. van der Gracht. Engineering the pupil phase to improve image quality. *Proc. SPIE*, 5108:1–12, 2003.

[43] E. Ben-Eliezer, E. Marom, N. Konforti, and Z. Zalevsky. Experimental realization of an imaging system with an extended depth of field. *Appl. Opt.*, 44:2792–2798, 2005.

[44] Z. Zalevsky, A. Shemer, A. Zlotnik, E. Ben-Eliezer, E. Marom, and N. Konforti. All-optical axial super-resolving imaging using a low-frequency binary-phase mask. *Opt. Exp.*, 14:2631–2643, 2006.

[45] A. Papoulis. Ambiguity function in fourier optics. *J. Opt. Soc. Am.*, 64:779–788, 1974.

[46] P. M. Woodward. *Probability and Information Theory with Applications to Radar.* Pergamon, New York, 1953.

[47] J. Ojeda-Castaneda, P. Andrs, and E. Montes. Phase-space representation of the strehl ratio: ambiguity function. *J. Opt. Soc. Am. A*, 4:313317, 1987.

[48] A. R. FitzGerrell, E. R. Dowski, and W. T. Cathey. Defocus transfer function for circularly symmetric pupils. *Appl. Opt.*, 36:57965804, 1997.

[49] Q. Yang, L. Liu, and H. Lang. Computation of the ambiguity function for circularly symmetric pupils. *J. Opt. A*, 7:431–437, 2005.

[50] Q. Yang, L. Liu, and H. Lang. Defocus transfer function for circularly symmetric pupils under polychromatic illumination. *Proc. SPIE*, 5896:166–173, 2005.

[51] C. E. Cook and M. Bernfeld. *Radar Signals.* Academic, New York, 1967.

[52] A.W. Rihaczek. *Principles of High Resolution Radar.* McGraw-Hill, New York, 1969.

[53] K. Brenner, A. Lohmann, and J. Ojeda-Castaneda. The ambiguity function as a polar display of the OTF. *Opt. Commun.*, 44:323–326, 1983.

[54] A. Manzanares Ituarte and J. Ojeda-Castaneda. Geometrical approaches to the defocused optical transfer function. *SPIE*, 3572:390–393, 1999.

[55] J. W. Goodman. *Introduction to Fourier Optics.* McGraw-Hill, New York, 2nd ed, 2000.

[56] Lord Kelvin. On the waves produced by a single impulse in water of any depth, or in a dispersive medium. *Phil. Mag.*, 23:252–255, 1887.

[57] G. N. Watson. The limit of applicability of the principle of stationary phase. *Proc. Camb. Phil. Soc.*, 19:49–55, 1918.

[58] G. Muyo and A. R. Harvey. Decomposition of the optical transfer function: wavefront coding systems. *Opt. Letters*, 30:2715–2717, 2005.

[59] G.W. Forbes. Using rays better. iv. theory of refraction and reflection. *J. Opt. Soc. Am. A*, 18:2557–2565, 2001.

[60] J. J. Stamnes. *Waves in focal regions.* Institute of Physics, London, 1986.

[61] Zemax. Optical design software from `http://www.zemax.com`.

[62] A. E. Savakis and H. J. Trussell. On the accuracy of psf representation in image restoration. *IEEE Transactions on Image Processing*, 2:252–259, 1993.

[63] E. Dowski and G.E.Johnson. Waveront coding: A modern method of achieving high performance and/or low cost imaging system. *SPIE*, 3779:137–145, 1999.

[64] A. Sauceda and J. Ojeda-Castaneda. High focal depth with fractional-power wave fronts. *Opt. Lett.*, 29:560–562, 2004.

[65] S. Mezouari. *Wavefront coding for the alleviation of aberrations in incoherent imaging systems.* PhD thesis, Heriot-Watt University, Department of Electrical, Electronic, & Computing Engineering, 2003.

[66] E.R. Dowski. Wavefront coding optics. US Patent 6,842,297 B2, 2005.

[67] Z. Zalevsky. Optical method and system for extended depth of focus. US Patent application 10/97494, 2004.

[68] S. Mezouari and A. R. Harvey. Combined amplitude and phase filters for increased tolerance to spherical aberration. *J. Mod. Opt.*, 50:2213–2220, 2003.

[69] X. Liu, X. Cai, S. Chang, and C. P. Grover. Optical system having a large focal depth for distant object tracking. *Opt. Express*, 11:3242–3247, 2003.

[70] D. Zalvidea, G. Colautti, and E. E. Sicre. Quality parameters analysis of optical imaging systems with enhanced focal depth using the wigner distribution function. *J. Opt. Soc. Am. A*, 17:867–873, 2000.

[71] G.W.Ritchey and H.Chretien. Prsentation du premier modle de tlescope aplantique. *Compt. Rend.*, 185:266–268, 1927.

[72] V. A. Borovikov. *Uniform Stationary Phase Method.* Institution of Electrical Engineers, London, 1994.

[73] A. Papoulis. *Signal Analysis.* McGraw-Hill, New York, 1977.

[74] S. S. Sherif, E. R. Dowski, and W. T. Cathey. Extended depth of field in hybrid imaging systems: circular aperture. *J. Mod. Opt.*, 51:1191, 2004.

[75] D. Malacara and S. DeVore. *Evaluation and Wavefront Fitting in Optical Shop Testing.* Wiley, New York, 1992.

[76] S. Kirkpatrick, G. D. Gelatt, and M.P. Vecchi. Optimization by simulated annealing. *Science*, 220:671–, 1983.

[77] L. Ingber. Adaptive simulated annealing (ASA) C code, available from `http://www.ingber.com`.

[78] K. Kubala, E. Dowski, and T. W. Cathey. Reducing complexity in computational imaging systems. *Opt. Express*, 11:2102–2108, 2003.

[79] C. S. Williams and O. A. Becklund. *Introduction to the Optical Transfer Function.* SPIE Press, Bellingham, WA, 2002.

[80] S. Mezouari and A. R. Harvey. Validity of fresnel and fraunhofer approximations in scalar diffraction. *J. Opt. A Pure Appl. Opt.*, 5:S86–S91, 2003.

[81] T. W. Cathey and E. Dowski. New paradigm for imaging systems. *Appl. Opt.*, 41:6080–6092, 2002.

[82] J.M. Ali, R.M. Tookey, J.V. Ball, and A.A. Ball. The generalised cornu spiral and its applications to span generation. *J. Comp. and Appl. Math.*, 102:37–47, 1999.

[83] D.J. Struik. *Lectures on Classical Differential Geometry.* Addison-Wesley, Reading, MA, 1950.

[84] S. Mezouari, G. Muyo, and A. R. Harvey. Circularly symmetric phase filters for control of primary third-rder aberrations:coma and astigmatism. *J. Opt. Soc. Am. A*, 23:1058–1062, 2006.

[85] P. W. Kruse. *Uncooled thermal imaging arrays, systems, and applications.* SPIE press, Bellingham, WA, 2001.

[86] R. D. Fiete and T. Tantalo. Comparison of snr image quality metrics for remote sensing systems. *Opt. Eng.*, 40:574–585, 2001.

[87] M. Bertero and P. Boccacci. *Introduction to Inverse Problems in Imaging.* Taylor and Francis, London, 1998.

[88] C. W. Helstrom. Image restoration by the method of least squares. *JOSA*, 57:297–303, 1967.

[89] B. R. Frieden. *Image enhancement and restoration in Topics In Applied Physics*, volume 6. T. S. Huang, Springer-Verlag, New York-London, 1979.

[90] S.Bradburn, E.R.Dowski, and W.T.Cathey. Realizations of focus invariance in optical-digital systems with wavefront coding. *Appl. Opt.*, 26:9157–9166, 1997.

[91] J. van der Gracht, J. Nagy, P.Pauca, and R. Plemmons. Iterative restoration of wavefront coded imaginero for focus invariante. *OSA Trends in Optics and Photonics (TOPS), Integrated Computational Imaging Systems,*, OSA Technical Digest, 2001.

[92] B. Plemmons *et al.* Computational imaging systems for iris recognition. *Proc. SPIE*, 57, 2004.

[93] S. S. Sherif, E. R. Dowski, and W. T. Cathey. Effect of detector noise in incoherent hybrid imaging systems. *Opt. Lett.*, 30:2566–2568, 2005.

[94] R. Vollmerhausen and R. Driggers. *Analysis of sampled imaging systems,* T*utorial texts in optical engineering.* SPIE press, Bellingham, WA, 2000.

[95] G.D.Boreman. *Modulation transfer function in optical and electrooptical systems.* SPIE press, Bellingham, WA, 2001.

[96] S.K.Park and Z.Rahman. Fidelity analysis of sampled imaging systems. *Opt. Eng.*, 38:786–800, 1999.

[97] W. Schneider and W. Fink. Integral sampling in optics. *Optica Acta*, 23:1011, 1976.

[98] R. Vollmerhausen. *Display of sampled imagery.* EO Imaging: Systems and Modeling, L. Biberman Ed., Andover, MA: ONTAR Corp., 2000.

[99] O. H. Schade. *Perception of Displayed Information.* L . M. Bibermann, Plenum, New York-London, 1973.

[100] R. Vollmerhausen, R. Driggers, and M. Tomkinson. Improved image quality metric for predicting tactical vehicle identification. *Proc. SPIE*, 4030:60–69, 2000.

[101] J. A. Ratches, R. H. Vollmerhausen, and R. G. Driggers. Target acquisition performance modeling of infrared imaging systems: Past, present, and future. *IEEE Sensors Journal*, 1:31–41, 2001.

[102] S.K.Park, R. Schowengerdt, and M. Kaczynski. Modulation-transfer-function analysis for sampled image systems. *Appl. Opt.*, 23:2572, 1984.

[103] M. Sensiper, A.D. Ducharme G.D. Boreman, and D.R. Snyder. Modulation transfer function testing of detector arrays using narrow-band laser speckle. *Opt. Eng.*, 32:395–401, 1993.

[104] Random transparency targets for modulation transfer function measurement in the visible and infrared regions. A. daniels and g.d. boreman and a.d. ducharme and eyal sapir. *Opt. Eng.*, 34:860–869, 1995.

[105] E.Findlay, B.Lucotte, G.Muyo, and A.R. Harvey. Artefact removal from phase encoded images. EU Patent application, 2006.

[106] University of Rochester. Magnetorheological finishing `http://qedmrf.com`.

[107] M. Riedl. *Optical design fundamentals for infrared systems.* SPIE press, Bellingham, WA, 2002.

[108] Y. Guimond, J. Franks, and Y. Bellec. Comparison of performances between gasir moulded optics and existing ir optics. *Proc. SPIE*, 5406, 2004.

[109] A.Crastes, J.L. Tissot, Y. Guimond, P.C. Antonello, J. Leleve, H.J. Lenz, P. Potet, and J.J. Yon. Low cost uncooled irfpa and molded ir lenses for enhanced driver vision. *Proc. SPIE*, 5251, 2004.

[110] A. Mann. *Infrared Optics and Zoom Lenses.* SPIE press, Bellingham, WA, 1999.

[111] R. E. Fischer and B. Tadic-Galeb. *Optical System Design.* McGraw-Hill, New York, 2000.

[112] D.S. Grey. Athermalization of optical systems. *J.Opt.Soc.Am.*, 38:542–546, 1948.

[113] R. L. Sinclair. High magnification zoom lenses for 35 μm applications. *Proc. SPIE*, 3429:11–18, 1998.

[114] M. Shechterman. Zoom athermal telescope having 18.5 magnification range for 812 μm range FLIR systems. *Proc. SPIE*, 2539:108–117, 1995.

[115] R. Simmons. Athermalisation of a fast infrared telescope objective. *Proc. SPIE*, 2539:137–1492, 1995.

[116] T.H. Jamieson. Thermal effects in optical systems. *Opt. Eng.*, 20:156–160, 1981.

[117] G.P.Berhmann and J.P.Bowen. Influence of temperature on diffractive lens performance. *Appl.Opt.*, 32:2483–2489, 1993.

[118] H.S.Kim, C.W.Kim, and S.M.Hong. Compact mid-wavelength infrared zoom camera with 20:1 zoom range and automatic athermalization. *Opt. Eng.*, 41:1661–1667, 2002.

[119] G.Muyo and A.Harvey. Feasibility study into the application of wavefront coding for electro-optic protection measures, DSTL, april 2006.

[120] P.Jansson. *Deconvolution with application in spectroscopy.* Academic Press, New York, 1984.

[121] R.C. Gonzales and R.E. Woods. *Digital Image Processing.* Prentice Hall, 2nd Ed., 2002.

[122] S. N. Torres and M. M. Hayat. Kalman filtering for adaptive nonuniformity correction in infrared focal-plane arrays. *J. Opt. Soc. Am. A*, 20:470–481, 2003.

[123] N. G. van Kampen. An asymptotic treatment of diffraction problems. *Physica*, 14:575–589, 1949.

[124] N. G. van Kampen. An asymptotic treatment of diffraction problems ii. *Physica*, 16:817–821, 1950.

[125] J. J. Stamnes. Uniform asymptotic theory of diffraction by apertures. *J.Opt.Soc.Am.*, 73:96–109, 1983.